TRINITY COLLEGE DUBLIN

Magnetic investigations of Mn-based and Mn-free potential half metals

Rui Zhang

School of Physics

University of Dublin

This thesis is submitted to the University of Dublin for the degree of

Doctor of Philosophy

March 2022

Declaration

I hereby declare that this thesis is original and has not been submitted in whole or in part for consideration for any other degree or qualification in this, or any other University.

This thesis is the result of my own work and includes nothing which is the outcome of work done in collaboration, except where specifically indicated in the text.

I agree to deposit this thesis in the University's open access institutional repository or allow the library to do so on my behalf, subject to Irish Copyright Legislation and Trinity College Library conditions of use and acknowledgement.

Rui Zhang

15th March 2022

Dedicated to my family

Acknowledgements

I would like to acknowledge my supervisor Prof. J. M. D. Coey firstly for allowing me the opportunity to do my research in his group. His enthusiasm and passion for research are always inspiring me. Words cannot describe how he helped me in developing my scientific knowledge and skills. Moreover, many thanks to my co-supervisor Dr. M. Venkatesan for his guidance and help anytime I needed, especially for teaching me the experimental techniques of preparing samples in bulk and interpreting the experimental data. His encouragement helped me come over the tough time during my PhD.

I do like to express my sincere gratitude to Dr. Z. Gercsi for his help and advice. His theoretical calculations promoted my research progress. Special thanks to Prof. P. Stamenov for his help in fitting and taking the measurement of the Mössbauer spectrum.

I'm very grateful to Dr. Yangkun for being a guide and a good friend of mine and for sharing his knowledge of physics with me. He spent numerous hours discussing the physical aspects that I present in this thesis and physics in general. Also, he always motivated and encouraged me whenever I was failing in the experiment. The climbing activity, almost every weekend, with Zexiang Hu and Dr. Yangkun is a very valuable experience.

My precious friend Dr Anup Kumar, I do thank you for sharing his chemistry knowledge and life experiences with me. The coffee time with him is a good memory and talking with him improved my spoken English. Special thanks to the former group member Dr. Hwachol Lee for his guidance and advice on thin film growth and characterization.

Here, I would like to thank the past and present members of the Magnetism and Spintronics group at Trinity College Dublin for their help and support throughout my PhD. They were always ready to offer help and advice when I needed it and working with them has been a privilege. I have learned many valuable skills and knowledge from them. I would like to thank the other group members: Dr. Karsten Rode, Dr. Katarzyna Siewierska, Dr. Jean Besbas, Dr. Gwenael Atcheson, Dr. Niclas Teichert, Dr. Hasan Ahmadian Baghbaderani, Zexiang Hu, Sruthy Poulose, Ajay Jha, Lucy Prendeville, Ross Smith, Simon Lenne, Brian Shortall, Jack O'Brien.

Abstract

This thesis is concerned with an unusual category of magnetically ordered material, the zero moments ferrimagnetic half metal, which has potential for applications in thin film memory and logic devices. The materials are all prepared in bulk form. Due to the problem of Mn diffusion into the MgO tunnel barriers in thin film devices, it is necessary to explore compensated ferrimagnetic Mn-free half metals.

Chapter 1 starts with the introduction of magnetism, including its history over the centuries and the main concepts of magnetism in solids, consisting of magnetic interactions, crystal field, critical behaviour *etc*. One type of magnetic material we are especially interested in is half-metal, showing 100% spin polarization. It has a band gap, behaving like an insulator, in one spin channel, while in the other one, it shows a non-zero density of states at the Fermi level. As a family of half-metals, the Heusler-type alloys with high Curie temperature are promising. The development of spintronic materials would boost non-volatile memory expansion in limited space, like magnetic random-access memory.

Chapter 2 is related to experimental procedures which were used during the investigations, including arc-melting, chemical vapour transport method, annealing treatments, x-ray diffraction, SQUID magnetometry, Mössbauer spectroscopy and point contact Andreev reflection measurement (PCAR).

In chapter 3, rare-earth-free ferrimagnets $Mn_{4-x}Z_xN$ (Z = Cu — Ge and Ag — Sn) were investigated, which exhibit a magnetic compensation at room temperature. Compensated ferrimagnets exhibiting the characteristics of antiferromagnets (zero moments) and ferromagnets (transport properties) create opportunities for applications in high-frequency spintronics and low-energy loss communications. Apart from the traditional linear antiparallel alignments of sublattices, the non-collinear frustrated 2.35 μ_B moments of Mn on 3c sites of the (111) Kagome planes tilt about 20° out-of-plane in Mn_4N and are easily influenced by substitutions on 1a sites, leading to different efficiency of compensation in $Mn_{4-x}Z_xN$. The manganese site moments are determined by Z, orbital hybridization, charge transfer and the tilt angle, analysed by constrained density functional theory. The Ga

compound with compensation at room temperature for x ≈ 0.26 we recommend for high-frequency spintronic applications.

However, the spin polarization of those ferrimagnets can never achieve the ideal value (100%) indicated by the band structures of the non-collinear Mn_4N ferrimagnets calculated by Dr. Zsolt Gercsi. Fully compensated ferrimagnetic half-metals are required for low energy loss communications and high frequency spintronics. They are magnetically ordered materials that show ideal spin polarization with zero stray fields. The crystallographically inequivalent magnetic sublattices with the antiparallel alignment of their spins lead to compensated ferrimagnetism with no net magnetization.

In chapter 4, Mn-based Heusler ferrimagnetic half metals are developed by two methods. One is tuning the Fermi level by doping V into Mn_2FeAl to obtain the same electron states in two spin channels, leading to zero moments. The other one is combining two half metals with magnetic moments of opposite signs (one with $Z_t = 22$, Mn_2VAl; the other with $Z_t = 25$, Mn_2FeAl)) to obtain a fully compensated ferrimagnetic half metal. These ideal half metals are potential candidates for spintronic devices. Up until now, we have developed three Mn-based ferrimagnets with low moments, but unfortunately, the problems of Mn diffusion into the tunnel barrier in thin film devices have been discussed recently.

We then moved to explore Mn-free alloys in chapter 5. Four Mn-free binary (V_3Al/Ga) and quaternary Heuslers (CrVTiAl/Ga) with 18 valence electrons and ideally ordered crystal structures, which have been theoretically predicted to be zero-moment half metals or spin gapless semiconductors, are studied experimentally. Experiments show that highly ordered quaternary structures cannot be obtained in bulk materials, consistent with the calculated 'Hull distance' that provides an idea of the absolute phase stability. Further study on the magnetism of itinerant elements, *e.g.* V, Pt, provides an idea to develop new Mn-free ferrimagnets by controlling the itinerant elements' bond length.

Chapter 6 investigates the critical behaviour and first-order transition in the low-spin pyrite CoS_2, which was recently identified as a topological ferromagnet with high spin polarization. Tricritical behaviour observed in scaling plots that indicates the appearance of ferromagnetism in CoS_2 is a first-order phase transition. Critical exponents $\beta = 0.196$, $\gamma = 0.972$ and $\delta = 5.27$ do not obey the Widom equality which suggests a first-order transition.

Finally, in chapter 7, the results were summarized, and future work is described.

List of publications

List of Publications (connected with the thesis)

1. **R. Zhang**, Z. Gercsi, D. M. Venkatesan, Karsten Rode and J. M. D. Coey**,** Pauli paramagnetism of cubic V_3Al, CrVTiAl and related 18-electron Heusler compounds with a group 13 element, Physical Review B **103**,174407 (2021).

2. **R. Zhang**, Z. Gercsi, D. M. Venkatesan, A. Jha, P. Stamenov, and J. M. D. Coey, Spin liquids and spin glasses in Mn-based alloys with the cubic A13 (β-Mn) structure, Journal of Magnetism and Magnetic Materials **501**, 166429 (2020).

3. **R. Zhang**, Yangkun He, Daniel Fruchart, J. M. D. Coey, Zsolt Gercsi, Rare-earth-free noncollinear metallic ferrimagnets $Mn_{4-x}Z_xN$ with compensation at room temperature, Acta Materialia, **234**, 118021 (2022).

Other Publications

1. **R. Zhang**, Chao Zhou, Kaiyun Chen, Kaiyan Cao, Yin Zhang, Fanghua Tian, Adil Murtaza, Sen Yang, Xiaoping Song, Near-zero magnetostriction in magnetostrictive FeCo alloys, Scripta Materialia **203**, 114043 (2021).

2. Anup Kumar, **R. Zhang**, M. Venkatesan, Plamen Stamenov and J. M. D. Coey, Exfoliation of hematite: Morphological, structural and magnetic investigations**,** Journal of Magnetism and Magnetic Materials **542**, 168507 (2022).

3. J. M. D. Coey, P. Stamenov, S. Porter, M. Venkatesan, **R. Zhang**, and T. Iriyama, Sm-Fe-N revisited; Remanence enhancement in melt-spun Nitroquench material, Journal of Magnetism and Magnetic Materials **480**, 186 (2019).

Glossary

Annealing: Heating the material uniformly; the time and temperatures required in the process are set. The longer the time taken to anneal, the more homogenous the sample will usually become

Quenching: Fast cooling by immersing in ice water or the atmosphere.

CVT: Chemical vapour transport.

SOI: Spin-orbit interaction

Magnetization: Magnetic dipole moment per unit volume of material.

FM: Ferromagnetic.

FiM: Ferrimagnetic

AFM: Antiferromagnetic.

PM: Paramagnetic.

Curie temperature T_C: The temperature where the long-range order of the magnetic moments vanishes.

Néel temperature T_N: The temperature where an antiferromagnetic substance becomes a paramagnet. This is analogous to the Curie temperature of ferromagnets.

Magnetic compensation temperature: The temperature appears at which the magnetic moments of the equivalent sublattice are antiparallel.

SQUID: Superconducting quantum interference device.

PCAR: Point contact Andreev reflection.

DSC: Differential scanning calorimetry

QS: Quadrupole splitting

EFG: Electric field gradient

Stray field: Equivalence of demagnetizing field in the volume of surrounding a magnet.

SGS: Spin gapless semiconductor

Contents

Chapter 1   Introduction

1.1 Main concepts to Magnetism

Magnetism describes an invisible 'force', attracting materials, like Fe, Ni and Co. This was first revealed, and the discovery traced back to the ancient world - lodestones (Fe_3O_4) in the ancient world. Utilizing this magic property, the navigational compass was the first technical application proposed [1]. In the following centuries, the knowledge of magnetism and magnetic materials has been constructed and developed. The most inspiring theory, the Curie-Weiss theory of ferromagnetism, is a modern understanding, which reveals that quantum mechanics cannot be separable from magnetism. In order to understand the origin of magnetism in solid materials, it is required to know the fundamental concepts of magnetism, from a quantum mechanical understanding to solid magnetic materials.

1.1.1 Magnetic moments

As the elementary quantity of magnetism, the magnetic moment is used to characterize the magnitude and orientation of the magnetic fields a magnet produces [1]. On an atomic scale, the spin of each electron and its orbital motions around the nucleus are associated with the intrinsic magnetic moments, *i.e.* the intrinsic magnetic moments come from the spin and orbital angular momentum. Consider the Bohr model of an atom, where electrons travel in circular orbits around the nucleus, which can be considered as a current loop. This is around an elementary area A and carries a current I. The magnetic moment $\mathfrak{m}$ is defined as

$$\mathfrak{m} = IA \tag{1.1}$$

and the unit of the magnetic moment is Am^2. The current I ($= -e/\tau$) is around the atom with the orbital period $\tau = 2\pi r/v$. The magnetic moment of an electron also can be represented in

terms of the orbital angular momentum $l = \mathrm{m_e} \boldsymbol{r} \times \boldsymbol{v}$ ($\boldsymbol{r}$, radius of the current loop; $\boldsymbol{v}$, velocity of the electron).

$$\mathrm{m} = IA = -\frac{1}{2}e\boldsymbol{r} \times \boldsymbol{v} = -\frac{e}{2m_e}\boldsymbol{l} \tag{1.2}$$

The orbital angular momentum is quantized in units of $\hbar$ along a given direction z-axis:

$$\mathrm{m}_z = -\frac{e}{2m_e}m_l\hbar = \mu_B m_l \tag{1.3}$$

where $-e\hbar/2m_e$ is a constant and defined as the Bohr magneton $\mu_B = 9.274\times10^{-24}$ JT^{-1}. The magnitude of the orbital angular momentum is $\sqrt{l(l+1)}\hbar$ ($-l \leq m_l \leq l$). Similarly, the intrinsic spin angular momentum of an electron is

$$\mathrm{m} = -\frac{e}{m_e}m_s\hbar = -\frac{e}{m_e}\boldsymbol{s} \tag{1.4}$$

where $\boldsymbol{s}$ is the *spin* magnetic quantum. The value of any component of the spin angular momentum only takes one of the $2s + 1$ possible values. Furthermore, the component of the spin moment along the z -axis is

$$\mathrm{m}_z = -\frac{e}{m_e}m_s\hbar \tag{1.5}$$

where m_s is equal to $\pm\frac{1}{2}$ corresponding to the spin-up and spin-down states. It is noted that the nucleus may have spins. However, its rest mass is nearly 2000 times larger than that of an electron, leading to negligible contributions to the magnetic moments.

Generally, the total magnetic moment of an atomic electron, which possesses both spin and orbital angular momentum, may stem from the spin-orbit coupling interactions, creating a total electron angular momentum $\boldsymbol{j} = \boldsymbol{l} \pm \boldsymbol{s}$. Therefore, it can be expressed as

$$\mathrm{m} = \mathrm{m}_s + \mathrm{m}_s = -g\mu_B\frac{\boldsymbol{j}}{\hbar}, \tag{1.6}$$

where g ($= g_s + g_l$) is Landé g-factor and g_s and g_l are the corresponding spin and orbital g-factor, respectively.

The spin-orbit interaction (SOI) comes from the interaction of the spin of a moving particle with a potential in respect of relativistic quantum mechanics. For example, in the classical single-electron model in an atom (atomic number Z), the electron orbits with v velocity at distance r and thus the orbiting nucleus is equivalent to a current loop $I = Zev/2\pi r$, generating a magnetic field ($B_{SOI} = \frac{\mu_0 I}{2r} = \frac{Z\mu_0 ev}{4\pi r^2}$) at the position of the electron. The potential energy is given by $\varepsilon = \boldsymbol{m} \cdot \boldsymbol{B}$, where $\boldsymbol{m}$ is from the electron and $\boldsymbol{B}$ is from the orbital motion. It can be rewritten as

$$\varepsilon_{SOI} = -\mu_B B_{SOI} = -\mu_B \frac{Z\mu_0 ev}{4\pi r^2} \tag{1.7}$$

If we approximate the value of $r \approx \frac{a_0}{Z}$ for an inner electron, where a_0 is the Bohr radius and $m_e vr \approx \hbar$. The SOI energy can be rearranged as

$$\varepsilon_{SOI} = -\mu_B \frac{Z\mu_0 ev}{4\pi r^2} \approx \frac{2Z^4 \mu_0 {\mu_B}^2}{4\pi {a_0}^3} \tag{1.8}$$

which is proportional to Z^4. Therefore, the effect of SOI is sensitive to the atomic number. That indicates that the SOI energy of the heavier elements is far more important, especially of the inner electrons, $e.g.$ Pt; inversely, the ε_{SOI} for light elements is weaker. The Hamilton operator of the SOI for a single electron is

$$\mathcal{H}_{\text{so}} = \lambda \hat{\boldsymbol{l}} \cdot \hat{\boldsymbol{s}} \tag{1.9}$$

where λ is the spin-orbit coupling energy and $\hat{\boldsymbol{l}}$ and $\hat{\boldsymbol{s}}$ are dimensionless operators. In the multielectron atom, the single-electron SOI becomes $(\Lambda/\hbar^2)$ $\hat{\boldsymbol{L}} \cdot \hat{\boldsymbol{S}}$. The capital letters $\boldsymbol{L}$ and $\boldsymbol{S}$ stand for the sums of l and s for the electrons. It should be noted that the sign of the constant Λ is positive for the 3d or 4f series and negative for the second half according to Hund's third rule.

In a magnetic solid, consisting of a large number of atoms with magnetic moments, its magnetization $\boldsymbol{M}$ ($= \frac{\sum_{i=0}^{N} m_i}{V}$) can be defined by the moment of an electron with N atoms in terms of the total magnetic moment per unit volume.

1.1.2 Magnetic fields

A magnetic field describes a vector field that is created by moving charged particles [2], which experience a force known as Lorentz force $f = q(E + v \times B)$ (q, charge of the particle; E, electric field; B, magnetic field). In electrostatics, charged particles experience the force only associated with the E-field due to the zero B-field, *i.e.* $f = qE$. The Lorentz force equation establishes B-field and its magnitude depends on the definition of the ampere. The relation between the B-field and the total current density j is well known as Ampere's law,

$$\nabla \times B = \mu_0 j = \mu_0(j_c + j_m) \tag{1.10}$$

where j_c is the conduction current and j_m is the Ampèrian magnetization current. The later current j_m is determined by

$$j_m = \nabla \times M \tag{1.11}$$

which is deduced from Stoke's theorem for the magnetization currents [3]. The B-field is measured in the unit of Tesla (1 T $\approx$ 800 kA m^{-1}).

The other magnetic field is H, which is useful to retain Ampere's law. It can be expressed as

$$H = \frac{B}{\mu_0} - M \tag{1.12}$$

Here, the H-field is introduced as an auxiliary magnetic field. The curl of the H-field can be deduced from Eq. 1.10 to Eq. 1.12

$$\nabla \times H = j_c \tag{1.13}$$

These two 'magnetic fields', the B-field and the H-field, in free space are linearly related by

$$B = \mu_0 H \tag{1.14}$$

where $\mu_0 = 4\pi \times 10^{-7}$ TmA^{-1} is the magnetic permeability of free space. In a magnetic solid, the condition changes to be more complicated and the general vector relation between the **B**-field and the **H**-field is normally arranged as

$$B = \mu_0 (H + M). \qquad (1.15)$$

Similarly, an **H**-field in any magnet can be decomposed into two components, H_c and H_m, where H_c is created by conduction currents and H_m consists of stray fields produced by magnetization distributions of other magnets and demagnetizing field H_d from the magnet itself, shown in Fig. 1.1 [1]. The units of **H** and **M** are Am^{-1}. Inside the magnet, the relation at point 'P' of the quantities **B**, **H,** and **M** of a uniformly magnetized bar magnet with zero external magnetic fields. The direction of **H** is opposite to both **B** and **M** inside the magnet, which originates from the external and internal surfaces of the magnet.
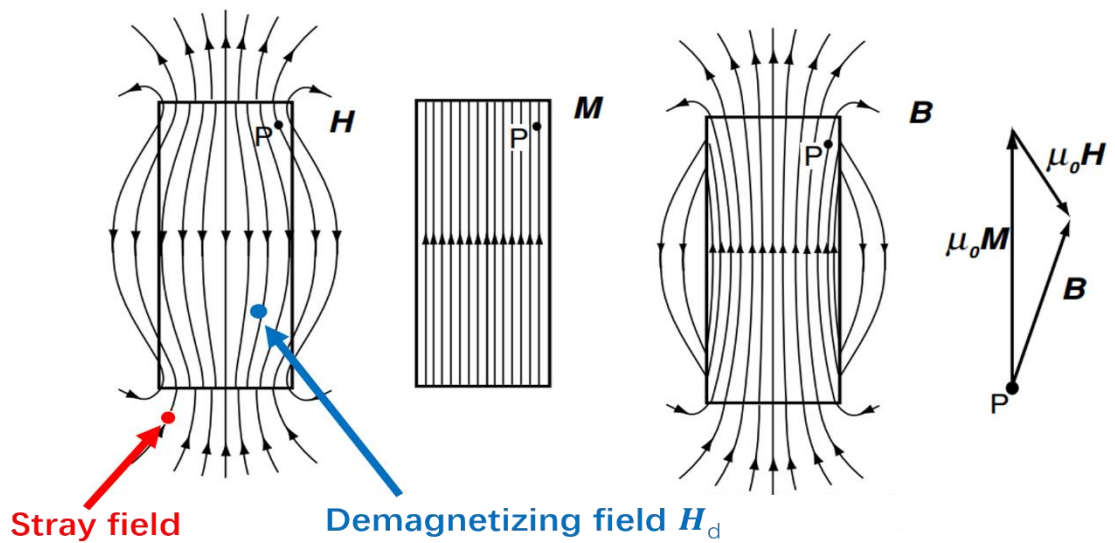
Fig. 1.1. The relationship of the **B**-field, **H**-field, and **M** at 'P' point for a uniform magnet [1]. The stray field outside a magnet and the demagnetizing field within it are illustrated. The demagnetizing field H_d is equal to $-\mathcal{N}M$ ($0 < \mathcal{N}$).

When considering a magnetization process, the **H**-field at points inside the material consists of the demagnetizing field H_d and the fields produced by external magnets and conduction currents. That is to say the internal field **H** in the magnet with a continuous

medium approximates a sum of the external field, produced by steady electronic currents or the stray field of magnets outside the sample volume, and the demagnetizing field produced by magnetization distributions of the sample itself. The relation between H_d and M is given by

$$H_d = -\mathcal{N}M \tag{1.16}$$

where $\mathcal{N}$ is the demagnetizing factor depending on the shape of the sample and the direction of M. It takes a value ranging from 0 to 1, *e.g.* toroid, long needle, and thin film with the magnetization along the long axis where $\mathcal{N} = 0$, and sphere with the magnetization along any direction where $\mathcal{N} = 1/3$. Therefore, depending on both demagnetizing factor and magnitude of the magnetization, the demagnetization field should be taken into consideration once H_d is comparable to the external field. While, if H_d is very small, the total field can approximately equal the external field.

1.2 Magnetism in solids

Solids consist of many atomic magnetic moments which can act together in a collaborative way. That means the atoms' magnetism in a solid might be quite different from what would be observed when all the magnetic moments were isolated from one another. And it tends to be destroyed by chemical interactions of the outermost electrons. It may occur in various ways. For example, in ionic compounds, electron transfers between anions and cations to form filled shells; covalent bond formation normally is established in semiconductors or band formation in metals.

With the help of the example of iron, the understanding of the magnetism of a solid becomes clear. The electronic configuration of atomic iron is (Ar) $3d^4s^2$, where four of the $3d$ electrons are unpaired, producing a maximal magnetic moment of 4 μ_B, whereas, in a solid, the outer $4s$ orbitals first overlap to form a broad $4s$-band, then the smaller $3d$ orbitals form a considerably narrow band. This leads to $4s$ to $3d$ charge transfer producing an electronic configuration, (Ar) $3d^{7.4}s^{0.6}$, in iron metal. The narrow $3d$ band will split

spontaneously to form a ferromagnetic state if the Stoner criterion is satisfied. In a normal αFe in its bcc phase, the electrons are paired perfectly in all the inner shells and largely paired in the 4s-band. Its 3d-orbital spin configuration is $3d^{\uparrow 4.8}d^{\downarrow 2.6}$. Therefore, 2.2 unpaired spins yield 2.2 μ_B magnetic moments. The $\uparrow$ and $\downarrow$ electrons occupy different spin-split sub-bands. Moreover, the magnetic moments are equal to the balance of the asymmetric splitting and occupation of spin-up and spin-down states.

It has to be emphasized that the nature of the chemical bonding determined by crystal structure and composition is very sensitive to solid magnetism. For example, γFe in its fcc (face-centred-cubic) phase might be antiferromagnetic but its magnetism is unstable which depends on the lattice parameter [1]. Other examples associated with Fe in different crystalline environments exhibiting different magnetism are included in Table 1.1.

Table 1.1. Atomic moments of iron in different crystalline environments [1].

Material	Magnetism	Magnetic moments (μ_B/Fe)
γ–Fe$_2$O$_3$	Ferrimagnetic	5
αFe	Ferromagnetic	2.2
γFe	Antiferromagnetic	unstable
YFe$_2$	Ferromagnetic	1.45
YFe$_2$Si$_2$	Pauli paramagnetic	0
FeS$_2$	Diamagnetic	0

The other point to be noted is that the behaviour of electrons in narrow bands for 3d orbitals can be explained in two limits: localized and delocalized. For the localized limit, the correlations of the electrons on the ion cores are strong due to the Coulomb interaction. Therefore, the utter electron is hard to transfer to its neighbours. In this limit, the magnetism is mainly dominated by the atom itself. However, in the delocalized limit, the Coulomb interaction between the nuclear charge and electron is not stronger anymore, of order 1 eV.

That is to say the outer electrons are not constrained to the atom and are liable to be shared with or transferred to its neighbours. Generally, the localized model is fit for $4f$ and $3d$ electrons in insulating compounds, where their inner $4f$ shell rarely participates in the bonding. This results in the integral number of unpaired spins per atom (e.g. Ni^{2+} $3d^8$, $m = 2$ μ_B) and discrete energy levels, which obey Boltzman statistics. Compared to the localized case, the delocalized model describes the magnetic electrons in wave-like extended states forming energy bands. The particular character of this model is that the number of electrons in bands crossing the Fermi level is not integral (*e.g.* Ni, $3d^{9.4}4s^{0.6}$, $m = 0.6$ μ_B) and the electrons obey Fermi-Dirac statistics. The common point of these two models is that neither localized nor delocalized moments vanish above the Curie temperature T_C and become paramagnetic. The magnetism in different types is going to be introduced in the following section.

1.2.1 Magnetic interactions

There are five main types of magnetism, ferromagnetism (FM), ferrimagnetism (FiM), antiferromagnetism (AFM), diamagnetism (DM) and paramagnetism (PM). Table 1.2 summarize the features of each type of magnetism. The Curie-Weiss theory describes the magnetic transition from FM to PM corresponding to the transition temperature T_C in ferromagnets. Similarly, from AFM to PM, the transition behaviour is called Néel transition, corresponding to the transition temperature T_N.

Table 1.2 Summary of five main magnetism types.

Type	Moment order	Susceptibility χ (SI)	Saturation magnetization
FM	Spontaneous parallel alignment of moments	~10^3	Large

FiM	Unequal ferromagnetic sublattice with antiparallel alignment, showing a net magnetisation.	$\sim 10^3$	Small
AFM	Equal ferromagnetic sublattice with antiparallel alignment, showing a zero magnetisation.	$\sim 10^{-1}\text{-}10^{-4}$	Zero
DM	Antiparallel alignment of induced moments to the applied magnetic field. The effect is weak.	$\sim -(10^{-3}\text{-}10^{-5})$	/
PM	Randomly oriented magnetic moments under zero field, showing zero net moment. Under an applied field, moments align along the field direction, but the effect is weak.	$\sim 10^{-3}\text{-}10^{-6}$	/

Ferromagnetic or ferrimagnetic materials which have magnetic order exhibit spontaneous magnetization without applied fields below the phase transition temperature T_C. The moments of all magnetic atomic species in a ferromagnet align in the same direction as the external magnetic fields, which all positively contribute to the magnetization (Fig. 1.2). In a ferrimagnet, inequivalent magnetic species are aligned anti-parallel to the external fields which leads to a weak magnetization (Fig. 1.2). It is noted that ferromagnetism is generated in materials with asymmetric d or f electrons in spin-up and –down states under zero magnetic field. In addition, thermal perturbations can destroy the spontaneous magnetic order above T_C resulting in a paramagnetic behaviour (Fig. 1.2).

Antiferromagnetic materials with equivalent magnetic sublattices arranged in antiparallel alignment produce zero magnetic moments (Fig. 1.2). Therefore, one outstanding characteristic of an antiferromagnet is that there is no stray field, which can reduce the energy loss. Generally, antiferromagnetic ordering exists at sufficiently low

temperatures and vanishes at or above the transition temperature T_N. It is noted that thermal perturbations may destroy the magnetic ordering as well. That means the antiferromagnetic materials will present paramagnetic behaviour above T_N.

Diamagnetic materials with an induced magnetization in an opposite direction to the applied field are repelled by a magnetic field. This repulsive force of diamagnet is in contrast to the attraction of ferro or ferri-magnetic materials. It is noted that the weak diamagnetic effect that is in most materials has its origin from the fact that magnetic moments produced by the electrons performing orbital motions align in the opposite direction to an applied field. The first discovery of diamagnetism was in bismuth, which was repelled by magnetic fields [4]. A rule of thumb that is used in chemistry to distinguish a material as paramagnetic or diamagnetic [5]: when all electrons are paired and there are no magnetic contributions, the material is diamagnetic; if unpaired electrons exist, the material is paramagnetic. One good example of a diamagnetic material is a superconductor.

Paramagnetic   Ferromagnetic   Ferrimagnetic   Antiferromagnetic

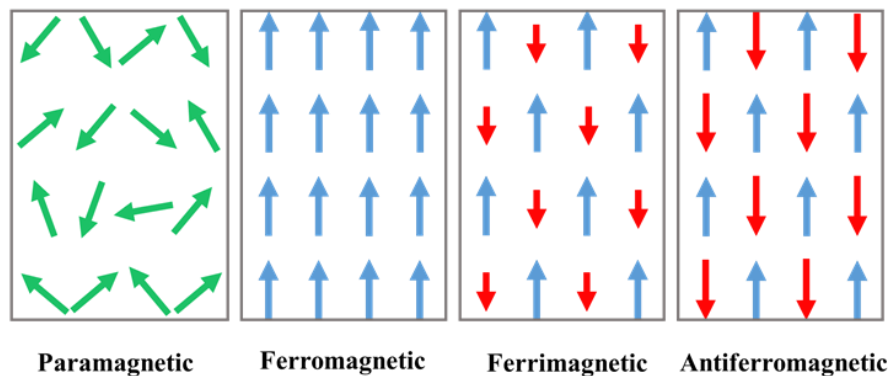Fig. 1.2. Schematic diagram of magnetic moments with alignment directions for paramagnetic, ferromagnetic, ferrimagnetic and antiferromagnetic materials.

The understanding of different magnetic interactions is helpful to establish the desired magnetic materials, like ferrimagnets, which is one purpose of our project.

1.2.1 Pauli paramagnetism

Paramagnetism is a form of magnetism where the magnetic moment induced by the

applied field is positive, proportional to the field strength and rather weak. The presence of unpaired electrons in the materials leads to paramagnetic behavior, which can be observed in most atoms and ions with incompletely filled atomic orbits. Compared to a ferromagnet, a paramagnet does not retain any magnetization when the external applied field is removed due to the thermal motion that randomizes the spin orientations. Even under the applied fields, their magnetization is small and proportional to the field strength owing to only a small fraction of the spins being oriented by the field.

Pauli paramagnetism occurs in metallic systems that are not magnetically ordered and have equal number of spin-up and spin-down electrons in zero applied field. Under a magnetic field, the conduction band splits apart into spin-up and spin-down sub-bands due to the Zeeman effect, which will create a magnetization. In order to keep the Fermi level identical for both bands, there will be an imbalance in the number of spin-up and spin–down (Fig. 1.3b). The positive Pauli paramagnetic susceptibility is given by $\chi_{pauli} = \frac{\delta M}{B} = D_F g \mu_B{}^2$, where D_F is the density of states at Fermi level. This expression shows that the Pauli paramagnetic susceptibility is *independent* of the temperature, unlike the Curie-law susceptibility for localized electrons. Temperature independence is the sign of the Pauli paramagnetism. It indicates that the Heusler alloy CrVTiAl and V_3Al in A2 structure are Pauli paramagnets, which will be introduced in Chapter 5.
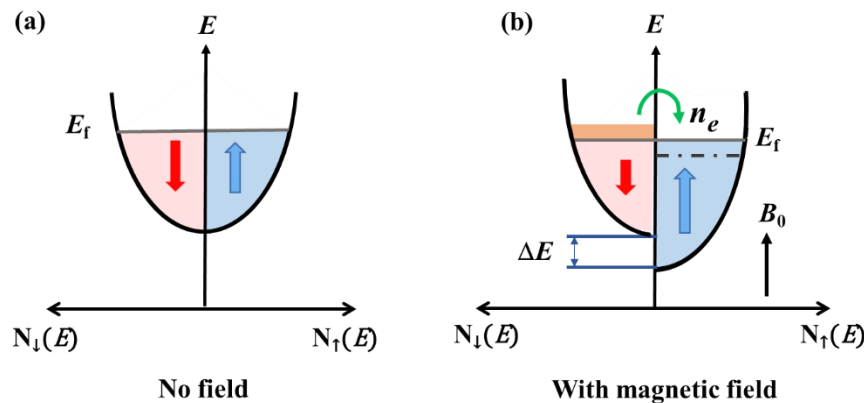

Fig. 1.3. Spin-up and spin-down state separation in a metal as per Pauli paramagnetism in the (a) absence of applied field ($B_0 = 0$) and (b) in the presence of field ($B_0 > 0$) [6].

1.2.2 Crystal field

Crystal field theory describes the degeneracy breaking of electron orbital states, usually d or f orbitals due to the Coulomb interaction produced by a surrounding charge distribution $\rho_0(r)$ of an ion or atom when it is embedded in a solid. Delocalized ions are nonmagnetic if their electronic shells are fully filled, while the shells of localized ions with a magnetic moment are partially filled. The crystal field interaction gives rise to the quenching of orbital angular momentum, which indicates that the magnitude of magnetic moments is only from spin for $3d$ ions. According to the Hund's rule, its magnetic moments $\boldsymbol{m} = -g(\mu_B/\hbar)\boldsymbol{J}$, where $\boldsymbol{J}$ is the total angular momentum and $\boldsymbol{J = S}$ for $3d$ ions.

The crystal field Hamiltonian is defined as

$$\mathscr{H}_{\mathrm{cf}} = \int \rho_0(r)\varphi_{cf}(r)d^3r \tag{1.18}$$

where φ_{cf} (r) is a potential produced by the charge distribution $\rho_0(r)$. And the total Hamiltonian of an ion or atom in a solid is expressed as

$$\mathscr{H} = \mathscr{H}_0 + \mathscr{H}_{\mathrm{so}} + \mathscr{H}_{\mathrm{cf}} + \mathscr{H}_Z \tag{1.29}$$

Where $\mathscr{H}_0$ is raised by the Coulomb interactions among the electrons and between the electrons and the nucleus, which produce the total spin and orbital angular momenta. The Hamiltonian operator of the Coulomb interaction is

$$\mathscr{H}_0 = \sum_i [-(\hbar^2/2m_e)\nabla^2 - Ze^2/4\pi\varepsilon_0 r_i] + \sum_{i<j} (e^2/4\pi\varepsilon_0 r_{ij}) \tag{1.20}$$

And $\mathscr{H}_{\mathrm{so}}$ (Eq. 1.9) and $\mathscr{H}_Z$ (Eq. 1.10) are the spin-orbit and Zeeman terms respectively. The relative magnitudes of interaction for $3d$ and $4f$ ions in solids are given in Table. 1.3. Here, $\mathscr{H}_Z$ is for 1 T.

Table 1.3 Typical magnitudes of energy terms in K for 3d and 4f ions in solids [1].

	$\mathcal{H}_0$	$\mathcal{H}_{so}$	$\mathcal{H}_{cf}$	$\mathcal{H}_Z$
3d	1-5×10^4	10^2-10^3	10^4-10^5	1
4f	1-6×10^5	1-5×10^3	≈ 3×10^2	1

As Table 1.3 shown, the crystal-field interaction for 4f electrons is weaker than the spin-orbit interaction because the 4f shell is buried deep inside the atom and the crystal-field potential is shielded by the outer electrons. That means $\mathcal{H}_{so}$ should be considered before $\mathcal{H}_{cf}$ in any perturbation scheme for 4f ions. On the contrary, for 3d ions, the crystal-field interaction is much stronger than the spin-orbit one. The $\mathcal{H}_{cf}$ becomes the first term to consider in a perturbation scheme not the $\mathcal{H}_{so}$, except the Coulomb interaction $\mathcal{H}_o$.

We start from the crystal-field interaction of one-electron p- and d- states. The density of states of an electron of an atom in any specific region can be described by a wave function. This one-electron model can be considered as a hydrogen-like atom. Therefore, the solution of the Schrödinger equation in polar coordinates contains radial and angular distribution functions. There are three eigenfunctions of $\mathcal{H}_{cf}$ for p-orbital, p_x, p_y, p_z ($l = 1$, $m_l = $ -1, 0, 1), which are not splitting. And there are five eigenfunctions of $\mathcal{H}_{cf}$ for d-orbital ($l = 2$, $m_l = $ -2, -1, 0, 1, 2) of which three of them are t_{2g}-orbital including d_{xy}, d_{yz}, d_{zx} and two of them are e_g orbital consisting of $d_{x^2-y^2}$, $d_{3z^2-r^2}$. Originally, these orbitals are degenerate for an isolated atom or ion, however, once the atom or ion in a crystal are subjected to a crystal field or ligand field by their neighbours, these orbital energy levels are split (Fig. 1.4).
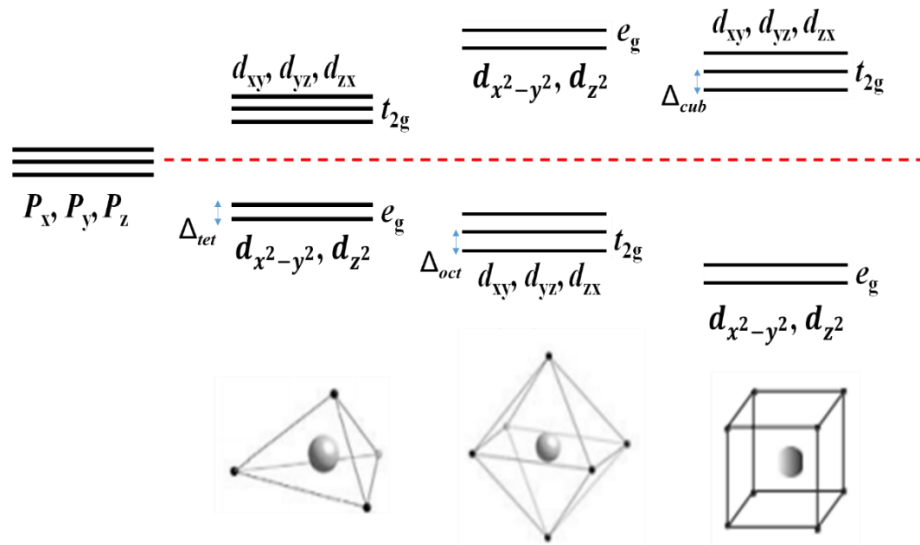
Fig. 1.4. Splitting of one-electron $3d$ energy levels in different coordination crystal fields with a cubic symmetry; $2p$ energy levels are unsplit [1]. It is noted that the mainly t_{2g} and e_g-orbitals for $3d$ ions in octahedral coordination is ~ 1-2 eV. The crystal-field splitting of tetrahedral coordination Δ_{tet} is $\frac{4}{9}\Delta_{oct}$. The relative magnitude of the energy splitting is shown.

The splitting of the $3d$-orbitals is determined by the specific coordination. Normally, $3d$ electrons localized in oxides or other ionic compounds are in six-fold coordination, such as Fe^{3+} in Fe_3O_4 [7]. Also, the relative splitting of the $3d$ crystal-field levels in different coordination with a cubic symmetry for the one-electron state are different as illustrated in Fig. 1.4. In an octahedral coordination, the energy level of the t_{2g}-obital is lower than that of e_g-orbital. While, for a tetrahedral or cubic coordination, the stabilized energy of t_{2g}-obital is higher than that of e_g-orbital and the energy difference is symbolized by Δ. The crystal-field splitting in a tetragonal ligand is smaller than that in an octahedral one. The specific relation was shown in Fig. 1.4. It is noted that the energy of these orbitals will change under a distortion, such as Jahn-Teller distortion on octahedral site and it can be further increased by a uniaxial distortion that splits the t_{2g} levels. This distortion effect also works on the many-electrons state.

In many-electrons state, the orbital configuration of d^n ion is defined by the Hund rule. However, owing to the overlap of multi-electron orbitals, the intense electrostatic field created by the ligand field sometimes manage to overturn Hund's first rule or second one. The crystal-field might drive the ion into a low-spin state or high-spin state (Fig. 1.5). Strong-field ligands cause a large splitting of the d-orbitals, and the lower energy orbitals are fully filled before population of the upper energy levels starts according to Aufbau principle. Complexes with this arrangement of ion configurations are called 'low-spin'. For example, S^{2-} is a strong-field ligand and produces a large Δ, and the octahedral site of Fe^{2+} in FeS_2, which has 6 d-electrons, would have the octahedral splitting diagram (Fig. 1.5) with all six electrons in the t_{2g} sub-bands. Conversely, a weak-field ligand causes a small splitting Δ of the d-orbitals, and it is easier to drive electrons to the sub-orbitals with higher energy than those with low-energy because two electrons in the same orbital repel each other. For example, Cl^- is a weak-field ligand and yields a small Δ, the Fe^{2+} in $FeCl_2$ with six d-electrons have an octahedral splitting diagram where all five singly d-sub-bands in one spin-direction are singly occupied firstly and then then remaining electron fills in a sub-band in the other spin-direction based on Aufbau principle (Fig. 1.5).
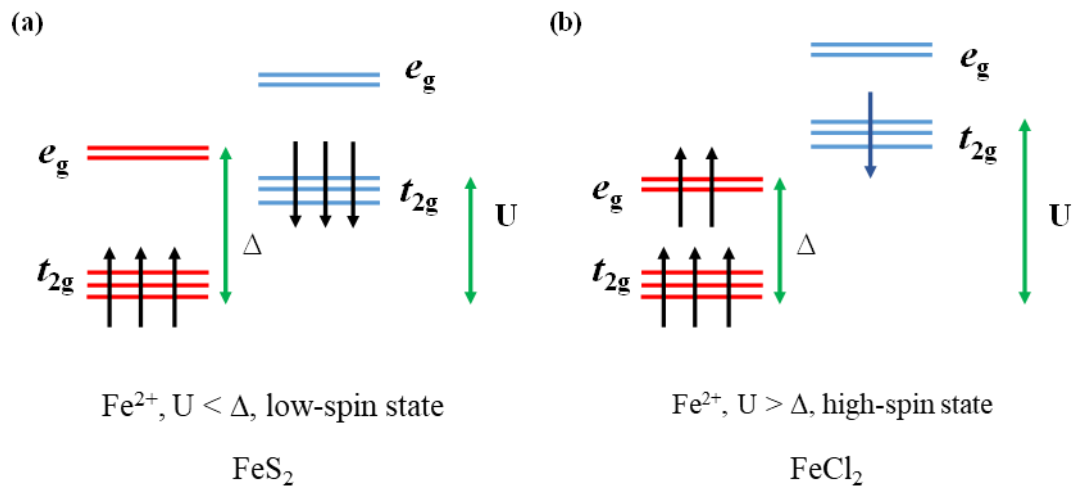

Fig. 1.5. (a) Comparison of the Fe ion energy levels for (a) FeS_2 [8], where the crystal field stabilized in low-spin state with $S = 0$ and (b) $FeCl_2$ [9], where the crystal field stabilized in high-spin state with $S = 2$.

The splitting diagrams are helpful to predict the magnetic properties of compounds. A compound with unpaired electrons in its splitting diagram is paramagnetic and is attracted by a magnetic field, while a compound lacking unpaired electrons in its splitting diagram is diamagnetic and will be repelled by magnetic fields.

1.2.3 Molecular field theory

There are many formulations of mean-field theory, which is a method to compute the values of the relevant thermodynamic quantities of a statistical mechanic model. The molecular field theory of ferromagnetism was firstly proposed by Pierre Weiss in 1906 [10]. It has been used in the Bragg-Williams approximation, models on Landau theory, Pierre-Weiss approximation and etc. Its original theory was based on the classical paramagnetism of Langevin, then soon it was extended to the more general Brillouin theory of localized magnetic moments. It assumed that in addition to any externally applied field H, there is an internal 'molecular field' that is proportional to the magnetization of the ferromagnet. This theory is used to explain partial ferromagnetic laws successfully, such as magnetic phase transition.

If n_W is the constant of proportionality related to the internal contribution of the external applied field, the internal magnetic field is expressed as

$$H_{\text{int}} = n_W M + H \tag{1.23}$$

where n_W is Weiss coefficient, M is the spontaneous magnetization and H is the external applied field. The magnetization $M = M_0 B_J(x)$ is given by Brillouin function

$$B_J(x) = \frac{2J+1}{2J} \coth\left(\frac{2J+1}{2J}x\right) - \frac{1}{2J} \coth\left(\frac{1}{2J}x\right) \tag{1.22}$$

and the magnetization at $T = 0$ K is expressed as $M_0 = nm_0 = ng\mu_B J$, where n is the number of magnetic atoms per unit volume, g is the Landé g factor and J is total angular momentum quantum number. Now $x = \mu_0 m_0 (n_W M + H)/k_B T$. Therefore,

$$M_s / M_0 = \mu_0 m_0 n_W M_s / M_0 k_B T \tag{1.23}$$

Where M_s is the spontaneous magnetization in zero field. Eq. 1.23 is rewritten as

$$M_s / M_0 = x_0 k_B T / n \mu_0 m_0^2 n_W \tag{1.24}$$

In a convenient expression in terms of the Curie Weiss constant $C (= \mu_0 n g^2 \mu_B^2 J(J + 1)/3k_B)$, Eq. 1.24 is rewritten as

$$M_s / M_0 = x_0 (J + 1) T/3JCn_W \tag{1.25}$$

The plots of reduced spontaneous magnetization M_s / M_0 versus T/T_C for different J are exhibited in Fig. 1.6a. The values of reduced spontaneous magnetization deduced from molecular field theory for J from 1/2 to ∞ are listed in Table 1.4. for localized cases. Fig. 1.6b shows the comparison of the theory and experiment for Ni.

Table 1.4 Reduced spontaneous magnetization deduced from molecular field theory [1].

T/T_C	1/2	1	3/2	2	5/2	7/2	∞
0	1.00000	1.00000	1.00000	1.00000	1.00000	1.00000	100000
0.1	1.00000	1.00000	1.00000	0.99998	0.99992	0.99964	0.96548
0.2	0.99991	0.99944	0.99833	0.99655	0.99428	0.98902	0.92817
0.3	0.99741	0.99297	0.98688	0.98019	0.97359	0.96179	0.88730
0.4	0.98562	0.97337	0.96043	0.94853	0.93815	0.92166	0.84157
0.5	0.95750	0.92657	0.91752	0.90169	0.88881	0.86006	0.78889
0.6	0.90733	0.87923	0.85599	0.83791	0.82383	0.80375	0.72588
0.7	0.82863	0.79624	0.77122	0.75262	0.73856	0.71904	0.64739
0.8	0.71041	0.67766	0.65365	0.63637	0.62358	0.60616	0.54455
0.85	0.62950	0.59852	0.57629	0.56051	0.54892	0.53325	0.47864
0.9	0.52543	0.49806	0.47880	0.46528	0.45543	0.44218	0.39660
0.95	0.37949	0.35871	0.34435	0.33436	0.32713	0.31747	0.28455
0.99	0.16971	0.16042	0.15400	0.14953	0.14631	0.14196	0.17198
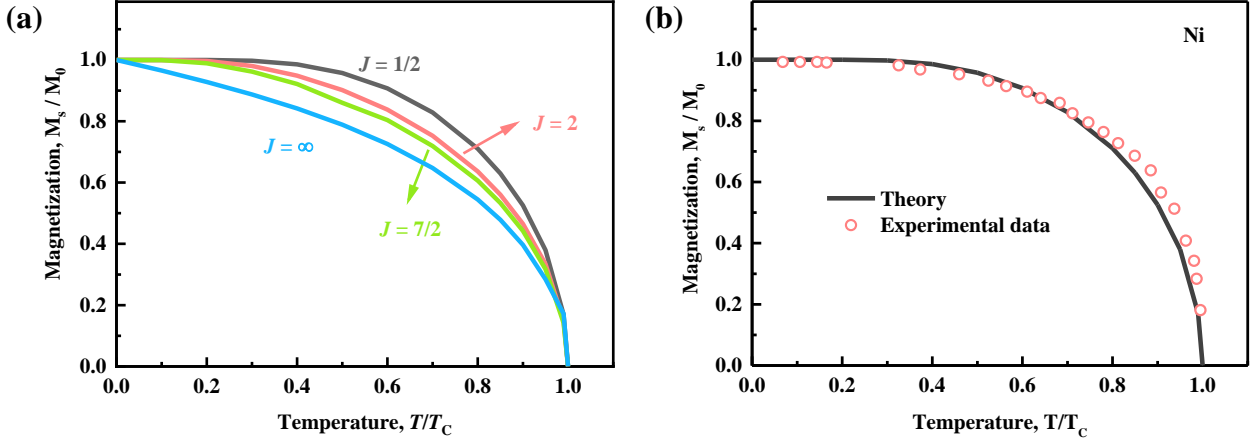
Fig. 1.6. (a) Spontaneous magnetization as a function of temperature calculated from molecular field theory, based on the Brillouin function for different values of J. The classical limit $J = \infty$ is based on the Langevin function. (b) The spontaneous magnetization for Ni, together with the theoretical curve for $J = 1/2$ from the molecular field theory [1]. Note that the theoretical curve is scaled to give correct values at each end.

Weiss's molecular field theory can be used to model the temperature dependence of spontaneous magnetization in a ferromagnet to achieve the Weiss coefficients, the sublattice magnetism and the transition temperature.

The Weiss molecular field theory is not unique for ferromagnets, but also can be applied to antiferromagnet or ferrimagnet. Here, we will introduce the latter one. A ferrimagnet can be considered as two unequal and oppositely directed magnetic sublattices 'A' and 'B', hence, the net magnetization M and the internal fields H_{int} for each sublattice in an external field H are

$$M = M^A + M^B \tag{1.26}$$

$$H_{int}{}^A = n_W{}^{AA} M^A + n_W{}^{AB} M^B + H \tag{1.27}$$

$$\boldsymbol{H}_{int}{}^{B} = n_W{}^{BB}\,\boldsymbol{M}^{B} + n_W{}^{AB}\,\boldsymbol{M}^{A} + \boldsymbol{H} \tag{1.28}$$

where $n_W{}^{AA}$, $n_W{}^{AB}$ and $n_W{}^{BB}$ are the Weiss coefficients, which represent the inter-and intrasublattice interactions. The essential interaction $n_W{}^{AB}$ is negative. The magnetization of each sublattice is represented by a Brillouin function in unit vectors $\boldsymbol{h}_{int}{}^{A}$ and $\boldsymbol{h}_{int}{}^{A}$:

$$\boldsymbol{M}^{A} = M_0{}^{A} B_J(x^{A})\,\boldsymbol{h}_{int}{}^{A} \tag{1.29}$$

$$\boldsymbol{M}^{B} = M_0{}^{B} B_J(x^{B})\,\boldsymbol{h}_{int}{}^{B} \tag{1.30}$$

The susceptibility and Curie constant can be expressed as

$$\chi^{A} = \mu_0{}^{A} m_0{}^{A} H_{int}{}^{A} / k_B T \tag{1.31}$$

$$\chi^{B} = \mu_0{}^{B} m_0{}^{B} H_{int}{}^{B} / k_B T \tag{1.32}$$

$$C^{A} = \mu_0\, n^{A}\, (m_{eff}{}^{A})^2 / 3k_B \tag{1.33}$$

$$C^{B} = \mu_0\, n^{B}\, (m_{eff}{}^{B})^2 / 3k_B \tag{1.34}$$

Above critical temperature T_C, $M = \chi H_{int}$, where $\chi = C/T$, Hence,

$$\boldsymbol{M}^{A} = (C^{A}/T)\,(n_W{}^{AA}\,\boldsymbol{M}^{A} + n_W{}^{AB}\,\boldsymbol{M}^{B} + \boldsymbol{H}) \tag{1.35}$$

$$\boldsymbol{M}^{B} = (C^{B}/T)\,(n_W{}^{BB}\,\boldsymbol{M}^{B} + n_W{}^{AB}\,\boldsymbol{M}^{A} + \boldsymbol{H}) \tag{1.36}$$

When $H = 0$, the magnetization of each subattice falls to zero at a critical temperature, which is the ferrimagnetic Néel temperature. The two sublattice magnetizations are equal and can cancel exactly at a temperature known as compensation temperature T_{comp}. The T_C for the ferrimagnet can be expressed in terms of the Weiss coefficients and Curie constants as

$$T_C = \tfrac{1}{2}[(\,C^{A} n_W{}^{AA} + C^{B}\, n_W{}^{BB}) + [(C^{A} n_W{}^{AA} - C^{B}\, n_W{}^{BB})^2 + 4C^{A} C^{B}(n_W{}^{AB})^2]^{1/2}] \tag{1.37}$$

Although this model is simple and can be easily implemented numerically, there are some disadvantages that are needed to be considered. Firstly, the mean field approximation is not accurate at low temperatures and the calculated T_C is overestimated. Secondly, the magnetization thermal scan should be over a wide range of temperatures to estimate T_C, which can be used to ensure the accuracy of Weiss coefficients. On the other hand, Weiss molecular field theory as a phenomenological theory, and it does not consider the anisotropy. The extended field theory can correct this term, but it creates convergence problems at low

temperatures. However, it is noted that this model does not account for non-collinear moments.

1.2.4 Critical behaviour

The critical behaviour in ferromagnets describes a power-law divergence of the magnetic susceptibility in a ferromagnetic phase transition, which is also called a second-order phase transition and is characterized by critical exponents $\alpha, \beta, \gamma, \delta$, which are common to all mean field theories. There is a mathematical singularity in the Gibbs free energy at the transition temperature T_C, where the order parameter drops continuously to zero. Also, there is a discontinuity in its temperature derivative. On the contrary, in a first-order transition, the critical fluctuations are invisible, where the order parameter is discontinuous.

There are several models to investigate the critical behaviour, where a pair of numbers representing the space and spin dimensionality $\{D, d\}$ are used to specify a universality class, e.g., the two-dimensional Ising model $\{2, 1\}$ or the three-dimensional Heisenberg model $\{3, 3\}$. Although slight differences of critical behaviour can be seen in different materials of each universality class, all the materials within a class behave similarly regardless of the phase structure or the compositions. A reduced temperature is defined as $\varepsilon = 1 - T/T_C$. When ε is very small, $M \approx \varepsilon^{\beta} \, (\varepsilon \geq 0)$, $M \approx H^{1/\delta} \, (\varepsilon = 0)$, $\chi = |\varepsilon|^{\gamma} \, (\varepsilon \approx 0)$ and $C \approx |\varepsilon|^{-\alpha} \, (\varepsilon \approx 0)$. Here, M is the order parameter, H is the conjugate field and χ is the susceptibility dm / dH. Another two critical exponents υ and η are used to describe the correlation length and the correlation function at T_C. It is noted that the static critical exponents are not totally independent. They are related by equalities such as

$$\alpha + 2\beta + \gamma = 2 \tag{1.38}$$

$$\beta (\delta - 1) = \gamma \tag{1.39}$$

$$2 - \upsilon D = \alpha \tag{1.40}$$

$$(2 - \eta)\upsilon = \gamma \tag{1.41}$$

In mean field theory, the critical exponents are $\alpha = 0$, $\beta = 1/2$, $\gamma = 1$, $\delta = 3$, $\upsilon = 1/2$ and $\eta = 0$. The mean field theory for the real critical fluctuations of magnetic materials could be consistent with the theory when $D = 4$ according to above equalities. Generally, the equation of state close to T_C region can be written as

$$(H/M)^\gamma = a(T - T_C) - bM^{1/\beta} \tag{1.42}$$

where M is the magnetization, H is the applied field, T_C is the critical temperature and a and b are constants.

A widely used tool is an Arrott plot, which is a plot of the magnetization square of a substance versus the ratio of the applied field to magnetization at several fixed temperatures. It provides an easy way to determine the presence of magnetic order in a material. According to the Ginzburg-Landau mean field theory for magnetism [11], the free energy close to a magnetic phase transition can be written as

$$F(M) = -HM + a(T - T_C) M^2 / T_C + bM^4 + \ldots \tag{1.43}$$

The relation for the magnetization close to the phase transition is given by

$$M^2 = H/4bM - a(T - T_C)/2bT_C. \tag{1.44}$$

In a graph plotting M^2 versus H/M for different temperatures, the isotherms are expected to be set of parallel straight lines. The one determining the critical temperature passes through the origin. Therefore, the Arrott plot not only provides the evidence for a ferromagnetic phase existence but can also be used to determine the critical temperature for the phase transition.

In my project, we investigate the critical behaviour of a single crystal CoS_2 (Chapter 6), which is related to three-dimensional model. Values for the practically three-dimensional Heisenberg model are list in Table 1.5.

Table 1.5. Critical exponents for the three-dimensional d-vector models [1].

d		α	β	γ	δ	υ	η
0	Polymer	0.236	0.302	1.16	4.85	0.588	0.03
1	Ising	0.110	0.324	1.24	4.82	0.630	0.03
2	XY	-0.007	0.346	1.32	4.81	0.669	0.03
3	Heisenberg	-0.115	0.362	1.39	4.82	0.705	0.03
∞	Spherical	-1	1/2	2	6	1	0

1.3 Spin electronics

Spintronics (spin electronics) is the science of spin-dependent electron transport, which exploits the angular momentum and magnetic moment of the electron to add new functionality to electronic devices. Compared to conventional electronics which ignores the spin of the electron, the manipulation of electron currents with the associated magnetic moments is the main goal in spintronics and this additional degree of freedom will improve the efficiency of data storage and transfer. The typical application of spintronics is ferromagnetic information storage, which has been the partner of semiconductor electronics in the information revolution. The magnetic storage density of spintronics is doubling even faster than that of semiconductors. It follows their own 'Moore's law' [1]. Fig. 1.7 shows the trend of the increase of areal density of HDD and flash disk to the year of production indicating that the rapidly increasing rate on the magnetic recording, which breaks the conventional Moore's law, and the magnitude of the areal density can be up to 10^3 Gb/in^2 [12]. Actually, it is feasible to manipulate the spin polarized electronic currents when high-quality metallic thin films in nanometer scale become available. It is different with the charge, the electron spin can be altered in some scattering events, arising a flip from spin up to spin down. The distance travelled by the electron along its path between spin flip is called spin diffusion length l_s, which is 10 times larger than the mean free path. Therefore, thin film spintronic devices are pursued, whose layer thickness is comparable to l_s, ranging from 1 to 20 nm. Depending on the thin film heterostructure design, layers of materials with

different magnetic and electronic properties will exhibit many interesting phenomena, like exchange bias, perpendicular magnetic anisotropy, giant magnetoresistance (GMR) and tunnelling magnetoresistance (TMR). GMR is an effect observed in thin film structures with alternating ferromagnetic and nonmagnetic layers, achieving a high resistance if the magnetizations in the ferromagnetic layers are oppositely aligned, conversely, low resistance if they are parallel aligned (Fig. 1.8). And TMR has the similar device structure but with an insulating non-magnetic layer. Besides, the promising applications of spintronic data transfer in the THz range and for electronics with ultra-low power consumption if suitable materials can be found, which also encourages and attracts researchers to the field. Here, there are two key features of spintronic materials we are concerned with spin polarization and spin currents.
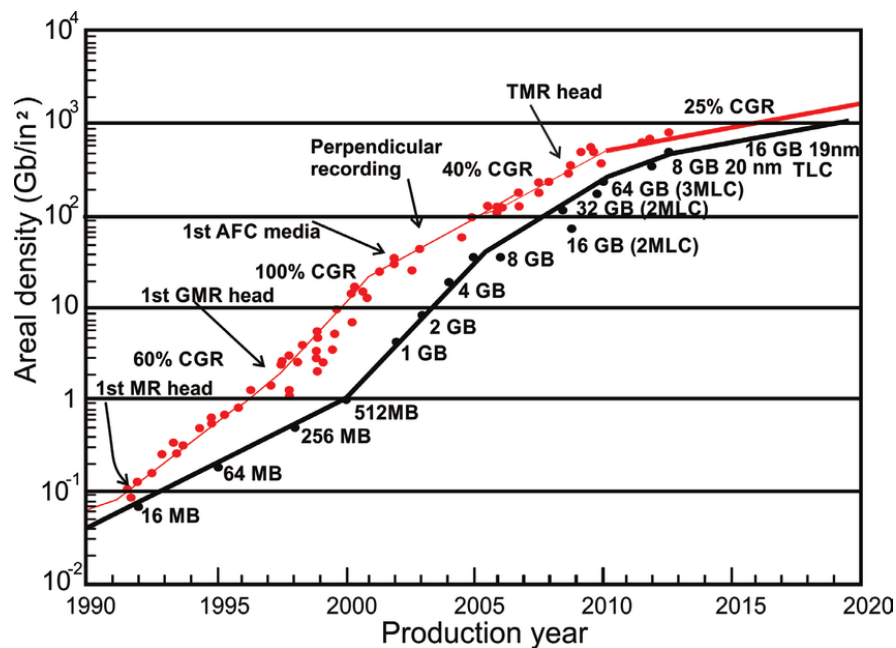

Fig. 1.7. Trend of the increase of areal density of HDD and flash disk with the year of production [12]. (AMR. anisotropic magnetoresistance; CGR, compound growth rate; AFC media, antiferromagnetically coupled.)
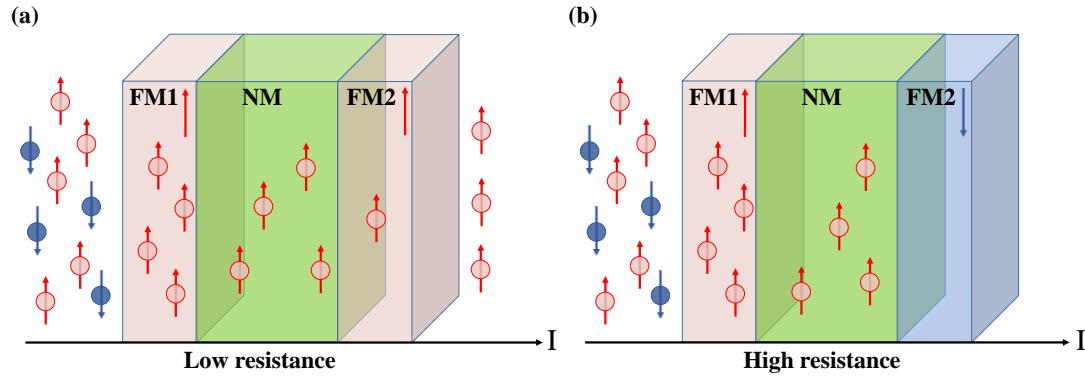
Fig. 1.8. A simplified illustration of GMR. A non-spin polarized current enters the GMR structure but only one of the spin conduction bands (CB) is available in ferromagnet (FM1, left). (a) For low resistance the same spin CB is available in ferromagnet (FM2, right). (b) For high resistance there is no available CB in FM2 for spins from FM1.

1.3.1 Spin polarization

In spintronics, the manipulation of the electrons' spin is connected to the fact that spin-up and spin-down electrons have different mobilities in a ferromagnet. A very important feature of the spintronic materials is the high spin polarisation. Spin polarisation describes the degree of spin imbalance, or in other words the intrinsic net angular momentum of the electrons oriented along a given direction [13]. Spin polarisation derives from the inequivalent populations of the spin down and up states. The spin polarisation P of the conduction electrons at Fermi-level can be defined as:

$$P = \frac{N_\uparrow - N_\downarrow}{N_\uparrow + N_\downarrow} \tag{1.45}$$

where $N_\uparrow$ and $N_\downarrow$ are the densities of states (DOS) of the spin-up and spin-down states at the Fermi energy E_f, respectively. According to the value of P, materials can be divided into three types: non-magnetic metal (NM), a ferromagnetic metal (FM) and a half metal (HM) and the corresponding schematic band structures are illustrated in Fig 1.9. The spin-up and spin-down densities of states at E_f are symmetric in non-magnetic metal and it will not yield any spin polarised current passing through, $i.e.$ $P = 0$. For a ferromagnetic metal, there is a

splitting between spin-up and spin-down states at the Fermi level of the conduction band due to Coulomb interactions. This generates a net magnetization and allows a spin current to pass through, which will be polarized to some degree ($0 < P < 1$), *e.g.* 0.44 for Fe, 0.34 for Co and 0.11 for Ni. While, compared to the classes mentioned above, the one with ideal spin polarisation ($P = 1$) has a special band structure: one spin direction showing a typical metallic band structure with nonzero density of states at E_f, and the other exhibiting a semiconducting or insulating property with a spin gap. This is called a half metal. The oxides (*e.g.* CrO_2, Fe_3O_4) and many Heusler alloys fall into this class. Although the values of P are deduced from the height of DOS, it is not perfectly consistent with experimentally measured ones owing to the measurement method or the inevitable objective factors, *e.g.* the sample's surface quality. Although there is no fully spin-polarised current pass through a half-metal in practice, such materials with very high spin-polarised currents are desirable in spintronic devices. It is noted that the transport measurements reflect the electrons mobility, therefore the experimental transport measurements for the $3d$ metals are sensitive to the polarisation of the $4s$ rather than $3d$ electrons, However, the ideal 100% spin-polarisation originates from the $3d$ electrons mobility. The normal transport measurements are no longer appropriate to the spin polarisation tests, instead other approaches, such as photoemission with polarization analysis, tunnel magnetoresistance, ballistic point contact and Andreev reflection, can deduce the spin polarisation.
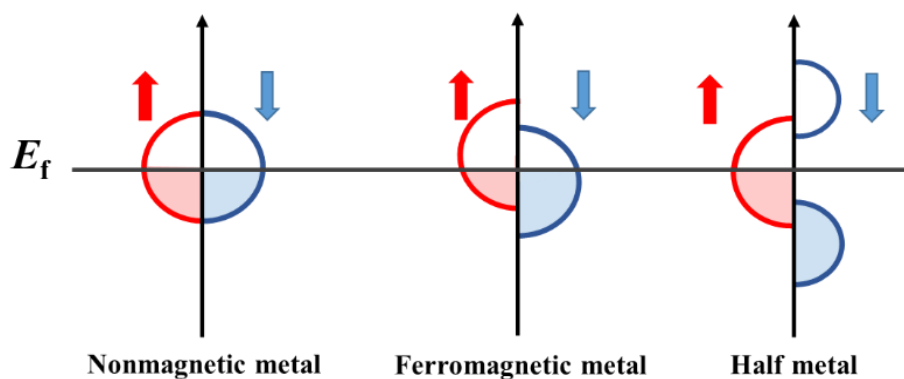

Fig. 1.9. The schemes of the electronic structures for non-magnetic metal, ferromagnetic metal and half metal.

In summary, the spin polarization can be given not only by experiments but also electronic structure calculations, which is a valid method to predict ideal half metals due to the drawbacks of the experiments.

1.4 Half metal

Several decades ago, the study of electronic structure of Heusler alloys motivated by their unusual magneto-optical properties presented an unexpected result: some of these alloys showed the transport properties of metals as well as insulators at the same time in the same alloy depending on the spin direction. A material with this character is called a half metal. Although ideal 100% spin polarized currents for half metals only can be approached in the limit of the absolute zero temperature and neglecting spin-orbit interactions, half-metals do show higher spin polarization than $3d$ ferromagnets (*e.g.* Fe, 40%; Co, 40%; Ni, 35% [1]) in reality. It is noted that, owing to the limits in experiments, it is not surprising that electronic structure calculations play an important role to search for new half metals. In my project, theoretical DFT calculation was used to verify the new half metals I obtained, which were carried out by Dr. Zsolt Gercsi.

Half metals included various materials with very different chemical and physical properties. Many of the known examples of half metals are Heusler alloys (Co_2MnAl [14]), zinc blends (CrO_2 [15]), double perovskites (Sr_2FeMoO_6 [16]) and magnetite (Fe_3O_4 [17]). Another class, sulphides with spinel structure is relatively rare. Due to the less correlation of electrons in sulphides, it is possible to optimize magnetic properties (ferro-, ferri and antiferromagnetic) by doping or substituting without the risk of losing its metallic properties in one spin direction. However, when the cation-cation distances are larger in sulphides, the magnetic coupling between these two cations will be weaker. This leads to the magnetic transition temperatures lower in comparison with the oxides. Nevertheless, this class of half metal is still worthwhile to pay attention, especially for other distinctive properties, for example, CoS_2 shows Weyl fermions [18]. It is noted that the fully compensated ferrimagnetic half metal is the ideal one we are pursuing due to its characteristics, including

half-metallicity as well as magnetic order with zero moment. This material will produce zero stray field which will reduce the energy losses in operation.

During my project, we worked on half-metallic ferromagnetic sulphide CoS_2 and I discuss the critical behaviour in chapter 3, and develop a new fully compensated ferrimagnetic half-metal based on the analysis of the spin band gap, which is introduced in chapter 5.
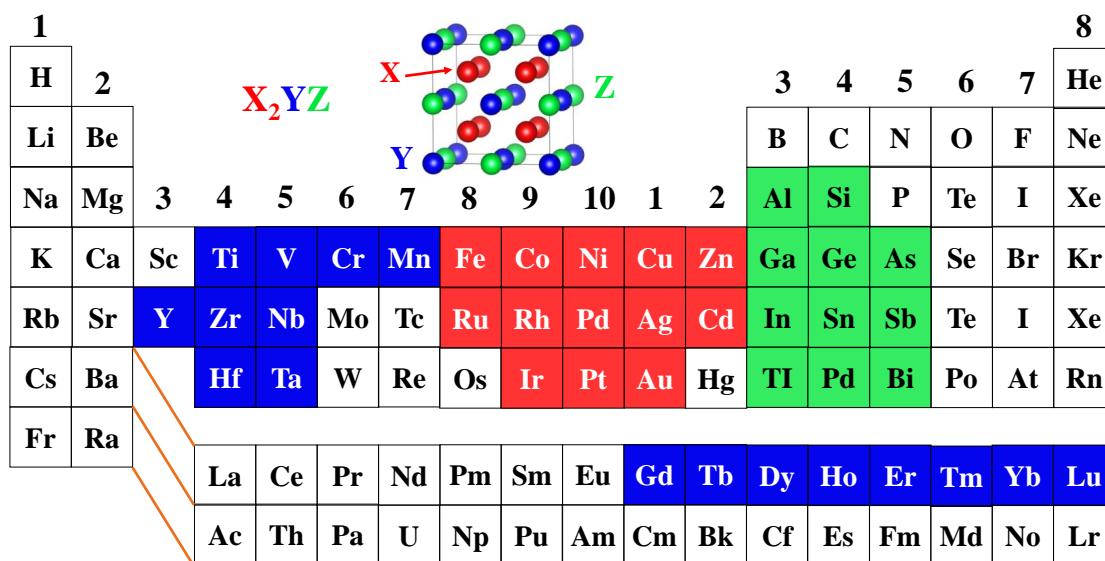
1.5 Heusler alloys

A magnetic alloy, Cu_2MnAl, was discovered in 1903 by Friedrich Heusler, which behaves like a ferromagnet although no constituent element is ferromagnetic by itself. Later, the concepts of antiferromagnetism and ferrimagnetism were introduced in the 1930s-1940s by Louis Néel. A vast collection of thousands of Heusler compounds exist with a 1:1:1 (Half Heusler) or a 2:1:1 (Full Heusler) stoichiometry.

Heusler compounds include binary, ternary and quaternary alloys exhibiting a wide range of properties. The properties of many Heusler compounds can be modified through chemical substitutions to tune the electronic structure and the structural motifs leading to their potential use in applications requiring as a shape memory alloys, half-metallic ferromagnets [19, 20], fully compensated ferrimagnets [21], G-type spin-gapless semiconductors [22], superconductors [23, 24] and recently as topological insulators [25, 26]. The latest study of topological insulators, which describe a new state of matter, in which spin-polarized edge and surface states are topologically protected against impurity scattering [25, 27] due to large spin orbit interaction on the surface [25], opens a new horizon. The magnetic Heusler compounds show many kinds of magnetic functionalities, such as magnetocaloric, magneto-optical [28], and shape memory effects due to martensitic transformation [26, 29]. Furthermore, the half-metallic Heusler compounds are semiconducting or insulating for electrons of one spin direction, while for the opposite spin direction they are metallic. This is ideal for spin electronics, when it is associated with large

magnetoresistance in spin valves, memory elements or high spin transfer torque efficiency in magnetic switches and oscillators [30].

The general ternary formula of a ternary Full-Heusler compound is X_2YZ or XYZ for a Half-Heusler compound, where X and Y are transition or rare-earth metals, and Z is the main group elements. The possible elements forming the magnetic Heusler compounds are shown in Fig. 1.10. There are over 1000 possible Heusler compounds. However, not all are stable.

Fig. 1.10. Periodic table of elements. The huge number of full-Heusler alloys are formed from X, Y transition or rare-earth metals elements (red, blue) and a *s-p* element (green) according to the colour scheme. The valence electrons are those electrons that reside in the outermost shell surrounding an atomic nucleus. For *d*-group elements, the valence electrons n equal to the number of the outer s and d electrons, *e.g.* Ti ($3d^2 4s^2$) with 4 valence electrons, V ($3d^3 4s^2$) with 5, Cr ($3d^5 4s^1$) with 6 and Mn ($3d^5 4s^2$) with 7, For main group elements, the valence electrons n equal to the number of the outer s and p electrons e.g. Al ($3s^2 4p^1$) with 3 valence electrons, Si ($3s^2 4p^2$) with 4 and Sb ($5s^2 5p^3$) with 5.

1.5.1 Half Heusler alloys

Generally, half-Heusler compounds XYZ crystalize in a non-centrosymmetric cubic structure (C1$_b$, F4$\bar{3}$m). There are three interpenetrating fcc sublattices occupied by the X, Y, Z atoms, which sit at 4a (0,0,0), 4b (1/2, 1/2, 1/2) and 4c (1/4, 1/4, 1/4). The three possible atomic arrangements within C1b-type structure are XYZ, ZXY, YZX along the diagonal (111) direction (Fig 1.11a). The crystal structure of a half-Heusler compound is a ternary ordered variant of the CaF$_2$ structure and can be derived from the tetrahedral ZnS-type structure by filling the octahedral lattice sites (Fig. 1.11b). In most Half-Heulser compounds, MgCuSb represents the atomic arrangement correctly. Although MgAgAs is assigned as the prototype of all Half-Heusler compounds, it forms a different atomic order than most other Half-Heuslers [31]. It is noted that a NaCl-type sublattice is formed by 4d Ag and As rather than the main group elements Mg and As. And in MgCuSb, the electropositive Mg and the electronegative Sb build the NaCl-type sublattice, which represents the atomic arrangements in the most half-Heuslers. Both variants have the same prototype, a LiAlSi-type [31]. The atomic arrangements in Half-Heusler are mainly determined by two factors. The first is the size difference between the atoms involved and the other is the kind of interatomic interactions.
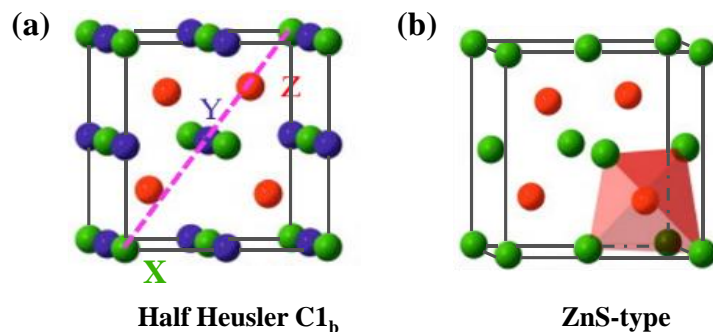

Half Heusler C1$_b$ **ZnS-type**

Fig. 1.11. (a) Half Heusler (XYZ) structure (C1b) and (b) zinc-blende (ZnS-type) structure. It is noted that the pink dashed line in (a) along a diagonal distinguishes the arrangements of atoms. In (b), the shaded octahedron is composed of Wyckoff positions 4a and 4c in which the octahedral sites are occupied by 4b sites [26].

1.5.2 Full Heusler alloys

The general formula X_2YZ of Full-Heusler compounds includes four interpenetrating fcc sublattice. Two of the sublattices are equally occupied by one X and a rock salt type lattice is formed by the least and most electropositive elements, Y and Z, which are coordinated octahedrally due to the ionic character of their interactions. The ionic bond between X and Z is shortest (~ $\sqrt{3}a_0/4$), leading to octahedral coordination. The covalent bond between X and Y present cubic coordination and the bond length is $a_0/2$. This structure also can be understood as a zinc blende-type sublattice built of X and Z, the second X sits on the remaining tetrahedral sites, and Y occupies the octahedral sites. There are three sites in the unit cell, 4a, 4b and 8c. There are several possible occupancy schemes, such as Cu_2MnAl-type ($L2_1$), $CuHgTi_2$-type (XA) and random W-type (A2). The ordered phase of the $CuHg_2Ti$-type (Fig. 1.12a) is the so-called inverse Heusler structure with $F\overline{4}3m$ space group. If the atomic number of Y is higher than that of X from the same period, the Full-Heusler compounds prefer to crystallize in the inverse, XA structure. In this scheme, X and Z form a rock salt lattice to achieve an octahedral coordination for X element. The second X and Y atoms fill the tetrahedral holes with fourfold symmetry. Compared to the $L2_1$ structure, the X atoms do not form a simple cubic lattice. X atoms are placed on the Wychoff positions 4a (0, 0, 0) and 4d (3/4. 3/4, 3/4). Y and Z atoms occupy 4b (1/2, 1/2, 1/2) and 4c (1/4, 1/4, 1/4) sites, respectively. In order to distinguish it from the normal Full Heusler structure, the inverse Heusler structure also can be expressed as XYX'Z, and it is frequently observed in Mn_2-based compositions with Z (Y) > Z (Mn), such as Mn_2CoSn [32, 33]. For the quaternary Heusler compounds, two different elements X and X' sit on 4a and 4d positions, respectively. Y is placed on 4d and Z occupies 4c sites, whose prototype is LiMgPdSn (Fig. 1.12b). There is a quite small difference between the ordering of $L2_1$ and XA structures. The 8c sites of $L2_1$ split into 4c and 4d sites (XA). From the x-ray diffraction pattern, except the tiny change of the intensities from superlattice reflections, it is still hard to judge which phase structure is formed. But the superlattice reflections, (111) and (200), still are the key to distinguish what is the real phase of a full-Heusler alloy. From the

definition of the superlattice structure, which describes a periodic structure of layers of two (or more), it should be seen in more complicated crystal structure. Therefore, the superlattice reflections are helpful to judge whether a highly ordered Heusler structure is formed or not. For example, in a completely disordered simple cubic A2 structure, there is a (200) reflection but no (100). In the partly ordered B2 structure (different atoms at the cube corner and the cube centre) there is a (100) and a (200) reflections. If you index the reflections on the cubic Heusler cell that has double the lattice parameter, you see (400), but not (200) if it is completely disordered; but if you have B2 type order, then you see (200) and (400) [1]. In A2, complete disorder, these two typical superlattice peaks cannot be seen.

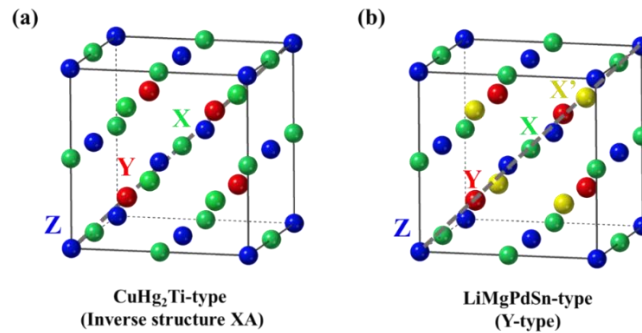Fig. 1.12. (a) The ternary Heusler compound with $CuHg_2Ti$-type (inverse Heusler, XA) structure and (b) the quaternary Heusler alloy with LiMgPdSn-type (Y-type). Their space groups are all $F\overline{4}3m$.
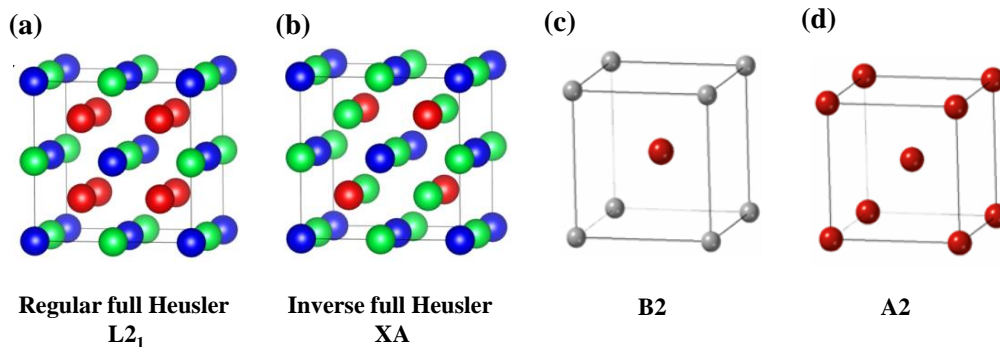

Fig. 1.13. The cubic crystal structure of full-Heusler $L2_1$, XA, B2 and A2. Two-types full-Heusler alloys (XA and $L2_1$) include 4 interpenetrating fcc lattices. B2 with two atom sites,

a (0,0,0) and b (1/2,1/2,1/2), and disordered A2 with one atom site, a (0,0,0), are simple cubic structures.

The electronic structure and magnetic properties are very sensitive to the atomic arrangements. Even a small concentration of antisite defects in the ordered phase can modify the magnetic moment and Fermi-level spin polarization.

1.5.3 Half-metallic Heusler alloys

Half-metallic Heuslers are a sub-class of Heusler alloys. First to be predicted was NiMnSb by de Groot and his co-workers in 1983 through *ab-initio* calculations [19]. The magnetic moment in both Heusler and half-Heusler compounds is associated with the number of valence electrons, and it obeys a Slater-Pauling rule, which provides an opening to design new half-metallic Heusler alloys with desired magnetic properties. The number of minority valence electrons per unit cell is an integer coming from the number of occupied valence bands, 9 for the half-Heusler and 12 for full-Heusler alloys. We must point out that spin-orbit coupling destroys the minority band gap in principle, and it also reduces the spin polarization in practice, but not too much. In fact, defects, interfaces or surfaces all tend to destroy the perfect spin polarization [34].

The total magnetic moment is the difference between the number of occupied spin-up and spin–down states, $m = N_\uparrow - N_\downarrow$. It also can be expressed as $m = Z_t - 2N_\downarrow$ μ_B, where Z_t is the total valence electrons. Since, in half-Heusler compounds with the $C1_b$ structure, 9 minority band states are fully occupied, the $m = Z_t - 18$ rule has been formulated by Jund *et al.* [35] and Galanakis *et al.* [36]. The similar $m = Z_t - 24$ rule for full-Heuslers is based on 12 valence electrons in the minority band. It is noted that in all cases the predicted moments per stoichiometric formula unit are integer for Heusler half-metals in theory. In Fig. 1.14, we have gathered the calculated total spin magnetic moments for the half- ($Z_t = 18$) and full-Heusler ($Z_t = 24$) alloys which we have plotted as a function of the total number of valence electrons separately. The dashed line represents the Slater-Pauling rule [37] of $m = Z_t - 18$ (and $m = Z_t - 24$). For the half-Heusler compound, the value 0 of the moment corresponds

to the semiconducting phase. The 0 μ_B moment of full-Heusler compounds arises from two magnetic sublattices, which have different chemical compositions or are associated with two different crystallographic sites, and they are fully compensated. This class of full-Heusler compounds is called fully compensated ferrimagnetic or antiferromagnetic Heusler half-metals owing to the net zero magnetization.
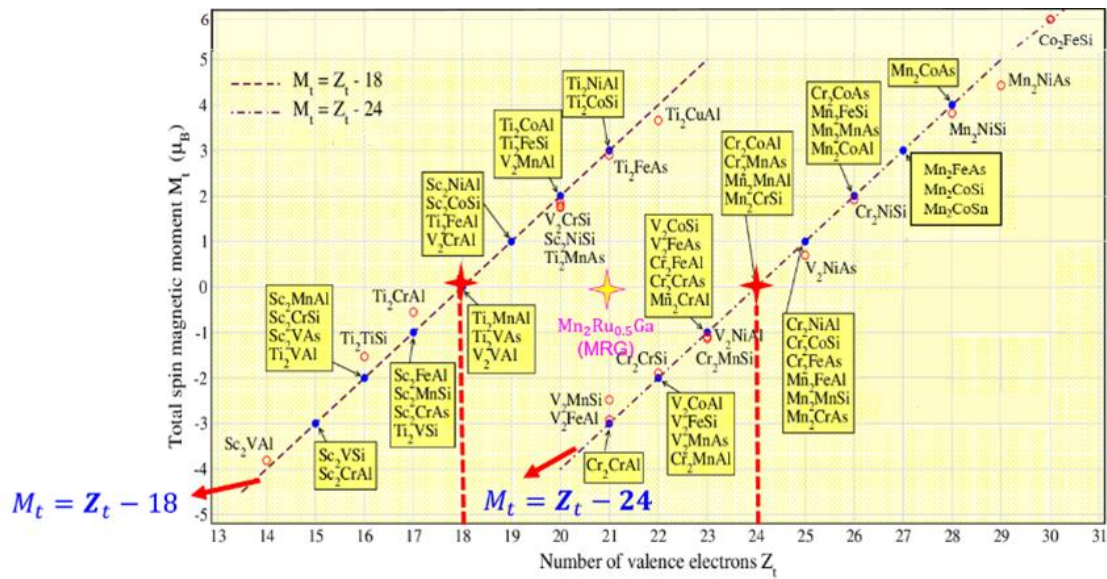
Fig. 1.14. Calculated total spin moments for half-Heusler (with 18 electrons) and (b) full-Heusler alloys (with 24 electrons). The dashed line represents the Slater-Pauling (SP) behaviour. With open circles the compounds deviate from the SP curve in Ref. [38]. MRG ($Mn_2Ru_{0.5}Ga$, $Z_t = 21$) is the first experimentally discovered zero-moment half metal [39].

Compared to the ferromagnetic Heusler half-metals, which produce large magnetic dipole fields that can reduce the performance of spintronic devices, fully compensated materials that exhibit 100 % spin polarization with no net magnetic moments and no stray fields are of special interest, both technologically and scientifically. One of the advantages of the absence of stray fields is reduced energy losses. In my project, we are exploring this special class of Heusler compounds with near-zero or zero net magnetic moments and with high spin polarization due to half-metallicity.

1.6 Spin gapless semiconductors

Spin-gapless semiconductors (SGS) are a special type of magnetic material, akin to half-metals, which have a closed gap for one spin band and a non-zero gap for the other [40, 41]. They can be considered as a combination of a gapless semiconductor [42] and a half-metallic ferromagnet. The conduction carriers in SGS materials are not only fully spin polarized but also excited easily due to the unique band structure at the Fermi level. Compared to the traditional semiconductors, the charge carriers have higher mobility in SGS. Also, their electrical conductivity is lower than that of half metals and hence they provide a better conductivity match with respect to spin injection to semiconductors. The above-mentioned advantages indicate that a SGS with these transport properties should offer novel functionalities in the field of spintronics. Compared to the other known spintronic semiconducting families, high Curie temperatures of Heusler-based alloys with SGS behaviour should provide another advantage for spintronics devices. In theory, many Heusler alloys have been identified as SGSs [40, 43-46] but very few have been confirmed experimentally. The first experimental confirmation of SGS behaviour in the Heulser family was reported in full-Heusler alloy Mn_2CoAl [47]. Later, some evidences of SGS behavior based on theory and experiment were found in quaternary Heusler alloys, CoFeMnSi [48] and CoFeCrGa [49]. A fully compensated ferrimagnetic SGS nature was claimed in the quaternary Heusler alloy CrVTiAl by Venkateswara *et al*. [50].

1.7 Summary

In this chapter, we started from introducing main concepts associated with the magnetization (magnetic moments and magnetic fields) in detail to discuss the magnetism in solids. The magnetic interactions can be divided into ferromagnetic, ferrimagnetic, antiferromagnetic, diamagnetic and paramagnetic based on the magnetic moments' performances. Once considering the ions experiencing a crystal field in a solid, the spin configurations (t_{2g} and e_g sub-bands) will be different in different crystal coordination or

ligands. This is very favourable to predict the magnetic and transport properties by figuring out how the electrons fill in the *d*-orbital sub-bands. On the other hand, due to the limits of high temperature measurements in magnetization, the molecular field theory is a valid way to explain and estimate the magnetic phase transition, which is a critical point in magnetic materials. Based on the mean-field model, there are some modified models (*e.g.* 3D-XY, 3D-Ising, 3D-Heisenberg) can be used to verify the existence of magnetic phase transitions, which are more close to the experimental results, as well as the interactions between ions or atoms.

The good understanding of magnetism and crystal-field effects support us to explore new fully compensated ferrimagnetic half metals, which have zero net moment. This material requires the characteristics of ferrimagnet with zero moment as well as half-metal with a spin gap simultaneously. Compared to other half metals, such as zinc-blende, double perovskites, magnetite or sulphides, Heusler alloys exhibiting high Curie temperature make it very attractive, as well as their tuneable composition in a formula X_2YZ or XYZ and their predictable magnetization by Slater-Pauling rule, which are all favourable to our purposes to search for new zero moment ferrimagnetic half-metal with high spin polarization and no stray field. This would be a very useful material for spintronics, which has very wide applications, such as computer memories (MRAM), magnetic sensors (GMR, TMR). And switching the dominated sublattice of compensated half metals is very promising for magneto-optic applications, either.

References

[1] J. M. D. Coey, *Magnetism and Magnetic Materials* (Cambridge university press, 2010).

[2] R. P. Feynman, R. B. Leighton, and M. Sands, *The Feynman lectures on physics*, American Journal of Physics **33**, 750 (1965).

[3] J. Stewart, *Caculus: Early Transcendentals senventh Edition*. Cengage Learining (2012).

[4] Y. Fuseya, M. Ogata, and H. Fukuyama, Transport properties and diamagnetism of dirac electrons in bismuth, Journal of the Physical Society of Japan **84**, 012001 (2015).

[5] T. Britannica, *Editors of Encyclopaedia* (Argon. Encyclopedia Britannica, 2020).

[6] S. O. Kasap, *Principles of electronic materials and devices* (Vol. **2**) (McGraw-Hill New York, 2006).

[7] A. Lennie, N. Condon, F. Leibsle, P. Murray, G. Thornton, and D. Vaughan, Structures of Fe_3O_4 (111) surfaces observed by scanning tunneling microscopy, Physical Review B **53**, 10244 (1996).

[8] V. Antonov, L. Germash, A. Shpak, and A. Yaresko, Electronic structure, optical and X-ray emission spectra in FeS_2, Physica Status Solidi (b) **246**, 411 (2009).

[9] Y. Song, D. Li, W. Mi, X. Wang, and Y. Cheng, Electric field effects on spin splitting of two-dimensional van der Waals arsenene/$FeCl_2$ heterostructures, The Journal of Physical Chemistry C **120**, 5613 (2016).

[10] L. P. Kadanoff, More is the same; phase transitions and mean field theories, Journal of Statistical Physics **137**, 777 (2009).

[11] N. Nagaosa and P. A. Lee, Ginzburg-Landau theory of the spin-charge-separated system, Physical Review B **45**, 966 (1992).

[12] M. Djamal and R. Ramli, *Giant magnetoresistance sensors based on ferrite material and its applications*, Magnetic Sensors: Development Trends and Applications; Asfour, A., Ed, 111 (2017).

[13] J. Kessler, *Polarized electrons* (Vol. **1**) (Springer Science & Business Media, 2013).

[14] I. Di Marco, A. Held, S. Keshavarz, Y. O. Kvashnin, and L. Chioncel, Half-metallicity and magnetism in the $Co_2MnAl/CoMnVAl$ heterostructure, Physical Review B **97**, 035105 (2018).

[15] J. M. D. Coey and M. Venkatesan, Half-metallic ferromagnetism: Example of CrO_2, Journal of Applied Physics **91**, 8345 (2002).

[16] H. Wu, Y. Ma, Y. Qian, E. Kan, R. Lu, Y. Liu, W. Tan, C. Xiao, and K. Deng, The effect of oxygen vacancy on the half-metallic nature of double perovskite Sr_2FeMoO_6: A theoretical study, Solid State Communications **177**, 57 (2014).

[17] X. Yu, C.-F. Huo, Y.-W. Li, J. Wang, and H. Jiao, Fe_3O_4 surface electronic structures and stability from GGA+ U, Surface Science **606**, 872 (2012).

[18] N. B. Schröter, I. Robredo, S. Klemenz, R. J. Kirby, J. A. Krieger, Ding. Pei, Tianlun Yu, S. Stolz, T. Schmitt, P. Dudin, T. K. Kim, C. Cacho, A. Schnyder, A. Bergara, V.N. Strocov, F. Juan, M. G. Vergniory, L. M. Schoop, Weyl fermions, Fermi arcs, and minority-spin carriers in ferromagnetic CoS_2, Science Advances **6**, eabd5000 (2020).

[19] R. De Groot, F. Mueller, P. Van Engen, and K. Buschow, New class of materials: half-metallic ferromagnets, Physical Review Letters **50**, 2024 (1983).

[20] P. Brown, K.-U. Neumann, P. Webster, and K. Ziebeck, The magnetization distributions in some Heusler alloys proposed as half-metallic ferromagnets, Journal of Physics: Condensed Matter **12**, 1827 (2000).

[21] S. Wurmehl, H. C. Kandpal, G. H. Fecher, and C. Felser, Valence electron rules for prediction of half-metallic compensated-ferrimagnetic behaviour of Heusler compounds with complete spin polarization, Journal of Physics: Condensed Matter **18**, 6171 (2006).

[22] X. Wang, Z. Cheng, G. Zhang, H. Yuan, H. Chen, and X.-L. Wang, Spin-gapless semiconductors for future spintronics and electronics, Report No. 0370-1573, 2020.

[23] J. Wernick, G. Hull, T. Geballe, J. Bernardini, and J. Waszczak, Superconductivity in ternary Heusler intermetallic compounds, Materials Letters **2**, 90 (1983).

[24] J. Winterlik, G. H. Fecher, A. Thomas, and C. Felser, Superconductivity in palladium-based Heusler compounds, Physical Review B **79**, 064508 (2009).

[25] S. Chadov, X. Qi, J. Kübler, G. H. Fecher, C. Felser, and S. C. Zhang, Tunable multifunctional topological insulators in ternary Heusler compounds, Nature Materials **9**, 541 (2010).

[26] T. Graf, C. Felser, and S. S. Parkin, Simple rules for the understanding of Heusler compounds, Progress in Solid State Chemistry **39**, 1 (2011).

[27] H. Lin, L. A. Wray, Y. Xia, S. Xu, S. Jia, R. J. Cava, A. Bansil, and M. Z. Hasan, Half-Heusler ternary compounds as new multifunctional experimental platforms for topological quantum phenomena, Nature Materials **9**, 546 (2010).

[28] J. Maxwell, *A Treatise on Electricity and Magnetism*, Volume I Clarendon Press (Oxford, UK, 1881).

[29] R. Kainuma, Y. Imano, W. Ito, Y. Sutou, H. Morito, S. Okamoto, O. Kitakami, K. Oikawa, A. Fujita, T. Kanomata and K. Ishida, Magnetic-field-induced shape recovery by reverse phase transformation, Nature **439**, 957 (2006).

[30] D. Betto, K. Rode, N. Thiyagarajah, Y.-C. Lau, K. Borisov, G. Atcheson, M. Žic, T. Archer, P. Stamenov, and J. M. D. Coey, The zero-moment half metal: How could it change spin electronics?, AIP Advances **6**, 055601 (2016).

[31] P. Villars, L. D. Calvert, *Pearson's Handbook of Crystallographic Data for Intermetallic Phases* (Materials Park, OH: ASM International, 1991).

[32] V. Surikov, V. Zhordochkin, and T. Y. Astakhova, Hyperfine fields in a new Heusler alloy Mn_2CoSn, Hyperfine Interactions **59**, 469 (1990).

[33] N. Lakshmi, A. Pandey, and K. Venugopalan, Hyperfine field distributions in disordered Mn_2CoSn and Mn_2NiSn Heusler alloys, Bulletin of Materials Science **25**, 309 (2002).

[34] S. Picozzi and A. J. Freeman, Polarization reduction in half-metallic Heusler alloys: the effect of point defects and interfaces with semiconductors, Journal of Physics: Condensed Matter **19**, 315215 (2007).

[35] D. Jung, H.-J. Koo, and M.-H. Whangbo, Study of the 18-electron band gap and ferromagnetism in semi-Heusler compounds by non-spin-polarized electronic band structure calculations, Journal of Molecular Structure: THEOCHEM **527**, 113 (2000).

[36] I. Galanakis, P. Dederichs, and N. Papanikolaou, Origin and properties of the gap in the half-ferromagnetic Heusler alloys, Physical Review B **66**, 134428 (2002).

[37] I. Galanakis, P. Dederichs, and N. Papanikolaou, Slater-Pauling behavior and origin of the half-metallicity of the full-Heusler alloys, Physical Review B **66**, 174429 (2002).

[38] S. Skaftouros, K. Özdoğan, E. Şaşıoğlu, and I. Galanakis, Generalized Slater-Pauling

rule for the inverse Heusler compounds, Physical Review B **87**, 024420 (2013).

[39] H. Kurt, K. Rode, P. Stamenov, M. Venkatesan, Y.-C. Lau, E. Fonda, and J. M. D. Coey, Cubic Mn_2Ga thin films: Crossing the spin gap with Ruthenium, Physical Review Letters **112**, 027201 (2014).

[40] X. L. Wang, Proposal for a New Class of Materials: Spin Gapless Semiconductors, Physical Review Letters **100**, 156404 (2008).

[41] X.-L. Wang, S. X. Dou, and C. Zhang, Zero-gap materials for future spintronics, electronics and optics, NPG Asia Materials **2**, 31 (2010).

[42] J. Tsidilkovski, *Electron spectrum of gapless semiconductors* (Vol. **116**) (Springer Science & Business Media, 2012).

[43] S. Skaftouros, K. Özdoğan, E. Şaşıoğlu, and I. Galanakis, Search for spin gapless semiconductors: The case of inverse Heusler compounds, Applied Physics Letters **102**, 022402 (2013).

[44] G. Xu, E. Liu, Y. Du, G. Li, G. Liu, W. Wang, and G. Wu, A new spin gapless semiconductors family: Quaternary Heusler compounds, EPL (Europhysics Letters) **102**, 17007 (2013).

[45] H. Jia, X. Dai, L. Wang, R. Liu, X. Wang, P. Li, Y. Cui, and G. Liu, Ti_2Mn Z (Z= Al, Ga, In) compounds: Nearly spin gapless semiconductors, AIP Advances **4**, 047113 (2014).

[46] L. Wang and Y. Jin, A spin-gapless semiconductor of inverse Heusler Ti_2CrSi alloy: First-principles prediction, Journal of Magnetism and Magnetic Materials **385**, 55 (2015).

[47] S. Ouardi, G. H. Fecher, C. Felser, and J. Kübler, Realization of spin gapless semiconductors: The Heusler compound Mn_2CoAl, Physical Review Letters **110**, 100401 (2013).

[48] L. Bainsla, K. Z. Suzuki, M. Tsujikawa, H. Tsuchiura, M. Shirai, and S. Mizukami, Magnetic tunnel junctions with an equiatomic quaternary CoFeMnSi Heusler alloy electrode, Applied Physics Letters **112**, 052403 (2018).

[49] L. Bainsla, A. Mallick, M. M. Raja, A. Coelho, A. Nigam, D. D. Johnson, A. Alam, and K. Suresh, Origin of spin gapless semiconductor behavior in CoFeCrGa: Theory and Experiment, Physical Review B **92**, 045201 (2015).

[50] Y. Venkateswara, S. Gupta, S. S. Samatham, M. R. Varma, K. Suresh, and A. Alam, Competing magnetic and spin-gapless semiconducting behavior in fully compensated

ferrimagnetic CrVTiAl: Theory and experiment, Physical Review B **97**, 054407 (2018).

Chapter 2   Methodology

In this Chapter, the relevant experimental techniques, such as arc-melting, annealing, x-ray diffractions, and other measurements, are introduced. The arc-melting method is used for bulk material preparation. After this, we annealed the ingot at high temperatures, from 500ºC to 1000ºC, for 7 days or longer and then we may either fast cool or slow cool the ingot depending on purposes. A different approach, chemical vapour deposition was used to grow single crystals of CoS_2. We used powder X-ray diffractometer to analyse the crystallographic properties. Superconducting quantum interference device (SQUID) magnetometry and Mössbauer spectroscopy were used to characterize the magnetization and the Fe atomic moment, respectively. Point contact Andreev reflection (PCAR) spectroscopy fitted by BTK (Blonder-Tinkham-Klapwijk) model [1] was used to deduce the spin polarization.

2.1   Arc-melting

Arc-melting is a typical method to prepare metal ingots with high chemical and mechanical homogeneity The metallic elements sit in a depression in a copper hearth where they heat up to 2000 to 4000 K in an argon atmosphere via an electric arc struck between a tungsten electrode and the metals (Fig. 2.1b). A welding power supply provides the electric current and it forms an electrical arc in the Ar atmosphere between the electrode and the metals. In order to attain compositional uniform alloys, the metal buttons should be repeatedly turned over and remelted for several times. Due to the ionized Ar, an electrical arc discharge is realized between two electrodes and generate high intensity beam to heat the metals. The temperature can be up to thousands centigrade.
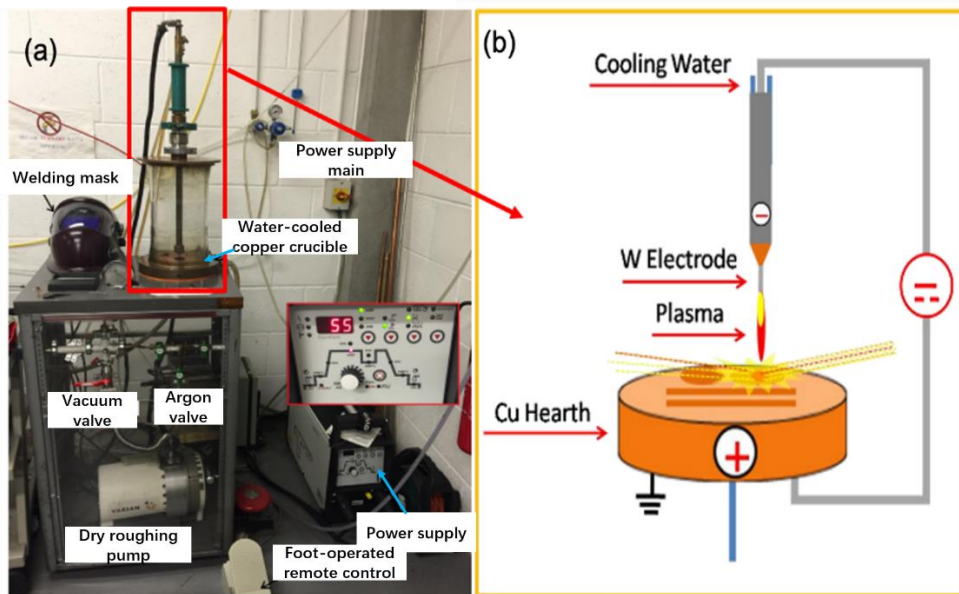
Fig. 2.1. (a) Arc-melting system includes 3 main parts- power source, chiller and vacuum chamber. (b) The schematic diagram to the electrical arc generation between the electrode and the elements [2].

The arc-melting system includes three main parts, power source, chiller and vacuum chamber with copper hearth and tungsten sword as Fig. 2.1a shown. The Cu electrode with a sharp W tip, which is made from 2% thoriated, red tungsten, 4.0 mm in a diameter. A Tetrix 230 AC/DC comfort power supply with rotary dial is used for arc melting and controlling the heating temperature. The welding voltage from 10.1 V to 19.2 V and DC current from 3 A to 220 A can be supplied. A foot-operated remote control (RTF 19POL 5) is used for adjusting the welding current (0% to 100%) depending on the preselected current range on the power supply. The melting starts after carefully placing the tungsten electrode sword onto the metals and pressing the torch trigger and lift arc current flows. In general, the metal ingot should be remelted four times or more to ensure its homogeneity. The cold circulation water from the chiller cools the electrode and copper hearth. The vacuum chamber is purged and vented five times under Ar and 10^{-2} bar vacuum, respectively. Melting occurs in a vacuum tight chamber with high purity Ar atmosphere (0.5 bar), which ensure protection from oxidization, on the water-cooled Cu hearth. A titanium pellet

gathering which changes its colour after melting and after oxygen absorption ensures it keeps the chamber oxygen-free as it getters oxygen gas. A batch of three alloys can be made in a single evacuation, as there are three crucibles in the copper hearth (2 small and 1 large). Around 5g of metals can be melted in a small pocket crucible and 12g in the large one.

A 55 – 75 A DC current is usually used for Mn-based alloys due to the high vapour pressure of Mn than that of other elements, which causes the Mn loss. While the current values increase up to 75 – 80 A for V-based alloys or titanium owing to high melting points. Current controlling, cooling rate of the chiller and electrode gap all influence on the solidification rate and process which allows production of defect free materials [3].
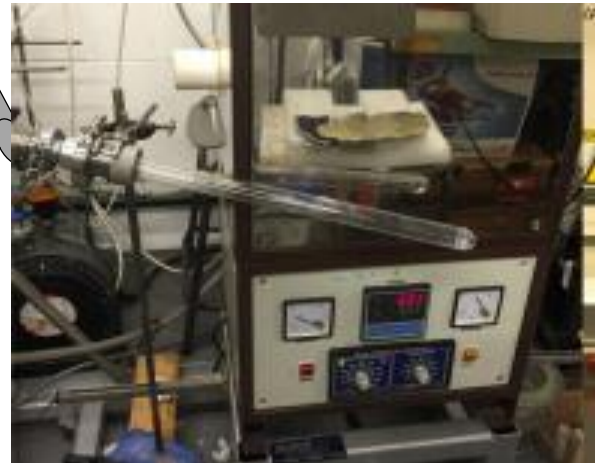
2.2 Annealing technique

Annealing is a heat treatment process which may change the physical and chemical properties of a compound to some degrees. The determination of the annealing temperature is based on the materials' recrystallization temperature. In addition, the annealing temperature and time are the two main factors to determine the ordered structure's formation. The cooling rate depends on the request of the types of the alloys being annealed. Such as, steel is usually left to cool down to room temperature in air while copper and silver either can be cooled in air slowly or quenched in ice-water mixture quickly. When we explore the best annealing temperature, the fast cooling is very helpful to obtain high-temperature phases, which might be a metastable one, *e.g.* FeV forming B2 at 773 K [4], which cannot be achieved with a slow cooling. And the heating process promotes atoms migrate in the crystal lattice and reduces the dislocations. The crystal grain size and phase composition depend upon the heating and cooling rates and also determine the material properties. The knowledge of phase diagrams and material compositions guide the annealing process to prepare expected samples for a further study. In our study, the annealing temperature for Mn-based alloys ranges from 600ºC to 800ºC due to the high vapour pressure of Mn, while for Mn-free alloys, that can be up to 1000ºC (*e.g.* CrVTiAl). Samples are subjected to anneal

at various temperatures and time at high vacuum (10^{-6} to 10^{-7} bar), following by furnace cooling or rapid quenching in the ice-water mixture in order to make the specimen homogeneous or pursue the ordered phase. The samples are loaded in a quartz tube and a Preiffer vacuum Hi Cube turbo-molecular pump is used to keep a high vacuum. Or the samples are sealed in a quartz tube with high vacuum (10^{-6} bar). The temperature of the furnace, which is used for annealing, is shown on temperature display confirmed by K-type thermocouple. The set-up of the annealing measurement as illustrated in Fig. 2.2. It includes a furnace (maximum temperature: 1000ºC) and a vacuum pump station with a quartz tube to keep samples in a high vacuum protecting from oxidation.
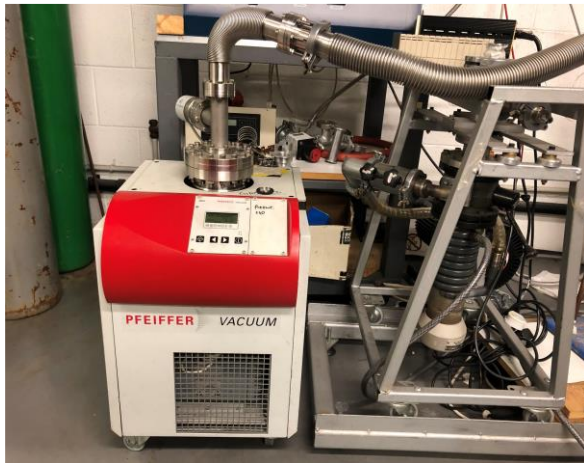
Vacuum station with turbo-molecular pump   **Resistive tube furnace**

Fig. 2.2. The quartz tube pumped by turbo-molecular pump was putting into a resistive tube furnace. The extreme high temperature of this furnace can be up to 1000ºC.

2.3 Chemical vapour transport method (CVT)

Chemical vapour transport is a method for crystal growth via the gas phase, which is popularized by Schäfer [5]. It is a process where a condensed phase, typically a solid has to be volatilized in a gaseous reactant (transport agent) due to the solid with insufficient pressure for its own volatilization and then deposited elsewhere in the form of crystals. Usually, the volatilization and crystallization temperatures are different. If a condensed

substance at the position of volatilization encounters a temperature gradient, it moves to the place of deposition (for crystallization) via the gas phase, from source to sink (Fig. 2.3).
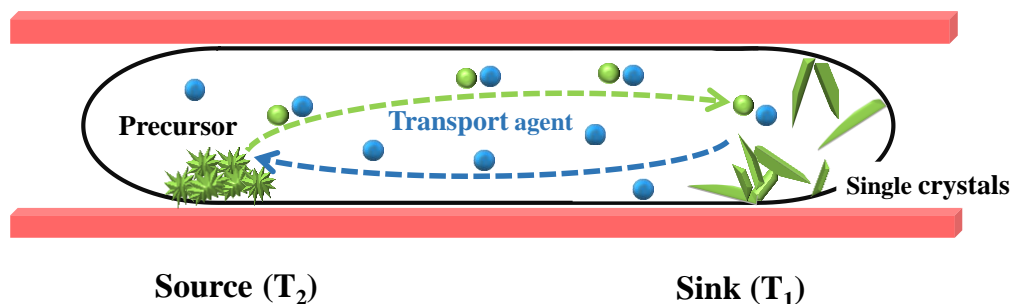

Fig. 2.3. Schematic diagram of CVT experiments for crystallization of solids in a temperature gradient. Generally, the temperature of the source (T_2) is slightly higher than that of the sink (T_1).

A character of CVT reactions is that the transport agent is required for the dissolution of a solid in the gas phase. Conventional transport agent is halogens or halogen compounds. A suitable transport agent transfers the components of the initial solid into gas phase, which is caused in almost every case by different temperatures leading to change the equilibrium position in source and sink. Transport directions are related to two reaction mechanisms: exothermic reactions transport from sink (T_1) to higher temperature (T_2) zone, and endothermic reactions transfer the solid (source T_2) to the cooler zone (sink T_1). The other important parameter is the rate of the mass transport. The rate-determining step is the gas motion, which is the slowest one in a CVT reaction in most cases. Therefore, optimising the parameters, including growth temperature, transport agent, transport direction and the free energy of the reaction, is a key to a successful CVT.

The set-up of CVT experiments consists of two-zone furnace (for source T_2 and sink T_1), the reactant and transport agent sealed in a quartz tube (see Fig. 2.3). The prepared ampoule for CVT is placed in the middle of the furnace reaching both temperature zones. It is noted that a high transport rate usually is chosen for the synthesis of a compound or the purification of it. While a crystal growth is required rather smaller transport rates. In our

study, we prepared CoS_2 in single crystal form. It is essential to avoid explosions due to the sulphur vapour pressure increasing on heating in a sealed ampoule. The single crystal of CoS_2 used this method was prepared by Dr. Yangkun He.

2.4 X-ray diffraction and Rietveld refinement

X-ray diffraction (XRD) is an experimental technique to identify the crystal phase structure of a material and can also provide information on unit cell dimensions. It can characterize a clean polished alloy, finely ground, homogenized bulk composition, chemical powder and thin films.

In 1912, Max von Laue discovered that crystalline substances act as three-dimensional diffraction grating for X-ray wavelengths similar to the spacing of planes in a crystal lattice, which is helpful to understand well of the properties connected with the structure of the studying substances. Fig. 2.4a presented the schematic diagram of beam path following Bragg diffraction Law. The constructive interference of monochromatic X-rays and a crystal is the basic theory of the X-ray diffraction. The interaction of the incident rays with the sample delivers constructive interference only occurs at the particular angles of incidence which obeys Bragg's law [6]:

$$2d\sin\theta = n\lambda \tag{2.1}$$

where λ is the x-ray wavelength, d is the lattice spacing, *i.e.* atomic layer (inter plane) separation of Bragg planes, n is the diffraction order and θ is the incident angel of the x-ray and the sample surface. These detected x-ray diffractions by scanning the sample through a range of 2θ angles are counted. Based on this equation, which is necessary but not sufficient for a reflection to occur, we can calculate the lattice constants which is related to the spacing lattice *d* for a given wavelength [7]. All X-ray diffractions carried out in my project are performed with Cu Kα radiation (λ = 1.5405 Å), which produces X-rays in an X-ray tube.
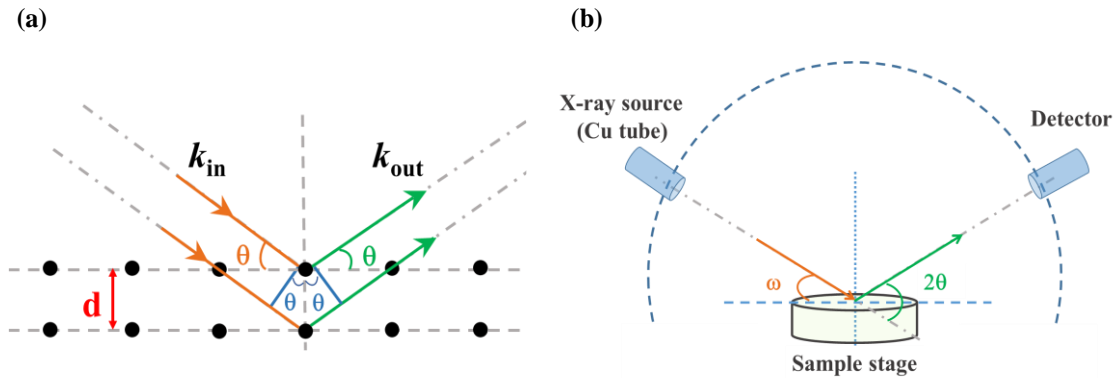
Fig. 2.4. (a) Schematic diagram of Bragg diffraction Law. X-ray radiation incident at an angle θ is reflected from parallel atomic planes with spacing d. (b) Basic XRD measurement geometry: X-ray source, detector and the sample stage. The related parameters of our measurements ω and 2θ are shown.

Our X-ray diffracted experiments were carried on the Philips Panalytical X'Pert Pro, which is equipped with multi-strip detectors to allow for the integration of each point along 2θ over the detector array for fast acquisition. A basic XRD measurement figure related our diffractions is illustrated in Fig. 2.4b. The mainly related parameters are ω and 2θ. Equipment calibration is performed by using the manual scan to align the beam path by adjusting ω and 2θ to ensure accurate diffractions with high intensity. On the other hand, high quality diffraction patterns require fine powders, which are crushed from our bulk polycrystalline samples and then spread out and flattened on a glass slide. It is noted that, in our study on Heusler alloys, the superlattice peaks are very significant to distinguish the truly crystalline structure. The superlattice peak comes from a periodic structure of a multilayer. In our case, the superlattice peaks in the Heuslers arise from the X and Y sublattices, which should sit at the specific sites without exchanging between each other. The intermixture between X and Y will lead to the disorder (A2 or B2 phase [8]) that explains the disappearance of superlattice peaks. It will affect the alloys physical properties and might be off the initial expectation. Fig. 2.5 exhibits the diffraction of an ordered Heulser-structure and disordered B2 structure for comparison.
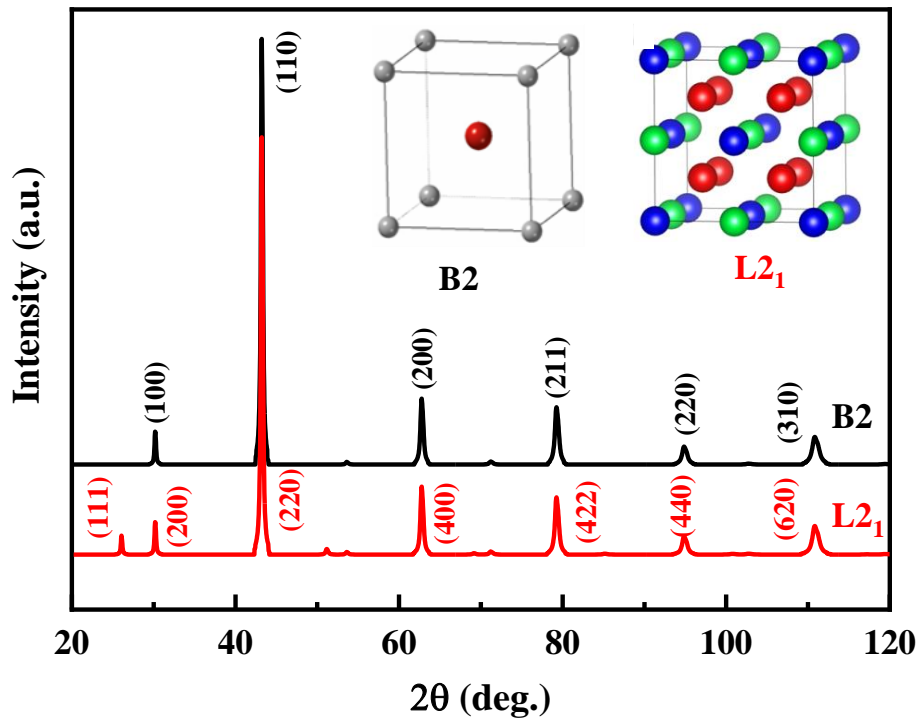
Fig. 2.5. The simulated X-ray diffractions of B2 and L2$_1$ phases. The intermixture of X (1/4, 1/4, 1/4) and Y (1/2, 1/2, 1/2) results in B2 phase. The absence of a (111) superlattice peak indicates B2 phase crystallization.

Rietveld refinement is the most common powder XRD refinement technique used in the characterisation of crystalline materials proposed by Hugo Rietveld in the 1960s. The Rietveld refinement method is used to fit a calculated diffraction pattern to experimental data by a least squares approach, but it requires a reasonable initial approximation of many free parameters, such as space group, lattice parameters, peak shape and coordinates of all atoms in the crystal structure, what can be refined from the observed diffraction data. Although limitations of background noise and resolution exist, it is still possible to determine the accurate lattice parameter and crystal structure by fitting a profile. This powerful refinement technique also can be used to explore the structural details, such as the grain size, phase fraction volumes, atomic coordinates, micro strain in crystal lattice [9].

The software, Fullprof Suite, is formed by a set of crystallographic programs (Fullprof, EdPCR, GFourier etc..). It is used for Rietveld analysis of x-ray powder diffraction data. And the structure to be refined is typically attained from a Crystallographic Information File (. CIF). In our work, the CIF file is obtained from Crystallography Open Database (COD) [10].

2.5 SQUID magnetometry

SQUID (Superconducting Quantum Interference Device) magnetometer is one of the most highly sensitive and effective methods to measure magnetization based on the change of flux through a coil. The magnetic flux change comes from the quick removal of a sample positioned at the centre of a coil in the field to a point far from the coil (Fig. 2.6) to modify the current in the superconducting loop, which consists of two superconductors separated by thin insulating layer to form two parallel Josephson junctions. The DC SQUID (Fig. 2.7) is based on the Josephson effect [11] describing a supercurrent phenomenon that a current that flows continuously without any voltage applied due to the tunnelling of the Cooper pairs through a tunnelling barrier. The supercurrent flowing through the junction is determined by

$$I(t) = I_c \, sin(\phi(t)) \tag{2.2}$$

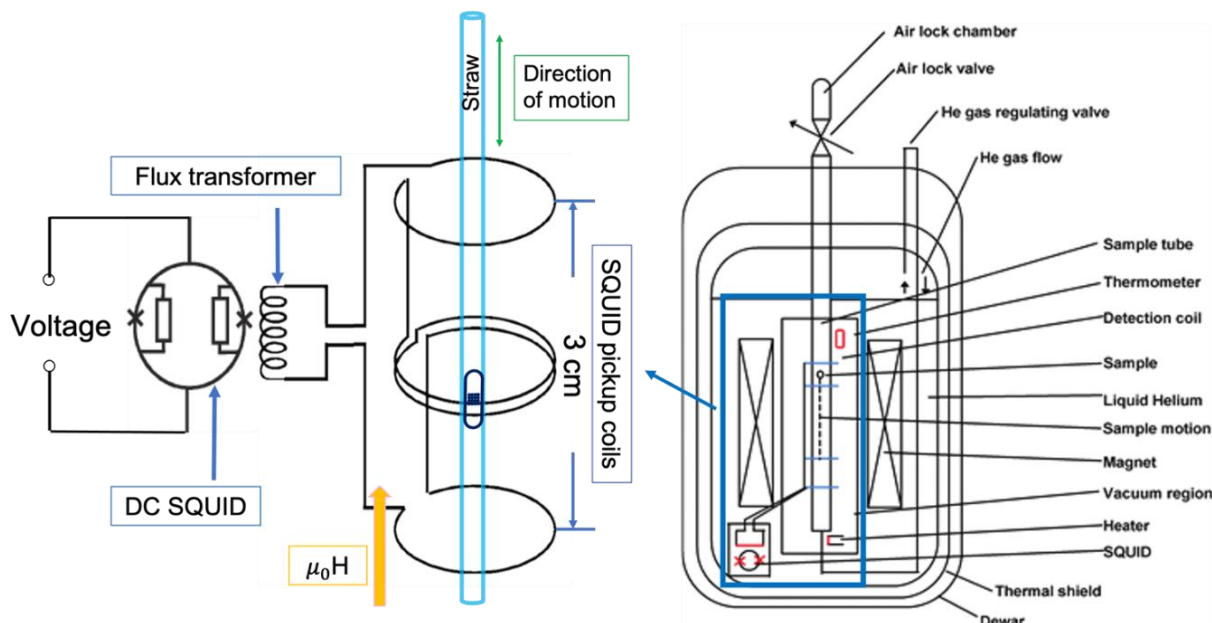where I_c is the critical current and $\phi(t)$ is the Josephson phase.

Fig. 2.6. Schematic plot of the DC SQUID magnetometer (right) [12]. The details of the main circuits (blue square labelled) showing on the left side. Extracting the straw to move the sample from the centre to a point yields an induced *emf.* due to the flux change and then the induced current is flowing in the coil and generate a magnetic field into the SQUID loop which delivers a magnetic flux.

Without the external magnetic field, the input current I_{tot} splits into two branches equally (Fig. 2.7a). If an external magnetic flux Φ threading this superconducting loop (Fig. 2.7b), it will generate a screening current I_s circulating in the loop to yield a magnetic field to cancel the applied external flux and create an additional Josephson phase which is proportional to Φ. In the two branches, the current becomes $I_b/2 + I_s$ and $I_b/2 - I_s$, respectively. Once the current in either branch exceeds I_c of the Josephson junction, there is a voltage produced across the junction. The Josephson relations in current and voltage is derived as,

$$\frac{\partial I}{\partial \phi} = I_C cos(\phi) \qquad \qquad \textbf{(2.3)}$$

$$\frac{\partial \phi}{\partial t} = \frac{2\pi}{\Phi_0} V(t) \qquad \qquad (2.4)$$

where $\Phi_0 = \frac{2\pi\hbar}{2e}$ (2.07×10^{-15} Tm^2) is the magnetic quantum flux. Rearranging the above equations and show the voltage-current characteristic of an inductor,

$$V(t) = \frac{\Phi_0}{2\pi I_c cos(\phi)} \frac{\partial I}{\partial t} = L(\phi)\frac{\partial I}{\partial t} \tag{2.5}$$

where $L(\phi)$ is the kinetic inductance as a function of the Josephson phase ϕ. Here, $L(0) = \frac{\Phi_0}{2\pi I_c}$ is called Josephson inductance L_J. One period of voltage variation corresponds to an increased flux quantum. Therefore, the SQUID acts as a magnetic flux-to-voltage transformer converting the magnetic flux into an electrical voltage. SQUID magnetometer can detect super low magnetic moment (10^{-10} Am^2). And the great sensitivity of order 10^{-11} Am^2 at low fields (below 250 mT) and 2 ×10^{-15} Am^2 at high fields [13], which performs in AC mode.
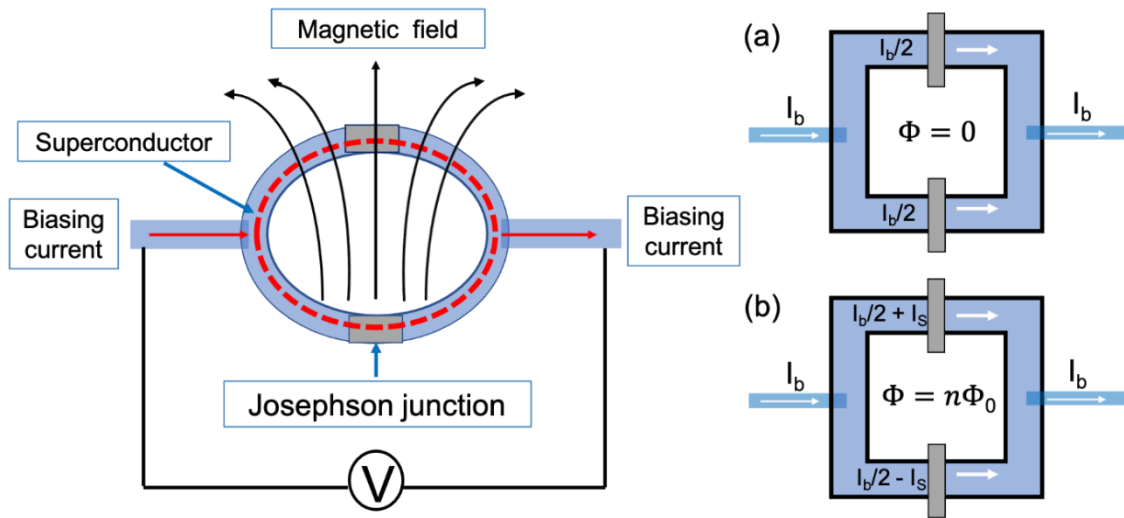

Fig. 2.7. Scheme of a DC SQUID (left). Electrical diagram of DC SQUID under the external magnetic flux Φ ($\Phi = 0$ (a); $\Phi = n\Phi_0$ (b)). I$_b$, bias current; I$_s$, screening current.

A Quantum Design Magnetic Property Measurement System (MPMS XL-15) is used to characterize the magnetic properties of the studied materials. A closed-helium cycle is used to cool the superconductors as well as the low temperature measurements. The

magnetization measurements can be run from 4 K to 400 K and the applied field can be up to 5 T. A small piece of the bulk material placed in a gel cap which is mounted on the centre of a drinking straw. The gel cap has small diamagnetic contributions to the measured signal. The weak ferromagnetic or fully compensated ferrimagnetic signal should be corrected by subtracting the gel cap contribution. It is noted that the magnetization of the thin films or magnetic liquids also can be measured by SQUID magnetometer, which is also needed to take the magnetic signal from the substrates or the holder into consideration.

2.6 Mössbauer spectroscopy

Mössbauer spectroscopy is a spectroscopic technique based on the Mössbauer effect, which was discovered by Rudolf Mössbauer in 1958 [14]. The Mössbauer Effect is used in gamma-ray spectroscopy, where the nucleus bound in a solid has a possibility of emitting or absorbing gamma rays with no loss of energy to a nuclear recoil (Fig. 2.8). The system obeys the conversation of momentum only on average, not for each event [15]. It requires a nucleus undergoes alpha or beta decay or electron capture and then falling into a lower energy ground state by emitting a gamma ray. For example, excited ^{57}Co decays to ^{57}Fe by electron capture and it can decay to the ground state (3/2 to 1/2) by emitting a gamma ray with $E_\gamma = 14.4$ keV (left-top of Fig. 2.8).

A simplified set-up of Mössbauer spectroscopy measurement was shown in the bottom of Fig. 2.8, which includes ^{57}Co source, sample container and detector. Mössbauer spectroscopy measures the transition energy (γ-absorption or emission) spectrum using a Doppler scale in mms^{-1}. If the emitting and absorbing nuclei are in the same chemical environments, the transition energy would be exactly same and where both materials are at rest, we can observe resonant absorption. Nevertheless, in the different chemical environments, the nuclear energy levels will shift in a few different ways. Although these shifted energies are

tiny (< 1 meV), the extremely narrow spectral linewidths of gamma rays make small energy shifts corresponded to large changes in absorption. Through Doppler modulation to bring the two nuclei back into the resonance, for some value of relative velocity. That will be observed in the Mössbauer spectra, which shows the gamma ray intensity as a function of the source velocity. The velocity corresponds to the resonant energy levels of the sample based on v /c $= \Delta E / E_\gamma$ (1 mm/s $= 4.8 \times 10^{-8}$ eV). Typically, there are three types of nuclear interactions might be observed through the spectrum: isomer shift, quadrupole splitting and hyperfine magnetic splitting [16, 17].

Isomer shift describes a shift in the resonance energy of a nucleus due to the transition of electrons within its *s* orbitals, which is a relative measure. It is useful for determining oxidation state, valence states, electron shielding and the electron-drawing power of electronegative groups [16].

Quadrupole splitting (QS) is the separation between two absorption peaks due to the electric field gradient (EFG), which reflects the interaction between the nuclear energy levels and surrounding EFG. Nuclei in states with spin quantum number $I > \frac{1}{2}$ exhibits non-spherical charge distributions, which may have a nuclear quadrupole moment. And the nuclear energy levels are split by an asymmetric electric field (produced by an asymmetric electronic charge distribution or ligand arrangement) splits the nuclear energy levels [16]. The quadrupole splitting can be used for determining oxidation state, spin state, site symmetry and the arrangement of ligand [16]. For singlets, the value of QS is zero or very small, which can be observed in a cubic symmetry.

Magnetic hyperfine splitting reflects an interaction between the magnetic moment of the nucleus and the magnetic field created by the surrounding magnetically ordered electrons due to Zeeman Effect. The spin energy of a nucleus split into $2l + 1$ sub-energy levels under a magnetic field, where *l* is the nuclear spin and the selection rule is $\Delta l = 0, \pm 1$. For example, the ^{57}Fe nucleus with spin state $l = 3/2$ will split into 4 non-degenerate sub-states with m_l values of $+3/2, +1/2, -1/2$ and $-3/2$, which will introduce 6 possible transitions for a 3/2 to 1/2 states [16] (see right-top of Fig. 2.8). The corresponding spectrum show sextet peaks as shown in right-bottom of Fig 2.8. For a randomly oriented crystalline, the ratio of the component of the sextet is 3:2:1:1:2:3. The magnetic transition from anti-ferromagnetism or

ferromagnetism to paramagnetism corresponding to the sextet transforming to quadrupole doublet. Further, the non-magnetic Fe in a compound usually shows a singlet. It is noted that the imperfections in the lattice may influence the magnetic hyperfine spectrum. Any quadrupole shifts are sensitive to the Fe oxidation, spin state and coordination. An extent of splitting is proportional to the magnetic field strength, which depends upon the electron distribution of the nucleus. Therefore, we can calculate the localized moment of Fe based on this principle. As a rule of thumb for Fe- metal, a moment of 1 μ_B/Fe produces a hyperfine field B_{eff} = 15 T, α-Fe metal has 2.2 μ_B and B_{eff} = 33 T.

Samples are prepared for Mössbauer spectroscopy by mixing 45 mg of powder sample with 30 mg of icing sugar. To determine the chemical and structural environment of iron atoms on a nearest neighbour length scale, site occupancies of atoms, and magnetic characteristic of the phases in iron- based materials. Transmission Mössbauer spectrometry was carried out using a ^{57}Co (Rh) source in the constant acceleration mode for a bulk sample with natural Fe (2% ^{57}Fe) or doped with pure ^{57}Fe. Spectra were analysed by means of a least-square fit to Lorentzian peaks and the isomer shift values are quoted relative to metallic α-Fe at 300 K. In this thesis, the measurements and fits of Mössbauer spectroscopy were conducted by Prof. P. Stamenov.
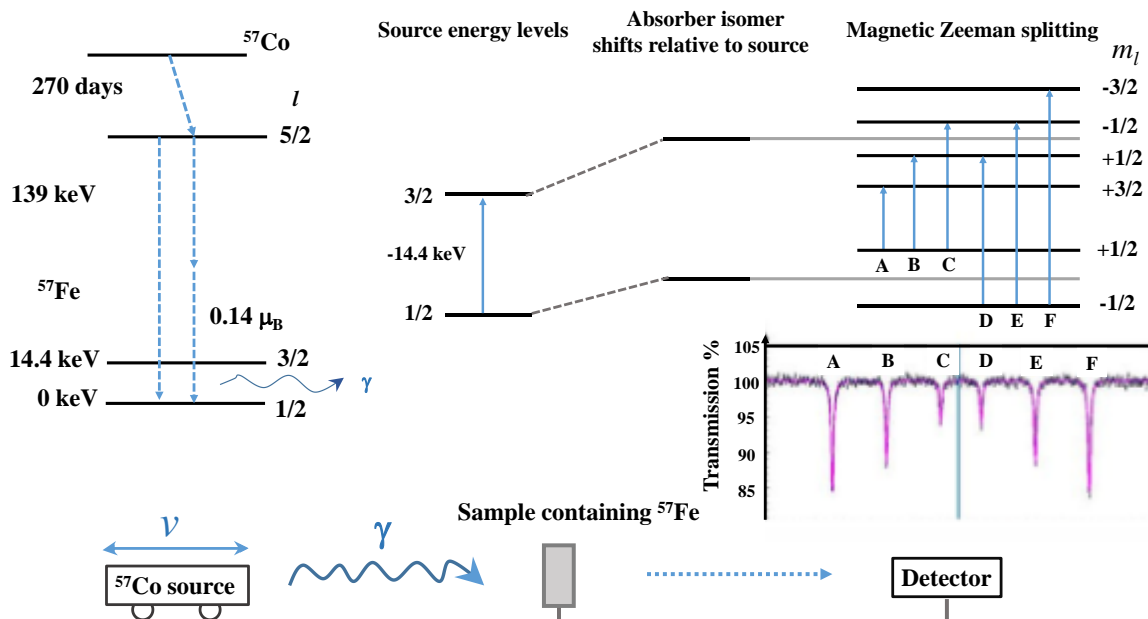
Fig. 2.8. Nuclear decay scheme of ^{57}Co which undergoes (n, γ) decay, populating the 14.4 keV excited state of ^{57}Fe. These γ-rays are resonantly absorbed in an absorber containing ^{57}Fe. Hyperfine structure in the absorption spectrum is revealed by modulating the energy of the source by moving it with constant acceleration with an electromagnetic transducer. A six-level hyperfine spectrum of a ferromagnetic α-Fe absorber is shown in right top. The bottom sketch shows the set-up of the Mössbauer spectroscopy measurements.

2.7 Point Contact Andreev Reflection (PCAR)

Point contact spectroscopy (PCS) [18] describes a tunnelling experiment, two metal electrodes physically touching each other with no intended tunnelling barrier at the interface. The electrical transport is realized by a narrow construction formed at the interface between the two metal electrodes. The ballistic contact is a priority method which can ensure the mean free path of the electrons in both the metals is greater than the diameter of the point contact. That means, with applying of a bias voltage, the electrons are accelerated across the ballistic contact diameter without undergoing any scattering and therefore do not dissipate energy. The

property of the PCS is utilized to get energy and momentum resolved information on different process at Fermi level.
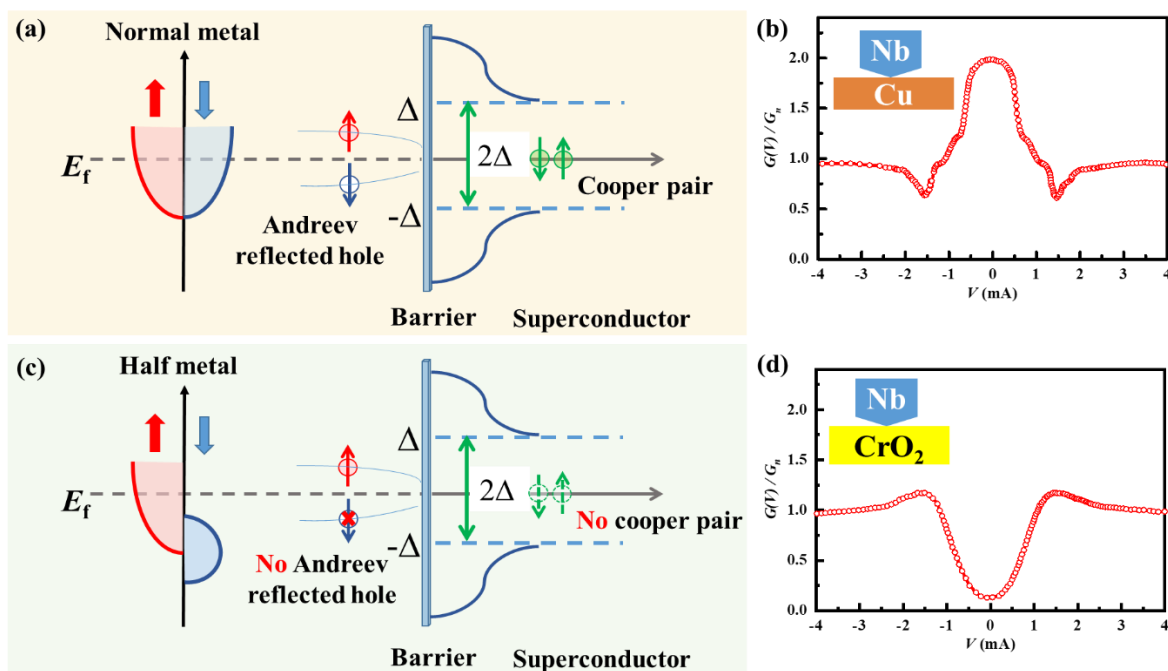

Fig. 2.9. Schematic of the Andreev reflection process for (a) a normal metal-superconductor interface and (c) a half metal- superconductor interface. The half metal has 100% spin polarized electrons at the Fermi level. The corresponding PCAR spectrum of a N-S (Cu-Nb) and a HM-S (CrO$_2$-Nb) interfaces are shown in (b) and (d) [19].

Compared to PCS, one of the normal metal (N) is replaced by a superconductor (S) in point contact is called Andreev reflection (PCAR) spectroscopy [20], which is a powerful technique for the measurement of Fermi level spin polarization in metallic and degenerate semiconducting materials. In Andreev reflection (Fig. 2.9a), an electron incident on the N-S interface gets reflected back as a hole in the opposite spin band of the metal and a Cooper pair propagates inside the superconductor. The process is elastic in nature and highly spin dependent. That means the excitation energy to the incident electron is as same as the reflected hole. At the extreme low temperature ($\sim$ 0 K), which is an ideal state, for an N-S interface with no barrier, the differential conductance ($G = dI/dV$) at low bias voltage ($|V| <$

Δ/e) is as large as twice that at its high value ($|V| \gg \Delta$/e).   However, the experiments cannot be carried out at 0 K and the barrier can never be completely removed, either, which is due to the Fermi velocity mismatch in two electrodes and the oxide barrier at the interface. There are two peaks appearing in the G-V spectrum close to $\pm\Delta$/e for such finite barriers (Fig, 2.8a, no polarized electron). Once the normal metal in Andreev reflection is replaced by a half metal, who has 100% spin polarized electrons, the Andreev reflection will be suppressed due to the absence of Cooper pairs (Fig. 2.9c, polarized electrons). It leads to zero conductance across the interface below the gap. Therefore, the value of spin polarization can be estimated from the degree of this suppression by using Blonder-Tinkham-Klapwijk (BTK) model [1].

The BTK model is used to calculate the current through the point contact for the PCAR spectroscopy. The BTK theory neglects some of the delicate surface phenomena, such as the lattice relaxation. There are drawbacks of this theory, like the step-function shape of the voltage drop across the barrier and the lateral momentum conservation. The modified BTK model solves some but not all the issues, which is the most satisfactory method to deduce the spin polarization. The spin-polarized current in the ferromagnet changes the conductance of the contact in Fermi level. This measurement offers several advantages on the sample preparation, testing requirements and accuracy. For example, no restrictions on the sample geometry, which avoids some complicated fabrication steps. And there is no requirement of an applied magnetic field and show excellent energy resolution (~0.1 meV). However, the possible surface modification coming from the uncontrolled surface oxides or other chemical reactions on both ferromagnets, and superconductors shows a negative side, which could not quantify. Although this drawback exists, compared with other methods which better controlling the surface oxidation, the values of the spin polarization is consistent with. Also, the PCAR measurement is considerably easier to put into practice. This is helpful to explore and widen the research of many new materials (metal or half-metal) that are too difficult to incorporate into tunnel junctions.

A standard PCAR measurement is done in a four-probe geometry (Fig. 2.10a). A DC voltage (V_{dc}) is modulated by a small AC voltage, $V_{ac} \cos (\omega t)$. The corresponding converted current ($I + i \cos (\omega t)$), which is passed through the tip-sample junction. The output of the contact voltage can be expressed by a Taylor series as

$$V(I + i cos(\omega t)) = \; V(I) + \frac{dV}{dI} i cos(\omega t) + \; \frac{1}{2}\frac{d^2 V}{d^2 I} \; i^2 cos^2(\omega t) + \cdots \qquad \textbf{(2.6)}$$

If the current is sufficiently small, the higher order terms can be neglected. The differential conductance $G(V) = dV/dI$ of the junction is recorded as a function of bias voltage (V). The PCAR spectra is generally depicted by the normalized conductance $G(V)/G_N$ vs the bias voltage (V).
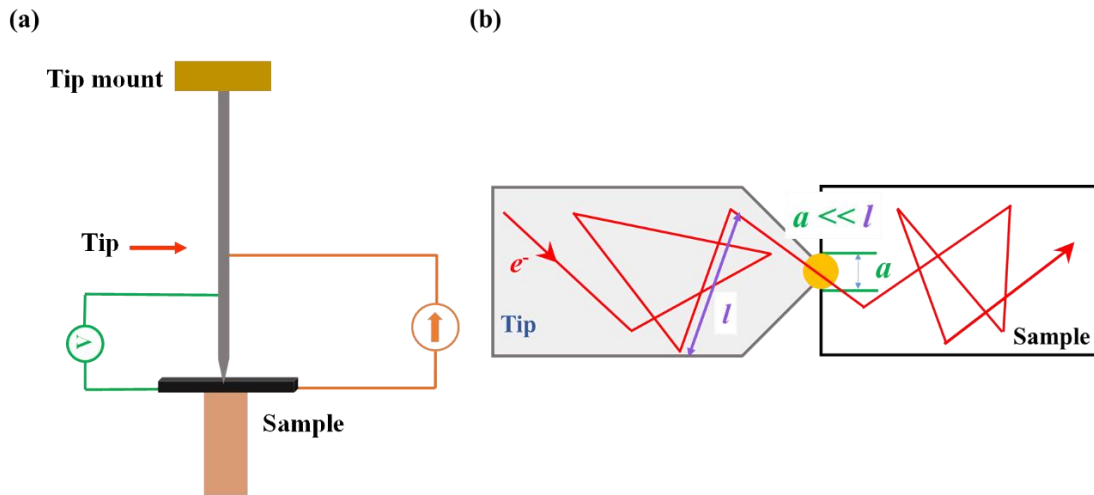

Fig. 2.10. (a) Schematic of a standard four-probe geometry technique to measure the differential conductance across the tip and sample. (b) Ballistic transport in a point contact experiment. a is the diameter of the ballistic contact and l is the mean free path.

In our work, a mechanically sharpen Nb superconducting tip lands on the surface of sample using a vertical micrometre screw gauge. In our measurements the transport regime mostly lies in the diffusion limit, where the contact area (a) is between ballistic ($a \ll l$) (Fig. 2.10b) and inelastic limit ($a \gg l$). The inelastic limit is always avoided in the PCAR measurement as in this regime both energy and momentum information are lost at the

junction. Although, in the diffusion regime elastic scattering of carrier preserve the energy the momentum information is lost. Since, in our case we are interested in measuring the energy gap of magnetic samples, the diffusion regime allows to measure the same. The differential conductance of PCAR spectra are fitted within modified-BTK model as described by P. Stamenov [21]. All of the PCAR measurements related to this thesis were conducted by *Ajay Jha*.

References

[1] G. E. Blonder, M. Tinkham and T. M. Klapwizk, Transition from metallic to tunneling regimes in superconducting microconstrictions: Excess current, charge imbalance, and supercurrent conversion, Physical Review B **25**, 4515 (1982).

[2] Yaser A. Alshataif, S. Sivasankaran, Fahad A. Al-Mufadi, Abdulaziz S. Alaboodi and Hany R. Ammar, Manufacturing methods, microstructural and mechanical properties evolutions of high-entropy alloys: A review, Metals and Materials International **26,** 1099 (2020).

[3] H. Fredriksson and U. Akerlind, Solidification and crystallization processing in metals and alloys (John Wiley & Sons, New York, USA, 2012).

[4] J. Muñoz, M. S. Lucas, O. Delaire, M. L. Winterrose, L. Mauger, Chen W. Li, A. O. Sheets, M. B. Stone, D. L. Abernathy, Yuming Xiao, Paul Chow, and B. Fultz, Positive vibrational entropy of chemical ordering in FeV, Physical Review Letters **107**, 115501 (2011).

[5] H. Schafer, *Chemical Transport Reactions*, Academic Press, New York, 1963

[6] N. Ashcroft and N. Mermin, *Solid State Physics*. Philadelphia: Saunders College, 1976.

[7] B. D. Cullity and J. W. Weymouth, *Elements of X-ray Diffraction*, American Journal of Physics **25**, 394 (1957).

[8] K. Seema, and Ranjan Kumar, Effect of disorder on electronic and magnetic properties of Co_2VGa Heusler alloy, AIP Conference Proceedings **1675** (1), 030036 (2015).

[9] V. Pecharsky and P. Zavalij, *Fundamentals of Powder Diffraction and Structural Characterization of Materials* (2nd Version) (2009).

[10] Crystallography Open Database (COD), http://www.crystallography.net.

[11] B. Josephson, Possible new effects in superconductive tunnelling, Physics Letters **1**(7), 251 (1962).

[12] G. Husnain and M. Madhuku, *In Ion Implantation-Research and Application* (IntechOpen, 2017).

[13] J. M. D. Coey, *Magnetism and Magnetic Materials* (Cambridge University press, 2010).

[14] P. Gutlich, Lecturer notes on Mössbauer spectroscopy : Principle and applications, Institut fur Anorganische Chemie und Analytische Chemie, Johannes Gutenberg-Universitat Mainz.

[15] International Board on the Applications of the Mössbauer Effect and Mössbauer Effect Data Center, Mössbauer Effect website, Accessed June 3, 2010.

[16] Mössbauer Spectroscopy Group, Royal Society of Chemistry website, Introduction to Mössbauer Spectroscpy Part 2, Accessed June 3, 2010.

[17] P. Gütlich, J. M. Greneche, F. J. Berry; Mössbauer Spectroscopy: A Powerful Tool in Scientific Research Archived 2011-11-29 at the Wayback Machine, Accessed June 3, 2010.

[18] Yu. G. Naidyuk and I. K. Yanson, Point contact spectroscopy, Spinger Science & Business Media (2005).

[19] R. J. Soulen, J. M. Byers, M. S. Osofsky, B. Nadgomy, T. Ambrose, S. F. Cheng, P. R. Broussard, C. T. Tanaka, J. S. Moodera, A. Barry and J. M. D. Coey, Measuring the spin polarization of a metal with a superconducting point contact. Science **282** (5386), 85 (1998).

[20] A. F. Andreev, The thermal conductivity of the intermediate state in superconductors, Soviet Physcis, Jouranal of Experimental and Theoretical Physics **19**, 1228 (1964).

[21] P. Stamenov, Point contact Andreev reflection from semimetallic bismuth—The roles of the minority carriers and the large spin-orbit coupling, Journal of Applied Physics **111** (7), 07C519 (2012).

Chapter 3 Rare-earth-free non-collinear ferrimagnets $Mn_{4-x}Z_xN$ with compensation at room temperature

3.1 Introduction

Magnetic materials with a very low net magnetic moment are highly sought after for low energy loss communications and high-frequency spintronics [1]. Although antiferromagnetic (AFM) materials have no net moment, apart from some exceptions with special symmetry [2, 3], they usually lack net spin polarization and they are insulators. Ferrimagnetic (FiM) metals exhibit transport properties just like ferromagnets, while their magnetization can also fall to zero if the net moments of the two antiparallel sublattices compensate, leading to the current interest in developing new compensated ferrimagnets for spintronics [4, 5].

Ferrimagnets comprise two sublattices with different magnetic moments where AFM exchange may coexist with a net ferromagnetic (FM) spin alignment. The most common types of collinear ferrimagnetism are shown in Fig. 3.1a; well-studied examples are Fe_3O_4, $Y_3Fe_5O_{12}$, amorphous Gd-Co [6] and Mn_2Sb [7]. In these materials, the moments within each sub-lattice are aligned parallel while the two sublattices are coupled antiferromagnetically. A less common non-collinear ferrimagnetic (ncFIM) magnetic structure can manifest, where the coupling is between a non-collinear magnetic sublattice, and a ferromagnetic sublattice, as shown in Fig. 3.1b. Notably, ferrimagnetism is non-collinear in second type; examples are $Ni(NO_3)_2$ [8], $MnCr_2O_4$ [9] and $Ho_2Fe_{14}B$ [10] at low temperature. Unlike oxides, which are usually insulating, metallic ferrimagnets are often R-

T-based, where R is a heavy rare-earth and T is Fe or Co, or else they can be Mn-based. The latter category avoids the use of rare-earth metals and often exhibits a high Curie temperature[1] that is useful for real-life applications.

The metallic perovskite Mn_4N crystallizes in face-centred cubic (fcc) structure (space group $Pm\bar{3}m$) where N atoms occupying the body-centered interstitial site are coordinated by an octahedron six Mn atoms in the $3c$ face-center positions, as shown in Fig. 3.2a. The Mn in the $1a$ corner positions is not in direct contact with the nitrogen. The magnetic order has been investigated both experimentally and theoretically. Initially, a collinear ferrimagnetic structure was suggested with the easy axis along [111] [11, 12]. A large magnetic moment $m_{1a} = 3.8$ μ_B is present on $1a$ sites (the majority sublattice) and there is a much smaller moment $m_{3c} = 0.9$ μ_B on $3c$ sites (the minority sublattice) that was thought to be greatly reduced by p-d hybridization with the neighboring nitrogen [12]. However, neutron diffraction with polarization analysis later revealed that triangles of $3c$ atoms in (111) planes, where they form a Kagome lattice shown in Fig. 3.2b, add a transverse, triangular antiferromagnetic component to the $3c$ sublattice spin structure, where the spins in the (111) plane either lie along axes that meet at the centre of the triangle (Γ^{4g} mode) or else lie along the sides of the triangle (Γ^{5g} mode). Only a small anisotropy energy separates the two modes, and the modes may coexist at finite temperature [13]. Calculations by Uhl *et al.* [14] confirmed a non-collinear 'umbrella' structure with the net sublattice moments aligned antiparallel along the [111] axis, producing a net moment close to the value of 1.1 μ_B that is found experimentally [12]. The Γ^{4g} mode has a topological character that is thought to account for the large anomalous Hall effect in many $Mn_{4-x}Z_xN$ materials [15]. The assumption that Mn_4N is a collinear ferrimagnet is therefore unwarranted and may lead to misleading conclusions [16].

In the Weiss mean-field model, the temperature-dependent magnetization (*M-T*) curves

---

[1] We call the magnetic ordering temperature the Curie temperature for both ferromagnets and ferrimagnets and the Néel temperature for antiferromagnetsm. Sometimes in ferrimagnets it is called the ferrimagnetic Néel temperature.

for ferrimagnets can be categorized into three types depending on the moment and main molecular field coefficients within and between sublattices (n_{1a1a}, n_{1a3c} and n_{3c3c}) [17]; corresponding curves are shown in Figs. 4.1c-f. The M-T curve of binary Mn_4N [18, 19] is Q-type, without compensation, where the magnetization of the $1a$ sublattice is always larger than that of the $3c$ sublattice and n_{1a3c} is the main molecular field coefficient. An N-type M-T curve with compensation may be achieved by substituting Z for Mn on $1a$ sites in $Mn_{4-x}Z_xN$ (Z = Co, Ni, Cu, Zn, Ga, Ge, As, Rh, Pd, Ag, Cd, In, Sn, Sb, Pt, Au and Hg with x < 1) [20, 21] to achieve compensation, and this has been investigated experimentally [22-25]. Though most dopants are nonmagnetic, it is found that compensation is achieved at quite different values of x for different nonmagnetic elements [26]. Therefore, it is necessary to analyze the compensation efficiency, which describes by how much moments are reduced per atom, in order to clarify the governing physical mechanisms that allow us to productively design novel Mn_4N-based compensated ferrimagnets for room temperature applications.
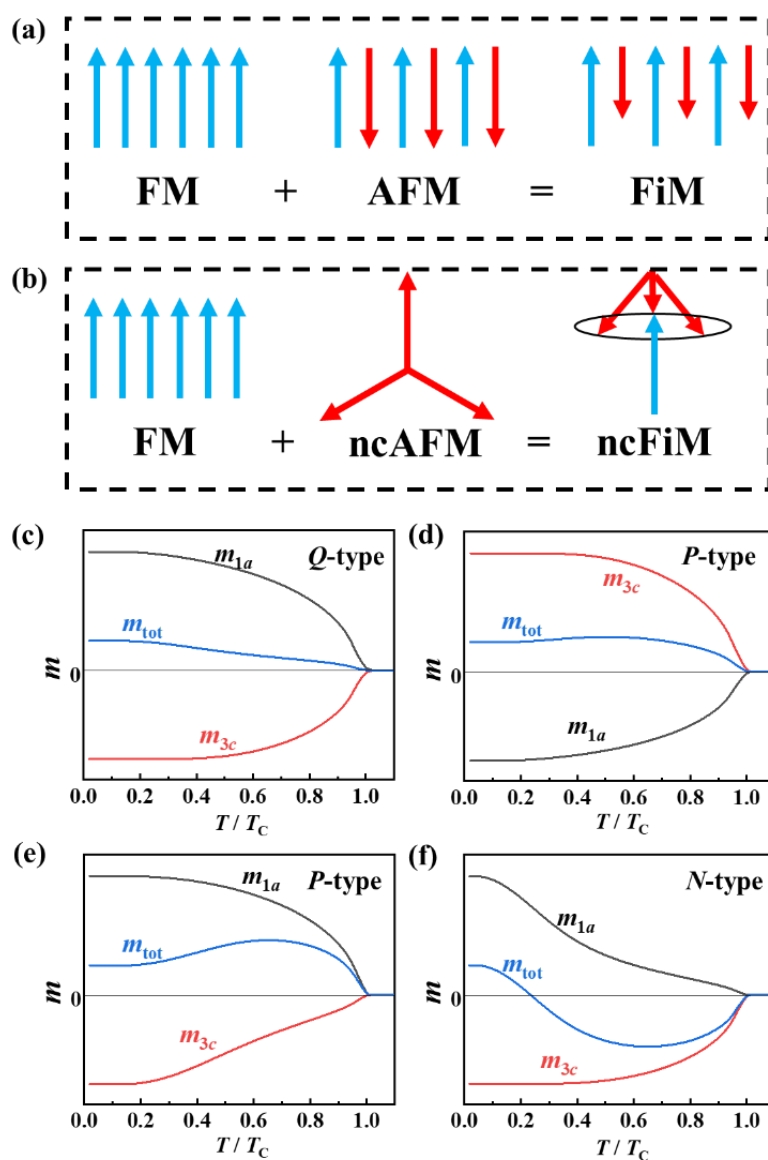
Fig. 3.1. **Ferrimagnetic prototypes.** (a) Collinear ferrimagnetic (FiM) spin structure is a combination of ferromagnetic (FM) and antiferromagnetic (AFM) spin structures. (b) Noncollinear ferrimagnetic (ncFiM) structure combines non-collinear antiferromagnetic (ncAFM) and FM structures. Three types of temperature-dependent magnetization curves are found for a ferrimagnet with two sublattices ($1a$ and $3c$ for Mn_4N) with (c) $m_{1a} > 3m_{3c}$ with n_{1a3c} as the main molecular field coefficient, (d) $m_{1a} < 3m_{3c}$ with n_{1a3c} as the main

molecular field coefficient, (e) $m_{1a} > 3m_{3c}$ with n_{1a1a} as the main molecular field coefficient or (f) $m_{1a} > 3m_{3c}$ and n_{3c3c} as the main molecular field coefficient. The difference is that (f) exhibits a compensation point but (e) does not. The collinear model is used here. In a noncollinear model, the chief difference in the shape of the curve is the non-zero slope at low temperatures (see Fig. 3.2c). In this study, we investigate the origin of the non-collinear ferrimagnetism of Mn_4N with extensive studies that show compensation at room temperature with various non-magnetic alloying elements, and we compare their magnetic compensation efficiency. We discuss the findings in relation to valence electron count, magnetic moment, tilt angle and lattice constant, based on the experimental data and constrained density functional theory calculations. Our measurements are all made on bulk materials.

3.2 Methods

The high purity ($> 99.99\%$) elements of Mn and $Z = Cu, Ga, Ge, In, Sn$ were arc-melted together five times to prepare homogeneous polycrystalline ingots. Extra Mn (2%) was added to compensate the loss due to its high vapor pressure. The ingots were then ground into powder and reacted with N_2 ($> 99.99\%$) at $750 - 800$ °C at a pressure of 50 kPa for 1 day. We found that if the N_2 pressure is too large (100 kPa) a Mn_2N impurity phase will form in some samples at small values of x. Nitrogen deficiency can lead to nitrogen vacancies or formation of γ- or β-Mn type impurities. Additional heat treatment (annealing at 660 °C in vacuum for one day was needed for Mn-Cu and Mn-Ge ingots before grinding them into powder to transform γ-Mn into β-Mn, owing to the ductile mechanical properties of γ-Mn which makes it very difficult to grind.

The composition of the polycrystalline sample was confirmed by energy-dispersive X-ray spectroscopy. The crystal structure was characterized by powder X-ray diffraction (XRD) that showed a single-phase cubic structure. Magnetization measurements were conducted using a 5 T superconducting quantum interference device magnetometer (SQUID, Quantum Design).

3.3 Results

3.3.1 Non-collinear ferrimagnetism in Mn$_4$N

The origin of non-collinear ferrimagnetism can be deduced from the interatomic distances and corresponding sign of the magnetic interactions in the crystal structure, identified by X-ray diffraction in Fig. 3.2a. The lattice parameter $a_0 = 3.865$ Å is also the nearest-neighbour distance between two Mn^{1a} atoms d_{1a1a}. The nearest distances between Mn^{3c} and Mn^{1a} or Mn^{3c} d_{1a3c} and d_{3c3c} are both equal to $a_0/\sqrt{2} = 2.733$ Å. Generally, Mn atoms separated by 2.5-2.8 Å have delocalized electrons and couple antiferromagnetically while Mn atoms with longer separations (> 2.9 Å) couple ferromagnetically [6]. Therefore, the Mn^{1a} moments lie parallel to each other, whereas the small d_{1a3c} distance favours antiparallel coupling between the sublattices. The separation of nearest-neighbour Mn^{3c} atoms d_{3c3c} is responsible for the non-collinear triangular antiferromagnetism of the $3c$ sublattice. Together, these interactions lead to the umbrella-like spin structure, and overall non-collinear ferrimagnetism.

Mn$_4$N has a high Curie temperature T_C (780 K) and a small saturation moment $m_{tot} = 1.1$ μ_B/f.u. along a [111] direction, as shown in Fig. 3.2c. The measured moment m_{tot} is the difference of the m_{1a} and three times the ferrimagnetic component of Mn^{3c} m_c^{FiM}, which are 3.8 μ_B and -0.9 μ_B per Mn, respectively [13] as shown in Fig 4.2a. It should be noted that the net moment in Fig. 3.2c remains a constant below 50 K and then drops with increasing temperature. By 160 K ($T/T_C = 0.2$), the moment has fallen by 13% of the 4 K value, in agreement with literature [18]. This is quite unusual, because according to the collinear mean-field model, the decrease at $T/T_C = 0.2$ should be smaller than 1% (see Fig. 3.1c-e). The inability to fit a P-type curve to a collinear mean-field model for Mn$_4$N [19] is a strong indication of the non-collinear nature of the magnetic order.
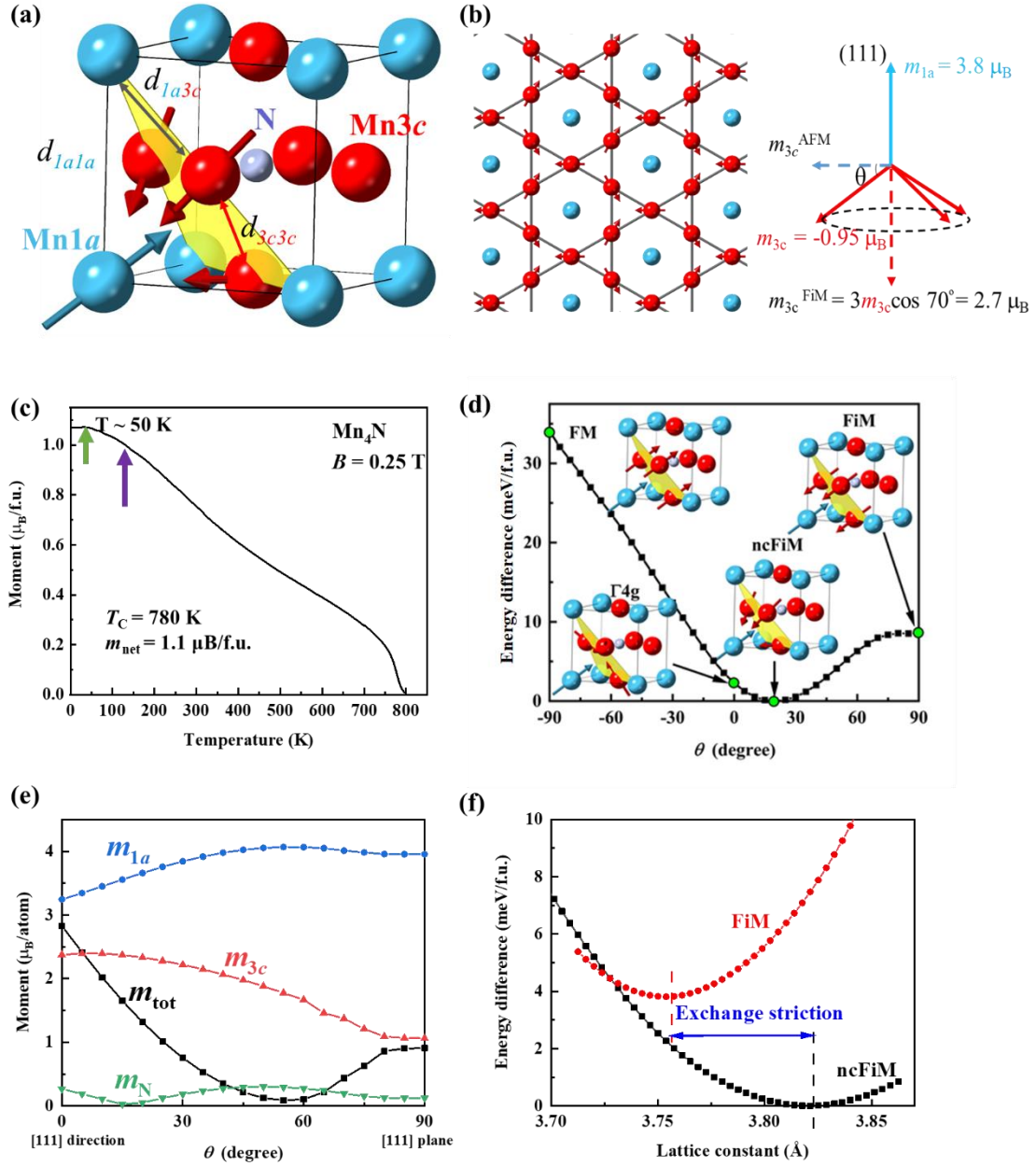
Fig. 3.2. **Non-collinear magnetic structure of Mn₄N.** (a) Crystal and magnetic structure showing the Γ^{4g} triangular ferrimagnetism. Grey, blue and red atoms represent N, Mn^{1a} and Mn^{3c}, respectively. The distances between 1a to 1a, 3c to 3c and 1a to 3c are labelled as d_{1a1a}, d_{3c3c} and d_{1a3c}. (b) Kagome lattice of Mn^{3c} projected into a (111) plane showing Γ^{4g}-like

magnetic structure. It is noted that its moments pointing to each other in 120° leads to zero moments. The out-of-plane magnetic component is ~ 2.7 μ_B, resulting in a net moment of 1.1 μ_B. That is consistent with the values at 4 K in (c) the thermal magnetization scan M(T) for Mn$_4$N. The magnetic moments per formula remain constant up to 50 K (green arrow) but drop significantly above. At 160 K (purple arrow) the moment has already fallen to 87% of the base temperature value. The following figures (d)-(e) show the details of calculations for Mn$_4$N carried out by Dr. Zsolt Gercsi. (d) Energy difference in the calculated magnetic structure as a function of tilt angle θ between m_{3c} and (111) plane. (e) Magnetic moments with varied tilt angle θ. (f) Comparison of calculated total energies as a function of lattice constant for the collinear and non-collinear ferrimagnetic structures.

The non-collinear spin structure was analysed further using a constrained DFT approach. Although our results suggest that the Mn^{3c} sublattice moments make an angle close to 70° with the Mn^{1a} moments, very far from the simplified picture of collinear ferrimagnetism often assumed, the DFT calculations show a screen of its stable atom arrangements and the moments dependency on the title angle (Fig. 3d-e). The details of the theoretic calculation are shown in Appendix II.

3.3.2 Doping for compensation

In order to achieve compensation, namely to change the temperature-dependent magnetization from Q-type to N-type, the main exchange should change from n_{1a3c} to n_{3c3c}, while the $1a$ site moment m_{1a} should be larger than three times the net $3c$ site moment $3m_{3c}^{FiM}$. This means that Mn on the $1a$ site should be substituted at the appropriate level x in Mn$_{4-x}$Z$_x$N (Z = Fe, Co, Ni, Cu, Zn, Ga, Ge, As, Rh, Pd, Ag, Cd, In, Sn, Sb, Pt, Au and Hg with x < 1). The candidates of dopants can be magnetic or nonmagnetic, which are located in a region defined by red lines in the periodic table in Fig. 3.3. In our work, we selected Cu, Ga, Ge, In and Sn as nonmagnetic elements, to dope into Mn$_4$N in order to understand the key factors influencing the exchange interactions of N_{1a3c} and N_{3c3c}.
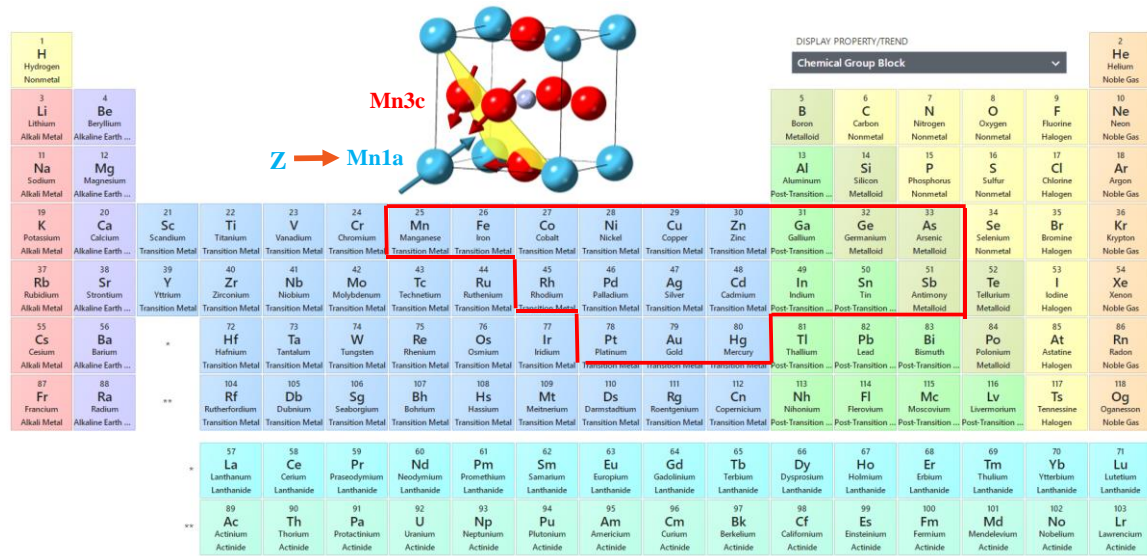
Fig. 3.3. **Periodic table.** The region defined by red lines includes the potential dopants for Mn_4N to realize magnetic compensation. The dopant can be magnetic or nonmagnetic.

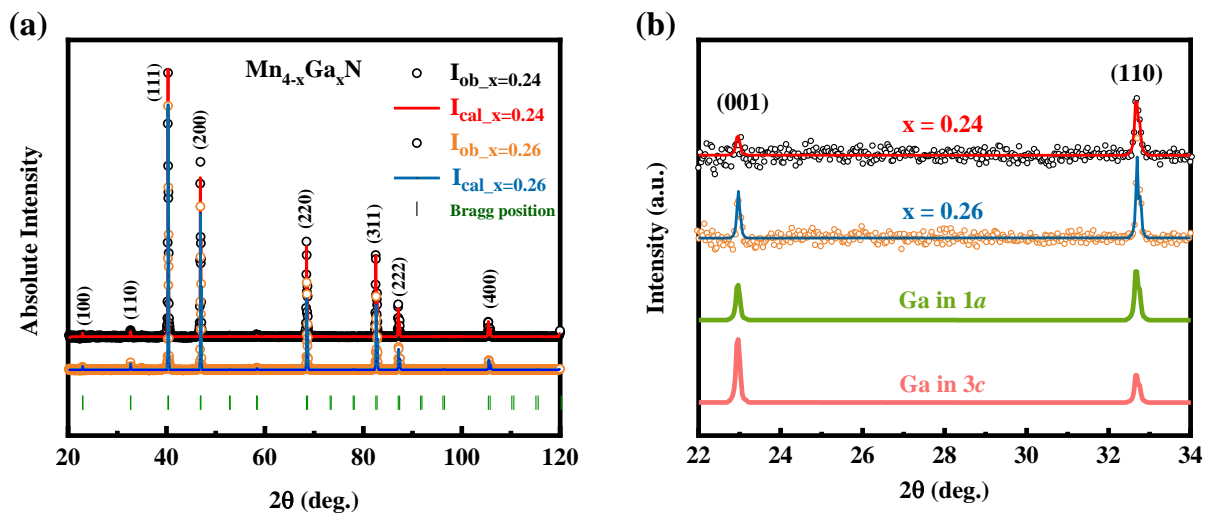Fig. 3.4. (a) X-ray diffractions of $Mn_{4-x}Ga_xN$ (x = 0.24, 0.26) with refinements by Rietveld method. The superlattice peaks (001) and (110), located in the low angle region (25°~ 32 °), of both compounds are all visible. (b) Comparing the ratio of (100) and (110) intensities (see

the simulated patterns (green from $1a$ sites and pink from $3c$ sites) in the bottom), the experiments indicate that Ga prefers to occupy 1a sites.

We start with Ga dopants. Fig. 3.4a shows the x-ray diffraction (XRD) patterns of $Mn_{4-x}Ga_xN$ (x = 0.24, 0.26). Their lattice constants are 3.873 Å and 3.870 Å for x = 0.24 and 0.26, respectively. The atomic radius of Ga (1.30 Å) becoming close to that of Mn (1.40 Å) leads to a little bit of contraction. The low-angle data are expanded in Fig. 3.4b. The larger intensity of the (110) superlattice peak indicates that $Mn_{4-x}Ga_xN$ crystallizes in a well-ordered structure with Ga atoms occupying the $1a$ site. According to the hysteresis loops of $Mn_{3.76}Ga_{0.24}N$ (Fig. 3.5a), the temperature dependence from 4 K to 350 K of magnetic moments at 5 T is summarized in Fig. 3.5b. We also include the data of $Mn_{3.74}Ga_{0.26}N$ in Fig. 3.5b. The value of the net moments for x = 0.24 decreases from 0.2 μ_B/f.u. at 4 K to 0.027 μ_B/f.u. at 350 K. That for x = 0.26 firstly falls from 0.14 μ_B/f.u. at 4 K to 0.034 μ_B/f.u. at 300 K and then increases to 0.053 μ_B/f.u. at 350 K. These are in agreement with thermal scans, as shown in Fig. 3.5c. Nonmagnetic Ga weakens the magnetic exchange leading to a decreased T_C = 610 K for x = 0.24. The net moment of 0.17 μ_B/f.u. at 4 K under 0.25 T indicates that each Ga decreases the moment by of ~3.8 μ_B, matching with the moment of m_{1a} from neutron diffraction [13] as well as our calculation. The compensation temperature is then T_{comp} = 408 K. Compared to x = 0.24, the composition x = 0.26 also presents a magnetic compensation at 291 K. Slightly higher Ga doping moves the compensation to lower temperature. Thus, in this case, the $1a$ sublattice dominates the magnetization at low temperatures, while the $3c$ sublattice is dominant above compensation. The *M-H* curves shown in Fig. 3.5a exhibit lower hysteresis indicating weak cubic magnetocrystalline anisotropy. Note the magnetization at 4 K is not saturated even in 5 T, further supporting the non-collinear ferrimagnetic structure where the tilt angle θ changes with magnetic fields.
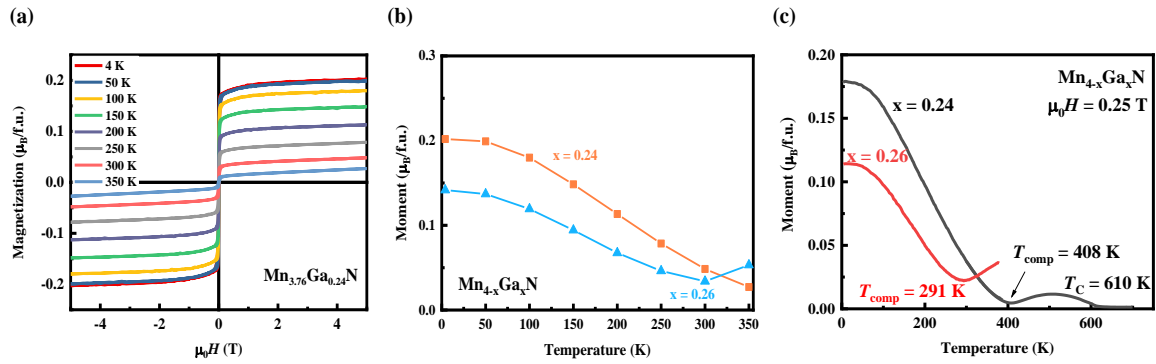
Fig. 3.5. (a) Isothermal magnetization curves for $Mn_{3.76}Ga_{0.24}N$ from 4 K to 350 K. The remanence M_r decreases from 0.07 to 0.007 μ_B/f.u. with temperature increasing from 4 to 350 K. (b) The saturation magnetization as a function of temperature in different Ga dopants (x = 0.24, 0.26). (c) Thermomagnetic scans M(T) for $Mn_{4-x}Ga_xN$ (x = 0.24 and 0.26) with applied field of 0.25 T. It is noted that the M(T) curves in this chapter are running in FC mode unless specially stated.

The compensation efficiency of different elements from Cu to Sn surrounding Ga in the periodic table is introduced in the following. Unlike Ga, that changes the net moment at the rate of ~3.8 μ_B/atom, the rates for the other elements influence are significantly different.

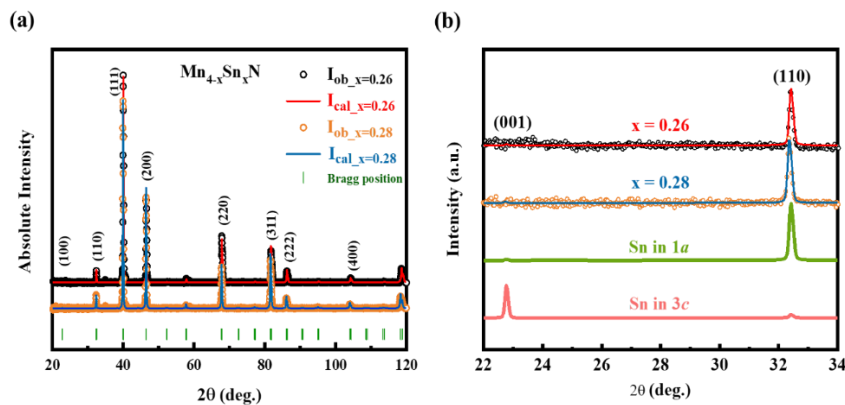Fig. 3.6. (a) X-ray diffraction patterns of $Mn_{4-x}Sn_xN$ (x = 0.26, 0.28) with Rietveld refinements. (b) The superlattice peaks are located in the low angle region. The higher (110) intensity indicates that Sn sits at the 1a site.

The X-ray diffraction pattern of $Mn_{4-x}Sn_xN$ confirms that Sn-doped samples form a well-ordered single phase (Fig. 3.6a). The lattice constants for x = 0.26 and 0.28 are 3.904 Å and 3.910 Å, respectively. Compared to the simulated diffraction patterns, the larger intensity of (110) denotes Sn also tend to occupy 1a site (Fig. 3.6b). The isothermal magnetization curves from 4 to 300 K are shown in Fig. 3.7a. The magnetic moments at 5 T for x = 0.26 and 0.28 as a function of temperature were summarised in Fig. 3.7b. For Sn with x = 0.26, the magnetization is reduced to 0.26 μ_B/f.u., but is much more than 0.12 μ_B/f.u. for Ga with the same x. It is noted that the magnetization curve at low temperature (4 and 50 K) shows a larger hysteresis (Fig. 3.7c), attributed to the Γ^{5g} antiferromagnetic configuration that co-exists all the way down from the Néel temperature of Mn_3SnN [27]. When the temperature rises beyond 100 K, the curve shape is similar as that at 300 K as shown in Fig. 3.7a.

The same magnetic behaviour at low temperature is also observed in the In-doped sample (x = 0.26) (Fig. 3.8a). The thermal scan for $Mn_{3.74}In_{0.26}N$ suggests the compensation is around 100 K (Fig. 3.8b), which agrees with the previous study [26]. There is a difference in the M-T curves measured after field-cooling (FC) and zero-field-cooling (ZFC) for $Mn_{3.74}Sn_{0.26}N$ shown in Fig. 3.7d. The compensation temperature is around 400 K for Sn substitution with x = 0.26. The magnetization is less sensitive to x for Sn than for Ga, while that is more significant to x for In than for Ga.
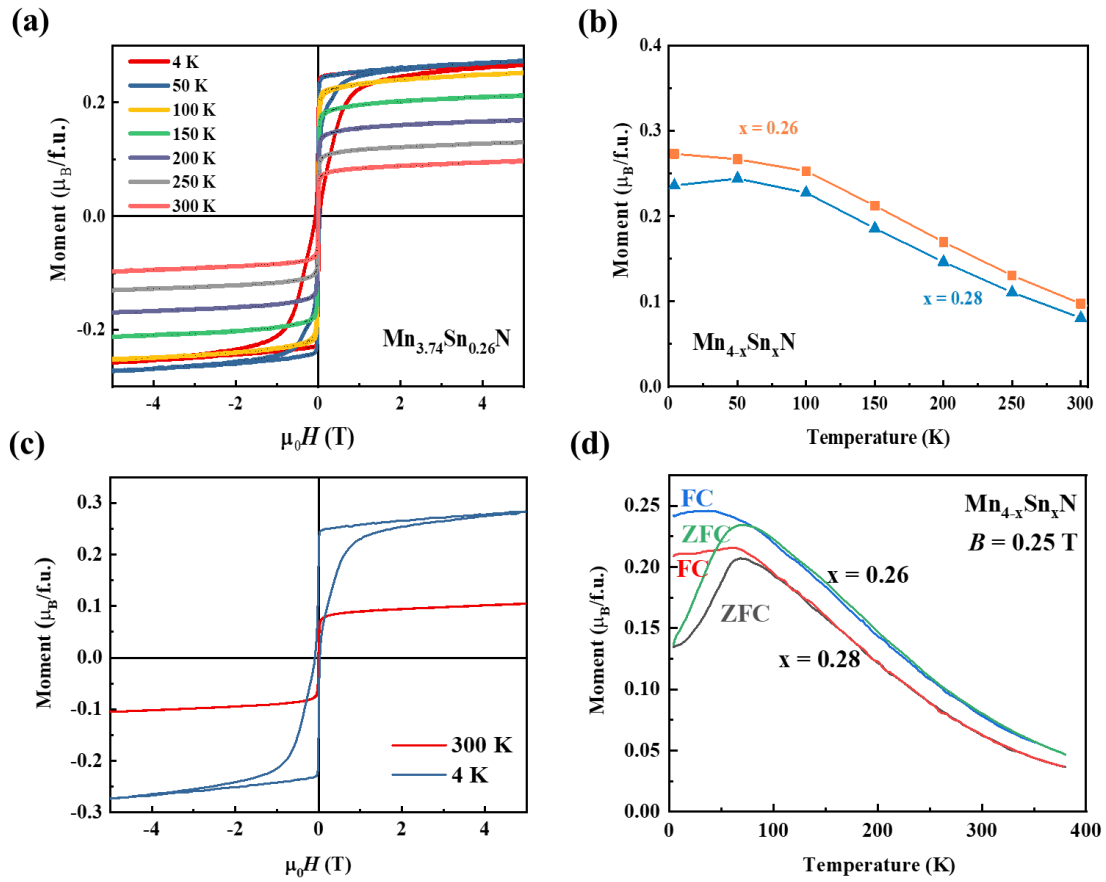
Fig. 3.7. (a) Isothermal magnetization curves for $Mn_{3.74}Sn_{0.26}N$ from 4 K to 300 K. The remanence M_r decreases from 0.09 to 0.018 μ_B/f.u. with temperature increasing from 4 to 300 K. (b) The magnetic moment at 5 T as a function of temperature for different Sn dopants (x = 0.26, 0.28). (c) Magnetization curve for $Mn_{3.74}Sn_{0.26}N$ at 4 K and 300 K. (d) Zero-field-cooled (ZFC) and field-cooled (FC) thermomagnetic scans for $Mn_{4-x}Sn_xN$.

(a)

(b)

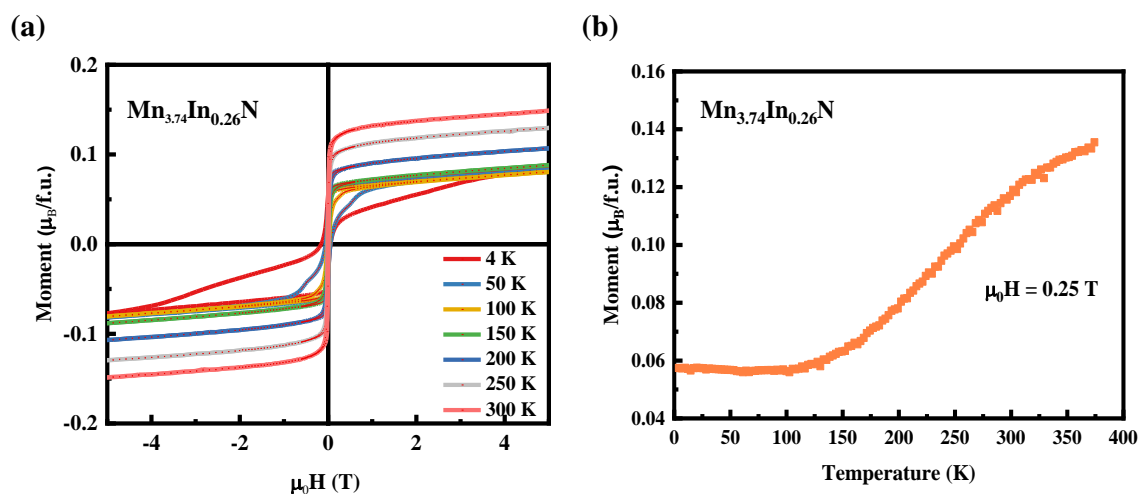
Fig. 3.8. (a) Isothermal magnetization curves for $Mn_{3.74}In_{0.26}N$ from 4 K to 300 K. (b) Thermomagnetic scans under 0.25 T applied field for $Mn_{3.74}In_{0.26}N$.

However, the trend towards low compensation efficiency is more significant for Ge than Sn. The magnetic moment of $Mn_{3.74}Ge_{0.26}N$ (0.49 μ_B/f.u) is higher than that of Sn-doped with the same x (0.26 μ_B/f.u.), as shown in Fig. 3.9b. The structures of $Mn_{4-x}Ge_xN$ (x = 0.26 and 0.35) as Fig. 3.9a illustrated suggest the expected phase form. The lattice parameters are 3.87(2) Å for x = 0.26 and 3.87(1) Å for x = 0.35, respectively. The unit cell is very stable. As in the magnetization curves, no compensation below 400 K was observed in thermal scans even in x = 0.35, although the magnetic moments at 4 K under 0.25 T changes from 0.49 μ_B/f.u. for x = 0.26 to 0.18 μ_B/f.u. for x = 0.35.
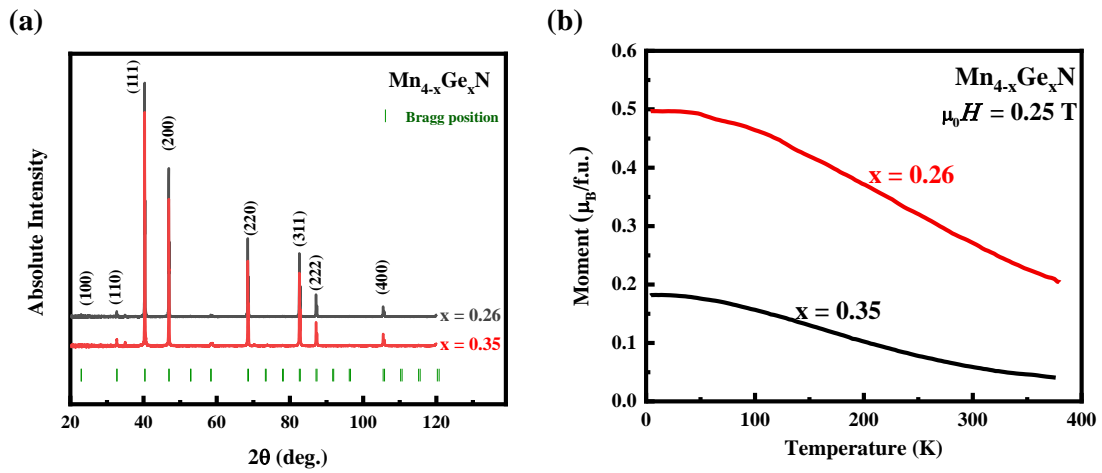
Fig. 3.9. (a) X-ray diffraction of $Mn_{4-x}Ge_xN$ (x = 0.26, 0.35). (b) Thermomagnetic scans under 0.25 T applied field for $Mn_{4-x}Ge_xN$ (x = 0.26, 0.35).

On the other hand, $Mn_{4-x}Cu_xN$ is very sensitive to compositional changes. Fig. 3.10 presents the x-ray diffraction (XRD) patterns of $Mn_{4-x}Cu_xN$ with x from 0 to 0.34. The lattice parameter changes from 3.879 Å for x = 0.26 to 3.885 Å for x = 0.34. The small concentration of Cu dopants is hardly able to expand the unit cell due to the close similarity of the atomic radii of Cu (1.35 Å) and Mn (1.40 Å). The Rietveld refinements for the low-angle data exhibited the higher superlattice peak intensity of (110) than that of (001), which indicates that $Mn_{4-x}Cu_xN$ crystallizes in a well-ordered structure with Cu atoms occupying the $1a$ site. The magnetic hysteresis loops of $Mn_{3.84}Cu_{0.16}N$ are shown in Fig. 3.11a. The rest compositions show almost identical M(H) curves. The isothermal saturated magnetization variations in different Cu are exhibited in Fig. 3.11b. The curve shapes are almost identical to their thermal magnetization scans (Fig. 3.11c), which gradually change from Q-type towards N-type and finally to P-type within a narrow range of x. The composition with N-type interactions presents compensation around x = 0.19.
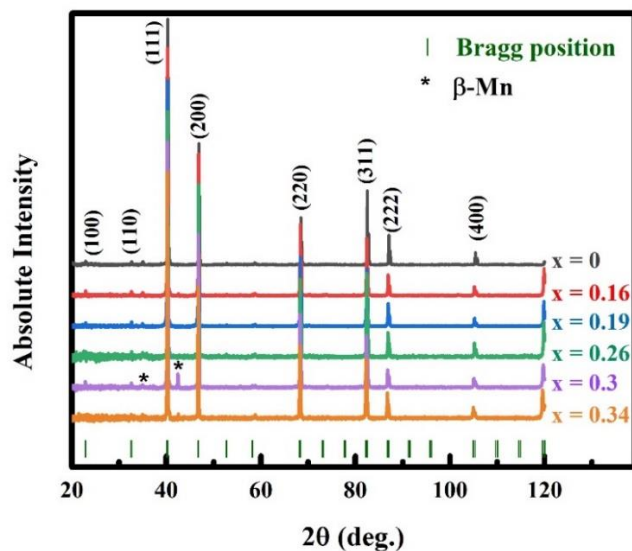
Fig. 3.10. X-ray diffraction patterns of $Mn_{4-x}Cu_xN$ (x = 0, 0.16, 0.19, 0.26, 0.3, 0.34).
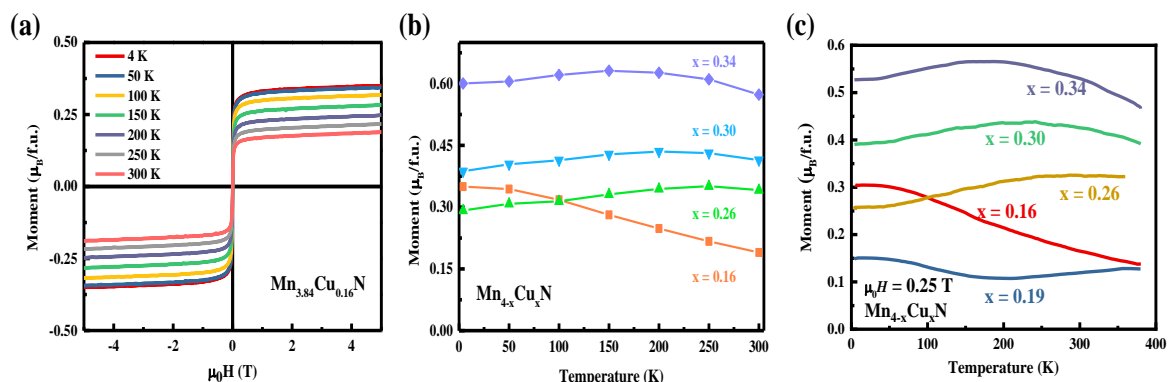
Fig. 3.11. (a) Isothermal magnetization curves for $Mn_{3.84}Cu_{0.16}N$ from 4 K to 300 K. (b) The saturation magnetization under 5 T as a function of temperature in different Cu dopants. (c) Thermomagnetic scans for $Mn_{4-x}Cu_xN$ (x = 0.16 to 0.34). Their thermo-magnetization curve shapes indicate that the compounds with x = 0.16 are *Q*-type and with x = 0.26, 0.30 and 0.34 are *P*-type. The compound with x = 0.19 shows a N-type curve without zero crossing due to the imperfect homogeneity.

The *M-T* curves for Cu, Ga, Ge, In and Sn with x = 0.26 are compared in Fig. 3.12. Copper has the highest compensation efficiency with a *P*-type *M-T* curve without compensation (T_{comp} < 0 K). In- and Ga-doped samples exhibit T_{comp} of 70 K and 298 K, respectively with *N*-type *M-T* curves. The difference between the magnetization at T_{comp} and zero is due to the inevitably imperfect homogeneity. While Sn-and Ge-doped ones leads to a complete disappearance of compensation (*Q*-type *M-T* curve). The Curie temperatures of Cu, Ga, Ge, In and Sn-doped are 653 K, 620 K, 632 K, 600 K and 547 K, respectively.
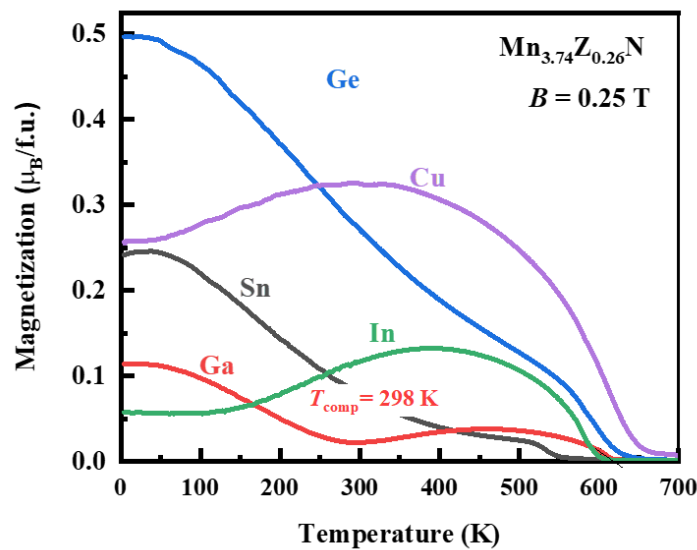
Fig. 3.12. Thermomagnetic scans for $Mn_{3.74}Z_{0.26}N$ (Z = Cu, Ga, Ge, In and Sn).

We plot data for different compositions of $Mn_{4-x}Z_xN$ at 4 K in Fig. 3.13a including both our own data and previous reports [26, 28-30]. The slope changes significantly from Ni (-6.20 μ_B/atom), Cu (-5.01 μ_B/atom), Zn (-4.35 μ_B/atom) [21], Ga (-3.70 μ_B/atom) to Ge (-2.52 μ_B/atom) with increasing valence electron for dopants in the fourth period. A similar trend is also found for dopants in the fifth period: Ag (-7.70 μ_B/atom) [31], In (-4.35 μ_B/atom) and Sn (-3.08 μ_B/atom). Based on this trend, the magnetic diagrams for different types of *M-T* curve are visualized in the maps of Figs. 4.13c and 4.13d. With lower concentrations of dopants, the interaction between 1*a* and 3*c* sites dominates and there is no compensation

below the Curie temperature leading to a *Q*-type *M-T* curve. With suitable *x*, the moment of the 1*a* sublattice is still larger than that of the 3*c* sublattice at low temperature, while at high temperature the 3*c* sublattice wins above compensation. Therefore, an *N*-type *M-T* curve is found. When heavily-doped, the 3*c* sublattice dominates throughout whole temperature range, and there is a *P*-type *M-T* curve with no compensation. Elements from the fifth period have a greater ability to compensate than those from the fourth period, and the magnetization is very sensitive to *x*. Therefore, the boundary for different *M-T* curves are shifted to the left (lower *x*) and the useful *N*-type region is narrower.
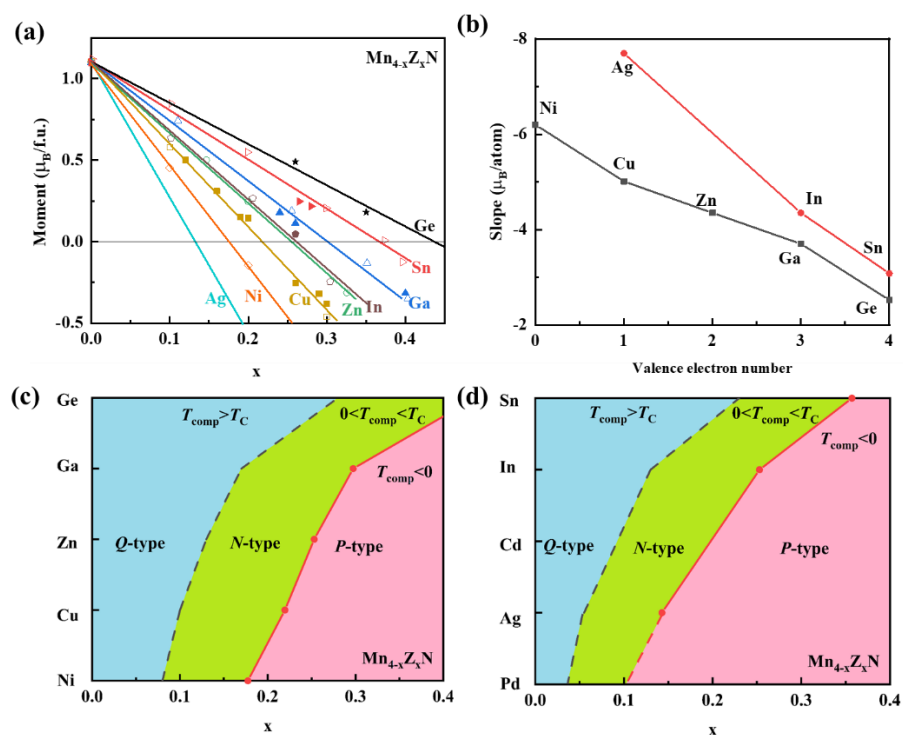

Fig. 3.13. (a) Summary of the net moment as a function of composition x in $Mn_{4-x}Z_xN$. We include our own data (solid points) and previous reports (open points). It is noted that the data shown here all obtained below ~ 4 K. (b) The slope in (a) shows different magnetic

efficiencies. Magnetic diagram for Q, N and P-type M-T curves, depending both on x and Z for elements from the fourth (c) and fifth (d) periods.

3.4 Discussions

The compensation efficiency of the dopants is analysed in view of the magnetic moment, non-collinear angle and lattice constant, using experimental and theoretical approaches.

3.4.1 Lattice constant

Compounds with the same x but different Z from the same group have the same valence electron number, and the main difference in their effects on the magnetic structure is related to the lattice parameter. Fig. 3.14a shows a_0 for $Mn_{4-x}Z_xN$ (Z = Cu, Ga, Ge, Ag, Sn and In). It is clear that Ag [31], In and Sn [26] lead to a greater increase in lattice parameter than Cu, Ga and Ge for the same x, because of their larger atomic radii. The increased lattice parameter translates to a larger atomic separation in the cubic crystal, leading to reduced p-d hybridisation of Mn^{3c} and increased Mn-Mn exchange that produce a relative increase of magnetism of the $3c$ sublattice. The Mn^{3c} moment is larger and more localized, leading to improved compensation efficiency for dopants from the 5th period.
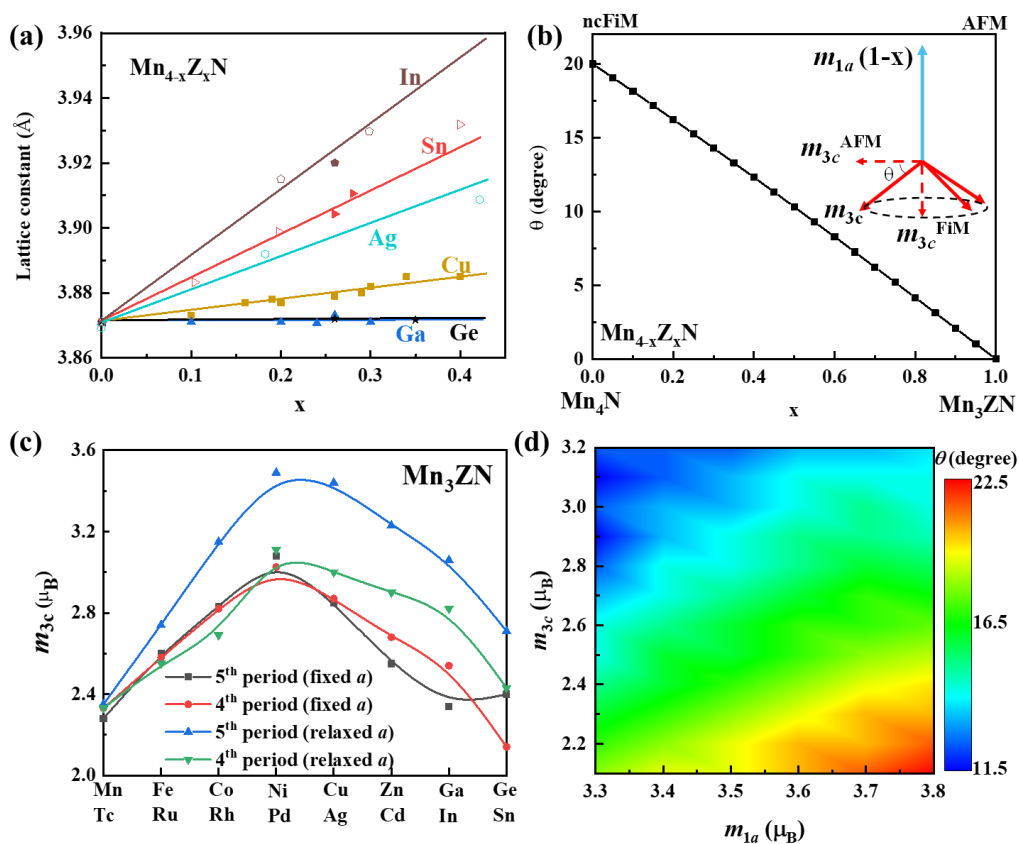
Fig. 3.14. (a) Lattice parameters for $Mn_{4-x}Z_xN$ (Z = Cu, Ga, Ge, Ag, Sn In), comparing our data (solid points) and previous reports (open points) [26, 31]. (b) Calculated tilt angle θ versus x from Eq. 3.6. (c) Calculated magnetic moment for Mn^{3c} in Mn_3ZN ($x = 1$). (d) Tilt angle θ for different m_{1a} and m_{3c} deduced from DFT. The bigger tilt angle indicates the spin directions of Mn^{3c} is more triangular. A value of $3m_{3c}$ similar to that of m_{1a} is favourable to obtain compensated magnetization, which is what we want.

3.4.2 Magnetic moment

Since the nearest-neighbour for Mn^{1a} is always Mn^{3c}, the magnetic coupling between Mn^{1a} atoms is weak. As a result, the moment for the remaining Mn^{1a} is not influenced significantly, as also indicated from neutron diffraction [32]. Therefore, the effect of doping on the net magnetization comes mainly from Mn^{3c}. We built our DFT model to capture

trends in the electronic and magnetic structures and used the simplest 5-atom unit cell model to model our experimental observation with different compositions. This model allows us to compare trends for $x = 1$, when the $3c$ site is fully occupied by Mn and the symmetry is cubic.

The calculated Mn^{3c} moment as a function of valence electron count in Mn_3ZN from Mn to Ge in the 4th period and from Tc to Sn in 5th period is plotted in Fig. 3.14c. The magnetic behaviour shows the same trend; an initial increase saturates around Ni and Pd, and drops monotonically afterwards. In order to separate the electronic effects from the impact of chemical pressure on the lattice parameter, we first fixed a_0 of all members of the series to that of Mn_4N (3.82 Å). This is shown by the solid red and black lines for the 4th and 5th periods in Fig. 3.14c. The peak at Ni, which has three electrons more than Mn, resembles a localized moment picture with striking similarities with the Slater-Pauling rule. These three extra electrons are shared by the three nearby Mn^{3c} atoms, and hence each of the Mn^{3c} atoms get one more electron becoming like iron, which shows the largest average moment in $3d$ alloys. The influence of the lattice constant on the moment expected on Mn^{3c} without constraint is also drawn in green and blue lines for comparison. The same trend is maintained, with peaks at Z = Ni and Pd. The main difference is found on the right-hand side of the curves, especially for elements from 5th period, as it relates to the expanded lattice parameters with additional valence electrons compared to the Z = Mn reference. The significant change in the amplitude of m_{3c} is one of the main reasons for the different compensation efficiencies. In addition, the orientation of m_{3c} also depends on its amplitude that further impacts the efficiency of compensation as we discuss it in the following section.

3.4.3 Tilt angle

Two questions concerning the tilt angle θ between $\boldsymbol{m}_{3c}$ and the (111) plane are: *How does θ change with x, and with different dopants?*

The $3c$ moment has two components, one component m_{3c}^{Fi} along the ferrimagnetic [111] axis and the other m_{3c}^{AFM} in triangular antiferromagnetic (111) plane. The molecular field

acting on $3c$ site also has two components, parallel and perpendicular to the [111] axis H^{Fi} and H^{AFM}, corresponding to the ferrimagnetism and in-plane antiferromagnetism. They satisfy the relationships

$$H^{\mathrm{AFM}} = -2\,n_{3c3c}\,m_{3c}\,\cos\theta\,\cos120° \tag{3.1}$$

$$H^{\mathrm{FiM}} = n_{1a3c}\,m_{1a}(1-x) - 2n_{3c3c}\,m_{3c}\,\sin\theta \tag{3.2}$$

$$m_{3c}^{\mathrm{Fi}} = m_{3c}\,\sin\theta \tag{3.3}$$

$$m_{3c}^{\mathrm{AFM}} = m_{3c}\,\cos\theta \tag{3.4}$$

$$\tan\theta = H^{\mathrm{FiM}} / H^{\mathrm{AFM}} \tag{3.5}$$

where n_{3c3c} and n_{1a3c} are the Weiss coefficients for interactions between $3c$-$3c$ Mn and $1a$-$3c$ Mn, as shown from the inset of Fig. 3.14b. In Eqs. 3.1 and 3.2, the in-plane antiferromagnetism considers the interaction from the other two nearest neighbor Mn^{3c} with 120° triangular spin structure; the negative sign of m_{3c} is already considered. Taking Eqs. 3.1 and 3.2 into Eq. 3.5, we get

$$\sin\theta = n_{1a3c}\,m_{1a}(1-x)/(3n_{3c3c}\,m_{3c}) \tag{3.6}$$

Previously θ was estimated from neutron diffraction to be about 70° (nearly collinear), with $m_{3c}^{\mathrm{Fi}} = 0.9\ \mu_{\mathrm{B}}$, $m_{3c}^{\mathrm{AFM}} = 0.36\ \mu_{\mathrm{B}}$, $m_{3c} = 0.97\ \mu_{\mathrm{B}}$, $m_{1a} = 3.8\ \mu_{\mathrm{B}}$ but with large error bars [13]. This means the compensation efficiency should be weaker than -(3.8+0.36) = -4.16 μ_{B}/atom, if we assume that the magnetic structure becomes collinear ferrimagnetic after doping. But from both our and previous experiments, dopants of Ni, Ag, Cu are much more effective, indicating that m_{3c}^{AFM} was underestimated. This is also found in our DFT calculations, where $\theta = 19.5°$ for binary $\mathrm{Mn_4N}$. Thus if we plot the relationship between x and θ in Eq. 3.6 (Fig. 3.14b), we find that θ decreases with x almost linearly. The umbrella-like triangular spin structure of Mn^{3c} rotates away from the [111] direction and becomes in-plane and therefore the net moment changes at a slower rate, as confirmed by comparative neutron study of $\mathrm{Mn_{3.2}Ga_{0.8}N}$ and $\mathrm{Mn_4N}$ [32]. Finally, when x = 1, Mn^{1a} is completely

replaced by the nonmagnetic dopant, Mn_3ZN is a triangular topological antiferromagnet in the (111) plane, if the crystal remains cubic.

When doped with different elements from Cu to Ge, or from Ag to Sn, the decrease of m_{3c} with increase of valance electrons leads to a rise of θ according to Eq. 3.6. This can weaken the effect of decreasing m_{3c}^{Fi} according to Eq. 3.3. Similarly, considering the increased lattice constant for dopants from the 5th period, the enhanced m_{3c} can also lead to a drop of θ, weakening the influence on m_{3c}^{Fi}. We further estimate θ by DFT calculation based on different m_{1a} and m_{3c} manganese site moments, as shown in Fig. 3.14d. We use the fixed spin moment (FSM) approach, where the amplitude of the magnetic moments on both sites is fixed. In Fig. 3.14d, we plot the angles for minimum total energy E_{tot} (m_{1a}, m_{3c}). The general trend is that the larger m_{3c} for a given m_{1a}, the smaller θ. The larger m_{3c} moment tends to stay in the (111) plane, and only the increasing moment on the $1a$ site could compensate for this rotation. This is in qualitative agreement with Eq. 3.6 and the vanishing moment on m_{1a} with increasing x, from experiment.

3.4.4 Best dopants for compensated ferrimagnetism

$Mn_{4-x}Z_xN$ thin films are already attracting attention for spintronics [33, 34]. Most studies have been done with Ni or Co [22-25], but they are not ideal for achieving compensation. Beside the demand for compensation, additional requirements must be considered when choosing the best dopants. Based on our analysis, Ga appears to be a suitable dopant in $Mn_{4-x}Z_xN$ films for spintronics for the following reasons: First, earlier elements from 4th period like Ni compensate the moment with small values of x. As the total moment is very sensitive to the composition, it is difficult to control the composition precisely and homogeneously. Second, for elements that have many additional valance electrons like Ge, a large value of x is needed due to the low compensation efficiency. As a result, the Curie temperature drops substantially, which is not beneficial for room temperature applications. Third, Ga does not significantly increase the lattice constant compared to elements from 5th period so that a series of thin films can be grown with

different compositions x and a similar tetragonal distortion is expected on the same substrate. The slight tetragonal distortion ($c/a \sim 0.99$) due to biaxial strain imposed at the interface of the film and substrate is the origin of perpendicular [001] anisotropy. A smaller lattice constant of the film than common substrates, such as $SrTiO_3$ with $a_{001} = 3.91$ Å, is the key for the in-plane tensile strain and perpendicular anisotropy [35, 36], which can be easily realized in Ga-doped samples. Finally, the compensation efficiency of Ga, -3.70 μ_B/atom coincides with m_{1a}. This is a consequence of a combination of an increased m_{3c} and a decreased θ rather than simply the nonmagnetic nature of the dopant.

3.5 Conclusion

From our experimental and theoretical study of the rare-earth-free non-collinear ferrimagnetic metals $Mn_{4-x}Z_xN$, we conclude that the non-collinear ferrimagnetism originates from the structure of the Mn^{3c} (111) Kagome planes with a small Mn-Mn interatomic separation that leads to frustration of the antiferromagnetic nearest-neighbour interactions. The tilt angle of the moments from the (111) planes, $\theta = 20°$, is smaller than previously thought from neutron experiments. There is a choice of substitutions to achieve magnetic compensation at room temperature. The efficiency of different elements in this respect decreases gradually with increasing valence electrons from group 11 (Cu, Ag) to group 14 (Ge, Sn). The Mn^{1a} moment is not sensitive to the dopants, while the Mn^{3c} moment peaks at Ni and Pd then drops with further valance electron addition. The higher efficiency of elements from 5th period is due to the larger lattice constant, which weakens the hybridization of Mn^{3c} and N and leads to an increase of m_{3c}. In addition, the tilt angle decreases with increasing m_{3c} and composition x. Based on the above results, Ga is the recommended dopant for $Mn_{4-x}Z_xN$ for thin film spintronics with perpendicular anisotropy.

3.6 Acknowledgement

Appendix

I.   Method of DFT calculations

Ab-initio calculations based on density functional theory were carried out using norm-conserving pseudopotentials and pseudo-atomic localized basis functions implemented in the OpenMX software package[2] [37]. Calculations were based on a minimal 5 atom basis cell of the cubic structure using $13 \times 13 \times 13$ k-points to evaluate the total energies. Pre-generated fully relativistic pseudo-potentials and the pseudo-atomic orbitals with a typical cut-off radius of 6 atomic units (a.u.) were used with $s^3 p^3 d^3$ for the metal and $s^3 p^3 d^2$ for the metalloid elements, respectively. An energy cut-off of 300 Ry was used for the numerical integrations. The convergence criterion for the energy minimization procedure was set to 10^{-8} Hartree. In the case of the non-collinear calculations, we show the results without spin-orbit interaction (SOI), whose influence on the total energy is negligible compared with the exchange interactions.

II.   DFT calculations of pure Mn$_4$N

In DFT approach, the directions of the individual spins are pinned to a selected angle but the magnitudes of the moments are allowed to vary freely in the total energy minimization process. The direction of Mn^{1a} is pinned to the body diagonal [111] and the tilt angle θ of the spins of the Mn^{3c} atoms is varied (also see inset of Fig. 3.14b). As the angle is rotated from the collinear ferrimagnetic configuration ($\theta = 90°$) into the (111) plane ($\theta = 0°$, Γ^{4g} spin structure) and then towards a ferromagnetic configuration at $\theta = -90°$ the energy and magnetic moments vary as shown in Fig. 3.2d and 3.2e One can visualize this

---

[2] All DFT calculations were carried out by Zsolt Gercsi on Mn$_s$XN compositions.

angle change like a closed umbrella (FiM) that opens out to close to 0° in regular usage and well beyond it on a windy day (FM, θ = -90°). The relative total energy change of the constrained angle approach is shown in Fig. 3.2d. Following the total energy minimum curve from the right to left, we witness a decrease in total energy E_{tot} with the Mn^{3c} moments canting away from the antiparallel spin arrangement into the (111) plane. The minimum of E_{tot} is found at around θ = 20°. The E_{tot} difference between the collinear ferrimagnetic and non-collinear ferrimagnetic ground state is significant, about 4.5 meV/atom. The calculations also confirm that the FM arrangement (θ = -90°) of the spins on Mn is very unfavourable with energy difference ~32 meV/atom. Our results therefore suggest that the Mn^{3c} sublattice moments make an angle close to 70° with the Mn^{1a} moments, very far from the simplified picture of collinear ferrimagnetism often assumed. For further analysis, Fig. 3.2e shows the calculated site-specific magnetic moments together with the total magnetic moment per formula unit in our range of interest (θ = 0 to 90°). A strong dependence of magnetization for both magnetic sites as a function of θ is revealed; the Mn^{1a} moment remains ~4 μ_B down to about θ = 45° and then a significant reduction to ~3.2 μ_B occurs on closing towards the (111) plane (θ = 0°). In contrast, the Mn^{3c} site moment increases from about 1.1 μ_B up to 2.4 μ_B when the angle closes from FiM towards the Γ^{4g}-like configuration. The E_{tot} minimum suggest magnetic values of m_{1a} = 3.65 μ_B, m_{3c} = 2.35 μ_B with m_{tot} = 1.24 μ_B/f.u. Indeed, the collinear ferrimagnetic spin configuration also yields a value of m_{tot} that is close to the experimental value, but we have relaxed both spin configuration for the equilibrium lattice parameters from DFT and find a value a_0 = 3.75 Å for the collinear ferrimagnetic state that is smaller than that for the non-collinear ferrimagnetic state a_0 = 3.82 Å, in Fig. 3.2f, which is closer to the experimental value of 3.865 Å at 300K. The earlier calculation by Uhl [14] found a greater tilt angle and a smaller $3c$ moment, fixing the lattice parameter and exploring a smaller range of θ. The energy difference can be ascribed to the electronic pressure caused by the altered magnetic spin configuration. This exchange interaction, like that in FeRh [38], explains the significantly expanded lattice constant for Mn_4N (3.86 Å) compared to its ferromagnetic analogs such as Fe_4N (3.79 Å), Co_4N (3.75

Å) and Ni_4N (3.72 Å) on the one hand and on the other hand it is also manifest throughout the rotation of the spins that alters exchange-split band energies by Coulomb repulsion. This non-Heisenberg like behaviour relates to the spin split d-bands crossing the Fermi level that influences the band filling and calculated magnetic moments.

References

[1] T. Jungwirth, X. Marti, P. Wadley, J. Wunderlich, Antiferromagnetic spintronics, Nature Nanotechnology **11**, 231 (2016).

[2] S. Nakatsuji, N. Kiyohara, T. Higo, Large anomalous Hall effect in a non-collinear antiferromagnet at room temperature. Nature **527**, 212 (2015).

[3] A. K. Nayak, J. E. Fischer, Y. Sun, B. Yan, J. Karel, A. C. Komarek, C. Shekhar, N. Kumar, W. Schnelle, J. Kübler, C. Felser, S. S. P. Parkin, Large anomalous Hall effect driven by a nonvanishing Berry curvature in the noncolinear antiferromagnet Mn_3Ge, Science Advances **2**, e1501870 (2016).

[4] S. K. Kim, G. S. D. Beach, K. J. Lee, T. Ono, T. Rasing, H. Yang, Ferrimagnetic spintronics, Nature Materials **21**, 24 (2022).

[5] H. A. Zhou, T. Xu, H. Bai, W. Jiang, Efficient Spintronics with Fully Compensated Ferrimagnets, Journal of the Physical Society of Japan **90**, 081006 (2021).

[6] J. M. D. Coey, *Magnetism and Magnetic Materials* (Cambridge Univ. Press, Cambridge, 2010).

[7] M. K. Wilkinson, N. S. Gingrich, C. G. Shull, The magnetic structure of Mn_2Sb, Journal of Physics and Chemistry of Solids **2**, 289 (1957).

[8] O. S. Volkova, V. V. Mazurenko, I. V. Solovyev, E. B. Deeva, I. V. Morozov, J.-Y. Lin, C. K. Wen, J. M. Chen, M. Abdel-Hafiez, A. N. Vasiliev, Noncollinear ferrimagnetic ground state in $Ni(NO_3)_2$, Physical Review B **90**, 134407 (2014).

[9] R. N. Bhowmik, R. Ranganathan, R. Nagarajan, Lattice expansion and noncollinear to collinear ferrimagnetic order in a $MnCr_2O_4$ nanoparticle, Physical Review B **73**, 144413 (2006).

[10] P. Wolfers, S. Miraglia, D. Fruchart, S. Hirosawa, M. Sagawa, J. Bartolome, J. Pannetier, Low temperature crystal and magnetic structures of $Ho_2Fe_{14}B$, Journal of the Less Common Metals **162**, 237 (1990).

[11] W. J. Takei, G. Shirane, B. C. Frazer, Magnetic Structure of Mn_4N, Physical Review **119**, 122 (1960).

[12] W. J. Takei, R. R. Heikes, G. Shirane, Magnetic Structure of Mn_4N-Type Compounds, Physical Review **125**, 1893 (1962).

[13] D. Fruchart, D. Givord, P. Convert, P. l'Heritier, J. P. Senateur, The non-collinear component in the magnetic structure of Mn_4N, Journal of Physics F: Metal Physics **9**, 2431 (1979).

[14] M. Uhl, S. F. Matar, P. Mohn, Ab initio analysis of magnetic properties in noncollinearly ordered Mn_4N, Physical Review B **55**, 2995 (1997).

[15] V. T. N. Huyen, M-T. Suzuki, K. Yamauchi, T. Oguchi, Topology analysis for anomalous Hall effect in the noncollinear antiferromagnetic states of Mn_3AN (A = Ni, Cu, Zn, Ga, Ge, Pd, In, Sn, Ir, Pt), Physical Review B **100**, 094426 (2019).

[16] T. Bayaraa, C. Xu, and L. Bellaiche, Magnetization Compensation Temperature and Frustration-Induced Topological Defects in Ferrimagnetic Antiperovskite Mn_4N, Physical Review Letters **127**, 217204 (2021).

[17] S. Chikazumi, *Physics of ferromagnetism,* (Oxford University Press, 1997).

[18] C. Li, Y. Yang, L. Lv, H. Huang, Z. Wang, S. Yang, Fabrication and magnetic characteristic of ferrimagnetic bulk Mn_4N, Journal of Alloys and Compounds **457**, 57 (2008).

[19] M. Mekata, J. Haruna, H. Takaki, Localized Magnetic Moments in Mn_4N, Journal of the Physical Society of Japan **21**, 2267 (1966).

[20] R. Niewa, Metal-Rich Ternary Perovskite Nitrides, European Journal of Inorganic Chemistry **2019**, 3647 (2019).

[21] J. C. Lin, P. Tong, W. Tong, Y. M. Zouc, C. Yang, F. Zhu, X. K. Zhang, L. F. Li, M. Wang, Y. Wu, S. Lin, W. H. Song, X. B. Zhu, Y. P. Sun, Large and constant coefficient of negative thermal expansion covering a wide temperature range in $Zn_{1-x}Mn_xNMn_3$ ($0 \leq x \leq 0.3$), Scripta Materialia1**52**, 6 (2018).

[22] S. Ghosh, T. Komori, A. Hallal, J. P. Garcia, T. Gushi, T. Hirose, H. Mitarai, H. Okuno, J. Vogel, M. Chshiev, J. Attané, L. Vila, T. Suemasu, S. Pizzini, Current-Driven Domain Wall Dynamics in Ferrimagnetic Nickel-Doped Mn4N Films: Very Large Domain Wall Velocities and Reversal of Motion Direction across the Magnetic Compensation Point, Nano Letters **21**, 2580 (2021).

[23] T. Komori, T. Gushi, A. Anzai, L. Vila, J. Attané, S. Pizzini, J. Vogel, S. Isogami, K. Toko, T. Suemasu, Magnetic and magneto-transport properties of Mn_4N thin films by Ni substitution and their possibility of magnetic compensation, Journal of Applied Physics **125**, 213902 (2019).

[24] K. Ito, Y. Yasutomi, S. Zhu, M. Nurmamat, M. Tahara, K. Toko, R. Akiyama, Y. Takeda, Y. Saitoh, T. Oguchi, A. Kimura, T. Suemasu, Manipulation of saturation magnetization and perpendicular magnetic anisotropy in epitaxial $Co_xMn_{4-x}N$ films with ferrimagnetic compensation, Physical Review B **101**, 104401 (2020).

[25] H. Mitarai, T. Komori, T. Hirose, K. Ito, S. Ghosh, S. Honda, K. Toko, L. Vila, J. Attané, K. Amemiya, T. Suemasu, Magnetic compensation at two different composition ratios in rare-earth-free $Mn_{4-x}Co_xN$ ferrimagnetic films, Physical Review Materials **4,** 094401 (2020).

[26] M. Mekata, Magnetic study on Mn_4N and its related compounds, Journal of the Physical Society of Japan **17,** 796 (1962).

[27] D. Boldrin, L.F. Cohen, The role of competing magnetic interactions on the abnormal expansion properties in manganese antiperovskites, $Mn_{3+x}A_{1-x}N$ (A = Ni, Sn), Journal of Alloys and Compounds **699**, 887 (2017).

[28] M. R. Fruchart, J. P. Bouchaud, M. E. Fruchart, M. G. Lorthioir, R. Madar, A. Rouault, Sur les transitions magnetiques du premier ordre dans les perowskites metalliques du manganese, Materials Research Bulletin **2**, 1009 (1967).

[29] W. J. Feng, D. Li, Q. Zhang, Y. F. Deng, S. Ma, Z. D. Zhang, Structure, magnetic and electrical transport properties of $Mn_{4-x}Ag_xN$ compounds, Materials Science (Poland) **27**, 33 (2009).

[30] R. Madar, Thesis, University of Paris, N° 686, Centre de Documentation du CNRS, Paris (1970).

[31] N. P. Lu, T. Xu, Z. X. Cao, A. L. Ji, Ternary $Mn_3NMn_{1-x}Ag_x$ compound films of nearly constant electrical resistivity and their magnetic transport behaviour, Journal of Physics D: Applied Physics **49,** 045308 (2016).

[32] D. Fruchart, Ph. L'Héritier, R. Fruchart, Transformations de phases dans les nitrures et carbures du manganese de structure-type perovskite, Materials Research Bulletin **15**, 415 (1980).

[33] T. Suemasu, L. Vila, J. P. Attané, Present Status of Rare-earth Free Ferrimagnet Mn_4N and Future Prospects of Mn_4N-based Compensated Ferrimagnets, Journal of the Physical Society of Japan **90**, 081010 (2021).

[34] Z. Zhang and W. Mi, Progress in ferrimagnetic Mn_4N films and its heterostructures for spintronics applications, Journal of Physics D: Applied Physics **55**, 013001 (2022).

[357] Y. Yasutomi, K. Ito, T. Sanai, K. Toko, and T. Suemasu, Perpendicular magnetic anisotropy of Mn_4N films on MgO(001) and $SrTiO_3$(001) substrates, Journal of Applied Physics **115**, 17A935 (2014).

[36] T. Hirose, T. Komori, T. Gushi, A. Anzai, K. Toko, and T. Suemasu, Strong correlation between uniaxial magnetic anisotropic constant and in-plane tensile strain in Mn_4N epitaxial films, AIP Advances **10**, 025117(2020).

[37] See http://www.openmx-square.org.

[38] U. Aschauer, R. Braddell, S. A. Brechbuh, P. M. Derlet, N. A. Spaldin, Strain-induced structural instability in FeRh, Physical Review B **94**, 014109 (2016).

Chapter 4   Fully compensated half-metallic Heusler alloys

4.1 Introduction

Half-metals take advantage of a band structure exhibiting metallic behaviour for one spin channel and a gap for the other one at Fermi level (E_f), to yield 100% spin polarized currents. This is very useful for thin film spintronic devices, such as spin valves, spin injectors, and spin transistors. It is noted that half metallicity is usually predicted by theoretical calculations [1-6] and confirmed by experiments. Traditional half-metallic materials are oxides (*e.g.* CrO_2 [7], EuO [8], $CaFeO_3$ [9]) or else, some diluted magnetic semiconductors [10], chalcogenides (*e.g.* CoS_2 [4]) and Heusler alloys [1] (*e.g.* NiMnSb [11], Co_2MnSi [12]). The latter is of particular interest due to its high Curie temperature well suited for applications at room temperature and tunable composition based on a formula X_2YZ, where X and Y are transition metals and Z is a main group element. The ideal half metal for thin film spintronics is a fully compensated ferrimagnetic half metal that produces no stray field.

The vast collection of Heuslers, more than 1000 alloys, and their tuneable magnetic moments often following Slater-Pauling rules lead to their use in many applications as half-metallic ferromagnets [13, 14], completely compensated ferrimagnets [15], nonmagnetic semiconductors [16], superconductors [17, 18] and recently as topological insulators [19, 20]. One large category of Heusler alloys is half-metal, which has a gap in one spin channel and the majority density of states in another one at the Fermi level (E_f). The conventional ferromagnetic Heusler half-metals are T-based, where T is Fe or Co, or else Mn-based, exhibiting high Curie temperatures. It is noted that a material combining the characteristics

of a ferrimagnet and a half-metal together is an ideal half metal, which is called a fully-compensated ferrimagnetic half-metal if it has a ferrimagnetic compensation temperature. This material has fully spin-polarized currents as well as a zero net magnetic moment. Traditionally, we can start with one parent half metal by doping electrons or holes to move the E_f up or down and achieve the ideal half metal. One good example is Mn_2Ru_xGa, where x ranges from 0.3 to 0.7 [21]. And the other potential 24-electron fully-compensated ferrimagnet is $Mn_{1.5}V_{0.5}FeAl$. Magnetic compensation could be realized by lowering the Fermi energy in Mn_2FeAl through partial replacement of Mn by V (Fig, 4.1). Another idea is to combine two half-metals with magnetic moments of opposite signs (one with $Z_t = 22$, Mn_2VAl; the other with $Z_t = 25$, Mn_2FeAl)) to obtain a fully compensated ferrimagnetic half-metal. Therefore, the ideal composition $Mn_2Fe_{0.67}V_{0.33}Al$ should generate zero moment in principle, which is in agreement with the DFT calculations by Dr. Z. Gercsi. Here we explore both approaches, but we found that when attempting to make a Mn_2FeAl Heusler alloy with the XA structure, it was nonmagnetic and crystallized in the β-Mn structure. This led us to investigate βMn, a spin liquid, with Fe, Al, and other substitutions.
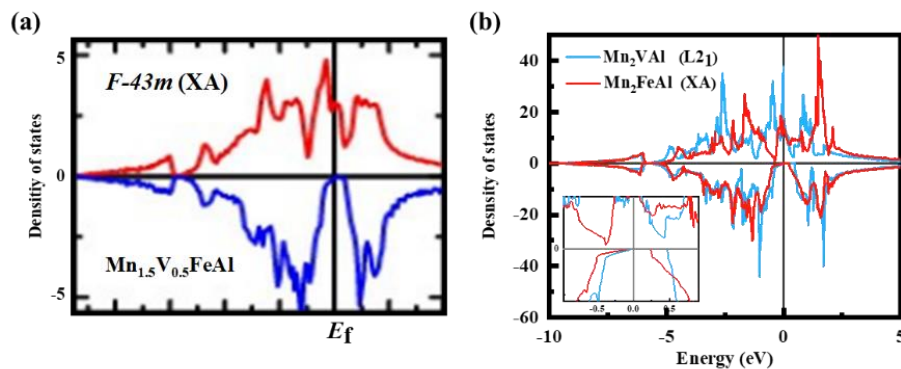
Fig. 4.1. The spin resolved density of states for (a) $Mn_{1.5}V_{0.5}FeAl$ with XA structure (space group: F$\bar{4}$3m) [22], (b) Mn_2FeAl with XA and Mn_2VAl with L2$_1$ (space group: Fm$\bar{3}$m)[3]. Partial replacements of Mn by V lead to lower Fermi energy level by introducing holes.

---

[3] The calculated spin resolved density of states for Mn_2FeAl with XA and Mn_2VAl with L2$_1$ were carried out by Dr. Z. Gercsi.

4.2 Fully compensated ferrimagnetic Mn$_{1.5}$V$_{0.5}$FeAl

4.2.1 Introduction

Half-metals have only one spin channel for conduction: the spin-polarized band structure exhibits metallic behaviour for one spin band, while the other exhibits a spin gap at the Fermi level. Because of the gap, the electronic states at the Fermi level are expected to be 100 % spin polarized at $T = 0$, but some spin mixing will result from spin-orbit coupling or thermal effects. Nevertheless, a highly spin-polarized current should be feasible in these compounds, which can maximize the efficiency of magnetoelectronic devices [23].

Cubic ferrimagnetic Heusler compounds are a family of materials [20], where crystallographically inequivalent magnetic sublattices with antiparallel alignment of their spins, may lead to a half-metallic compensated ferrimagnet with magnetic order but no net magnetization. The L2$_1$ alloys have an X$_2$YZ composition, with an ordered bcc structure, composed of four interpenetrating fcc lattices [24]. X and Y are transition metal atoms, and Z is an *s-p* element, which is important for stabilizing the structure. The magnetic properties of Heusler compounds [25-28] are rather sensitive to the distribution of atoms over the atomic sites.

The L2$_1$ Heusler compounds with X = Co or Mn occupy a unique position in the spectrum of half metals because of their high Curie temperatures. Their magnetic moments usually follow a Slater–Pauling curve where the moment in Bohr magnetons per formula unit obeys the $m = Z_t - 24$ rule, where Z_t is the total number of valence electrons. The 24 arises because there are 12 occupied majority-spin states per formula unit below a spin gap (four *sp* states from the Z element that lie well below the Fermi level and eight bonding or non-bonding *d* states from the hybridized X and Y *d* orbitals. There are then a further seven antibonding or nonbonding *d* states above the gap, accounting for the 15 spin up electrons of the three 3*d* atoms. The pattern is repeated for the minority-spin electrons, but the spin gap is at a higher energy due to the exchange splitting of the bands. Reducing the number of valence electrons to 24 per formula unit could therefore lead to a zero-moment compensated ferrimagnetic half metal when the spin gaps match, but other possibilities are a nonmagnetic

ground state — zero moment with no exchange splitting or magnetic order [29] — or a semiconducting state with the Fermi level lying in both spin gaps, or a change of structure from cubic to tetragonal $D0_{22}$.

Twenty years elapsed between the theoretical prediction of a compensated ferrimagnetic half-metal in 1995 [28] and the experimental discovery of the first such material, thin films of the 21-electron Heusler compound $Mn_2Ru_{0.5}Ga$ (MRG) by our group in 2014 [21]. MRG has since then been extensively investigated including studies of the anomalous Hall effect, XMCD, Kerr effect [30] and domain observations [31] especially around the compensation temperature T_{comp}. Single-pulse all-optical switching has been found [32]. One of the two manganese sublattices exhibits a spin gap, so the material combines the advantages of an antiferromagnet (no stray fields at compensation) with those of a ferromagnetic metal (highly spin polarized electrons at the Fermi level).

In 2017, Stinshoff $et\ al.$ [22, 33] reported another such ferromagnetic material, the first bulk 24- electron Heusler compound $Mn_{1.5}V_{0.5}FeAl$. The magnetization is always small, and T_{comp} and T_C were found to vary with heat treatments. XMCD showed small net moments on the Fe and V, and large oppositely-directed moments on two inequivalent Mn sublattices. Their calculations showed a gap in the DOS of one band for both $L2_1$ and XA structures (Fig. 4.2a and b). Al occupies $4a$ and Mn and V occupy $4b$ in both structures but in $L2_1$ Mn and Fe share the $8c$ site but in XA $4c$ is occupied by Mn and $4d$ by iron.
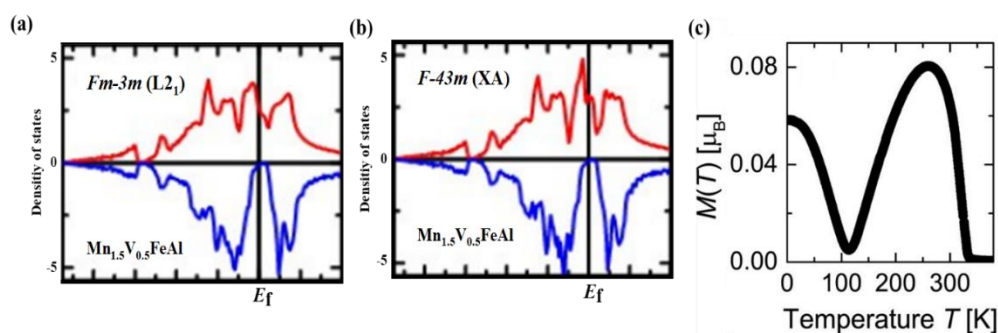

Fig. 4.2. The spin resolved density of states for $Mn_{1.5}V_{0.5}FeAl$ is shown for $Fm\overline{3}m$ in (a) and for $F\overline{4}3m$ in (b) [22]. (c) The temperature dependence of the magnetization $M(T)$ for $Mn_{1.544}Fe_{1.035}V_{0.369}Al_{1.051}$, which compensates at 120 K [33].

Here, we investigate a series of these as-cast bulk Mn-V-Fe-Al alloys with 0, 2 or 4% Mn excess, as well as annealed samples with no Mn excess to reveal the sensitivity of their compensation behaviour to Mn contents. We find that the compensation behaviour is very sensitive to lattice constants changes by different heat treatments. There are two types of behaviour, one with a larger lattice parameter is ferromagnetic, with a large moment and high Curie temperature, the other with ferrimagnetic compensation and a low moment.

4.2.2 Experiments

A series of polycrystalline $Mn_{1.5}V_{0.5}FeAl$ ingots with excess amounts of Mn (0, 2 and 4 %) were prepared by arc melting from a mixture of elements of very high purity Mn, V, Fe and Al in an argon atmosphere. Before melting the $Mn_{1.5}V_{0.5}FeAl$ ingots, special care was taken to clean the surface of Mn metal, and a shiny metallic alloy ingot was obtained by arc melting. To study the effect of heat treatment on magnetic properties, as-cast samples with no excess Mn were wrapped in Ta foil and sealed in evacuated quartz tubes before annealing at 900°C for a week followed by either slow cooling or quenching in an ice-water mixture.   The three sample types are therefore 'as-cast', 'annealed' and 'quenched'. Powder x-ray diffraction measurements were carried out on the compounds using Cu Kα_1 (λ = 1.5405 Å) radiation to identify the phase purity and the crystal structure. Magnetization measurements (both at 300 K and 4 K in a 5 T field) and the temperature dependence of magnetization from 4 K to 400 K in an applied field of 0.1 T were performed using a SQUID MPMS XL magnetometer. ^{57}Fe Mössbauer spectra [4] were collected in transmission geometry at room temperature. The constant acceleration mode spectrometer was equipped with ^{57}Co(Rh) source. The spectrometer was calibrated using α-Fe and the spectra were fitted by the least–squares method. Spin polarization was measured on three polished as-cast samples (bulk) using point contact Andreev reflection (PCAR) spectroscopy[5].

---

[4] The Mössbauer spectra measurements and fits were carried out by Prof. Plamen Stamenov.
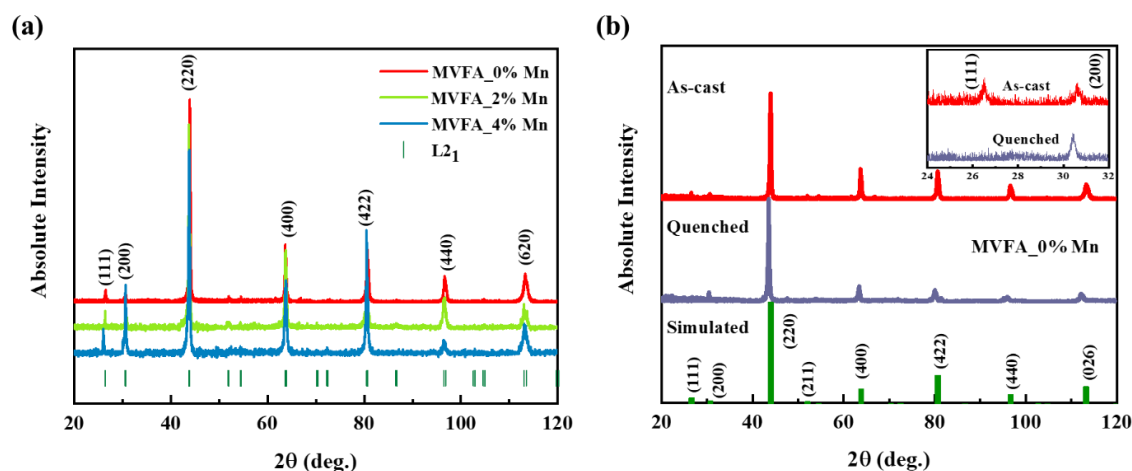[5] The PCAR measurements and fits were performed by Ajay Jha

Fig. 4.3. (a) X-ray diffraction patterns of as-cast $Mn_{1.5}V_{0.5}FeAl$ alloys prepared with an excess of 0%, 2% or 4% Mn. (b) The long-scan (48 hrs.) x-ray diffraction patterns for as-cast and quenched $Mn_{1.5}V_{0.5}FeAl$ (0% excess Mn), and the simulated x-ray pattern of the perfectly ordered $L2_1$ structure (using CrystalDiffract software) shown at the bottom. The inset shows the zoom-in patterns of the superlattice peaks. The higher intensity of (111) peak than that of (200) indicates that the as-cast alloy prefers to form $L2_1$ structure.

4.2.3 Results and discussion

The X-ray diffraction patterns of as-cast $Mn_{1.5}V_{0.5}FeAl$ alloys with an excess of 0, 2 or 4% Mn, presented in Fig. 4.3a. The observed superlattice peaks (111) and (200) for as-cast sample with extra 0% Mn (Fig. 4.3b) confirm that it tends to form the cubic $L2_1$ structure with space group $Fm\bar{3}m$. The lattice parameter is 5.84 Å in our as-cast samples, which is similar to that reported for annealed alloys of $L2_1$ Heusler. The lattice parameter for our annealed samples is greater (5.88 Å), and they exhibit different magnetic behavior. Stinshoff *et al.* [33] found, through electronic structure calculations, that Al and V are disordered and do not contribute to the magnetization; only Mn and Fe sublattices contribute to the net magnetization with the major contribution from Mn. Although all our as-cast samples show a single $L2_1$ cubic phase with similar peak positions (Fig. 4.3a), the relative intensities of the reflections are slightly different — absence of (200) and increase in intensity of (422) in the 0% Mn sample compared to the others. There can be a considerable atomic disorder in

Mn$_{1.5}$V$_{0.5}$FeAl due to the substitution of V at Mn sites. Any changes in stoichiometry and atomic order will greatly affect the structural stability and magnetic properties of the system. The XRD patterns of the quenched samples (Fig. 4.3b) show weak (200), (422), (420) peaks but no (111) superlattice peak, which suggest that our quenched samples are likely to be disordered (B2).
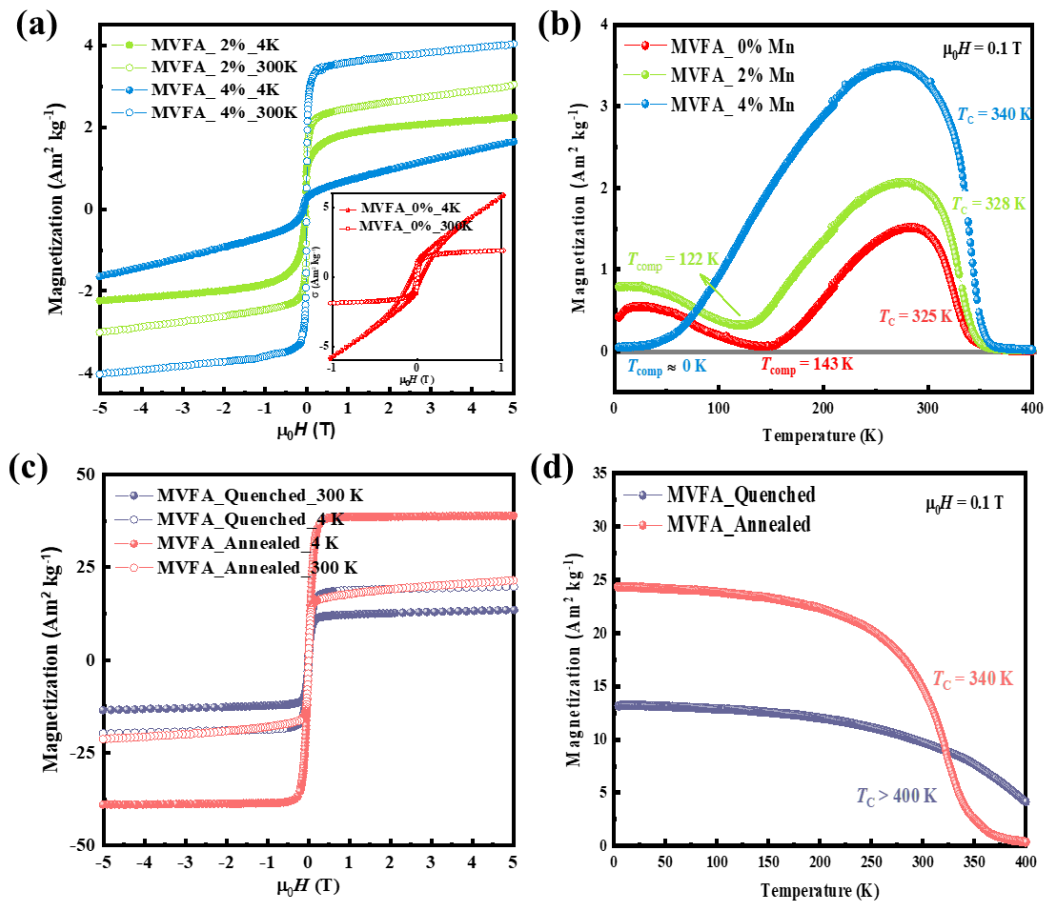
Fig. 4.4. (a) Magnetization curves of as-cast Mn$_{1.5}$V$_{0.5}$FeAl (MVFA) with different excess Mn at 300 K and 4 K. (b) Thermal scans on increasing temperature showing compensation and Curie temperatures. (c) Magnetization curves of quenched and annealed Mn$_{1.5}$V$_{0.5}$FeAl at 300 K and 4 K. (d) Thermal scans on increasing temperature showing $T_C > 400$ K for the quenched sample and $T_C = 340$ K for the annealed one.

Our main objective is to explore new zero-moment compensated ferrimagnetic half-metallic Heusler alloys. Magnetization curves at 300 K and 4 K for as-cast $Mn_{1.5}V_{0.5}FeAl$ with different Mn excesses are shown in Fig. 4.4a and the temperature dependence of magnetization in Fig. 4.4b. The magnetization varies as a function of Mn contents in $Mn_{1.5}V_{0.5}FeAl$ alloys both at 300 K and 4 K. The low saturation magnetization of 1.6 Am^2kg^{-1} (0.05 μ_B per formula), measured at 4 K in a field of 5 T on a small piece, is obtained for a sample with 4 % excess Mn. Magnetization is $\lesssim 0.1$ μ_B/f.u. at all temperatures, but there is a strong para process at 4 K in the 0 % sample. It seems that, unlike $Mn_2Ru_{0.5}Ga$ where there are well-defined moments of about 2 μ_B on both Mn sites, the present alloys lie very close to the threshold for the appearance of magnetism. Thermal scans on increasing temperature in Fig. 4.4b show both compensation and Curie temperatures. The Curie temperature (T_C) of all samples is found to be above 300 K. The value of T_C increases with increasing Mn content, from 325 K (0% Mn) to 340 K (4% Mn) for the as-cast samples. All three samples show compensation points at low temperature and there is systematic variation in the compensation temperature T_{comp} with Mn content. It decreases from 143 K for 0% Mn to 0 K for 4% Mn. The magnetic behavior suggests that there are two kinds of compensation [34] — the sample with 4% excess Mn is fully compensated in the ground state ($T_{comp} = 0$), while the samples with 0 and 2% Mn are overcompensated ($T_{comp} > 0$). The completely compensated state for 4% Mn excess can only be achieved owing to the different exchange and temperature dependencies experienced by the sublattices [15] and the compensation point is shifted to higher temperatures by reducing the Mn content.

Interestingly, our samples subjected to annealing heat treatments behave differently and do not exhibit compensation, as shown in Fig. 4.4d. The values of saturation magnetization are 39 Am^2kg^{-1} (1.3 μ_B per formula) for annealed alloy and 19 Am^2kg^{-1} (0.7 μ_B per formula) for quenched one at 4 K (Fig. 4.4c). They appear to be ferromagnetic with a higher T_C, 340 K for annealed and 450 K for quenched (Fig. 4.4d).
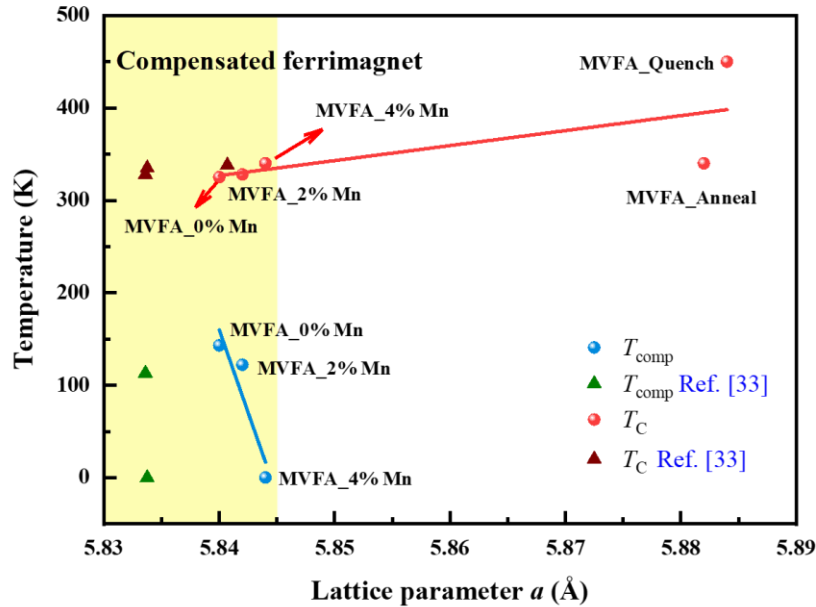
Fig. 4.5. Summary of T_{comp} and T_C as a function of lattice parameter for $Mn_{1.5}V_{0.5}FeAl$ (MVFA) with extra 0%, 2% and 4% Mn. When $a < 5.846$ Å, the alloy can show magnetic compensation temperature from 0 K to 150 K. The compensation behavior disappears when $a > 5.85$ Å and magnetization and T_C increase. Our data of T_{comp} and T_C are symbolized by blue and red balls, respectively. The data from the previous report [33] for T_{comp} and T_C are symbolized by green and maroon balls, respectively.

Combining our data with that in the previous report [33], the compensation and Curie temperatures of these Heusler alloys are sensitive to the unit cell volumes and they are raised by excess Mn contents and annealing heat treatments. The T_{comp} and T_C as a function of lattice parameters are illustrated in Fig. 4.5. The compensation behavior coming from the antiparallel spin alignments of two different Mn sublattices can be observed in the sample with lattice parameter $a < 5.845$ Å. But when $a > 5.85$ Å, compensation disappears, and T_C is higher. Here, excess Mn doping, or heat-treatment is a means to control the size of the unit cell. The results suggest that optimizing the lattice parameter to achieve a ferrimagnet with high compensation temperature is feasible.
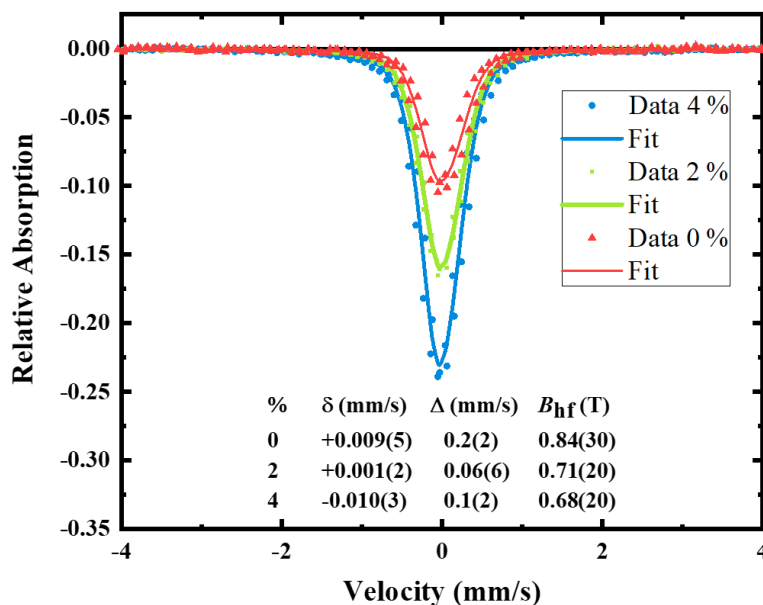
Fig. 4.6. Room-temperature ^{57}Fe Mössbauer spectra of the as-cast $Mn_{1.5}V_{0.5}FeAl$ powders. The average hyperfine field is ~ 0.7 T.

^{57}Fe Mössbauer spectrum of all three as-cast $Mn_{1.5}V_{0.5}FeAl$ samples is shown in Fig. 4.6. The spectra show a single broadened absorption line that is best fitted with a very small hyperfine field of 0.7 - 0.8 T at room temperature. The average hyperfine field is 0.7 T. Using the conversion factor of 15 T/μ_B for metallic iron, the 0.7 T hyperfine field corresponds to an atomic moment of only 0.05 μ_B. The hyperfine field decreases with increasing Mn excess. The magnitude is similar to that found in the weak itinerant ferromagnet Fe_2VGa [29]. From this we can conclude that there is practically no magnetic contribution from the iron sublattice to the total room-temperature magnetization, which is dominated by the contributions of the Mn sublattices.
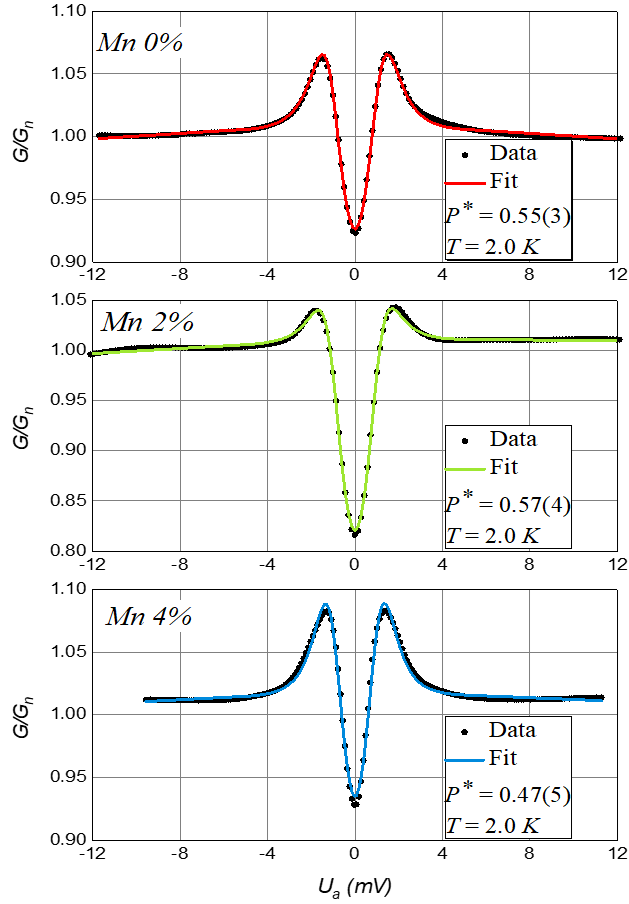
Fig. 4.7. Point contact Andreev reflection spectroscopy of polycrystalline as-cast $Mn_{1.5}V_{0.5}FeAl$ ingots at 2 K (measured by Ajay Jha).

The spin polarization of all three as-cast samples of $Mn_{1.5}V_{0.5}FeAl$ was measured using point contact Andreev reflection (PCAR) spectroscopy at 2.2 K [35, 36] with superconducting niobium point contacts. The data is fitted using modified BTK theory. The fitting model takes full account of a number of parameters such as series resistance, superconducting proximity effect, and electronic heating, as described previously [36]. The highest spin polarization of 57% at the Fermi level is obtained on sample with 2% excess Mn. The value of P is 55% for that has been measured by PCAR on any Heusler compound.

Diffusive spin polarization measurements on bulk Heusler alloys are never much in excess of 60% [35,37, 38] probably because the band dispersion is different at the surface and in the bulk, or because of spin-orbit scattering. That measurement on Co_2FeSi, for example, yielded 51% [37].

4.2.4 Conclusion

The compensated ferrimagnetic half-metallic $Mn_{1.5}V_{0.5}FeAl$ alloys show near-zero magnetization and exhibit a compensation temperature that is sensitive to manganese content and heat treatment. Magnetization is $\lesssim 0.1$ μ_B/fu at all temperatures. We find compensation at a temperature ranging from $0 - 140$ K that is tuneable by varying the manganese stoichiometry in as-cast samples. The balance of the ferrimagnetism is very sensitive to heat treatment and atomic order. Samples subjected to annealing or quenching treatments did not exhibit compensation, but only they exhibit a high enough T_C for practical room-temperature applications. Mössbauer spectroscopy reveals a surprisingly small contribution to the magnetization from the Fe sublattice. The 57 %, spin polarization measured by point contact Andreev reflection is one of the highest values reported in a bulk Mn-based Heusler compound.

4.3 Spontaneously compensation and half-metallicity in the Heusler ferrimagnet $Mn_2Fe_{1-x}V_xAl$

4.3.1 Introduction

The zero-moment half metals, which present high-frequency dynamics and ideal spin polarization, are highly sought after in THz spintronics. The ideal spin polarization is attributed to the distinctive characteristic of half metal, whose band gap contains the Fermi level in the insulating spin channel. The traditional method, doping electrons or holes into the parent half metal to balance the spins in two channels and maintain the half-metallicity. This is adopted to make Mn_2Ru_xGa. But, unfortunately, it is found that the half metal only

can be found when Ru concentration ranges from 0.3 to 0.7. This limited composition range reduces the half metals suitable for spintronics. Then we come up with another approach: using two-parent half metals with opposite magnetic signs to balance spins in two directions. In principle, it ensures the whole series will be half metallic.

The band gap of half metal can be of four types depending on the number of d electrons occupying the gapped channel (d^0-, d^2-, d^3-, and d^5-type). A d^0-type band gap is found in CrO_2 [39]. Two electrons occupy the t_{2g} band below E_f with spin-up after four electrons of Cr transferring to the two oxygen atoms (Fig. 4.8a). A d^2-type band gap presents in spin-down at the Mn^{4b} site (Co_2MnGa) [40, 41]. The crystal field splitting of Mn^{4b} with cubic coordination leads to an e_g level below a t_{2g} one [42]. Two electrons fill in the spin-down e_g band below the E_f and the other four electrons fill in the $3d$ band at E_f in spin-up (Fig. 4.8b). At Co site (CoS_2) [30], the splitting of the $3d$-orbitals in the octahedron coordination leads to a d^3-type band gap between e_g and t_{2g} bands in spin-down [42] (Fig. 4.8c). Fe^{2+} (Fe_3O_4 [43]) with a high-spin state presents a d^5-type gap. The e_g and t_{2g} bands in spin-down are all below the E_f and filled (Fig. 4.8d), while the rest electron occupies the $3d$-band crossing the E_f in spin-up. d^N-type band gaps ensure their half metallicity. Therefore, the half-metallic band structure in each $3d$ constituent of alloys or compounds is key to guaranteeing their half-metallicity. Therefore, combining half metals with different type gaps together ensures the half metallicity of the new alloys, either. For the compensated one, the more important thing is to distinguish the opposite magnetic signs of the fundamental half metals. It is easier to tell for the Heusler alloys by the Slater-Pauling rule. For example, when the number of the valence electrons is above 24, the magnetic moment is positive. Whereas the number is less than 24, it is negative. Then regulate and control the ratio of the fundamental half metals to make the new one with 24 electrons, producing zero moments.
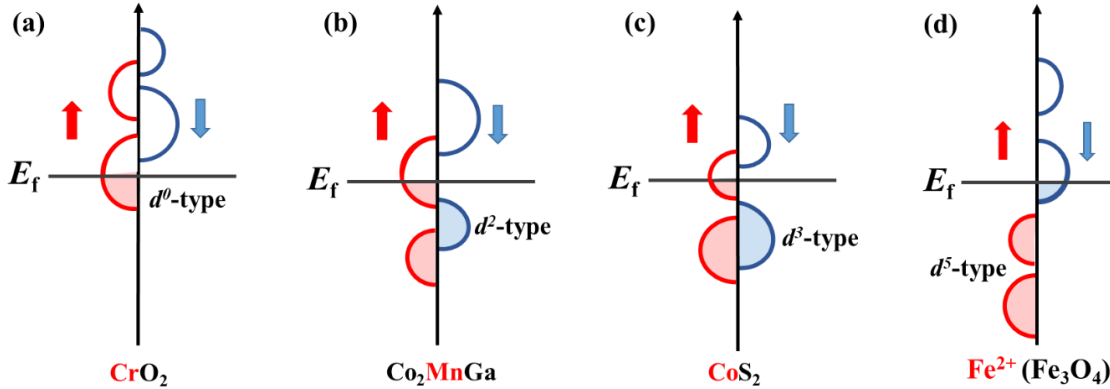
Fig. 4.8. (a) Schematic densities of states of Cr in CrO_2 [39]. The empty $3d$-band in spin-up direction leads to a d^0-type band gap at Cr site. (b) Mn^{4b} in Co_2MnGa in cubic coordination with crystal field split d-levels with the e_g band lower. Two $3d$ electrons fill in the spin-down e_g band forming a d^2-type band gap and four others occupy the spin-up $3d$ bands [40]. (c) In CoS_2 [30], the Co has a d^3-type band gap due to the spin splitting of the t_{2g}-orbitals in octahedral coordination. (d) In Fe_3O_4, Fe^{2+} is in a $3d^6$ high-spin state where five electrons occupy the $3d$-orbitals of the spin-up band, presenting a d^5-type band gap [43].

Here, we take $Mn_2Fe_{1-x}V_xAl$ Heusler alloy as the example to examine the new approach on establishing new fully compensated half metals: balancing two half metals with opposite magnetic moments. The new Heusler can be considered as a combination of two ferrimagnetic half metals (Mn_2FeAl with 25-electrons and Mn_2VAl with 22-electrons). A fully compensated ferrimagnetic half metal $Mn_2Fe_{0.75}V_{0.25}Al$ obtained experimentally in bulk form, has a composition close to the expected $Mn_2 Fe_{0.67}V_{0.33}Al$.

4.3.2 Band structures

Half metallic Mn_2VAl and Mn_2FeAl exhibit different spin configurations due to their different structural symmetry. Ordered Mn_2VAl and Mn_2FeAl crystalized in the $L2_1$ and XA structures, respectively (Fig. 4.19 in Appendix I). Here, covalent bonds form between Al and $3d$ elements. The covalent electrons in $3p$ orbitals are not spin-polarized and are non-magnetic. The nearest neighbours of Al^{4a} are on 4c and 4d sites and the next-nearest

neighbours are the 4b sites. Therefore, the covalent bonds tend to form between Al with $Mn^{4c/4d}$ in the $L2_1$ structure or with Mn^{4c} and Fe^{4d} in the XA structure, and the 4b sublattice does not share any electrons with Al. The bond length from 4c to 4d site is ~ 2.94 Å, indicating ferromagnetic exchange interaction between these two sites with Mn, while that from 4c/4d to 4b site is ~ 2.55 Å, leading to antiferromagnetic exchange. The antiparallel alignment of magnetic moments from 4c/4d and 4b sites result in ferrimagnetism in these alloys.

In Mn_2VAl with the $L2_1$ structure (Fig. 4.9a), the short distance between $Mn^{4c/4d}$ and V^{4b} (2.55 Å) leads to antiferromagnetic coupling, which is the main interaction. Note that $4c$ and $4d$ sites are equivalent in the $L2_1$ structure. They are the $8c$ sites occupied here by Mn. The large distances between Mn^{4c}-Mn^{4d} (~ 2.94 Å) and V^{4b}-V^{4b} (~ 4.15 Å) lead to ferromagnetic interactions within the Mn and V sublattices [42]. The schematic band structures of its $3d$ constituent are shown in Fig. 4.9a. Mn at 4c and 4d sites share five electrons with Al^{4a} and 4.5 electrons remain in the $3d$-orbitals of each Mn. The splitting of the $3d$-orbitals at $Mn^{4c/4d}$ in an octahedral coordination leads to a d^3-type band gap, shown in Fig. 4.9a. Each Mn with a $d^{1.5\uparrow 3\downarrow}$ configuration has a ~ 1.5 μ_B magnetic moments [44]. The crystal field splitting of V^{4b} site with cubic coordination leads to a d^2-type band gap (Fig. 4.9a). The spin configuration of V^{4b} is $d^{3\uparrow 2\downarrow}$, yielding a 1 μ_B magnetic moment [44]. Therefore, half metallicity of Mn_2VAl is guaranteed by its $3d$ constituent sublattices with d^N-type band gaps (d^3-type for Mn and d^2-type for V). The antiparallel alignment of Mn and V spin sublattices results in a total magnetic moment of -2 μ_B in Mn_2VAl, which agrees with the Slater-Pauling rule $m = Z_t$-24 ($Z_t = 22$, total valence electrons) [45] and the experiments [46].
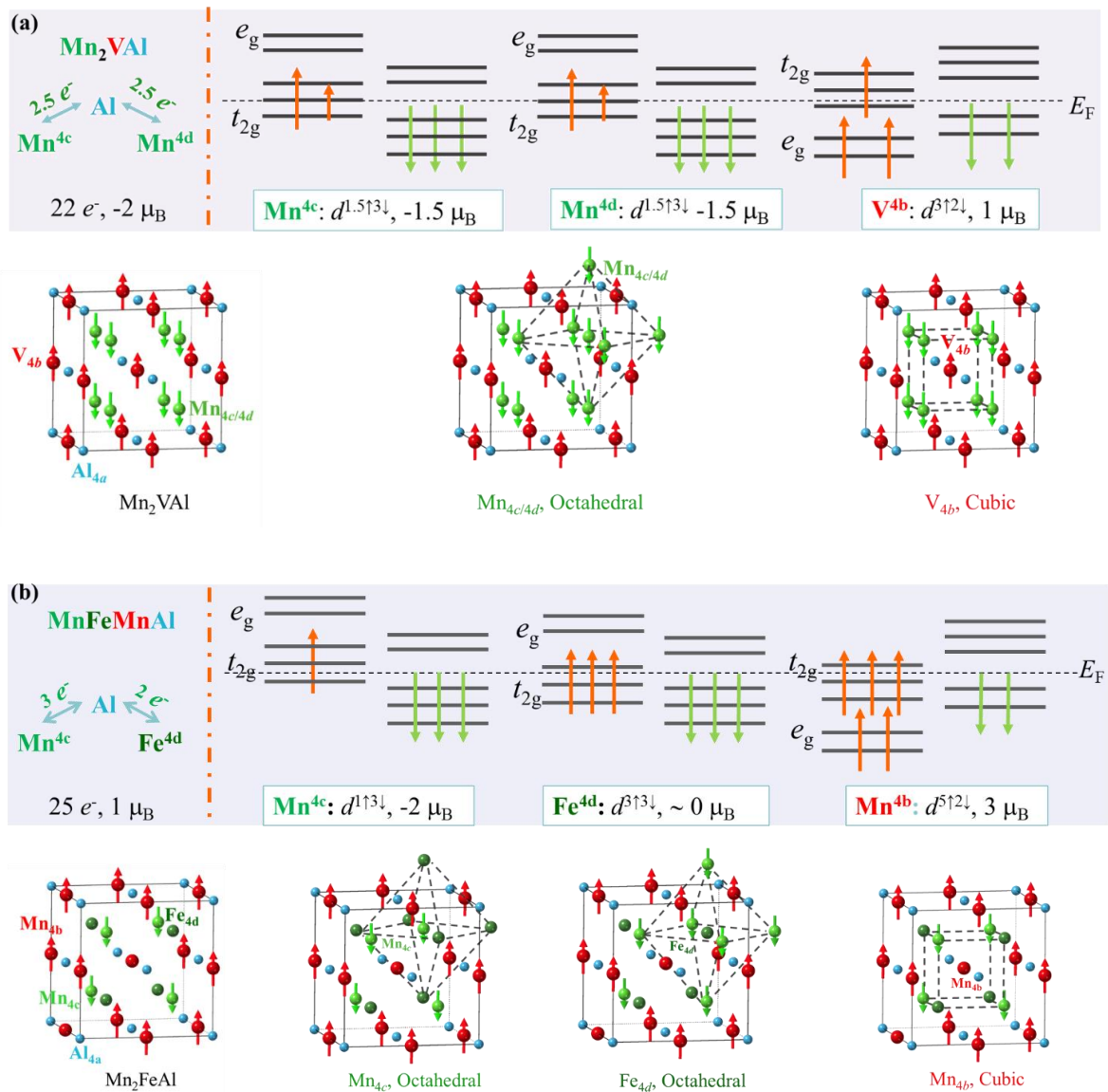
Fig. 4.9. The schematic band structures of (a) Mn_2VAl and (b) Mn_2FeAl. In $L2_1$ Mn_2VAl, two equivalent sublattices 4c and 4d with octahedral coordination produce $-1.5 \times 2 = -3$ μ_B in total; V_{4b} site with a cubic coordination yields 1 μ_B. The total magnetic moment is -2 μ_B. $Mn^{4c/4d}$ with d^3-type gap and V^{4b} with d^2-type gap ensure the alloy's half-metallicity. In XA Mn_2FeAl, both Mn^{4c} and Fe^{4d} are in octahedral coordination with a d^3-type gap. Their spin configurations indicate that -2 μ_B and 0 moments are obtained in Mn^{4c} and Fe^{4d} sites. Without

covalent bonds at Mn^{4b}, its splitting in a cubic coordination leads to a d^2-type gap and generates 3 μ_B moments. Mn_2FeAl possesses $1\mu_B$ magnetic moment, agreeing with the Slater-Pauling rule $m = Z_t - 24$ [45].

In Mn_2FeAl with the XA structure (Fig. 4.9b), antiferromagnetic interaction between Mn^{4b} and Mn^{4c} are determined by the bond lengths of ~ 2.55 Å, while the 4b-4b and 4c-4c interactions are ferromagnetic ($d = 2.94$ Å). The schematic band structures of each $3d$ sublattice of Mn_2FeAl are shown in Fig. 4.9b. The nearest neighbours of Al are Mn^{4c} and Fe^{4d} which form covalent bonds with Al sharing three and two electrons, respectively. Therefore, the number of localized electrons that produce magnetism are 4 for Mn^{4c} and 6 for Fe^{4d}. The splitting of $3d$-orbitals at the Mn^{4c} site in an octahedral coordination results in a d^3-type gap at E_f. It shows $d^{1\uparrow 3\downarrow}$ spin configuration and produces -2 μ_B magnetic moments. Fe^{4d} in octahedral coordination is in a low-spin state (spin configuration: $d^{3\uparrow 3\downarrow}$), exhibiting a d^3-type gap and no magnetic moment as shown in Fig. 4.9b. There is no covalent bond between Al^{4a} and Mn^{4b} atoms due to a 2.94 Å bond length that is longer for other sites. The splitting of $3d$-orbitals at Mn^{4b} in cubic coordination leads to a d^2-type gap at E_f. The spin configuration $d^{5\uparrow 2\downarrow}$ indicates that it has a 3 μ_B magnetic moment. The total magnetic moment of the half metal Mn_2FeAl is therefore 1 μ_B, consistent with the Slater-Pauling rule $m = Z_t - 24$ ($Z_t = 25$) and other published calculations [47].

Based on the virtual band structure discussions on Mn_2ZAl (Z = V and Fe), it is possible to obtain a new compensated ferrimagnetic half-metal $Mn_2Fe_{1-x}V_xAl$ by balancing the weight of Mn_2VAl (-2 μ_B) and Mn_2FeAl (1 μ_B). The magnetic moment can be expressed as

$$m = (1 - x) - 2x = 1 - 3x \tag{4.1}$$

where x is the proportion of Mn_2VAl in $Mn_2Fe_{1-x}V_xAl$. The fully compensated ferrimagnet ($m = 0$) can be obtained at $x = 1/3$, which agrees with the DFT[6] calculations (Fig. 4.10a).

---

[6] DFT calculations were carried out by Dr. Zsolt Gercsi.

Half-metallicity has been ensured by the $3d$ band gap of each constituent, consistent with the calculations of the density of states, as shown in Fig. 4.10b.
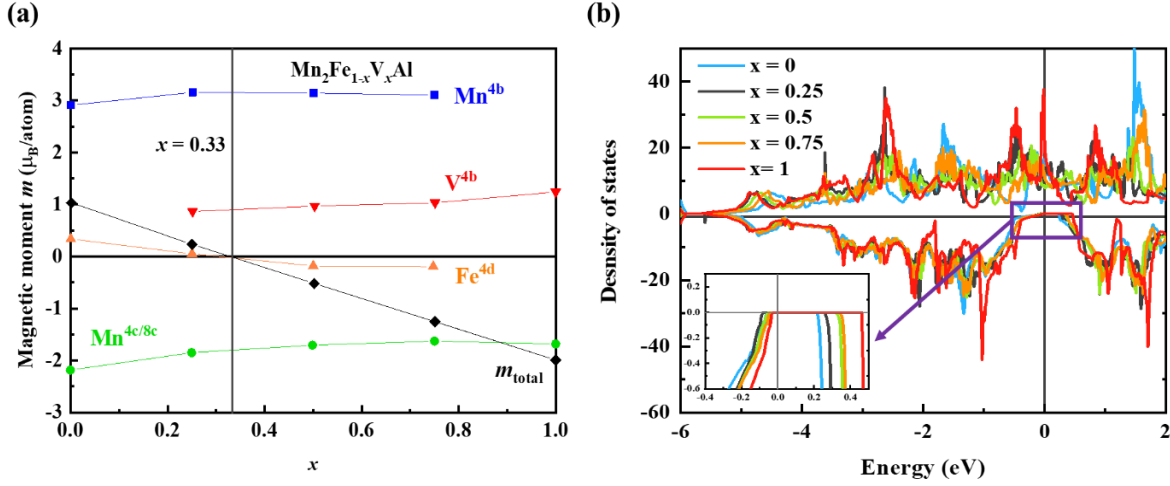
Fig. 4.10. (a) The magnetic moments of each $3d$ sublattice and total moments with V changing. In Mn_2FeAl, the magnetic moments of Mn^{4c} and Mn^{4b} is -2 μ_B and 3 μ_B, respectively. In Mn_2VAl, each Mn has a $\sim$ 1.5 μ_B magnetic moments and -1 μ_B magnetic moment is obtained for V. The ideal composition with $x = 0.33$ shows zero moment. (b) Calculated density of states for $Mn_2Fe_{1-x}V_xAl$ with x from 0 to 1. All compositions show a half-metallic property at E_f, as shown in the inset.

The above discussion suggests that by combining two fundamental half-metals with magnetic moments of opposite signs (Mn_2VAl with $Z_t = 22$, Mn_2FeAl with $Z_t = 25$), a fully-compensated ferrimagnetic half metal $Mn_2Fe_{1-x}V_xAl$ can be realized.

4.3.3 Experiments

A series of polycrystalline ingots $Mn_2Fe_{1-x}V_xAl$ ($x = 0$-1) were prepared by arc-melting mixtures of high-purity Mn, Fe, V and Al elementals (99.99%) in an argon atmosphere. In order to ensure homogenous as-cast samples, the arc-melting was repeated four times. Crystallographic structures were determined by using Panalytical XRD Cu K_α ($\lambda = 1.5405$ Å) radiation. Magnetization measurements and the temperature dependence of

magnetization between 4 - 300 K in an applied field of 0.5 T were carried out by using the superconducting quantum interference device (SQUID) magnetometer.

Ab-initio calculations[7] based on density functional theory were carried out using norm-conserving pseudopotentials and pseudo-atomic localized basis functions implemented in the OpenMX software package [48]. Calculations were based on a minimal 16 atom basis cell of the cubic structure to evaluate the total energies. An energy cut-off of 300 Ry was used for the numerical integrations. The convergence criterion for the energy minimization procedure was set to 10^{-8} Hartree (4 μeV).

4.3.4 Results

I.   Crystal structure

X-ray diffractions of as-cast $Mn_2Fe_{1-x}V_xAl$ ($x = 0$ - 1) are shown in Fig. 4.11a. An A13 (β-Mn) structure, exhibiting a complicated diffraction profile, is formed with $x = 0$ [49]. The main diffraction peaks (100), (111), (220) (400), (420), (440) and (026) suggest that alloys with $x = 0.25$ to 0.75 crystalize in a Heusler-like structure (simulated $L2_1$ and XA diffraction patterns shown in Fig. 4.11b). The ratio of the intensities of the superlattice peaks (100) and (111) drops with increasing x, indicating that XA is preferred for $x < 0.5$ and $L2_1$ is more favourable for $x > 0.5$. The lattice parameter increases slightly from 5.87 Å for $x = 0.25$ to 5.88 Å for $x = 0.75$ in a wide composition region (Fig. 4.11c), due to a small difference of their metallic radius (Fe, 1.26 Å; V, 1.34 Å). When the composition moves to the V-rich direction, the (100) peak becomes weaker and at $x = 1$, the almost invisible (100) peak indicates that the disordered B2 phase is obtained (Fig. 4.11b) [46]. Compared to the ordered Mn_2VAl ($a = 5.92$ Å) [50], the lattice constant of the disordered variant ($a = 5.925$ Å) is higher, which is similar to other alloys, *e.g.* FeV, 2.93Å in A2 and 2.91 Å in B2 [51]. The atomic disorder may come from the substitution of Al at V sites. A proper annealing

---

[7] DFT calculations on $Mn_2Fe_{1-x}V_xAl$ were performed by Dr. Zsolt Gercsi.

treatment improves the $L2_1$ ordering for Mn_2VAl [46] but does not work for Fe-rich compositions (an A13 phase is formed after annealing instead) [49].
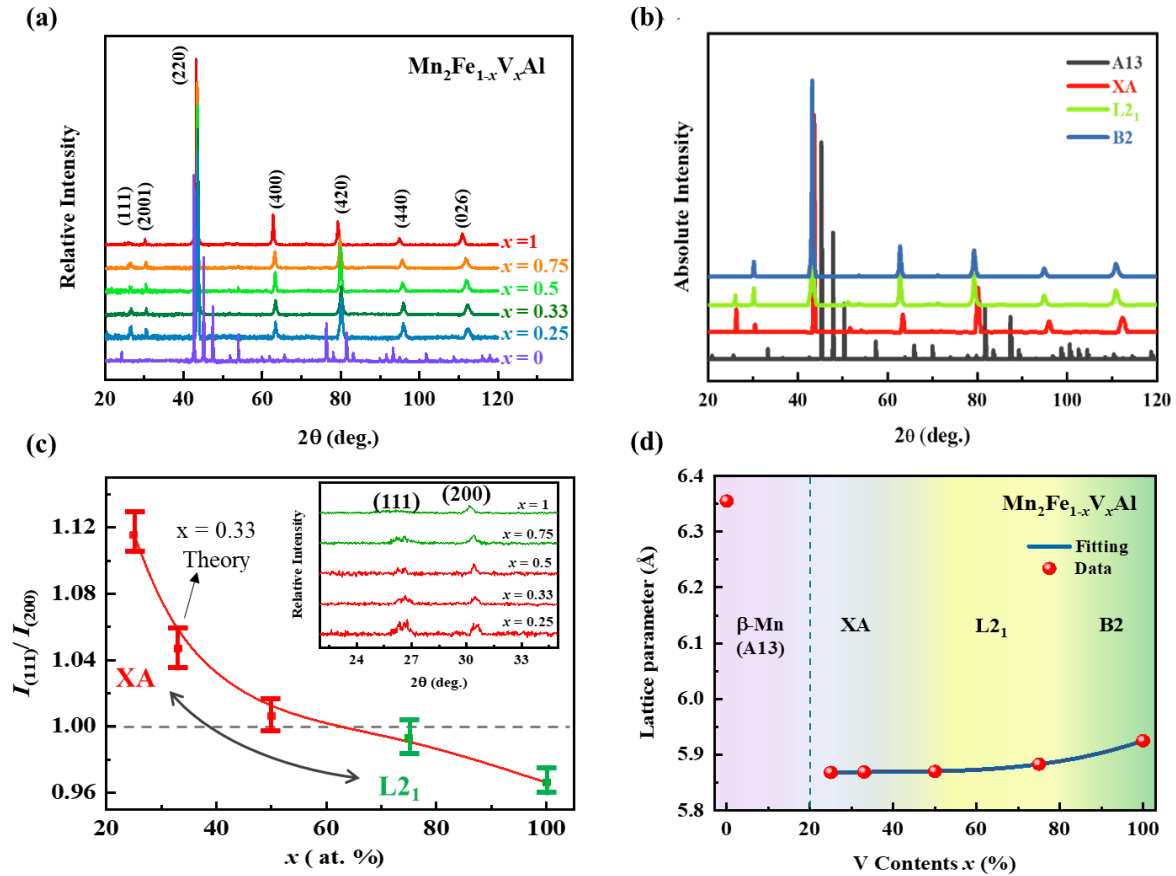
Fig. 4.11. (a) X-ray diffraction patterns of as-cast $Mn_2Fe_{1-x}V_xAl$ (x = 0, 0.25, 0,33, 0.5, 0.75 and 1) alloys. (b) The simulated x-ray diffraction profiles of A13, B2, XA and $L2_1$ structures for the $Mn_2Fe_{1-x}V_xAl$ alloys. Except for the A13 structure, the others can be distinguished by the superlattice peaks located in the low angle region ($25°$ to $33°$). For the B2 ordering, only one superlattice peak (100) shows up around $30°$. While, in the Heusler ordering ($L2_1$ & XA), both peaks, (111) & (200), can be observed. In order to tell what kind of the Heusler ordering the alloys form, we plot (c) the ratio of the intensities of superlattice peaks (100) and (111) as a function of x. The inset shows the x-ray patterns of alloys with x from 0.25 to 1. With the value of $I_{(111)}/I_{(200)}$ decreasing, the preferred Heusler crystallographic ordering changes from XA to $L2_1$ in $Mn_2Fe_{1-x}V_xAl$ with x from 0.25 to 1. (d) The lattice parameters

as a function of x. The start ($x = 0$) and end ($x = 1$) compositions tend to form β-Mn (A13) and B2 phases, respectively. It is noted that Mn_2VAl ($x = 1$) prefers to form the $L2_1$ structure after high temperature annealing ($\sim$ 1173 K [50]).

II.   Magnetic properties

Although diffraction patterns of $L2_1$ (space group : $Fm\bar{3}m$) and XA ($F\bar{4}3m$) are nearly identical, their sublattice spin configurations are different owing to structural symmetries variations. Fig. 4.12a shows magnetization curves for $Mn_2Fe_{1-x}V_xAl$ at 4 K. The saturated magnetic moments at 4 K varies from 0.03 to 1.83 μ_B/f.u for alloys with x changing from 0.25 to 1. The alloy with $x = 0$ is a Pauli paramagnet [49]. The variation of magnetization at 300 K is similar to that at 4 K, from 0.25 μ_B/f.u. for $x = 0.25$ to 1.73 μ_B/f.u. for $x = 1$ (Fig. 4.12b). Actually, we don't see the compensated moments in the expected alloy ($x = 0.33$) but we do find a very tiny moment in alloy with $x = 0.25$. The saturation magnetic moments, at 4 K (green line) and 300 K (blue line), as a function of x are summarised in Fig. 4.12b. There is a small discrepancy between the Slater-Pauling rule (red) and the experimental results because the experimental samples cannot be made fully ordered due to the close atomic number of the $3d$ elements, such as Fe and Mn. Zero moments we observe in $Mn_2Fe_{0.75}V_{0.25}Al$ at 35 K (Fig. 4.12d), close to the expected value of 0.33.
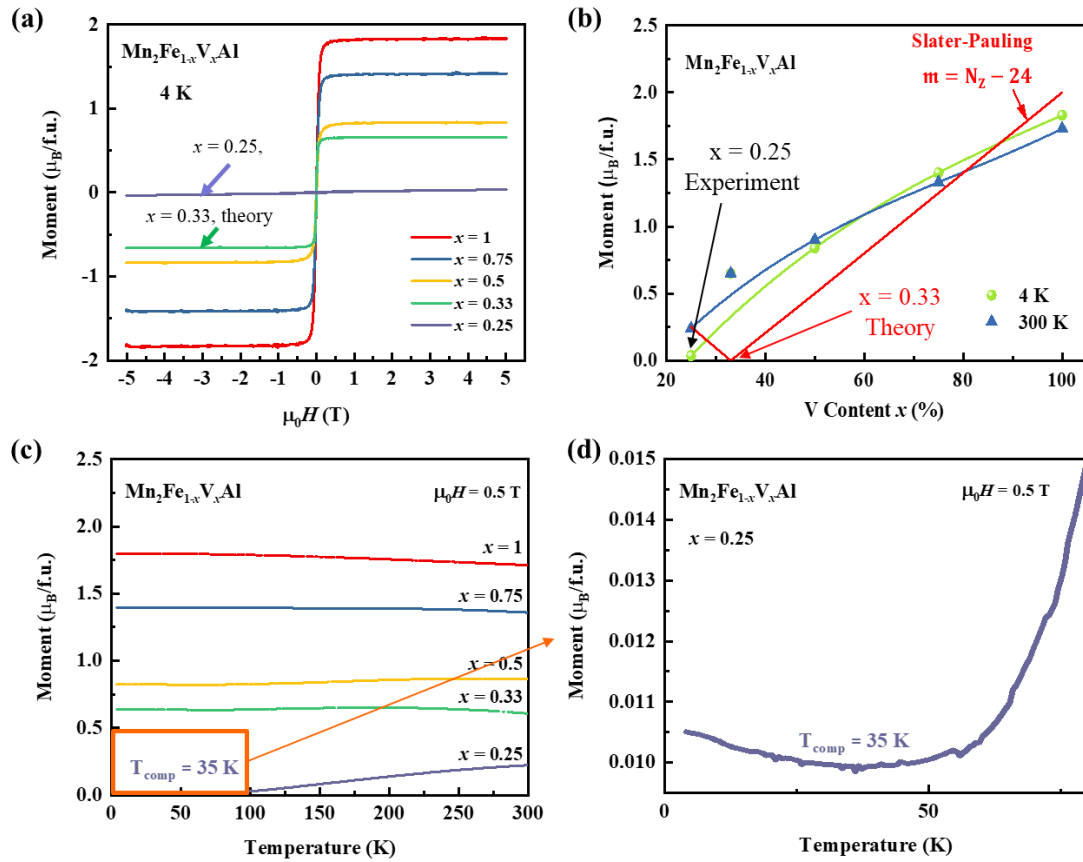
Fig. 4.12. (a) The magnetization curves of as-cast $Mn_2Fe_{1-x}V_xAl$ with x from to 1 at 4 K. The predicted composition $Mn_2Fe_{0.67}V_{0.33}Al$ doesn't show zero moments, but the one with $x = 0.25$ yield extremely low moments. (b) The saturated magnetic moments as a function of V content with Slater-Pauling rule (red) at 4 K (green) and 300 K (blue). (c) Thermal magnetization scans under 0.5 T external applied field for $Mn_2Fe_{1-x}V_xAl$ ($x = 0.25$ to 1) from 4 K to 300 K. (d) The magnetic compensation for $x = 0.25$ is shown up at 35 K.

Furthermore, thermomagnetic scans under 0.5 T for $Mn_2Fe_{1-x}V_xAl$ ($x \sim 0.25$ to 1) are illustrated in Fig. 4.12c. we do observe the fully compensated ferrimagnetic behaviour in $x = 0.25$ (Fig. 412d). The compensation temperature T_{comp} is around 35 K and the Curie temperature is above 300 K. When more Fe is replaced by V, the initial slope of the $M(T)$ curve at low temperature is zero and the magnetization increases, with a higher T_C.

4.3.5 Discussion

As we mentioned above, small discrepancies of experimental and calculated compensated compositions come from imperfect Heusler ordering. Annealing is expected to improve the ordering, but it does not work for Fe-rich compositions, which prefer the A13 structure, although annealing is helpful for V-rich alloys; Mn_2VAl develops a 2.07 μ_B magnetic moment after annealing (at 900ºC), which matches the Slater-Pauling rule. Slight doping with Co is a way to improve Heusler ordering because of the electronegativity difference of Mn with Co is larger than that with Fe.

Mn_2CoAl also tends to form the XA Heusler structure. The nearest neighbours of Al are Mn^{4c} and Co^{4d}. They form covalent bonds with Al. The band structures of Mn^{4c} and Mn^{4b} for Co composition is identical to those for the Fe one. Although the distance of Co^{4d} to Mn^{4b} is quite short, ferromagnetic exchange exists between these two sites due to Co, as similar as hcp Co [52]. Co^{4d} with a spin configuration $d^{4\uparrow3\downarrow}$ (Fig. 4.13) carries 1 μ_B magnetic moment. Its splitting field leads to a d^3- type gap crossing the E_f (Fig. 4.13). Therefore, the d^N-type band gap in each 3d element (d^3-type for Mn^{4c} and Co^{4d}, and d^5-type for Mn^{4b}) confirms the half-metallicity of Mn_2CoAl (Fig. 4.13), which produces a 2 μ_B net magnetic moment that is as same as expected from the Slater-Pauling rule ($m = Z_t - 24$, $Z_t = 26$).
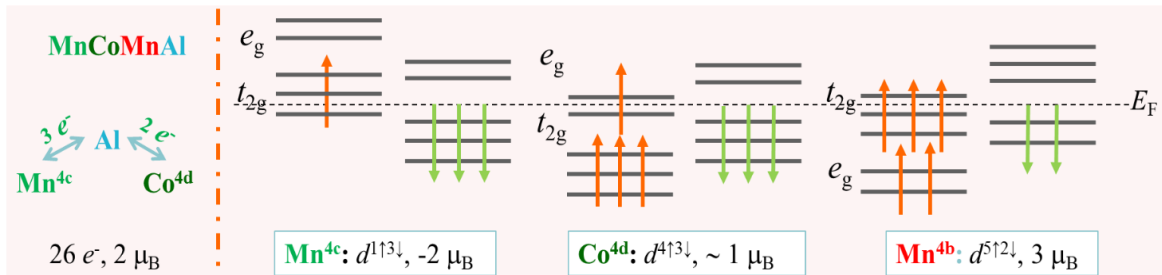
Fig. 4.13. The schematic band structures of XA Mn_2CoAl. Both Mn^{4c} and Co^{4d} with d^3-type gap, are in octahedral coordination and share 3 and 2 electrons with Al, respectively. Their spin configurations indicate that moment of -2 μ_B and 1 μ_B are obtained in the Mn^{4c} and Co^{4d} sites, respectively. If there was no electron sharing at Mn^{4b} with a cubic coordination, which forms a d^5-type gap, there would be a 3 μ_B moment. Therefore, Mn_2CoAl possess a 2 μ_B net magnetic moment, agreeing with the Slater-Pauling rule $m = Z_t - 24$ [45].

According to the above discussion, another new compensated ferrimagnetic half-metal $Mn_2Co_{1-x}V_xAl$ can be made by combining Mn_2VAl (-2 μ_B) and Mn_2CoAl (2 μ_B). Eq. 4.1 can be modified to

$$m = 2(1 - x) - 2x = 2 - 4x \qquad (4.2)$$

The alloy with $x = 0.5$ has zero moment. Therefore, it is possible to substitute Fe by Co in a wide range of x to tune the compensation temperature. In addition, compared to Fe with ~ 0 moment, the greater ferromagnetic exchange of magnetic Co (~ 1 μ_B) results in an increase in T_C [53].

4.3.6 Conclusion

In summary, we have investigated a new fully-compensated half-metallic ferrimagnet $Mn_2Fe_{1-x}V_xAl$ that reveals a mechanism of magnetic compensation, which is verified by the experiments as well as DFT calculations. The d^N- type band gaps of the $3d$ constituents in an alloy guarantee its half-metallicity, $e.g.$ Mn_2VAl: Mn^{8c} with d^3-type and V^{4b} with d^2-type gaps; Mn_2FeAl: Mn^{4c} with d^3-type and Mn^{4b} with d^5-type gap. The new ferrimagnetic alloy $Mn_2Fe_{1-x}V_xAl$ is made of Mn_2VAl (-2 μ_B) and Mn_2FeAl (1 μ_B). A fully-compensated bulk half metal is observed in $x = 0.25$, exhibiting a compensation behaviour at ~ 0 K, rather than the expected value of $x = 0.33$. Imperfect Heusler ordering in as-cast alloys is the main reason for the small discrepancy between the experiments and calculations. Co doping can improve its Heusler ordering as well as the T_{comp} and T_C. Thus, besides the existing method by tuning the E_f by varying the composition, our study has validated a new approach to develop new fully-compensated ferrimagnetic half-metals by combining two half-metals with opposite magnetic moments.

4.4 Spin liquids and spin glasses in Mn-based alloys with the cubic A13 (β-Mn) structure

4.4.1 Introduction

The discovery of a nonmagnetic 24-electron Heusler compound with β-Mn structure (see in section 4.3.4) led us to investigate βMn, a spin liquid, with Al, and other substitutions. Pure βMn, with the cubic A13 structure, is in equilibrium between 1000 K and 1370 K, but it can be stabilized at room temperature in solid solutions $Mn_{100-x}Z_x$ with Z = Al, Co, Ga, Ge or Sn; many other elements will enter the structure at higher temperatures [54]. The pure phase is usually obtained at room temperature by quenching an ingot annealed at about 1200 K in iced water. Here we have been able to obtain both the pure phase, and a wide range of polycrystalline solid solutions using a slightly different method — repeated arc melting and rapid cooling. We report the structural and magnetic properties, as well as preliminary point-contact Andreev reflection measurements on these as-cast materials and discuss the results in the light of electronic structure calculations based on the fixed moment method (Appendix II), and previous experimental reports.

The A13 unit cell, space group $P4_132$, has 20 atoms in two 12-coordinated crystallographic sites, $8c$ (Mn-I) and $12d$ (Mn-II). The latter form four linked triangles, each perpendicular to a different direction, in a sublattice with strongly frustrated $12d$ – $12d$ antiferromagnetic bonds that resembles a three-dimensional version of the Kagomé lattice [55-57]. The structure is illustrated in Fig. 4.14a. βMn does not order magnetically down to 1.4 K, although the $12d$ Mn atoms carry delocalized magnetic moments. Nakamura *et al.* proposed that βMn is the only element with a quantum spin liquid ground state [55]. The development of a magnetic moment on manganese, and the sign and magnitude of the Mn-Mn exchange interactions, depend critically on the Mn-Mn bond lengths, which accounts for variety of the magnetism found in Mn allotropes. As a rule of thumb, manganese with the shortest bonds, $\lesssim 2.40$ Å, is nonmagnetic. When the bond distance lies in the range 2.60 – 2.80 Å, there are small itinerant moments that couple antiferromagnetically, while for

longer bonds, $\gtrsim$ 2.90 Å, manganese atoms with large localized moments couple ferromagnetically. The $8c$ manganese atoms, have three short $8c - 8c$ bonds of 2.36 Å and an average nearest-neighbour distance of 2.56 Å, whereas the shortest $12d - 12d$ distances are two of 2.58 Å and two of 2.63 Å, with an average of 2.64 Å. We can therefore anticipate a small or vanishing Mn moment on $8c$ sites and reduced itinerant moments of order 1 μ_B on $12d$ sites that would like to couple antiferromagnetically to each other (and to their $8c$ neighbours if they are magnetic). Calculated moments range from $0.1 - 0.8$ μ_B for $8c$ sites and $0.4 - 2.48$ μ_B for $12d$ sites [58].

Several neutron scattering studies of pure and doped βMn [55, 57, 59-63] have revealed no long-range magnetic order, but short-range antiferromagnetic correlations. The spin liquid is characterized by an almost temperature-independent paramagnetic susceptibility $\chi_{SI} = 8 \times 10^{-4}$ [55] and a large electronic specific heat coefficient $\chi = 70 - 80$ mJmol^{-1}K^{-2}, that falls off rapidly with increasing x [64]. The ratio of these two quantities is twice the value R = $\pi^2 k_B^2 / 3\mu_0 \mu_B^2 = 5.8 \times 10^6$ expected in the free-electron model, indicating strong correlations in the manganese d-band. The zero-point energy has been estimated at 40 meV [55].

The quantum spin liquid is the magnetic ground state in *pure* βMn. Whenever some of the Mn atoms in the A13 structure are replaced by another element, a spin glass characterized by a difference between the field-cooled (FC) and zero-field cooled (ZFC) susceptibility usually appears below a freezing temperature T_f of order 10 K. This has been reported for $Mn_{100-x}Z_x$, when Z = Al [55], Co [62], and In [63] with x < 20. Single crystals of Co-doped βMn are an exception. There the spin liquid persists down to 50 mK [57].

Metallic βMn and its alloys are unlike the frustrated insulating oxides with the pyrochlore, garnet or hyperkagome structures that have been the subject of much recent interest [65, 66]; these compounds have localized moments, and are thought to form quantum spin liquids when the moments are small ($Na_4Ir_3O_8$) [67], and classical spin liquids above a spin freezing temperature when the moments are large ($GdGa_5O_{12}$) [68].

4.4.2 Results

I. Structure

X-ray diffractions of the as-cast samples show nice single-phase diffraction patterns that can be indexed on the A13 structure. This is true of pure βMn, and βMn$_{100-x}$Z$_x$ with Z = Al, x < 40, Z = Ge, x < 8, Z = Fe, x < 30 and Z = Co, x < 20. A selection of data is shown in Fig. 4.14b. The lattice parameter a_0 increases with x for Z = Al, Ga, it remains almost unchanged for Z = Co, and decreases for Z = Fe. The data are plotted in Fig. 4.14c, together with some other data from the literature [55, 62, 63]. The metallic radius of Mn is 1.27 Å, whereas the radii of Al, Fe, Co, Ga, In, Ru and Ge are 143, 126, 125, 135, 167, 134 and 1.39 Å respectively. The Vegards law initial slope da_o/dx is included in Table 4.1. There is a fair correlation with the size of the dopant metal.
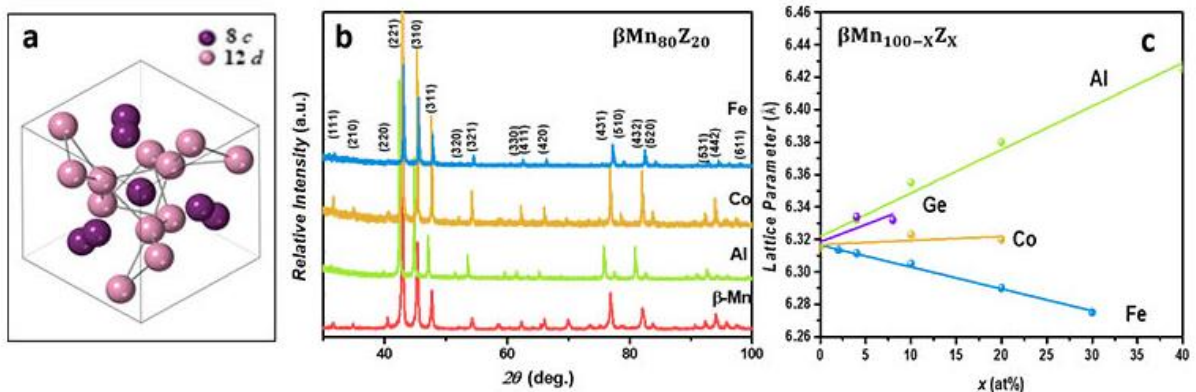
Fig. 4.14. (a) The βMn structure, illustrating the connectivity of the 12d sites, which form a three-dimensional Kagomé-like lattice. (b) X-ray powder diffraction of some as-cast alloys (Mn$_{80}$Z$_{20}$) that crystallize in the βMn structure. (c) Lattice parameters of the four solid solutions (Al, Ge, Co, Fe) considered. The data shown here are from our own as-cast alloys with $x = 0$ to 40.

Table 4.1. Influence of doping in $\beta Mn_{100-x}Z_x$ on lattice parameter a_0, spin freezing temperature T_f and difference in FC and ZFC susceptibility. Listed are the relative changes for x = 1.

Z	d(lna_0)/dx Calculated %	d(lna_0)/dx Measured %	dT_f/dx Measured K	d($\chi_{FC} - \chi_{ZFC}$)/dx Measured ppm
Al	0.10	0.051	1.3	27
Ge	0.11	0.045	3.7	/
Fe	-0.02	-0.020	3.0	5
Co	nd	0.004	3.7	9

As regards the site preference of the dopant, in the case of Z = Al this is readily deduced by fitting the X-ray powder patterns, because the atomic scattering factors of Mn and Al differ significantly. The Al has a strong preference for 12d sites, in agreement with reference [55]. For Fe and Co there is little X-ray contrast with Mn, but from neutron diffraction, Co has been shown to solely occupy 8c sites [57, 62]. For iron, a direct measurement is possible by ^{57}Fe Mössbauer spectroscopy. Manganese on the 12d site is known from ^{55}Mn NQR to be subject to a large, asymmetric electric field gradient at the nucleus [55, 69], but the quadrupole interaction for Mn at 8c sites is much smaller. The iron in our samples with the larger quadrupole splitting (0.65 and lower isomer shift (0.02 mms^{-1} relative to αFe) is associated with 12d and the smaller splitting and higher isomer shift (0.10 and 0.24 mms^{-1}) is associated with 8c. On this basis, the iron in our samples, and those studied earlier [70] prefers 8c sites, but about 30% is present in 12d. Ru strongly prefers 8c [71], but In strongly prefers 12d [63].

II.   Magnetization

The magnetic susceptibility χ of pure βMn is essentially independent of temperature from 4 K to 300 K, with no difference between the field-cooled and zero-field-cooled results,

in agreement with previous literature. The measured paramagnetic susceptibility is 8 x 10^{-4}, with only a very weak maximum near 140 K [55, 63]. However, for every dopant, we found that even a small amount, x $\approx$ 1, created an upturn or a peak in susceptibility at low temperature, accompanied by a bifurcation of the field-cooled (FC) and zero-field-cooled (ZFC) scans as shown in Fig. 4.15. A vertical shift of the field-cooled $M(H)$ magnetization curves is also observed. The behaviour is characteristic of a spin-glass. The freezing temperature T_f increases with x, as shown in Fig. 4.16a. Differences in FC and ZFC magnetization in an applied field of 1 T are plotted in Fig. 4.16b for Al, Fe and Co.
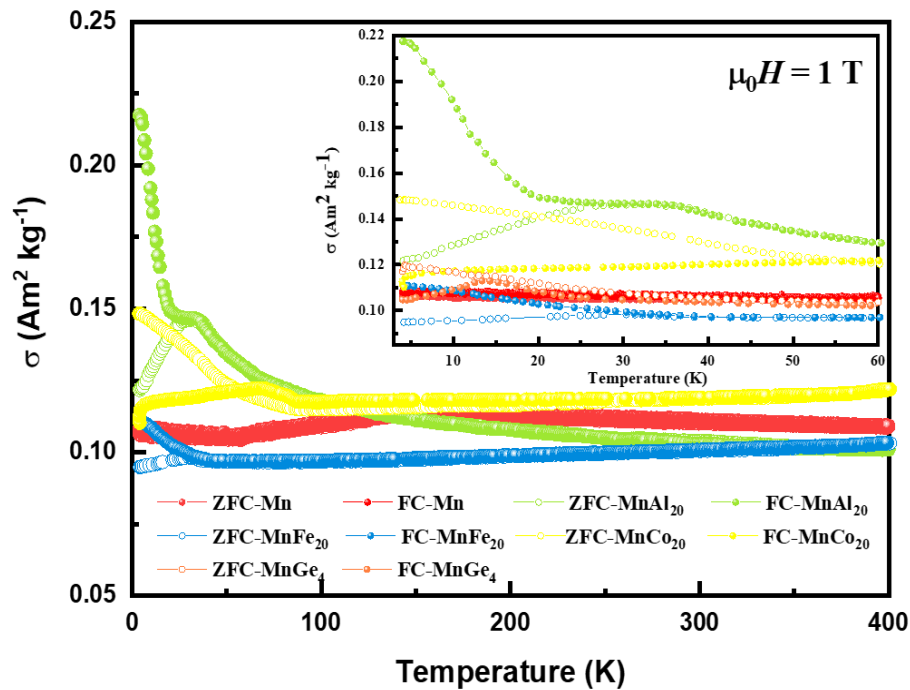
Fig. 4.15. A selection of susceptibility vs temperature data for $Mn_{80}Z_{20}$ (Z = Al, Fe, Co) and $Mn_{96}Ge_4$. Solid points – field cooled, open points – zero field cooled.
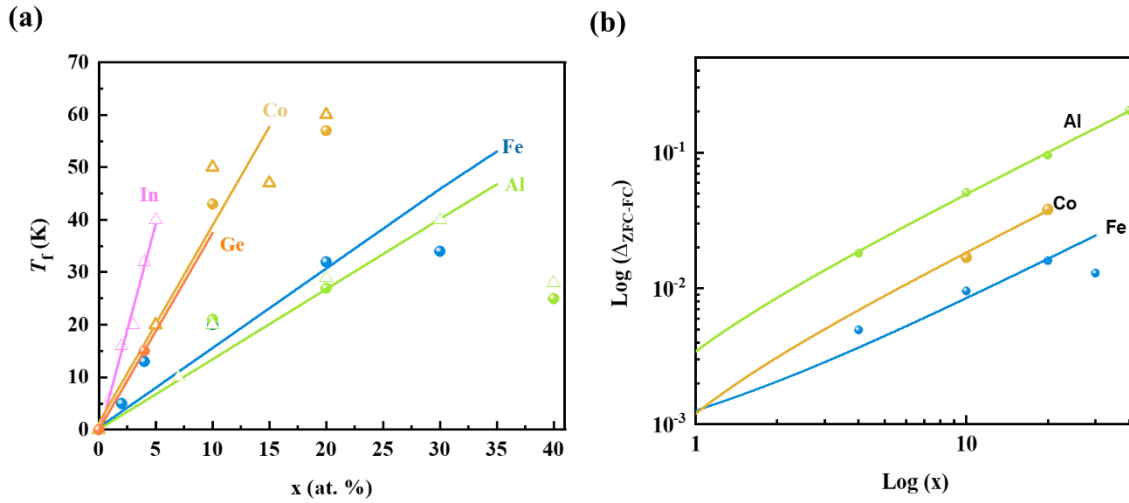
Fig. 4.16. (a) Spin freezing temperatures for $\beta Mn_{100-x}Z_x$; Solid points, this work, open triangles from Refs. [55, 62, 63]. (b) Difference between magnetic moment at 4 K vs x in the field-cooled and zero-field-cooled states, plotted on a log-log scale.

III.   Point contact Andreev reflection[8]

Some results have been obtained for a pure βMn sample and a $\beta Mn_{65}Al_{32}Ru_3$ alloy that shows a spin glass transition at 32 K. Measurements are performed in a flow of helium vapour using a mechanically-sharpened Nd tip, in the absence of an external magnetic field: care is needed to avoid oxidation of the βMn surface prior to the measurement. Data are analysed using the modified BTK model, as detailed elsewhere [72]. The best fit to βMn is found with an essentially zero spin polarization 3(6) %. The best fit to the spin glass is obtained with a spin polarization of 8(2) %. The data are shown in Fig. 4.17, with fit parameters and errors.

---

[8] PACR measurements and fits were carried out by Ajay Jha
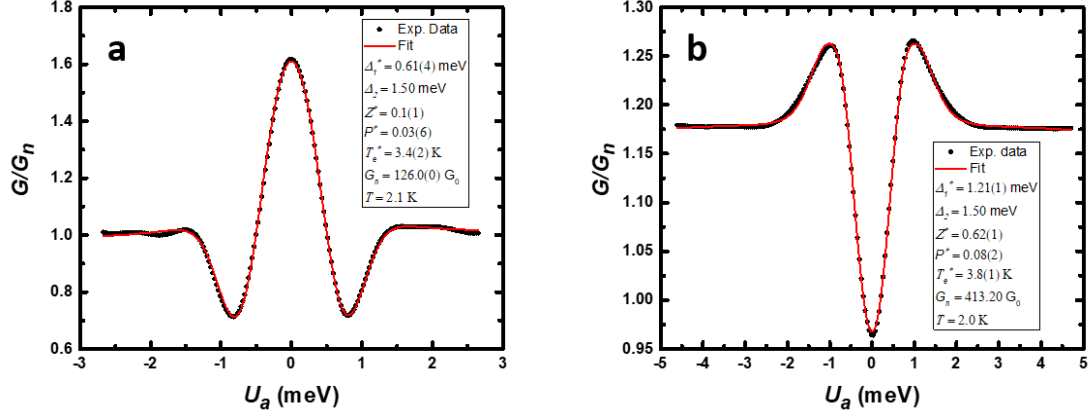
Fig. 4.17. Point-contact Andreev reflection measurements with fits (a) βMn (a spin liquid) at 2.1 K and (b) βMn$_{65}$Al$_{32}$Ru$_3$ (a spin glass) at 2.0 K.

4.4.3 Discussion

The magnetic susceptibility of our as-cast samples of pure and doped βMn agrees well with previously-published literature on quenched material. Only in pure βMn does the quantum spin liquid phase persist to the lowest temperatures. Any amount of a magnetic or nonmagnetic dopant converts the spin-liquid ground state into a spin glass below a freezing temperature T_f. Al has a strong preference for the 12d site, where it forms bonds with three neighbouring atoms in the same sublattice, as illustrated in Fig. 4.14a, but all the other dopants are expected to be present to some extent on 12d sites in the as-cast samples, as we confirmed by Mössbauer spectroscopy for iron. It seems that any disruption of the topology of the Kagomé-like lattice, even by a magnetic 3d atom, spells the end of the spin liquid at low temperature, and its replacement by a spin glass with at least some frozen spins. The freezing temperature T_f tends to zero with x; alloys with Z = Fe or Co show temperature-independent spin-liquid-like susceptibility at higher temperatures, whereas alloys with Z = Al or Ge develop a temperature-dependent susceptibility. A Curie-Weiss analysis of the Al sample with $x = 40$ gives an effective manganese moment $p_{eff} = 4.8$ μ$_B$, corresponding to a spin S = 1.9.

The theoretical calculations (Appendix II) suggest that βMn is near the brink for the appearance of magnetism. The $8c$ site is barely magnetic at equilibrium due to the short 2.36 Å $8c$ - $8c$ bonds. However, a little increase of this distance can turn on the site magnetism, as demonstrated by the plot with orange squares in Fig. 4.18b (Appendix II). On the other hand, the $12d$ - $12d$ distances are large enough to support moderate magnetic moments. The $12d – 8c$ distance could also enable magnetic moments to develop. The very shallow energy minima as a function of Mn moment seen in the calculations of Fig. 4.18 (Appendix II) are an unusual and characteristic feature of βMn. When the stabilization energy is so small, it falls in the range of the zero-point energy, and spontaneous magnetic fluctuations is the spin liquid may be expected to persist down to $T = 0$.

The picture changes radically with the introduction of non-magnetic elements; both Al and Ge deepen the total energy minima and help to form well-defined moments. This effect is linked to the lattice expansion that facilitates the appearance of stable magnetic moments on $8c$ sites. Fe has a smaller, compressive effect to the lattice parameter, suggesting that there is no significant $8c$ moment, similar to undoped βMn. Indeed, our experimental results also find the smallest change in magnetisation for the Fe dopant.

Doping tends to decrease the susceptibility when $T > T_{\mathrm{f}}$ for Fe and Al alloys but increase it when Z = Co or Ge. The decrease probably reflects a weakening of the electronic correlations in the spin liquid, which is accompanied by a reduction in the large value of the electronic specific heat coefficient [64, 73]. The increase may be associated with an increase in the density of states at the Fermi level.

There are large variations in the difference in the field-cooled and zero-field cooled susceptibility with different dopants, plotted on a logarithmic scale in Fig. 4.16b. The difference is a measure of the rigidity of the spin-glass state, and the relative weight of ferromagnetic to antiferromagnetic bonds in the distribution of exchange interactions. The neutron study by Paddison *et al.* [57] on Co-doped single crystals shows that the most important exchange bonds are the antiferromagnetic nearest-neighbour (2.60 Å) bond, and a ferromagnetic fifth-neighbour (4.20 Å) bond. The difference between the field-cooled and

zero-field-cooled moments is largest for Al or Ge, both of which remove three antiferromagnetic bonds per $12d$ site atom, and smallest for Fe and Co, where the coupling with Mn may remain antiferromagnetic.

No spin polarization is observed for pure βMn in the PCAR measurements at 2.0 K but the observation of spin polarization for the spin glass was surprising. Recent studies of spin correlations in MnO above its Néel temperature of 118 K [74] where Mn ions form a partly-frustrated fcc lattice reveal that unlike the long-range order below T_N, the short-range order in the paramagnetic state is not type II antiferromagnetism [42]. Without the constraint of long-range ordering, it is possible to satisfy the exchange bonds locally better than it is in the antiferromagnetic state, and the spin correlation length is then longer than expected. In the case of βMn, the weight of ferromagnetic bonds in the distribution of exchange interactions could be responsible for the spin polarization of $8 \pm 2\%$ measured in PCAR. The characteristic timescale for the measurement is defined by the 1.5 meV superconducting gap of Nb; it is therefore of order tens of picoseconds. In spatial language, the characteristic length-scale of the correlations is longer than typical electronic phase coherence lengths, which are tes of nanometres close to E_f.

4.4.4 Conclusions

The existence of a quantum spin liquid in βMn at low temperatures depends on the integrity of the $12d$ kagomé-like lattice. Disrupting its topology by doping with either nonmagnetic atoms or a different magnetic $3d$ atom localizes the moments at T ≈ 0 and turns the spin liquid into a spin glass. The spin liquid may then appear above the freezing temperature T_f.

The fixed-moment DFT calculations show that there is a well-defined average Mn moment in an expanded lattice− the case for Al or Ge doping but no Mn moment for a compressed lattice− the case for Fe doping. At the experimental lattice parameter, the stabilization energy of the Mn moment at any value between 0 and 0.4 μ_B is much less than the estimated zero-point fluctuation energy [55].

The spin polarization of ~ 8 % revealed by PCAR in the spin glass phases is attributed to a weakly ferromagnetic character of the spin correlations measured on the characteristic timescale/length-scale of the measurements.

Revisiting the metallic Mn quantum spin liquids may help to throw some light on the behaviour of the rare-earth oxide candidates with strongly-frustrated pyrochlore or kagomé-type lattices. The metals have the advantage of strong exchange interactions, which allow representative behaviour to be observed at easily-accessible temperatures.

4.5 Summary

In this chapter, we focused on exploring cubic fully compensated ferrimagnetic Heusler half metals, which combined the characteristics of ferrimagnets and half metals. The ferrimagnet has magnetic order but at compensation produces zero magnetic moment. And the half metal yields 100% spin polarized currents due to a band gap in one spin channel at the Fermi level. The first material we introduced was fully compensated ferrimagnet $Mn_{1.5}V_{0.5}FeAl$, whose parent compound is ferrimagnetic half-metal Mn_2FeAl. Its compensation and Curie temperatures are very sensitive to the unit cell volume, which is raised by manganese contents or heat treatments. The results suggest that when the lattice parameter is less than 5.845 Å, compensation behaviour can be observed although the T_C is above room temperature. With expanding the lattice parameter, the magnetic compensation disappears and the T_C increases, > 400 K. Then, we moved to another cubic Heusler ferrimagnetic half metal $Mn_2Fe_{1-x}V_xAl$, which is considered as a combination of Mn_2VAl ($Z_t = 25$) and Mn_2FeAl ($Z_t = 22$) with magnetic moments of opposite signs. The d^N- type band gaps of the $3d$ constituents in the alloys guarantee their half-metallicity (Mn_2VAl: Mn^{8c} with d^3-type and V^{4b} with d^2-type gaps; Mn_2FeAl: Mn^{4c} with d^3-type and Mn^{4b} with d^2-type gap). the fully compensated ferrimagnetic half metal $Mn_2Fe_{0.75}V_{0.25}Al$ is realized. Through the analysis of its constituents' spin configurations, the mechanism of magnetic compensation was revealed. Knowledge of compensation in half-metals inspired us to develop new ideal fully-compensated ferrimagnetic half-metals with high T_C. The DFT

calculations agree well with our experiments. It is noted that Heusler-ordered Mn_2FeAl cannot be obtained in ingots, because the equilibrium phase is A13 (β-Mn).

4.6 Acknowledgement

Appendix

I. Heusler-order stability in $Mn_2Fe_{1-x}V_xAl$
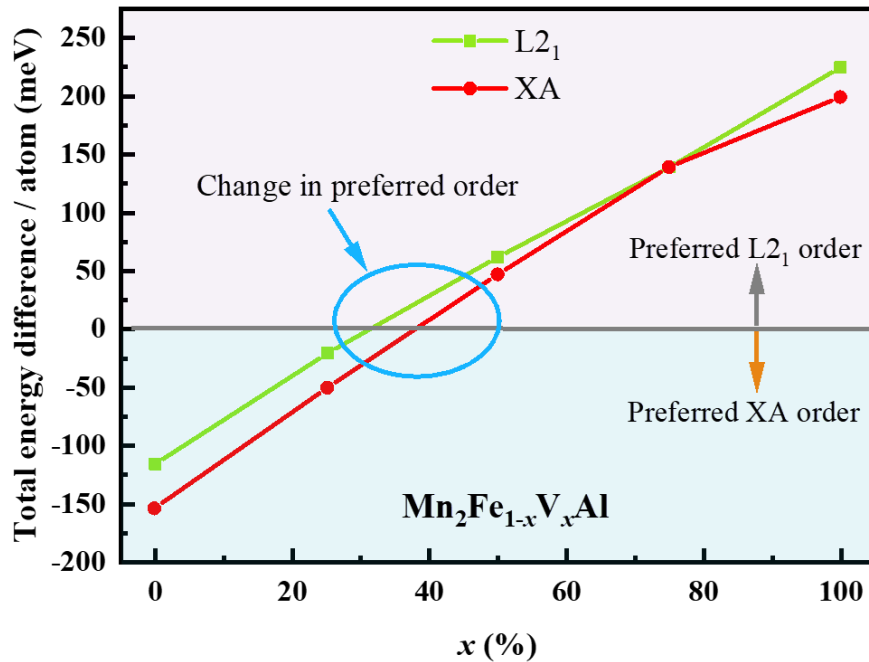
Fig. 4. 19. The total energy difference per atom of $L2_1$ and XA structures as a function of V concentration x. The preferred $L2_1$ order is in alloy with $x > 0.5$, while the preferred XA order is in that with $x < 0.5$. The theoretical calculations were carried out by Dr. Z Gercsi.

II. Details of calculations on βMn and $\beta Mn_{95}Z_5$

The Vienna ab initio Simulation Package (VASP) [75], based on DFT with the projector augmented wave (PAW) method [76] and Perdew-Burke-Ernzerhof (PBE) parametrization was used. We took the minimal, 20-atom cell and replaced a single $8c$ or $12d$ atom to examine the effect of doping with Fe, Al or Ge. The lattice was fully relaxed in

a non-magnetic (NM) equilibrium configuration with a lattice parameter of 6.00 Å. For isovolumic expansion/ compression, we relaxed the internal atomic positions. The fixed-spin moment (FSM) approach [77] allows the total magnetic moment to be fixed at a specific value, and the magnitude and direction of the local magnetic moments are free to relax in a collinear fashion.

A remarkably broad and shallow energy minimum (< 1 meV) appears for βMn at the relaxed equilibrium lattice parameter for moments running from 0 to 0.4 μ_B /atom (Fig. 4.18a). Moments above ~ 0.4 μ_B /atom are energetically unfavourable. The site-specific moments were shown in Fig. 4.18b, indicating the nature of the magnetic coupling. Significant magnetic moments are found on $12d$ sites, while the $8c$ moments of are < 0.12 μ_B. Stable antiferromagnetic sublattice coupling of develops in this shallow energy range, but when the total moment is forced to be > 0.4 μ_B/atom, the $8c$ moments flip to an unfavourable ferromagnetic configuration.

There is a striking difference in magnetic stability with 2% lattice expansion or compression. Compression destroys the magnetism of βMn, but expansion stabilizes the magnetic state, and increases the moments.
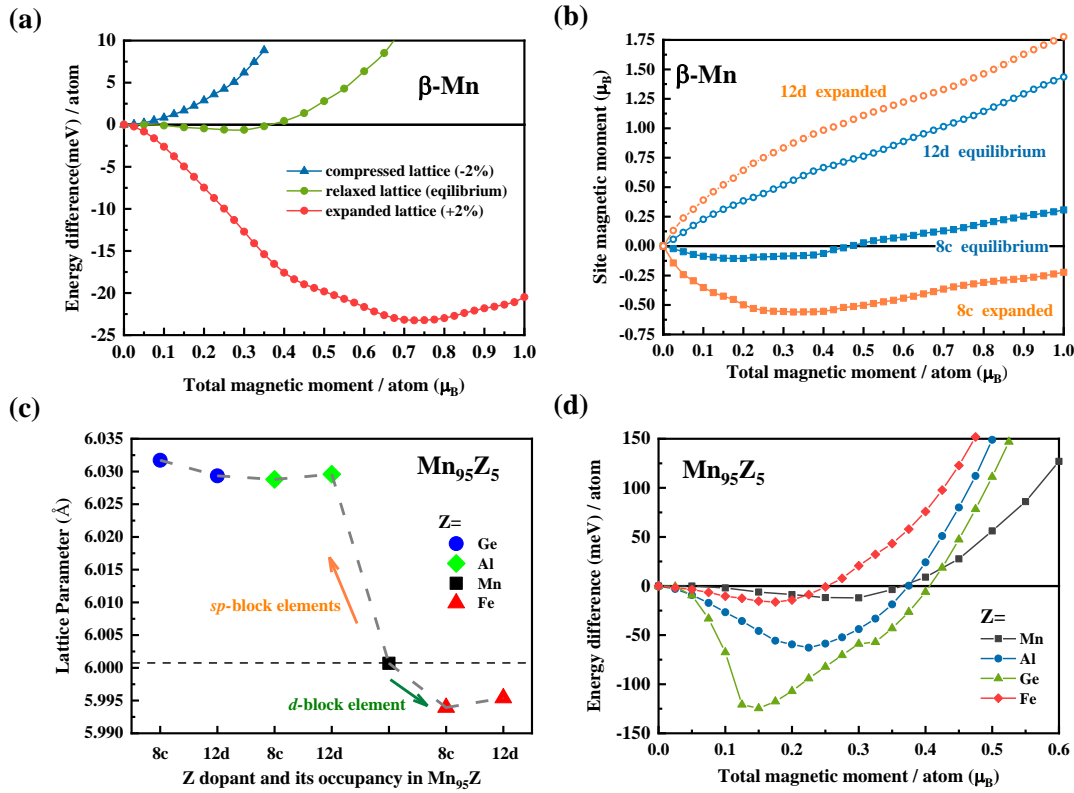
Fig. 4.18. (a) FSM results of the relaxed, compressed and expanded lattice of βMn. (b) site specific magnetic moments in βMn as calculated from FSM method. (c) Lattice parameter as a function Z dopant and its occupancy in βMn. (d) FSM results for the effect of dopants on the 12d site.

We now turn to the chemical pressure induced by dopants, which were allowed to occupy either site. The lattice parameter shrinks slightly with the addition of Fe, while the main group elements Al and Ge expand the lattice (Fig. 4.18c). Doping on either site has almost the same effect. We regard the shallow energy minima found for βMn is a characteristic of the spin liquid state. The magnetic states are considerably more stable than the parent βMn (Fig. 4.18d).

The calculations for βMn$_{95}$Z$_5$ for Z = Al and Ge show a 0.5% lattice expansion for the two main group dopants, and there is a smaller 0.1% compression for Fe.

References

[1] N. A. Zarkevich, P. Singh, A. V. Smirnov, and D. D. Johnson, Effect of substitutional doping and disorder on the phase stability, magnetism, and half-metallicity of Heusler alloys, Acta Materialia **225**, 117477 (2022).

[2] S. Zeffane, M. Sayah, F. Dahmane, M. Mokhtari, L. Zekri, R. Khenata, and N. Zekri, Prediction of electronic and half metallic properties of Mn_2YSn (Y= Mo, Nb, Zr) Heusler alloys, arXiv preprint arXiv:2103.15542 (2021).

[3] M. Shakil, S. Mushtaq, I. Zeba, S. Gillani, M. I. Khan, H. Arshad, and M. Rafique, Structural, electronic, magnetic and thermoelectric properties of full heusler alloys Co_2YZ (Z= S, Ge, Se): A first principles calculation, Physica B: Condensed Matter **602**, 412558 (2021)

[4] N. B. Schröter, J. A. Krieger, D. Pei, Tianlun Yu, Samuel Stolz, T. Schmitt, P. Dudin, T. K. Kim, C. Cacho, A. Schnyder, A. Bergara, V. N. Strocov, F. de Juan, M. G. Vergniory, L. M. Schoop, Weyl fermions, Fermi arcs, and minority-spin carriers in ferromagnetic CoS_2, Science Advances **6**, eabd5000 (2020).

[5] T. Hadji, H. Khalfoun, H. Rached, and A. Azzouz-Rached, Ab-initio prediction of high T_C half-metallic ferrimagnetism in Li-based Heusler compounds Mn_2LiZ (Z= Si, Ge and Sn), Computational Condensed Matter **27**, e00557 (2021).

[6] Y. Güleşci Kartal, E. G. Özdemir, and Z. Merdan, Electronic, magnetic and elastic calculations on half-metallic Heusler Ti_2RuTl compound, Philosophical Magazine **102** (2), 153 (2022).

[7] S. He, P. Zhou, Y. Yang, W. Wang, and L. Sun, $1T-CrO_2$ monolayer: a high-temperature Dirac half-metal for high-speed spintronics, Nanoscale Advances **3**, 3093 (2021).

[8] A. Schmehl, V. Vaithyanathan, A. Herrnberger, S. Thiel, C. Richter, M. Liberati, T. Heeg, M. Röckerath, L. F. Kourkoutis, S. Mühlbauer, P. Böni, D. A. Muller, Y. Barash, J.

Schubert, Y. Idzerda, J. Mannhart and D. G. Schlom., Epitaxial integration of the highly spin-polarized ferromagnetic semiconductor EuO with silicon and GaN, Nature Materials **6**, 882 (2007).

[9] R.-W. Zhang, D.-S. Ma, J.-M. Zhang, and Y. Yao, Weyl nodal-line surface half-metal in $CaFeO_3$, Physical Review B **103**, 195115 (2021).

[10] T. Jungwirth, J. Sinova, J. Mašek, J. Kučera, and A. MacDonald, Theory of ferromagnetic (III, Mn) V semiconductors, Reviews of Modern Physics **78**, 809 (2006).

[11] I. Galanakis, P. Mavropoulos, and P. H. Dederichs, Electronic structure and Slater–Pauling behaviour in half-metallic Heusler alloys calculated from first principles. Journal of Physics D: Applied Physics, **39**(5), 765 (2006).

[12] S. Ishdia, S. Fujii, S. Kashiwagi, S. Asano, Search for Half-metallic compounds in Co_2MnZ, Journal of the Physical Society of Japan **64**, 6, 2152 (1995).

[13] R. De Groot, F. Mueller, P. Van Engen, and K. Buschow, New class of materials: half-metallic ferromagnets, Physical Review Letters **50**, 2024 (1983).

[14] P. Brown, K.-U. Neumann, P. Webster, and K. Ziebeck, The magnetization distributions in some Heusler alloys proposed as half-metallic ferromagnets, Journal of Physics: Condensed Matter **12**, 1827 (2000).

[15] S. Wurmehl, H. C. Kandpal, G. H. Fecher, and C. Felser, Valence electron rules for prediction of half-metallic compensated-ferrimagnetic behaviour of Heusler compounds with complete spin polarization, Journal of Physics: Condensed Matter **18**, 6171 (2006).

[16] D. Jung, H.-J. Koo, and M.-H. Whangbo, Study of the 18-electron band gap and ferromagnetism in semi-Heusler compounds by non-spin-polarized electronic band structure calculations, Journal of Molecular Structure: THEOCHEM **527**, 113 (2000).

[17] J. Wernick, G. Hull, T. Geballe, J. Bernardini, and J. Waszczak, Superconductivity in ternary Heusler intermetallic compounds, Materials Letters **2**, 90 (1983).

[18] J. Winterlik, G. H. Fecher, A. Thomas, and C. Felser, Superconductivity in palladium-based Heusler compounds, Physical Review B **79**, 064508 (2009).

[19] S. Chadov, X. Qi, J. Kübler, G. H. Fecher, C. Felser, and S. C. Zhang, Tunable multifunctional topological insulators in ternary Heusler compounds, Nature Materials **9**, 541 (2010).

[20] T. Graf, C. Felser, and S. S. Parkin, Simple rules for the understanding of Heusler compounds, Progress in Solid State Chemistry **39**, 1 (2011).

[21] H. Kurt, K. Rode, P. Stamenov, M. Venkatesan, Y.-C. Lau, E. Fonda, and J. M. D. Coey, Cubic Mn_2Ga thin films: Crossing the spin gap with Ruthenium, Physical Review Letters **112**, 027201 (2014).

[22] R. Stinshoff, A. K. Nayak, G. H. Fecher, B. Balke, S. Ouardi, Y. Skourski, T. Nakamura, and C. Felser, Completely compensated ferrimagnetism and sublattice spin crossing in the half-metallic Heusler compound $Mn_{1.5}FeV_{0.5}Al$, Physical Review B **95**, 060410 (2017).

[23] J. D. Boeck, W. V. Roy, J. Das, V. Motsnyi, Z. Liu, L. Lagae, H. Boeve, K. Dessein and G. Borghs, Technology and materials issues in semiconductor-based magnetoelectronics, Semiconductor Science and Technology **17** (4), 342 (2002).

[24] M. Gilleßen and R. Dronskowski, A combinatorial study of full Heusler alloys by first-principles computational methods, Journal of Computational Chemistry **30** (8), 1290-1299 (2008).

[25] D. J. Singh and I. I. Mazin, Electronic structure, local moments, and transport in Fe_2VAl Physical Review B **57** (22), 14352-14356 (1998).

[26] C. S. Lue, H. R. Joseph, Jr., K. D. D. Rathnayaka, D. G. Naugle, S. Y. Wu and W. H. Li, Superparamagnetism and magnetic defects in Fe_2VAl and Fe_2VGa, Journal of Physics: Condensed Matter **13** (7), 1585 (2001).

[27] M. P. Raphael, B. Ravel, Q. Huang, M. A. Willard, S. F. Cheng, B. N. Das, R. M. Stroud, K. M. Bussmann, J. H. Claassen and V. G. Harris, Presence of antisite disorder and its characterization in the predicted half-metal Co_2MnSi, Physical Review B **66** (10), 104429 (2002).

[28] H. van Leuken and R. A. de Groot, Half-Metallic Antiferromagnets, Physical Review Letters **74** (7), 1171-1173 (1995).

[29] M. Hakimi, M. Venkatesan, K. Rode, K. Ackland and J. M. D. Coey, The zero-magnetization Heusler ferrimagnet, Journal of Applied Physics **113** (17), 17B101 (2013).

[30] D. Betto, N. Thiyagarajah, Y.-C. Lau, C. Piamonteze, M.-A. Arrio, P. Stamenov, J. Coey, and K. Rode, Site-specific magnetism of half-metallic Mn_2Ru_xGa thin films determined by X-ray absorption spectroscopy, Physical Review B **91**, 094410 (2015).

31] K. Siewierska, N. Teichert, R. Schäfer, and J. M. D. Coey, Imaging domains in a zero-moment half metal, IEEE Transactions on Magnetics **55**, 1 (2018).

[32] C. Banerjee, K. Rode, G. Atcheson, S. Lenne , P. Stamenov, J. M. D. Coey , and J. Besbas, Ultrafast double pulse all-optical reswitching of a ferrimagnet, Physical Review Letters **126**, 177202 (2021).

[33] R. Stinshoff, G. H. Fecher, S. Chadov, A. K. Nayak, B. Balke, S. Ouardi, T. Nakamura, and C. Felser, Half-metallic compensated ferrimagnetism with a tunable compensation point over a wide temperature range in the Mn-Fe-V-Al Heusler system, AIP Advances **7**, 105009 (2017).

[34] M. B. Stearns, Internal-Field Variations with Temperature for the Two Sublattices of Ordered Fe_3Al and Fe_3Si, Physical Review **168** (2), 588-592 (1968).

[35] R. J. Soulen, J. M. Byers, M. S. Osofsky, B. Nadgorny, T. Ambrose, S. F. Cheng, P. R. Broussard, C. T. Tanaka, J. Nowak, J. S. Moodera, A. Barry and J. M. D. Coey, Measuring the spin polarization of a metal with a superconducting point contact, Science **282** (5386), 85-88 (1998).

[36] P. Stamenov, Point contact Andreev reflection from semimetallic bismuth—The roles of the minority carriers and the large spin-orbit coupling, Journal of Applied Physics **111** (7), 07C519 (2012).

[37] L. Makinistian, M. M. Faiz, R. P. Panguluri, B. Balke, S. Wurmehl, C. Felser, E. A. Albanesi, A. G. Petukhov and B. Nadgorny, On the half-metallicity of Co_2FeSi Heusler alloy: Point-contact Andreev reflection spectroscopy and ab initio study, Physical Review B **87** (22), 220402 (2013).

[38] H. Kurt, K. Rode, M. Venkatesan, P. Stamenov and J. M. D. Coey, High spin polarization in epitaxial films of ferrimagnetic Mn_3Ga, Physical Review B **83** (2), 020405 (2011).

[39] V. N. Antonov, V. P. Antropov, B. N. Harmon, A. N. Yaresko, and A. Y. Perlov, Fully relativistic spin-polarized LMTO calculations of the magneto-optical Kerr effect of d and f ferromagnetic materials. I. Chromium spinel chalcogenides, Physical Review B **59**, 14552 (1999).

[40] K. Özdoğan, E. Şaşıoğlu, B. Aktaş, I. Galanakis, Doping and disorder in the Co_2MnAl and Co_2MnGa half-metallic Heusler alloys, Physical Review B **74**, 172412 (2006).

[41] A. Miyashita, M. Maekawa, Y. Shimoyama, N. Seko, A. Kawasuso and R. Y. Umetsu, High-density magnetic-vacancy inclusion in Co_2MnGa single crystal probed by spin-polarized positron annihilation spectroscopy, Journal of Physics: Condensed Matter **34**, 045701 (2021).

[42] J. M. D. Coey, *Magnetism and Magnetic Materials* (Cambridge university press, 2010).

[43] Y. Xiaohu, C.-F. Huo, Y.-W. Li, J. Wang, H. Jiao, Fe_3O_4 surface electronic structures and stability from GGA+ U, Surface Science **606**, 872, (2012).

[44] I. Galanakis, K. Özdoğan, E. Şaşıoğlu, and B. Aktaş, Doping of Mn_2VAl and Mn_2VSi Heusler alloys as a route to half-metallic antiferromagnetism, Physical Review B **75**, 092407 (2007).

[45] I. Galanakis, P. Dederichs, and N. Papanikolaou, Slater-Pauling behavior and origin of the half-metallicity of the full-Heusler alloys, Physical Review B **66**, 174429 (2002).

[46] R. Gavrea, A. Bolinger, V. Pop, O. Isnard, M. Coldea, and D. Benea, Influence of Cu Doping on the Electronic Structure and Magnetic Properties of the Mn_2VAl Heusler Compound, Physica Status Solidi (b) **254**, 1700160 (2017).

[47] B. Lv, Z. Lian, Y. Miao, C. Gao, M. Si, D. Xue, F. Yu, and J. Yao, Realization of a Heusler alloy Mn_2FeAl with B2 ordering, Applied Physics Letters **116**, 132404 (2020).

[48] See http://www.openmx-square.org.

[49] S. Dash, A. Lukoyanov, D. Mishra, U. M. Rasi, R. Gangineni, M. Vasundhara, and A. K. Patra, Structural stability and magnetic properties of Mn_2FeAl alloy with a β-Mn structure, Journal of Magnetism and Magnetic Materials **513**, 167205 (2020).

[50] C. Jiang, M. Venkatesan, and J. M. D. Coey, Transport and magnetic properties of Mn_2VAl: Search for half-metallicity, Solid State Communications **118**, 513 (2001).

[51] T. Ziller, G. Le Caër, O. Isnard, P. Cénédèse, and B. Fultz, Metastable and transient states of chemical ordering in Fe-V nanocrystalline alloys, Physical Review B **65**, 024204 (2001).

[52] D.A. Papaconstantopoulos, J. L. Fry, and N. E. Brener, Ferromagnetism in hexagonal-close-packed elements, Physical Review B **39**, 2526 (1989).

[53] R. Gavrea, R. Hirian, O. Isnard, V. Pop, and D. Benea, Investigations on compensated ferrimagnetism in the $Mn_2Co_{0.5}V_{0.5}Al$ Heusler alloy, Solid State Communications **309**, 113812 (2020).

[54] T. Kohara and K. Asayama, NMR Study of Antiferromagnetic β-Mn Alloys, Journal of the Physical Society of Japan **37**, 401 (1974).

[55] H.Nakamura, K.Yoshimoto, M.Shiga, M.Nishi and K.Kakurai, Strong antiferromagneitc spin fluctuations and the quantum spin-liquid state in geometrically frustrated β-Mn, and the transition to a spin-glass state caused by non-magnetic impurity, Journal of Physics: Condensed Matter **9**, 4701 (1997).

[56] B. Canals, Mean-field study of the disordered ground state in the β-Mn lattice, Physical Review B **61**, 11251 (2000).

[57] J. A. M. Paddison, J. R. Stewart, P. Manuel, P. Courtois, G. J. McIntyre, B. D. Rainford and A. L. Goodwin, Emergent Frustration in Co-doped β-Mn, Physical Review Letters **110**, 267207 (2013).

[58] H. Ehteshami, P.A. Korzhavyi, Thermodynamic properties of paramagnetic α- and β-Mn from first principles: The effect of transverse spin fluctuations, Physical Review Materials **1**, 073803 (2017).

[59] J. R. Stewart, R. Cywinski, Nuclear and magnetic short-range order in some dilute β-Mn alloys, Journal of Magnetism and Magnetic Materials **272**, 676 (2004).

[60] J. R. Stewart, A. S. Wills, C. J. Leavey, B. D. Rainford, C. Ritter, The magnetic structure of β-MnRu, Journal of Physics: Condensed Matter **19**, 145291 (2007).

[61] J. R. Stewart, K. H. Andersen, R. Cywinski, Neutron polarization analysis study of the frustrated magnetic ground state of β-Mn$_{1-x}$Al$_x$, Physical Review B **78**, 014428 (2008).

[62] J. R. Stewart, R. Cywinski, Magnetic short-range order in β-Mn$_{1-x}$Co$_x$, Journal of Physics: Condensed Matter **21**, 124216 (2009).

[63] J. R. Stewart, A. D. Hillier, J. M. Hillier, R. Cywinski, Structural and dynamical study of moment localization in β-Mn$_{1-x}$In$_x$, Physical Review B **82**, 144439 (2010).

[64] T. Shinkoda, K. Kumagai and K. Asayama, Effect of Spin Fluctuations on the Specific Heat in β-Mn Metal and Alloys, Journal of the Physical Society of Japan **46**, 1754 (1979).

[65] L. Balents, Spin liquids in frustrated magnets, Nature **464** (7286) 199 (2010).

[66] J. Wen, S.-L. Yu, S. Li, W. Yu, J.-X. Li, Experimental identification of quantum spin liquids, npj Quantum Materials **4**, 12 (2019).

[67] Y. Singh, Y. Tokiwa, J. Dong, and P. Gegenwart, Spin liquid close to a quantum critical point in Na$_4$Ir$_3$O$_8$, Physical Review B **88**, 220413 (2013).

[68] O. A. Petrenko, C. Ritter, M. Yethiraj, D. McK Paul, Investigation of the Low-Temperature Spin-Liquid Behavior of the Frustrated Magnet Gadolinium Gallium Garnet, Physical Review Letters **80**, 4570 (1998).

[69] Y. Kohori, Y. Noguchi and T. Kohara, Observation of [55]Mn NMR and NQR signals from site II in β-Mn Metal, Journal of the Physical Society of Japan **62**, 447 (1993).

[70] Y. Nishihara, S. Ogawa and S. Waki, Mössbauer study of β-Mn alloys with Iron and Tin -Weak Itinerant-Electron antiferromagnetic of β-Mn Alloys-, Journal of the Physical Society of Japan **42**, 845 (1977).

[71] C. J. Leavey, J. R. Stewart, B. D. Rainford and A. D. Hillier, Magnetic ground states and spin dynamics of β-Mn$_{1-x}$Ru$_x$ alloys, Journal of Physics: Condensed Matter, **19**, 145288 (2007).

[72] P. Stamenov, Point contact Andreev reflection from semimetallic bismuth—The roles of the minority carriers and the large spin-orbit coupling, Journal of Applied Physics **113**, 17C718 (2013).

[73] K. Sasao, R.Y. Umetsu, K. Fukamichi, Atomic site preference, the Néel temperature and specific heat of β-Mn Ru alloys, Journal of Alloys Compounds **24**, 325 (2001).

[74] J. A. M. Paddison, M. J. Gutmann, J. R. Stewart, M. G. Tucker, M. T. Dove, D. A. Keen, A. L. Goodwin, Magnetic structure of paramagnetic MnO, Physical Review B **97**, 014429 (2018).

[75] G. Kresse and J. Furthmüller, Efficient iterative schemes for ab initio total-energy calculations using a plane-wave basis set, Physical Review B **54**, 11169 (1996).

[76] K. B. John, P. Perdew, Matthias Ernzerhof, Generalized Gradient Approximation Made Simple, Physical Review Letters **77**, 3866 (1996).

[77] K. Schwarz and P. Mohn, Itinerant metamagnetism in YCo_2, Journal of Physics F: Metal Physics **14**, L129 (1984).

Chapter 5　Mn-free ferrimagnetic alloys

5.1　Introduction

Half-metallic ferromagnets exhibit 100% spin polarization due to a gap in one of the spin channels. Traditional half-metals include CrO_2 and Co-based Heusler alloys such as 28-electron Co_2MnSi [1]. More recently, Mn-based ferrimagnetic half metals Mn_2Ru_xGa (MRG) have been developed that exhibit spin compensation at a temperature T_{comp} that can be tuned by varying the Ru content and they exhibit Curie temperatures of order 500 K, well suited for applications [2]. However, Mn-diffusion into the MgO barrier of MRG-based magnetic tunnel junctions has proved to be a problem [3]. Therefore, it would be desirable to find a new Mn-free half-metallic ferrimagnet.

Firstly, we investigated the magnetic properties of bulk, single-phaseV_3Al, CrVTiAl and the corresponding Ga compounds (V_3Ga & CrVTiGa) experimentally, which are predicted as ferrimagnetic half metals, spin-gapless semiconductor and metallic antiferromagnet in different atomic arrangements by density functional theory calculations[9]. It is noted that both magnetism and semi-conductivity are destroyed by disorder. All the as-cast alloys show some degree of B2-type ordering, but all of them are Pauli paramagnets with dimensionless susceptibilities close to the average of the atomic constituents. We find that even the prolonged annealing did not improve any atomic order, suggesting the expected ordering is inaccessible in alloys prepared from the melt.

However, the character of light $3d$ elements in alloys, exhibiting non-magnetic or magnetic behavior, points out one way to develop new ferrimagnetic alloys without Mn. We

---

[9] These are in studies performed by Dr. Z. Gercsi.

investigated the magnetism of V in ordered (B2) and disordered (A2) $Fe_{1-x}V_x$ alloys, revealing the influence of the bond lengths on magnetism: V atoms with the shortest bonds (< 2.9 Å) behave nonmagnetically, those with the longest bonds (> 3.8 Å) show long-range ferromagnetic coupling and the V sites with bonds of 2.9 – 3.8 Å couple antiferromagnetically. Similar behaviour also can be seen in the other light transition elements, which is applied on the more localized side of the boundary between the completely itinerant and more localized regions (Fig. 5.10c).

5.2 Cubic V_3Al, CrVTiAl and related 18-electron Heusler compounds with a different group 13 element

5.2.1 Introduction

The Heusler structure made by light $3d$ elements attracts more attention due to the high magnetic transition temperatures [4, 5], which is made out of four interpenetrating fcc lattices ($4a$, $4b$, $4c$, and $4d$) as illustrated in Fig. 5.1. Structures can be distinguished by the sequence of atoms W, X, Y and Z in the $4a$, $4c$, $4b$ and $4d$ sites along a body diagonal direction. The origin can be chosen at any one of them. The compounds may form A2, $Im\bar{3}m$ (XXXX); B2, Pm3m (XYXY); $D0_3$, $Fm\bar{3}m$ (XYYY); $L2_1$, $Fm\bar{3}m$ (XYXZ); XA, $F\bar{4}3m$ (XXYZ); and Y-type, $F\bar{4}3m$ (XWYZ), named by the Strukturbericht symbol and space group, respectively. There are crystallographically-distinct variants in each case except A2, depending on how the atoms are identified as WXY or Z. In the LiMgPdSn Y-type structure, $4! = 24$ permutations of the atoms are possible on the four sublattices, but only three of them are crystallographically distinguishable. We denote them as I, II and III. The order of the atoms along the diagonal in CrVTiAl, for example, can be I; Al-Cr-Ti-V, II; Al-Ti-Cr-V or III Al-Cr-V-Ti. The Y-type and XA structures have no centre of inversion but $L2_1$, $D0_3$, B2 and A2 all have one.
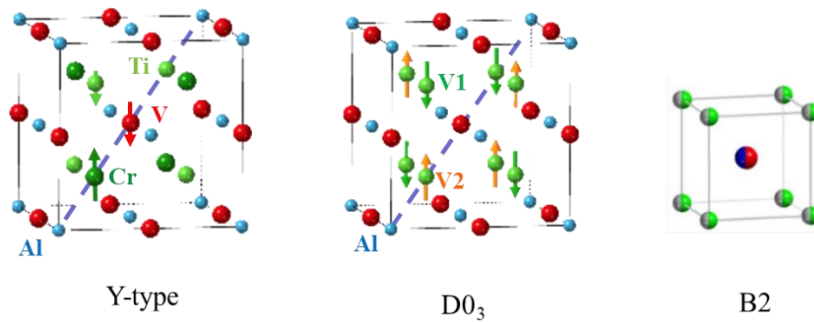
Fig. 5.1. (a) An arrangement of four different atoms, Cr, V, Ti, Al on the four fcc sublattices along the body diagonal of the cubic Heusler Y-type structure. In the $D0_3$ structure, 4a is occupied by the group 13 element and 4b, 4c and 4d sites are occupied by V, whereas in the B2 structure, 4a and 4b sites are occupied by a mixture of elements and 4c and 4d sites by a different mixture. (In $D0_3$ the 4c and 4d sites are crystallographically equivalent and are referred to as $8c$ sites).

Galanakis *et al.* suggest that many inverse XA Heusler alloys are half-metals [6], following the Slater-Pauling rule, $m = n - 18$, where m is the moment per formula in Bohr magnetons and n is the number of valence electrons in the formula (3 for Al, Ga, 4 for Ti, 5 for V and 6 for Cr, for example). This is analogous to the '$m = n - 24$' Slater-Pauling rule that was established experimentally for $L2_1$ compounds, including the Co_2YZ series [6-8]. That means when n = 18 or 24, the materials are expected to be compensated ferrimagnetic half metal. An extensive study by Ma *et al.* of the calculated electronic structure of 127 such inverse Heuslers confirmed that the presence of spin gaps and (n – 18) half metallicity [9]. However, very few such materials have been realized in experiments. In addition, the great majority have differences of formation energy that are so small (50 - 100 meV/atom) with respect to other, stable phases or combinations of phases that they were thought unlikely to be synthesizable in equilibrium [9]. These formation energy differences are generally quoted with reference to the convex 'hull', which is an energy surface in compositional space, based on the energies of huge numbers of computed compounds archived in the AFLOWLIB or Open Quantum Materials (OQMD) databases. Many computational studies of binary,

ternary and quaternary Heuslers have tested potential new candidates for stability with respect to the hull [7, 9-14]. These calculations were carried out by Dr. Zsolt Gercsi.

The group 13 elements Al or Ga have eight spin-unsplit states at the bottom of the valence band arising from the $3s/3p$ or $4s/4p$ orbitals, respectively. The nine 3d electrons may or may not occupy spin split orbitals, with or without a gap at the Fermi level [15]. Some possible schematic densities of states are illustrated in Fig. 5.2, including one variety of spin gapless semiconductors [16]. The 18-electron compounds could be antiferromagnets or compensated ferrimagnets. Compensated ferrimagnetic semiconductors with different gaps in the ↑ and ↓ densities of states [5, 17] arepotential spin filters [18].
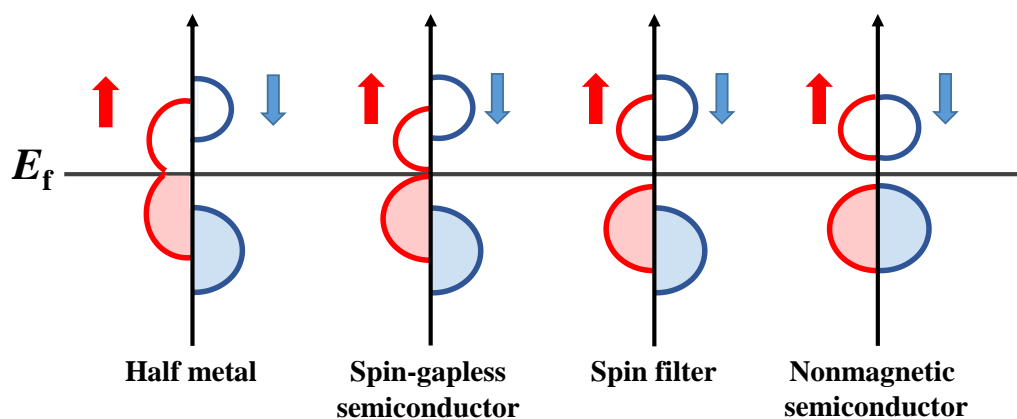
Fig. 5.2. Schematic densities of states suggested for 18-electron Heusler compounds. They might be half-metal, spin-gapless semiconductor, spin filter and nonmagnetic semiconductor. The last panel can also represent an antiferromagnetic semiconductor.

We first summarize published density functional theory (DFT) calculations of the electronic structure of the 18-electron D0$_3$ and Y-type intermetallics [5, 18]. There have been several calculations for D0$_3$-V$_3$Al. (The low-temperature equilibrium phase is an A15 superconductor with T_{sc} = 11.7 K that becomes bcc above 600°C [19]). First calculations found it to be a nonmagnetic gapless semiconductor [20]. Subsequently, it was identified as an antiferromagnetic semiconductor [4, 6]. Antiferromagnetism is possible because the vanadium on 4b sites has no moment, and the vanadium on the surrounding 8c sites forms two equivalent antiferromagnetically coupled sublattices (4c and 4d) in a G-type spin

structure, with moments of about 1.5 μ_B/atom and a calculated Néel temperature of 600 – 1000 K. The nonmagnetic state lies 0.039 eV/atom above the ordered antiferromagnetic state [21]. D0$_3$-type V$_3$Ga is calculated to be nonmagnetic [9], or else a G-type antiferromagnet [4, 18] with a Néel temperature of 500 – 850 K. In both V$_3$Al and V$_3$Ga, a broad maximum in the temperature dependence of magnetization is observed at 600 K [21] or 390 K [18] respectively, amounting to 1 - 2% of the susceptibility. The equilibrium phase for V$_3$Ga at these temperatures is A15-type.

The 18-electron quaternaries, CrVTiAl and CrVTiGa, were predicted to follow the XA ternary Heusler alloys and behave as fully-compensated half-metallic ferrimagnets with a gap for one spin direction in the spin-polarized density of states (DOS). Calculations for CrVTiAl based on an ordered LiMgPdSn-type structure predicted a spin gap in both $\uparrow$ and $\downarrow$ densities of states, and an antiferromagnetic ordering temperature T_N in excess of 2000 K [17]. This is considerably higher than the value for cobalt, the metal with the highest known Curie temperature. There are equal and opposite moments on the Cr and V+Ti sublattices of about 3 μ_B, but very little magnetism on Al [17]. On the basis of such electronic structure calculations, CrVTiAl was proposed as a spin filter for spin electronics [17, 22], or as a spin-gapless semiconductor where the spin gap in one band is practically zero [5]. The constituent elements behave quite differently. Three of them are Pauli paramagnets (Ti, V and Al); the fourth (Cr) hosts an incommensurate antiferromagnetic spin density wave arising from 'Fermi surface nesting' with an amplitude of 0.43 μ_B that is largely orbital in character. The Néel temperature T_N is 313 K [22].

The CrVTiAl alloy was subsequently prepared in bulk [5, 22, 23] and thin film form [24, 25]. It crystallizes in a cubic structure with $a_0 \approx 6.10$ Å and there is some evidence of B2 atomic ordering [23, 24], but not Y-type or D0$_3$ ordering. The bulk alloy has a temperature-independent magnetic susceptibility $\chi = 4.5 \times 10^{-8}$ m^{3}kg^{-1} with no sign of any net moment from 4 – 400 K according to one report [22]. In another report, the susceptibility is similar with a small upturn below 10 K [24], but evidence of a very small net moment of 10^{-3} μ_B/fu and a little coercivity at 3 K together with some temperature-dependence in the

susceptibility around 750 K, were later attributed to an oxide impurity [24]. All samples studied showed a metallic residual resistivity ρ_0 in the range 160-280 $\mu\Omega$ cm. The temperature coefficient of resistance becomes negative at high temperature, which was interpreted as semiconducting behaviour with a gap of 0.16 eV. The Hall coefficient is positive, consistent with hole densities of 10^{22} cm^{-3}. (The atom density in the compound is 7×10^{22} cm^{-3}). A small nonlinear component of magnetization observed in thin films saturates in about 2 T. These data were interpreted as showing that CrVTiAl is a fully-compensated ferrimagnetic half metal with a very high T_C. However, real materials are considered to exhibit a considerable degree of atomic disorder compared to the ideal structures in Fig. 5.1a, and only a small fraction of any sample was estimated to be in a fully-ordered Y structure or one with only Cr/V disorder, both of which exhibit spin gaps [5].

There is no publication on these materials showing direct evidence of magnetic ordering such as magnetic neutron diffraction, anomalous Hall effect or measurement of magnetic hyperfine interactions. Nor are there data showing hysteresis measured by the magneto-optic Kerr effect, domains or spin-torque switching such as have been reported in Mn_2Ru_xGa, the most-thoroughly studied example of a compensated half metal [26]. Nevertheless, absence of evidence is not evidence of absence.

Our primary aim here was to try to prepare the 18-valence electron Heusler compounds with $D0_3$ or Y structures and investigate their magnetism experimentally to see whether they fulfil any of the interesting theoretical predictions. Materials selected for the study are bulk V_3Al and CrVTiAl, together with their Ga counterparts. Samples doped with 1 wt. % of ^{57}Fe are included for Mössbauer spectroscopy. Then we compare our experimental results with the calculated dependence of magnetism on atomic order in the four sublattices using DFT calculations, which are extended to cover two other group 13 elements, B and In. The calculations suggest that the G-type AFM spin arrangement appears to be generic feature of the 18-electron $D0_3$-ordered series, but our data show little evidence for the formation of the ordered structure in bulk material. The stability of the magnetically ordered configurations is investigated in the binary and quaternary series as well as the stability of the atomic order,

and the structures themselves.

5.2.2 Experiments

Alloys were prepared by arc melting the elements (99.99 % pure) Cr, V, Ti and Al or Ga under Argon. Samples were also prepared with 1 wt. % of ^{57}Fe. The alloys were first studied in the as-cast state, and then after annealing for 10 days in vacuum at 650°C or 900°C, followed by furnace cooling or quenching to ambient temperature. Some representative x-ray diffraction data for as-cast material are shown in Fig. 5.3. All the as-cast alloys were single phase, with the exception of V_3Ga, which showed a trace of an A15 Cr_3Si-structure secondary phase. The main peaks in all cases correspond to the A2 bcc structure, but a weak 200 reflection found in all of them indicates some tendency towards B2 atomic order. The X-ray diffraction patterns of the ^{57}Fe-doped samples were no different. There was no sign of a (111) reflection, which is a marker for $D0_3$, $L2_1$, XA and Y-type order, even after long counts around $2\theta = 25°$. Data are included in Fig.5.3.

Analysis of the ratio of the 002/004 peak heights [27] for CrVTiAl, compared with the ratio of the 001/002 peak heights for B2-ordered (V+Cr)/(Ti+Al), allowed the degree of B2 order to be quantified as $S_{B2} = 0.46$. The corresponding result for the Ga alloys is $S_{B2} = 0.41$. Estimated errors are ±0.05. The as-cast alloys are therefore partly ordered at the level of the B2 bcc sub-cell, but not at the level of the 8x larger Heusler cell (Fig. 5.1).
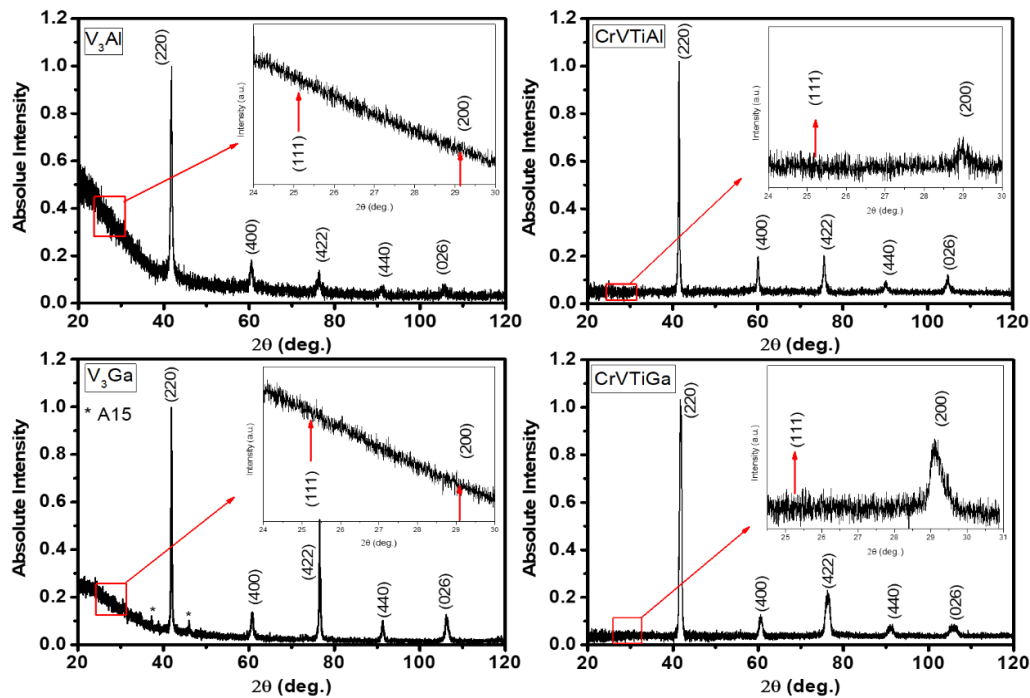
Fig. 5.3. X-ray diffraction patterns of as-cast alloys: V$_3$Al & V$_3$Ga (left) and CrVTiAl & CrVTiGa (right).

Prolonged annealing of the as-cast ingots at 650 °C or 900 °C failed to improve the atomic order. On the contrary, the as-cast single cubic phase with partial B2 order disproportionate into two or more separate cubic phases with different lattice parameters. The example of CrVTiAl is shown in Fig. 5.4. From differential scanning calorimetry (DSC) at 10°C per minute, the phase segregation is found to occur in the range 400 – 500°C. The quaternary appears to decompose into VCr and TiAl solid solutions, with lattice parameters of 2.95 Å and 3.09 Å, respectively. The phase segregation temperature for CrVTiGa was a little higher.

V$_3$Ga was different. It showed a trace of A15-structure impurity already in the as-cast state and annealing at 650°C or 900°C transformed it completely into the superconducting A15 structure, as anticipated from the phase diagram. Refinement of the structure in the

space group Pm$\bar{3}$n gives $a_0 = 4.62$ Å and a composition of V$_{2.9}$Ga. A15-type V$_3$Al was not obtained after these anneals.
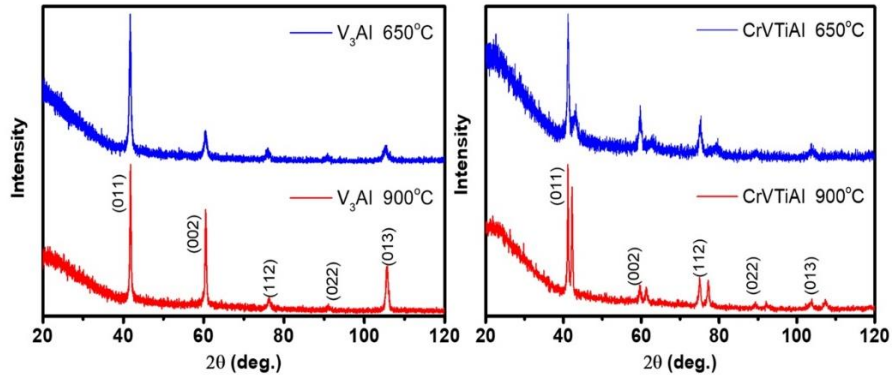
Fig. 5.4. X-ray diffraction patterns of as-cast alloys after annealing at 650 °C or 900 °C.

Magnetization data are presented in Fig. 5.5 for as-cast, single-phase samples. In every case, the magnetization is linear in the field of up to 5 T at temperatures ranging from 4 K - 400 K. The ^{57}Fe-doped samples behave similarly. There is no sign of any weak moment, and the susceptibility is temperature-independent to within ±1. Changes seen at higher temperatures, up to 900 K, were irreversible and associated with phase segregation. They amount to less than 2% of the room-temperature susceptibility.
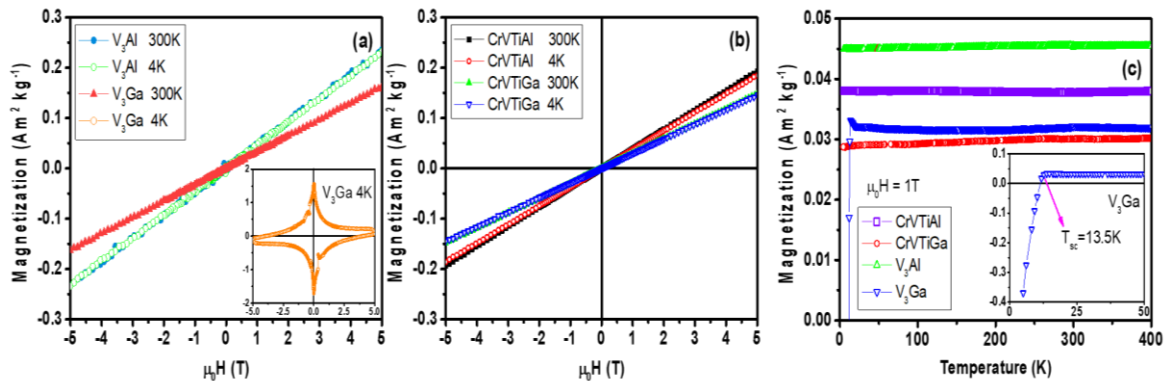
Fig. 5.5. Magnetization data. Field variation at 4 K and 400 K for (a) V$_3$Al/Ga and (b) CrVTiAl/Ga. (c) Temperature scans of the susceptibility in 1 T.

Only V_3Ga behaves differently. Due to the trace of the superconducting A15 phase in the alloy, it exhibits a Meissner effect below $T_{sc} = 13.5$ K (Fig. 5.5a and c inserts).   From the initial negative susceptibility of -0.031at 4 K, the volume fraction of A15 in the as-cast sample is estimated as 3%.

Table 5.1. summarizes the lattice parameters, density, mass susceptibility and dimensionless susceptibility for the as-cast 18-electron alloys. The magnitude of the temperature-independent paramagnetic moment in 5 T lies in the range $1.0 - 1.5 \times 10^{-3}$ μ_B per atom. Values of the dimensionless susceptibility χ for the alloys fall about 40% short of the value required for the appearance of spontaneous ferromagnetism according to the Stoner criterion [28]. The susceptibility of the 1% iron-doped alloys was likewise temperature-independent down to 4 K.

Table 5.1. Lattice parameter, density and susceptibilities of the as-cast alloys.

Compound	a_0 (Å)	ρ (kgm^{-3})	χ_m (10^{-9} m^{3}kg^{-1})	χ (10^{-6})
CrVTiAl	6.17	5042	44.8	226
CrVTiAl (^{57}Fe)	6.14	5115	33.8	173
CrVTiGa	6.12	6389	37.1	237
CrVTiGa (^{57}Fe)	6.11	6435	37.0	238
V_3Al	6.08	5311	56.5	300
V_3Al (^{57}Fe)	6.10	6273	57.7	362
V_3Ga	6.05	6669	41.3	275

Values of density and susceptibility for the pure elements are provided in Table 5.2 for comparison. It is remarkable that the volume-averaged dimensionless susceptibility of the

elements χ_{av} agrees very well with the measured susceptibility of all four alloys (Table 5.3). Furthermore, the susceptibility of vanadium is temperature-independent below room temperature [29] and that of chromium is temperature-independent above the Néel temperature, and decreases by 4% at lower temperatures [30]. The susceptibilities of bcc VCr [31] and VTi [32] solid solutions show little temperature dependence either.

Table 5.2. Density and susceptibility of the pure elements [33].

Element	Structure	ρ (kgm^{-3})	χ_m (10^{-9} m^{3}kg^{-1})	χ (10^{-6})
Al	fcc	2698	7.7	21
Ga	ortho	5907	-3.9	-23
Ti	hcp	4540	40.1	182
V	bcc	6110	62.8	384
Cr	bcc	7190	44.5	320

Table 5.3. Comparison of the dimensionless susceptibility of the compounds with the averaged values of the constituent elements.

Compound	χ_{av} (10^{-6})	χ (10^{-6})
CrVTiAl	227	226
CrVTiGa	216	237
V$_3$Al	293	300
V$_3$Ga	282	275

No evidence of any reversible antiferromagnetic transition in V_3Al or V_3Ga was observed in DSC in the range 30 – 1000 ^oC, where compounds were thought to order antiferromagnetically [18, 21]. Instead, there is an irreversible exothermic transition at 380^oC for V_3Al, which is associated with a very small, irreversible decrease in susceptibility at the same temperature. In V_3Ga there is a larger exothermic transition at 490 $^{\circ}C$, which is associated with the irreversible transformation to the A15 structure. In the quaternaries, we find exothermic events at 445 $^{\circ}C$ for CrVTiAl and at 506 $^{\circ}C$ for CrVTiGa, where the irreversible phase segregation takes place (Fig. 5.6). A small ($\sim$ 2%) irreversible step appears in susceptibility at the same temperature.
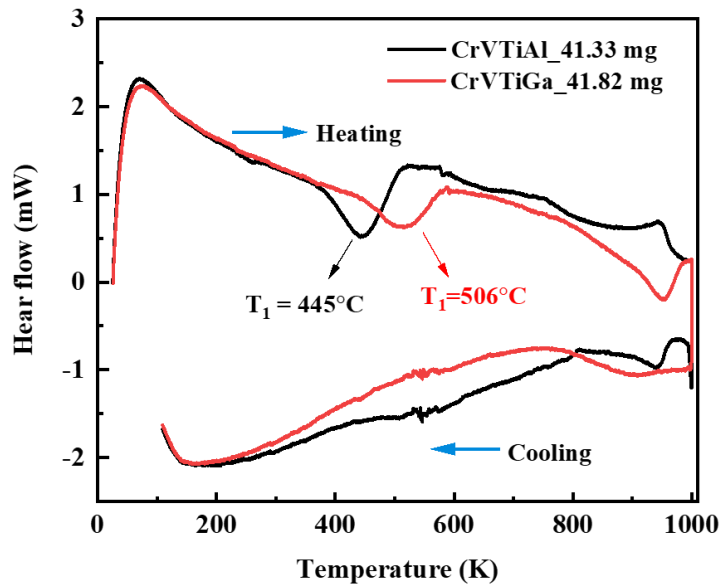
Fig. 5.6. DSC thermograms for as-cast quaternary alloys CrVTiAl and CrVTiGa. The exothermic reactions happen at 445 $^{\circ}C$ for CrVTiAl and at 506 $^{\circ}C$ for CrVTiGa, respectively, where the single phase of the as-cast alloy decomposes into two separate phases (see Fig. 5.4).

A direct probe of any magnetic order is provided by Mössbauer spectroscopy of 1% ^{57}Fe-doped samples[10]. There is no perceptible difference in the X-ray patterns in the samples with or without 1% of iron, and only minor changes are found in the magnetic susceptibility (Table 5.1). The room temperature spectra for the iron-doped alloys shown in Fig. 5.7, indicate that the iron is paramagnetic, with an isomer shift of -0.14 mms^{-1} with respect to the source, ^{57}Co in Rh. The quadrupole splitting of 0.42 mms^{-1} for CrVTiAl and CrVTiGa (Fig. 5.7a), reflects a range of disordered atomic environments for the ^{57}Fe impurity. In V$_3$Al (Fig. 5.7b), there is an unsplit central peak which is due to ~ 20 % of the iron that is situated in a locally-symmetric nearest neighbour environment. There is no magnetic hyperfine splitting in any of the alloys and the hyperfine field is less than 1T. The above information indicates that *none* of the alloys are magnetically-ordered at room temperature.
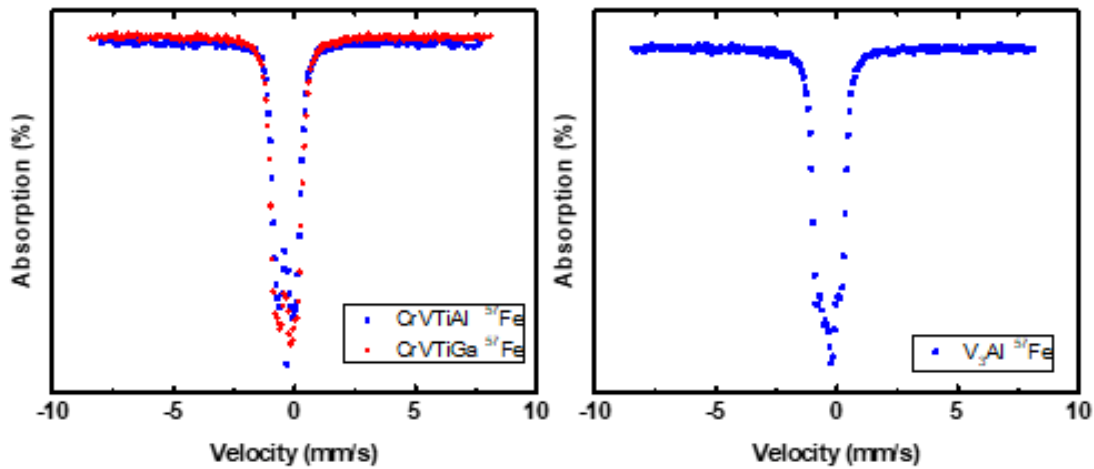
Fig. 5.7. ^{57}Fe Mössbauer spectra of 1 wt. % iron impurities in a) CrVTiAl and CrVTiGa and b) V$_3$Al.

5.2.3 Analysis and comparison electronic structure calculation

The antiferromagnetic order in this 18-electron system is expected with chemically-identical sublattices as a fully compensated ferrimagnetic half-metal at a specific

---

[10] The Mössbauer experiments were conducted by Prof. Plamen Stamenov.

compensation temperature, T_{comp} = 0 K [34]. The compensation temperature dependence relevant to the sublattice magnetizations varies with distinct exchange interactions of crystallographic sublattices, which is analogues to thin films of the 21-electron Heusler half-metal $Mn_2Ru_{0.5}Ga$ [35-37] with a compensation at T = 0 K while a nonzero net moment at other temperatures. The 24-electron bulk Heusler $Mn_{1.5}V_{0.5}FeAl$ behaves similarly [36]. However, none of the binary V_3X or quaternary CrVTiX alloys exhibit spontaneous magnetization at any temperature.

According to the DFT calculations[11] (Appendix I), electronic structures of the binary and quaternary alloys exhibit its half-metallic or semi-conductive character (see Fig. 5.2) as we expected. We start with the 18-electron binary V_3X (X = B, Al, Ga and In) with $D0_3$ order. The calculations have shown that the equivalent antiparallel spins at V1 atoms (4c site) and V2 atoms (4d site), leading to zero net moment, and each atom with magnetic moments of 1.4 -1.7 μ_B, whilst there is no magnetic moment on V2 (4b site). The details of the magnetic moments can be seen in Appendix II. Therefore, the electronic structures of V_3X indicate that the ordered $D0_3$ alloys are predicted to be antiferromagnetic semiconductors due to a symmetrical electronic structure in respect to spin-up and spin-down channels (Fig. 5.8).

---

[11]   DFT calculations were carried out by Zsolt Gercsi.
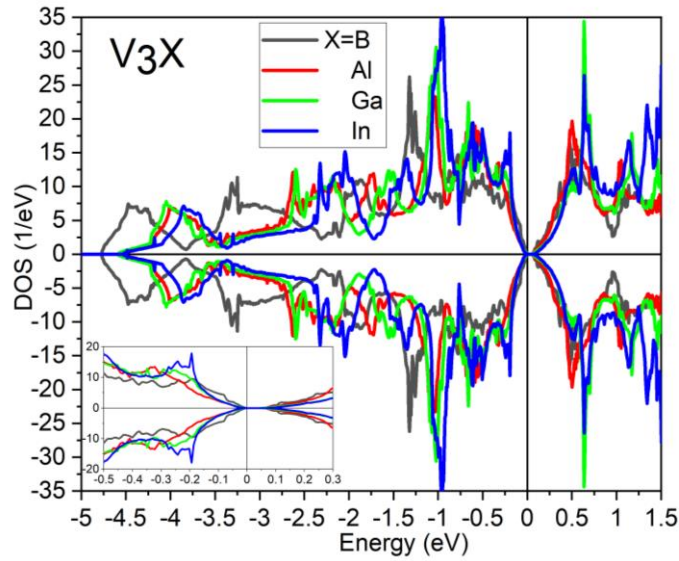
Fig. 5.8. Calculated densities of states for the 18-electron antiferromagnetic D0$_3$-type V$_3$X binary alloys with different Group 13 elements (B, Al, Ga, In).

However, the calculated D0$_3$ ordered binaries manifests little benefits for spintronic applications. Further alloying elements are needed to transform the D0$_3$-type order into a possible XA- or Y-type atomic arrangement by partial replacement of V. This approach could produce a ferrimagnetic spin structure with asymmetric spin states at the Fermi level, as predicted for CrVTiAl [17, 24, 25], which also retains the balance of 18 electrons and zero net magnetic moment.

There are three possible variants in CrVTiX and the corresponding energies as a function of lattice parameter (Fig. 5.9) indicate that the ferrimagnetic variant III is more favourable except CrVTiB. Although the ferrimagnetic alloys could be realized [17], the practical difficulties to achieve fully ordered single-variant quaternary ones from the melt seem insuperable. The close vicinity in energy of variants I, II and III, some of them differing in energy by less than 25 meV (k$_B T$ at ambient temperature), suggests that a disordered high-entropy alloy prefer to form rather than an ordered phase [38]. There is little benefit from mixing magnetic and non-magnetic atoms together in terms of useful magnetic functionality.
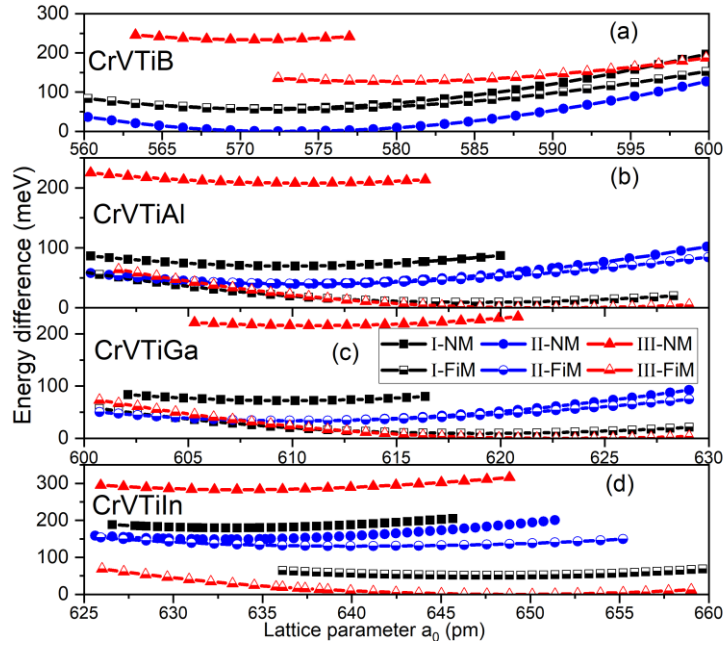
Fig. 5.9. Energies of the three variants (I, II, III) of the quaternary CrVTiX alloys, as a function of lattice parameter distinguishing ferrimagnetic and nonmagnetic solutions.

Unfortunately, none of these ordered phases that we have discussed are thermodynamically stable. Furthermore, all DFT calculations indicate that the ordered phase is not ever stable in the ground state. It is noted that the disorder is going to destroy the spin gap and magnetic order, which is the exactly same as what we find in our experiments.

We then use the hull distance to check the phase's stability. The hull distance ΔE_{hull} is equal to the difference between the formation energy and hull energy. And here, the hull describes the energy surface in compositional space with all the more stable alloys. When the ΔE_{hull} is zero, the stable phase is lying on the convex hull. When the ΔE_{hull} is negative, that means the new phase is below the hull, the new hull will be re-established. Therefore, the new stable phase is on the new hull. While the ΔE_{hull} is positive, the new phase will be above the hull. Then it is potentially unstable and could decompose into a combination of more stable compounds lying on the hull. Our quaternary Heusler alloys all tend to decompose into phase mixtures due to the positive Hull distance (Table 5.4). That means when the energy distance from the convex energy curve in compositional space connecting

the most stable mixtures of phases are less than 50 - 100 meV/atom, the phase may not form in practice. Our experiments are fully consistent with this prediction.

Table 5.4. Calculated electronic states of Y- type variants in CrVTiX compounds, together with the hull distance of the most stable variant.

CrVTiX	I	II	III	Stable phases	Hull distance (eV/atom)
B	Metallic	NM/ Metallic	SGS	$TiB+V_3B_2+TiCr_2+Ti$	-0.465 (Y–III)
Al	HM	Metallic	SGS	TiAl+VCr	-0.114 (Y–III)
Ga	HM	Metallic	SGS	TiGa+VCr	-0.125 (Y–III)
In	HM	Metallic	SGS	TiIn+VCr	-0.238 (Y–III)

5.2.4 Conclusion

Our work emphasizes that we need to be more cautious when attempting to make the real bulk materials in practice and built a relationship with the results of DFT calculations. The calculations predict that the four idealized D03-ordered binary vanadium phases can be antiferromagnetic gapless semiconductors with nonmagnetic vanadium on 4b sites. However, low-energy antisite defects eliminate the semiconductivity and tend to destroy the magnetism. In the case of the Y-phase quaternary alloys, differently-ordered variants with or without magnetic order are calculated to differ in energy by such a small amount, ~ 50 meV. And further, the high entropy of the disordered alloys contributes to the atomic disorder. Moreover, a fully-ordered D03 binary or any Y-type quaternary variant is never the most stable solution for any of these compounds according to the hull energy.

Our experimental study establishes that the single-phase 18-electron binary Heusler alloys with A2 order and the quaternaries with partial B2-type order in the as-cast state after arc melting all behave like the Pauli paramagnetic metals. The prolonged annealing process

does not improve their atomic order at all. The quaternary alloys prefer to disproportionate irreversibly into two stable cubic phase mixtures, as predicted thermodynamically.

Therefore, theoretical claims for the discovery of new ternary and higher intermetallic phases with outstanding physical properties should be critically screened for stability. Then, lengthy discussions of magnetic order and electronic structure of phases would be avoided, as well as misidentifications of small, irreversible features in the temperature-dependent susceptibility as Néel points. The opportunities for Fermi-level engineering and stabilizing unusual electronic or magnetic structures are wider for thin films with a surface on a substrate than they are for bulk crystalline materials. So we might have a chance to obtain highly ordered Heusler alloys in thin-film.

5.3 Tailoring the magnetism of vanadium by crystallographic ordering in Fe-V alloys

5.3.1 Introduction

Generally, the magnetic $3d$ elements are considered to be Cr, Mn, Fe, Co and Ni.   The light $3d$ transition element vanadium is usually nonmagnetic, and even exhibits superconductivity in some of its alloys (V_3Ga [39], CsV_3Sb_5 [40], V_3Si [41], ZrV_2 [42]). However, in contrast with a common understanding, vanadium does sometimes exhibit ferromagnetism [43] and antiferromagnetism in its alloys [39]. The conditions for obtaining nonmagnetic or magnetic vanadium are still debated.

$3d$ vanadium in $Fe_{1-x}V_x$ was predicted to be nonmagnetic for the disordered A2 structure but magnetic for the ordered B2 structure. Although DFT calculations [44-46] predicted V to be antiferromagnetic, experimental techniques, including neutron scattering, Mössbauer spectroscopy and nuclear magnetic resonance spectroscopy [47], do not support this predicted magnetism in both chemically ordered and disordered alloys. This inconsistency between the experiments and calculations calls for further investigation of the $Fe_{1-x}V_x$ system.

The literature suggests that the itinerant elements, such as Rh [48], Pt [49] and Pd [50], can be either nonmagnetic or magnetic. The changes in magnetic moments and transition temperatures from the disordered to the ordered phase[12] are summarized in Fig. 5.10a and b. Crystallographic ordering is the key to the magnetism of the itinerant elements. However, to obtain magnetic vanadium controlled by its local environments in $Fe_{1-x}V_x$ is a challenging task and as far as we know no progress has been reported in this direction.

Thus, we investigate the magnetism of V in ordered (B2) and disordered (A2) $Fe_{1-x}V_x$ alloys and discuss the influence of the local environment on magnetism. The findings related to the magnetization and the Curie temperature for different x and degrees of atomic ordering. Extending the analysis to other itinerant magnets containing V or other weakly-polarized transition elements, exhibiting tunable magnetism (pale green boxes in the periodic table, Fig. 5.10c), reveals the relationship between magnetism and local coordination.

---

[12] The details of dopants' magnetic moments and transition temperatures in disordered and ordered phases are listed in Tables 5.5 and 5.6 of Appendix III.
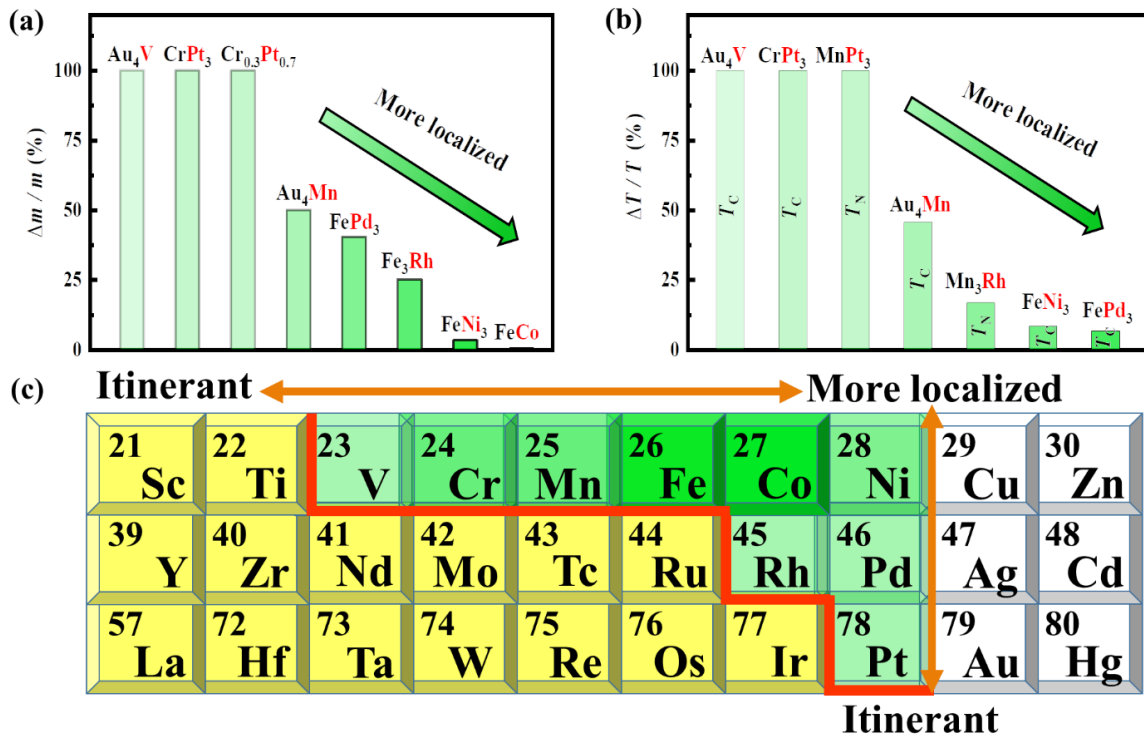
Fig. 5.10. (a) The bar graphs show the relative difference of magnetic moments of an itinerant transition metal alloy element (red) in its ordered and disordered states. V and Pt completely lose their magnetism in the disordered state. (b) The difference of magnetic ordering temperatures in ordered and disordered atomic structures. Elements with the most localized moments (Fe and Co) are the least sensitive to change in local environments. (c) Periodic table of transition elements. The elements in the pale green boxes can be either itinerant magnetic or nonmagnetic based on the local environments in their alloys. Elements in the yellow and white boxes are Pauli paramagnetic and diamagnetic, respectively.

5.3.2 Experiments

$Fe_{1-x}V_x$ (x = 0.25, 0.33, 0.4, 0.5, 0.6, 0.67, 0.75) polycrystalline ingots were synthesized by arc-melting high-purity iron (99.99%) and vanadium (99.95%) under high purity Ar atmosphere. In order to make the as-cast samples more homogenous, the arc-melting was repeated four times. The buttons were sealed under vacuum into a quartz tube and annealed at 500°C for a week before quenching into an ice-water mixture. The structures were characterized with an X-ray diffractometer using $CuK\alpha$ radiation (λ = 1.5405 Å). The

magnetization measurements were carried out by using the 5 T superconducting quantum interference device (SQUID) magnetometer.

5.3.3 Results

I. Crystal structure

X-ray diffraction patterns were obtained at room temperature for the series of $Fe_{1-x}V_x$ ($x = 0.25 – 0.75$) alloys both in as-cast (Fig. 5.11a) and annealed (Fig. 5.11b) states. The lattice constant for the as-cast samples in the disordered A2 phase changes from 2.91 Å to 2.97 Å as x increases from 0.25 to 0.75 due to the larger atomic radius of V than that of Fe. The lattice constant changes linearly with composition (red) following Vegard's law as shown in Fig. 5.11c. Whereas, after annealing at 500°C, the lattice constant increases nonlinearly from 2.91 Å to 2.96 Å with x = 0.33 to 0.67 (see blue line in Fig. 5.11c), because of the crystallographic ordering. It is extremely difficult to see the superlattice peak (001) of B2 phase (*CsCl*-type) in a traditional XRD pattern, even at high angles, due to the similar atomic scattering factors of Fe and V [45]. The existence of at least partial B2 ordering after annealing at low temperature can be inferred from the decrease of lattice constant deduced from the shifts of the (110) bcc Bragg peak towards higher 2θ angles [51]. This is most distinct for x = 0.5 where the reduction of the lattice constant ($\sim$ 2.91 Å) due to B2 ordering is as high as 0.7% in agreement with a previous report [52]. The similar trend is observed in annealed alloys with $x = 0.4$ and 0.6.
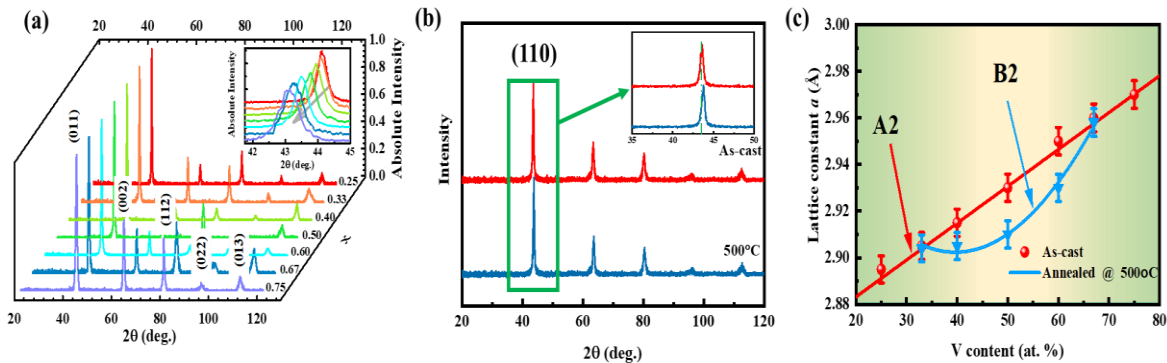
Fig. 5.11. The x-ray diffraction patterns of (a) as-cast $Fe_{1-x}V_x$ alloys (inset, the zoom-in diffraction peaks of (110)) and (b) Comparison of x-ray diffractions for as-cast and annealed (500°C) $Fe_{0.5}V_{0.5}$. The pattern for the annealed alloy shifts toward higher 2θ angles. The inset shows the zoom-in of the (110) diffraction peak. (c) The lattice constant as a function of x both in the as-cast and 500°C annealed $Fe_{1-x}V_x$ alloys.

II.   Magnetic properties

Crystallographic ordering gives rise to different magnetic properties of $Fe_{1-x}V_x$ in A2 and B2 structures. Fig. 5.12a presents the thermo-magnetization scans of $Fe_{0.5}V_{0.5}$ (A2 and B2) and the fits using the mean-field method [28]. The fitted moments in the B2 structure, 1.12 and 0.37 μ_B for Fe and V (antiparallel to Fe) respectively, agree with previous work [45]. The T_C for $Fe_{0.5}V_{0.5}$ decreases from 480 K (A2) to 350 K (B2), due to weakening of the ferromagnetic interactions by antiferromagnetically coupled V. The influence of crystallographic ordering is weaker but also observable in $Fe_{0.6}V_{0.4}$, which is located at the A2/B2 phase boundary, and there are distinctive differences of initial slopes of m_{av}(T) curves (m_{av}, average atomic magnetization), shown in Fig. 5.12b. The m_{av} of as-cast alloys decreases with increasing temperature. However, m_{av} for the annealed alloy rises with increasing temperature below 60 K ($T/T_C < 0.1$), showing ferrimagnetic-like behavior. This is quite unusual, because the initial slope of M(T) curve in the mean-field model is normally zero for a common ferrimagnet like yttrium iron garnet [53]. The behavior indicates that V gradually and reversibly loses its magnetism on heating rather than simply becoming

magnetically disordered for this composition lying at the A2/B2 phase boundary.
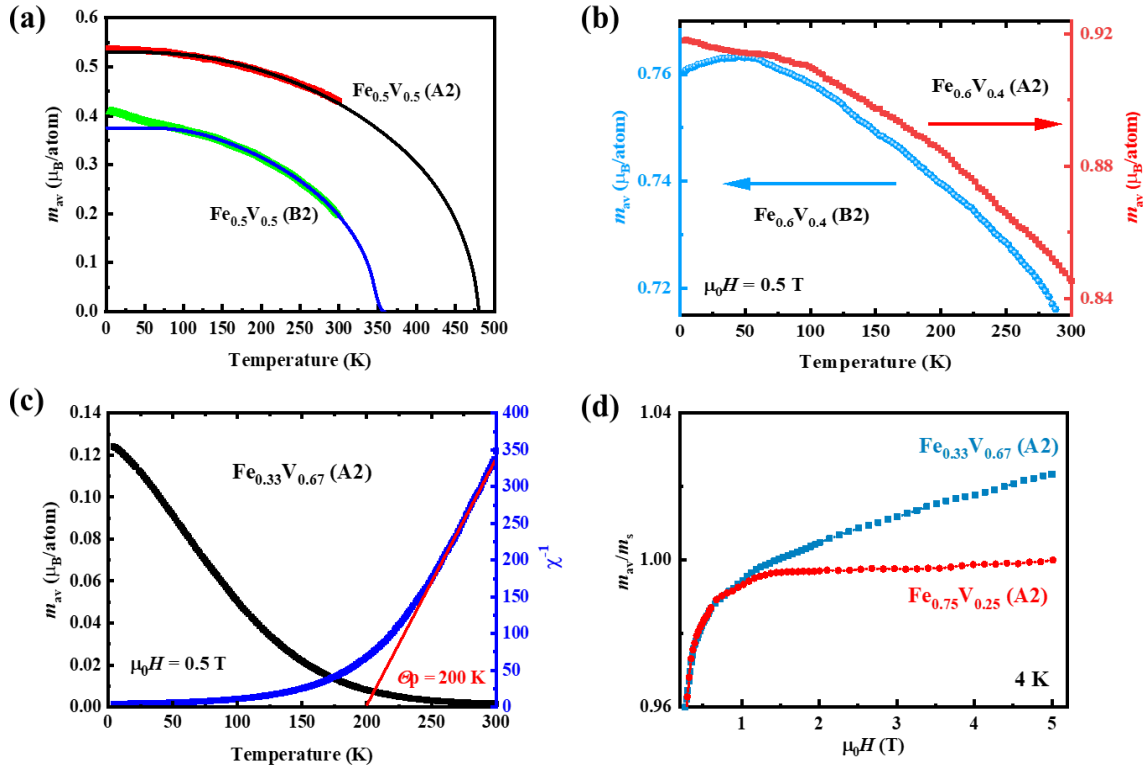
Fig. 5.12. (a) Thermal scans of saturation magnetization of $Fe_{0.5}V_{0.5}$ in A2 (red line) and B2 (green line) ordered structures with mean-field model fits (black for A2 and blue for B2). The drop in magnetization in B2 phase below 50 K is due to a trace of the weakly-magnetic σ phase. (b) The shape of the $m_{av}(T)$ curve at low temperature indicates that B2 $Fe_{0.6}V_{0.4}$ (light blue line) is ferrimagnetic, which is unlike the as-cast A2 alloy (red line) at low temperature. The magnetization first increases and then decreases on heating. The induced moment on V gradually disappears during heating, for this composition near the A2/B2 boundary. (c) The $m_{av}(T)$ curve and inverse susceptibility of $Fe_{0.33}V_{0.67}$. The positive θ_p (200 K) verifies the ferromagnetism. (d) The m_{av}/m_s curves of $Fe_{0.75}V_{0.25}$ (A2) and $Fe_{0.33}V_{0.67}$ (A2). The saturation magnetizations of the two alloys are 1.4 and 0.12 μ_B/atom, respectively.

Unlike V, the significant influence on the Fe moment is the alloy composition rather than crystallographic ordering. When x increases to 0.67, the thermal magnetization does

not behave like a typical ferromagnet with a fast drop of magnetization at T_C (Fig. 5.12c), although the ferromagnetism is confirmed by a positive paramagnetic Curie temperature θ_p of 200 K deduced by fitting the inverse susceptibility in the paramagnetic state. This fitting gives an effective paramagnetic moment $m_{eff} = 2.3$ μ_B for $Fe_{0.33}V_{0.67}$. According to the Rhodes-Wohlfarth plot of the ratio m_c/m_s versus Curie temperature, where $m_c = (1 + m_{eff}^2)^{1/2} - 1$ and m_s is the saturation moment in Bohr magnetons, the large ratio $m_c/m_s = 3.2$ indicates that $Fe_{0.33}V_{0.67}$ is an itinerant ferromagnet [54]. Compared with the Fe-rich alloys, such as $Fe_{0.75}V_{0.25}$, the thermal scan and field-induced magnetization of this V-rich composition (Fig. 5.12d) illustrate that Fe is only weakly magnetic in the V-rich region. The above results suggest that the increased number of V neighbors of Fe is the main factor that weakens its magnetism.

Fig. 5.13a summarizes the average atomic moment m_{av} as a function of x in the A2 and B2 phases, respectively. For the A2 disordered alloys, m_{av} at 4 K *linearly* drops from 1.1 μ_B/atom ($x = 0.25$) to nearly zero ($x = 0.75$). This linear trend is as same as that found for Ni with nonmagnetic Cu neighbours [28]. However, in the B2 ordered phase, m_{av} decreases nonlinearly from 0.99 μ_B/atom ($x = 0.33$) to 0.12 μ_B/atom ($x = 0.67$), following a similar trend to the lattice constant. This nonlinear dependence is similar to that of Fe with ferromagnetic Co neighbours and Ni with antiferromagnetic Mn neighbours [28] (Fig. 5.13a).

The maximum and minimum Curie temperatures T_C are found in $Fe_{0.75}V_{0.25}$ (1025 K) and $Fe_{0.25}V_{0.75}$ (45 K) with disordered structures, respectively (Fig. 5.13b). T_C for the B2 phase is always lower than that for disordered A2 phase with the same composition. The maximum difference appears for alloys with $x = 0.5$, which exhibit T_C of 350 K for B2 and 480 K for A2. This result indicates the different roles that V plays in magnetism, based on ordering. In disordered A2, V is confirmed to be nonmagnetic by both theoretical and experimental studies when x > 25 at. % [47, 55, 56]. The linear Curie temperature dependence is similar to those found for Ni-Cu [57] and Co-Zn [58] (Fig. 5.13b), with a

nonmagnetic element (Cu or Zn) partly replacing the ferromagnetic host (Ni or Co) to weaken the exchange interactions by decreasing the number of nearest magnetic neighbors. However, in ordered B2 alloys, V is antiferromagnetically coupled to Fe, decreasing the net moment and T_C nonlinearly, which is also observed for T_C or T_N in other alloys with a magnetic dopant, such as Co-Pt [59] and Fe-Cr [60].
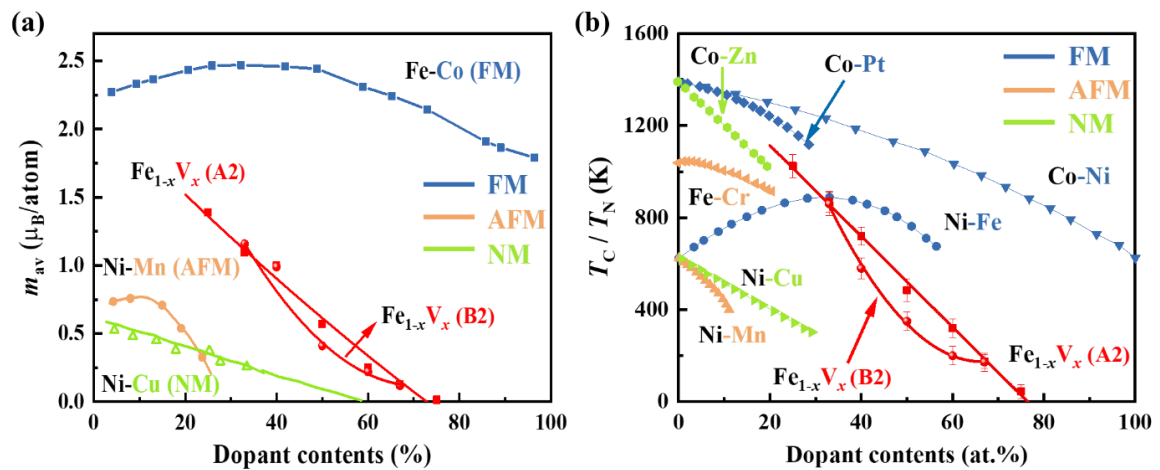
Fig. 5.13. (a) Average atomic moment m_{av} and (b) the magnetic transition temperatures (T_C or T_N) of $Fe_{1-x}V_x$ alloys with varying x. Non-linear behaviour appears in the B2 structure, and other alloys of Fe, Co and Ni with ferromagnetic, antiferromagnetic or nonmagnetic elements [28, 57- 60]. The magnetism of the elements is distinguished by the different colours.

5.3.4 Discussions

I.   Relationship between bond length and magnetism of V

$3d$ elemental iron in Fe-V alloys is always ferromagnetic when $x < 0.75$ regardless of atomic ordering, while the interaction for the itinerant V is sensitive to its bond length. Fig. 5.14a describes the magnetism variations with the bond length d between V nearest neighbours. The details of the associated materials are listed in Table 5.7 of Appendix III. Generally, the shortest V - V bonds (< 2.9 Å) are nonmagnetic; the longest bonds (> 3.8 Å) are ferromagnetic and the bonds of $2.9 – 3.8$ Å behave antiferromagnetically. Taking Au_4V as an example, disordered Au_4V with $d = 2.7$ Å is nonmagnetic, while the ordered phase

with $d = 4.96$ Å is ferromagnetic [43]. A similar trend can be seen for Cr and Mn (Fig. 5.16 in the Appendix III). Details of Cr-based and Mn-based materials are listed in Table 5.8 and 5.9 of Appendix III. Cr-Cr bond lengths less than 2.5 Å or greater than 3.44 Å are nonmagnetic or ferromagnetic, respectively, while Mn-Mn bonds are nonmagnetic when d < 2.43 Å and ferromagnetic when d > 2.83 Å. The magnetic phase is determined by the shortest bond length for V, Cr and Mn, as shown in Fig. 5.14b. In the A2 phase, the shortest bond length of V is ~ 2.53 Å, corresponding to a nonmagnetic structure, and the magnetism only arises from ferromagnetic interactions between Fe atoms. After annealing, the V-V bond length in $Fe_{0.5}V_{0.5}$ with B2 ordering (~ 2.91 Å) corresponds to antiferromagnetic V-V bonds. Compared to the disordered state, additional antiferromagnetic exchange between Fe and V must be taken into account because V possesses a moment in the B2 ordered alloy. The interaction with Fe weakens magnetization and lowers T_C.
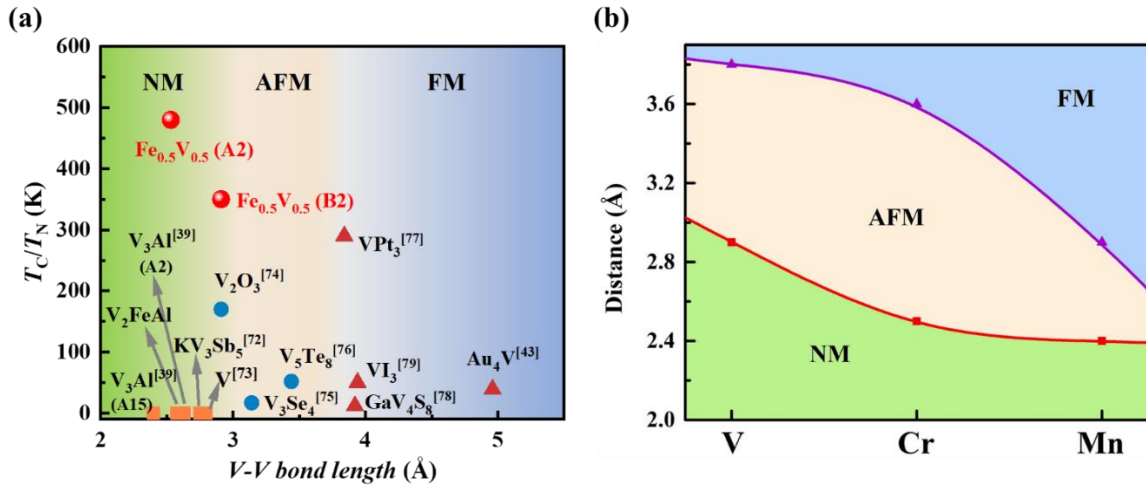
Fig. 5.14. (a) Magnetic transition temperatures (T_C or T_N) as a function of V-V bond lengths in the V-based materials. Note that, V-V bond lengths of 2.53 Å and 2.91 A are deduced in non-magnetic V sites (A2) and antiferromagnetic V sites (B2) respectively in $Fe_{0.5}V_{0.5}$. (b) A magnetic phase diagram based on the nearest neighbour bond length for the light $3d$ elements V, Cr and Mn.

II.   Composition-dependent moment and T_C

Vanadium is less electronegative than iron, therefore electrons are transferred from V to Fe, increasing the d band occupancy and decreasing the Fe moment. Assuming each V donates c electrons to Fe in A2 $Fe_{1-x}V_x$ alloys, each Fe atom obtains $cx/(1 - x)$ electrons and its magnetic moment is roughly $(m_0 - cx/(1 - x))$ μ_B/Fe, where m_0 is the magnetic moment of Fe before charge transfer. The total magnetic moment for A2 $Fe_{1-x}V_x$ can be expressed as

$$m = (m_0 - cx/(1 - x))\,(1 - x) = m_0 - (c + m_0)x \tag{5.1}$$

In Eq. 5.1, m decreases linearly with x. By fitting the magnetization vs. x in Fig. 5.13a, m_0 is found to be 2.07 μ_B, close to the value for metallic Fe of 2.2 μ_B and the charge transfer number c is 0.9. In the B2 structure, the additional contribution of V modifies Eq. 5.1 to

$$m = m_0 - (c + m_0)x - m'x \tag{5.2}$$

where m' is the magnetic moment per V. Since m' is a function of x (in B2, m' increases from 0 for $x = 0.4$, to 0.36 μ_B for $x = 0.5$, and finally drops back to 0 for $x = 0.6$), m decreases nonlinearly with x in Fig. 5.13a.

The trends of T_C for A2 and B2 $Fe_{1-x}V_x$ alloys as a function of x are similar to those of magnetization for the following reason. The Curie temperature is proportional to the exchange interaction J [28]. Fe has 8 nearest-neighbour (NN) and 6 next-nearest-neighbour (NNN) in A2. Therefore, in A2 $Fe_{1-x}V_x$ the total exchange interaction, also the exchange of Fe sublattice, can be expressed as

$$J_{tot} = J_{Fe\text{-}Fe} = 8J_{NN}(1 - x) + 6J_{NNN}(1 - x) \tag{5.3}$$

Eq. 5.3 gives a linear relationship between composition x and total exchange, suggesting that T_C is linear with x, as shown in Fig. 5.13b. In B2, total interactions of the ordered alloy include three components, one ferromagnetic exchange interaction from Fe to Fe and two antiferromagnetic interactions associated with V. For example, in B2 $Fe_{0.5}V_{0.5}$, Fe has 4 NN (V) and 6 NNN (Fe), and V has 8 NN (Fe) and 6 NNN (V). However, the antiferromagnetic V - V exchange may be neglected because a bond length of 2.91 Å sits at the nonmagnetic/antiferromagnetic boundary. Therefore, the exchange interaction between

magnetic V and Fe is the dominant factor explaining the offset from the linear trend in Fig 5.13b, because J_{FeV} is most significant when $x \sim 0.5$.

III.   Band structure

Based on above analysis of the local environment and magnetic moment, the schematic band structures of the A2 and B2 variants of $Fe_{0.5}V_{0.5}$ are summarized in Fig. 5.15. The magnetic moment of Fe with a $\sim 3d^9$ configuration is ~ 1 μ_B for both structures, taking into account the charge transfer with $c \sim 0.9$ from V, deduced from the fit of Eq. 5.1 to the data. In the A2 structure, the crystal field splitting of $3d$-orbitals of Fe in the two coordination, octahedral and cubic (see Fig. 5.15a), leads to hybridized t_{2g} and e_g bands. There is no band splitting for nonmagnetic V. In the B2 structure, the coordination of $3d$-orbitals of Fe and V are octahedral and cubic, respectively (see Fig. 5.15b). The different local environments of V and Fe cause a different crystal field splitting for e_g and t_{2g} bands: The e_g energy is greater than that of t_{2g} band for Fe, while for V the e_g band lies below the t_{2g}. The antiparallel coupling of the Fe and V moments gives a ferrimagnetic structure, with more occupied orbitals in spin-up channel of V and the spin-down channel Fe.
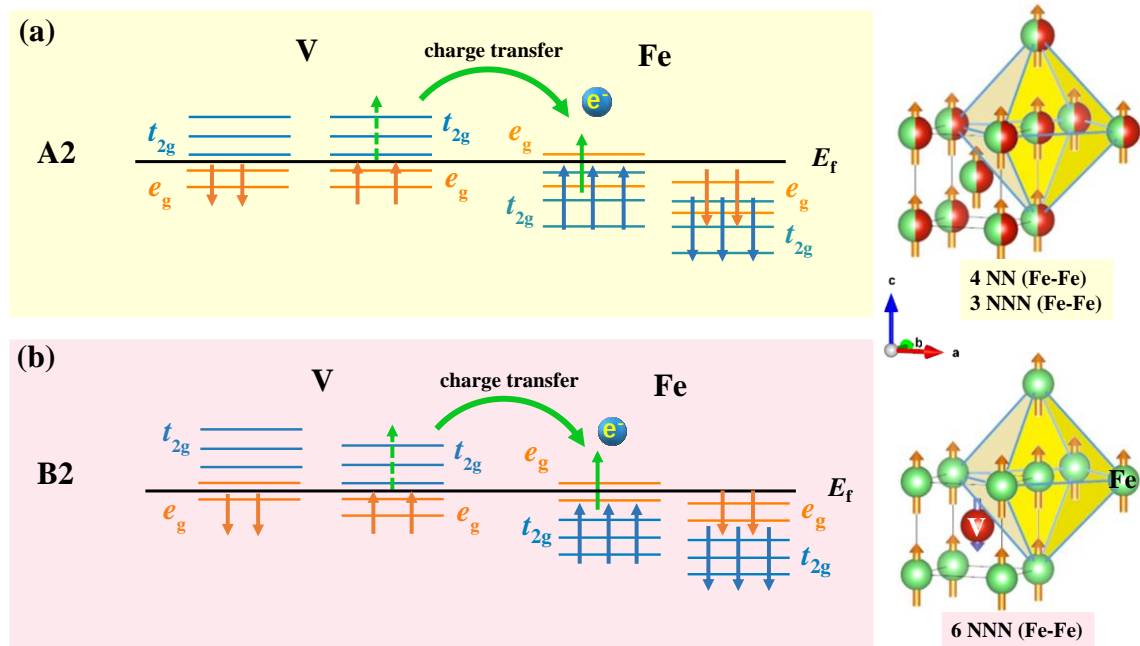
Fig. 5.15. The schematic band structure of $Fe_{0.5}V_{0.5}$ in A2 (a) and B2 (b) structures. In the A2 structure, the 8 NN and 6 NNN of Fe form a cubic and an octahedral coordination polyhedron respectively, among which half are magnetic elements. With charge transfer, Fe has a $\sim 3d^9$ atomic configuration with a magnetic moment of ~ 1 μ_B. In the B2 structure, the coordination of Fe and V are cubic and octahedral, respectively. There are more occupied orbitals in spin-up channel of V and spin-down in Fe, leading to ferrimagnetism.

5.3.5 Conclusion

In summary, our study reveals the behaviour of the individual atomic magnetic moments of $Fe_{1-x}V_x$ alloys in the ordered (B2) and disordered (A2) bcc structures. The as-cast alloys have an A2 structure, while annealing leads to a partially-ordered B2 structure. The magnetism of Fe is determined by the number of Fe neighbours which dominates the ferromagnetic interactions in the A2 as well as in the B2 structure. The magnetism of V is sensitive to the bond length, which varies with atomic ordering. The linear dependences of magnetization as well as T_C as a function of V concentration for A2 alloys (V > 25 at. %) indicate that V is nonmagnetic ($d < 2.9$ Å), while the nonlinear dependences for B2 alloys indicate that V has developed a moment that is antiferromagnetically coupled (2.9 Å < d <

3.8 Å) with the moment of Fe. The additional V – Fe exchange interaction due to the magnetic moments carried on V is responsible for the distinctive changes of its magnetic properties, including magnetization and T_C. Based on our study of the $Fe_{1-x}V_x$ system, it is noteworthy that elements sitting on the borderline between the itinerant and localized regions (pale green boxes in Fig. 5.10c) may change their magnetism when the bond length is changed, even slightly. The tuneable magnetic moment of weakly-polarized elements provides a method to develop new magnetic materials.

5.4 Summary

We did not succeed in making a Mn-free ferrimagnetic half metal, which was our original objective, although the DFT calculations indicate that the idealized $D0_3$-ordered binary vanadium phases or extended Y-type quaternaries should have formed ferrimagnetic half metals or spin-gapless semiconductors. Low-energy antisite defects eliminate semiconductivity (in V_3Al) and also tend to destroy the magnetism. That means a fully-ordered $D0_3$ binary or any Y-type quaternary variant is never the most stable solution for *any* of these compounds, which is verified by the Hull energy. Therefore, future claims based on theoretical calculations for discovery of ternary, and especially higher intermetallic alloys, with brilliant physical properties must make clear on the composition stability of the phases to avoid lengthy discussion of magnetic order and electronic band structures, as well as misidentification of small, irreversible features in the temperature-dependent susceptibility as Néel points. While disorder may improve the mechanical properties, it is inimical to collective magnetic order, which depends sensitively on local atomic arrangements and unusual structure in the electronic density of states. Growth methods that avoid the melt, such as physical or chemical deposition on a substrate might run a better chance of success. The opportunities for Fermi-level engineering and stabilizing unusual electronic or magnetic structures are wider for thin films with a surface on a substrate than they are for bulk crystalline materials. It is as thin films that new electronic materials are likely to be applied.

On the other hand, light itinerant elements in alloys provide a chance to obtain Mn-free ferrimagnets, through control of the crystallographic ordering. Our investigation of the V magnetism of bcc $Fe_{1-x}V_x$ alloys in different ordered states reveals that the magnetism at V site is determined by the bond length (see Fig. 5.14a). In B2 ordered $Fe_{0.5}V_{0.5}$, ferrimagnetism is realized due to the antiparallel alignment of Fe and V moments. Further, we find that itinerant alloys including of weakly-polarized transition elements like Pt, Rh and Pd, display similar magnetic properties based on crystallographic and atomic order. Therefore, the tuneable magnetic moment of weakly-polarized elements provides a method to develop new ferrimagnetic materials.

5.5 Acknowledgement

Appendices

Appendix I. DFT calculations method

Ab-initio calculations based on DFT calculations were carried out using norm-conserving pseudopotentials and pseudo-atomic localized basis functions as implemented in the OPENMX software package [61]. The Y-type ordered calculations were based on a minimal 4-atom basis cell of the Heusler structure using $15\times15\times15$ k-points to evaluate the total energies. The conventional 16-atom basis cell was used for the investigation of antisite (V-X) swapping in the binary V_3X alloys. Pre-generated fully relativistic pseudopotentials and the pseudo-atomic orbitals with a cut-off radius of 7 atomic units (au) were used with $s^2p^2d^2$ for the metal and $s^2p^2d^1$ basis orbitals for the group 13 metalloid elements with an energy cut-off of 220 Ry (3 keV) for the numerical integrations. The convergence criterion for the energy minimisation procedure was set to 10^{-8} Hartree (4 µeV). Spin-orbit interaction (SOI) was not considered in the calculations. The reason is that SOI is only a small perturbation to the electronic structure in case of 3d-orbitals in high symmetry crystal field (cubic), typically do not yield significant SOI. Here we are interested in the total magnetization and the fermi level spin polarisation. These conditions were tested on other previously-reported full Heusler alloys, and excellent reproducibility was confirmed. The plotted densities of states (DOS) were evaluated on a denser ($19\times19\times19$) k-grid for more detail.

Appendix II. Magnetic moments of V in D0₃-type V₃X (X= B, Al, Ga, In)

	a_0 (Å)	m_{v4b}/m_{total} (μB)	Band structure	$m_{v8c\text{-}total}$ (μB)	Band structure	Stable phase	Hull distance (eV/atom)
V₃B	5.71	0/0	Metallic/NM	0	Metallic/NM	V₃B₂ +V	0.486
V₃Al	6.12	1.10/0	Metallic/AFM	1.26	Metallic/FiM	AlV₂ +V	0.011
V₃Ga	6.13	1.2/0	Metallic/AFM	1.68	Metallic/FiM	V₃Ga (A15)	0.164
V₃In	6.36	2.03/0	Metallic/AFM	1.24	Metallic/FiM	In +V	0.218

AFM – Antiferromagnetic; FiM – Ferrimagnetic

Appendix III. Details of collected materials comparing with $Fe_{1-x}V_x$

Table 5.5. The magnetic moments on dopants of disordered (DO) and ordered (O) alloys. The dopants were underlined.

Material	Dopant moment[DO] (μB)	Dopant moment[O] (μB)	Reference
Au₄<u>V</u>	0	0.41	[43]
Cr<u>Pt</u>₃	0	-0.27	[62]
Cr₀.₃<u>Pt</u>₀.₇	0	-0.47	[49]
Au₄<u>Mn</u>	2	4	[43]
Fe<u>Pd</u>₃	0.34	0.57	[50]
Fe₃<u>Rh</u>	0.75	1	[48, 63]

Ni$_3$Fe	0.6	0.62	[64]
Fe<u>Co</u>	1.7	1.705	[65]

Table 5.6. Magnetic transition temperatures (T_C or T_N) in disordered (DO) and ordered (O) alloys. The dopants were underlined.

Material	T_C/T_N^{DO} (K)	T_C or T_N^O (K)	Reference
Au$_4$<u>V</u>	NM	39	[43]
Mn<u>Pt</u>$_3$	0	380	[66, 67]
Cr<u>Pt</u>$_3$	0	494	[68]
Au$_4$<u>Mn</u>	203	473	[43]
Mn$_3$<u>Rh</u>	700	840	[69]
<u>Ni</u>$_3$Fe	863	940	[70]
Fe<u>Pd</u>$_3$	476	499	[71]

Table 5.7. V-V bond length in V-based alloys with their magnetic transition temperatures (T_C or T_N). (NM < 2.9 Å; FM > 3.8 Å)

Material	V-V bond length (Å)	Magnetism	T_C or T_N (K)	Reference
Fe$_{0.5}$V$_{0.5}$(A2)	2.53	NM	480	This work
Fe$_{0.5}$V$_{0.5}$(B2)	2.91	AFM	350	This work
V$_3$Al (A15)	2.4	NM	0	[39]
V$_2$FeAl	2.57	NM	0	/
V$_3$Al (A2)	2.63	NM	0	[39]

KV_3Sb_5	2.75	NM	0	[72]
V	2.79	NM	0	[73]
V_2O_3	2.91	AFM	170	[74]
V_3Se_4	3.14	AFM	17	[75]
V_5Te_8	3.44	AFM	52	[76]
VPt_3	3.84	FM	290	[77]
GaV_4S_8	3.92	FM	12	[78]
VI_3	3.94	FM	50	[79]
Au_4V	4.96	FM	39	[43]
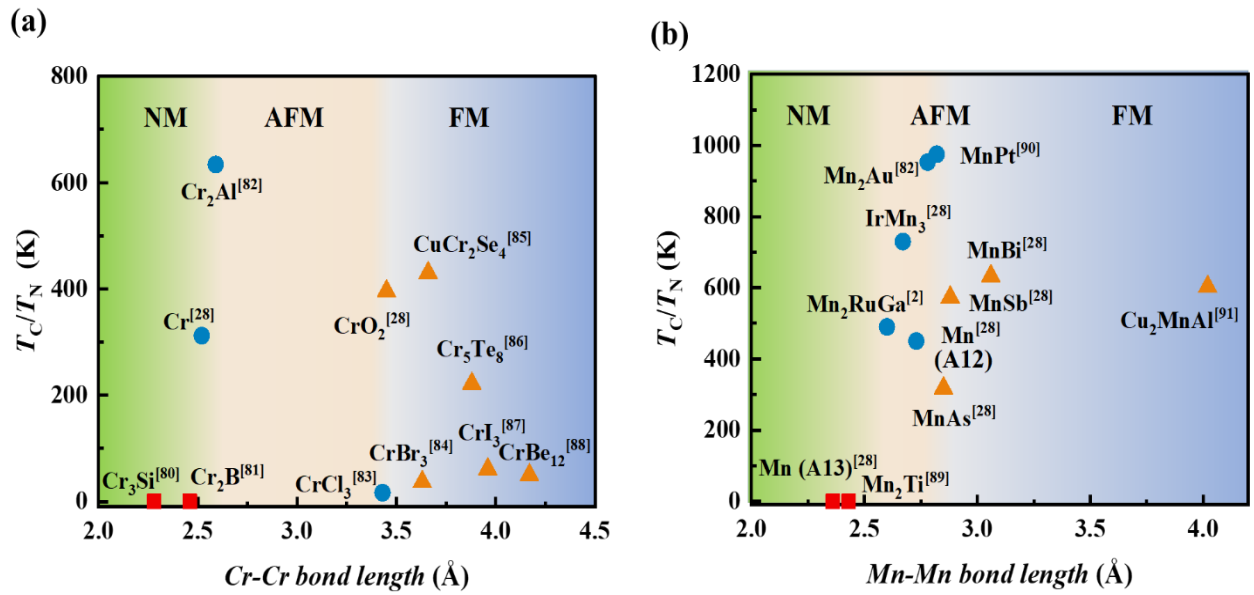
Fig. 5.16. The transition temperatures (T_C or T_N) as a function of (a) Cr-Cr and (b) Mn-Mn bond length in Cr-based and Mn-based alloys, respectively.

Table 5.8. Cr-Cr bond length in Cr-based alloys with their magnetic transition temperatures (T_C or T_N). (NM < 2.5 Å; FM > 3.44 Å)

Material	Cr-Cr bond length (Å)	Magnetism	T_C or T_N (K)	Reference
Cr_3Si	2.28	NM	0	[80]
Cr_2B	2.46	NM	0	[81]
Cr	2.52	AFM	312	[28]
Cr_2Al	2.59	AFM	634	[82]
$CrCl_3$	3.43	AFM	16.8	[83]
CrO_2	3.45	FM	396	[28]
$CrBr_3$	3.63	FM	37	[84]
$CuCr_2Se_4$	3.66	FM	430	[85]
Cr_5Te_8	3.88	FM	222	[86]
CrI_3	3.96	FM	61	[87]
$CrBe_{12}$	4.17	FM	50	[88]

Table 5.9. Mn-Mn bond length in Mn-based alloys with their magnetic transition temperatures (T_C or T_N). (NM < 2.43 Å; FM > 2.83 Å)

Material	Mn-Mn bond length (Å)	Magnetism	T_C or T_N (K)	Reference
Mn (A13)	2.36	NM	0	[28]
Mn_2Ti	2.43	NM	0	[89]
Mn_2RuGa	2.6	AFM	490	[2]

IrMn$_3$	2.67	AFM	730	[28]
Mn (A12)	2.73	AFM	450	[28]
Mn$_2$Au	2.78	AFM	953	[82]
MnPt	2.82	AFM	975	[90]
MnAs	2.85	FM	318	[28]
MnSb	2.88	FM	573	[28]
MnBi	3.06	FM	633	[28]
Cu$_2$MnAl	4.02	FM	603	[91]

References

[1] S. Ishdia, S. Fujii, S. Kashiwagi, S. Asano, Search for Half-metalic compounds in Co_2MnZ, Jouranl of the Physical Society of Japan **64**, 6, 2152 (1995).

[2] K. Siewierska G. Atcheson, A. Jha, K. Esien, R. Smith, S. Lenne, N. Teichert, J. O'Brien, J. M. D. Coey, P. Stamenov and K. Rode, Magnetic order and magnetotransport in half-metallic ferrimagnetic Mn_yRu_xGa thin films, Physical Review B **104**, 064414 (2021).

[3] G. Atcheson, K. Siewierska, J. M. D. Coey, K. Rode, and P. Stamenov, Stability of Mn_2Ru_xGa-based Multilayer Stacks, Thin Solid Films 139104 (2022).

[4] I. Galanakis, Ş. Tırpancı, K. Özdoğan, and E. Şaşıoğlu, Itinerant G-type antiferromagnetism in $D0_3$-type V_3Z (Z= Al, Ga, In) compounds: A first-principles study, Physical Review B **94**, 064401 (2016).

[5] Y. Venkateswara, S. Gupta, S. S. Samatham, M. R. Varma, K. Suresh, and A. Alam, Competing magnetic and spin-gapless semiconducting behavior in fully compensated ferrimagnetic CrVTiAl: Theory and experiment, Physical Review B **97**, 054407 (2018).

[6] S. Skaftouros, K. Özdoğan, E. Şaşıoğlu, and I. Galanakis, Generalized Slater-Pauling rule for the inverse Heusler compounds, Physical Review B **87**, 024420 (2013).

[7] C. Felser and A. E. Hirohata (Editor), *Heusler Alloys: Properties, Growth, Applications* (Springer, 2016).

[8] J. Ma, V. I. Hegde, K. Munira, Y. Xie, S. Keshavarz, D. T. Mildebrath, C. Wolverton, A. W. Ghosh, and W. H. Butler, Computational investigation of half-Heusler compounds for spintronics applications, Physical Review B **95**, 024411 (2017).

[9] J. Ma, J. He, D. Mazumdar, K. Munira, S. Keshavarz, T. Lovorn, C. Wolverton, A. W. Ghosh, and W. H. Butler, Computational investigation of inverse Heusler compounds for spintronics applications, Physical Review B **98**, 094410 (2018).

[10] F. Kuroda, T. Fukushima, and T. Oguchi, First-principles study of magnetism and phase stabilities of V_2-based antiferromagnetic Heusler alloys, Journal of Applied Physics **127**, 193904 (2020).

[11] S. Jiang and K. Yang, Review of High-throughput Computational Design of Heusler Alloys, Journal of Alloys and Compounds, 158854 (2021).

[12] V. D. Buchelnikov, V. V. Sokolovskiy, O. N. Miroshkina, D. R. Baigutlin, M. A. Zagrebin, B. Barbiellini, and E. Lähderanta, Prediction of a Heusler alloy with switchable metal-to-half-metal behavior, Physical Review B **103**, 054414 (2021).

[13] J. Balluff, K. Diekmann, G. Reiss, and M. Meinert, High-throughput screening for antiferromagnetic Heusler compounds using density functional theory, Physical Review Materials **1**, 034404 (2017).

[14] Q. Gao, I. Opahle, and H. Zhang, High-throughput screening for spin-gapless semiconductors in quaternary Heusler compounds, Physical Review Materials **3**, 024410 (2019).

[15] K. Özdoğan, E. Şaşıoğlu, and I. Galanakis, Slater-Pauling behavior in LiMgPdSn-type multifunctional quaternary Heusler materials: Half-metallicity, spin-gapless and magnetic semiconductors, Journal of Applied Physics **113**, 193903 (2013).

[16] X. Wang, Proposal for a new class of materials: spin gapless semiconductors, Physical Review Letters **100**, 156404 (2008).

[17] I. Galanakis, K. Özdoğan, and E. Şaşıoglu, High-T_C fully compensated ferrimagnetic semiconductors as spin-filter materials: the case of CrVXAl (X= Ti, Zr, Hf) Heusler compounds, Journal of Physics: Condensed Matter **26**, 379501 (2014).

[18] M. E. Jamer, B. Wilfong, V. D. Buchelnikov, V. V. Sokolovskiy, L. H. Lewis, A. Pulkkinen, B. Barbiellini, A. Bansil, and D. Heiman, Superconducting and antiferromagnetic properties of dual-phase V_3Ga, Applied Physics Letters **117**, 062401 (2020).

[19] L. Pendrys and D. Douglass, Superconductivity of V_3Al, Solid State Communications **18**, 177 (1976).

[20] G. Y. Gao and K.-L. Yao, Antiferromagnetic half-metals, gapless half-metals, and spin gapless semiconductors: The $D0_3$-type Heusler alloys, Applied Physics Letters **103**, 232409 (2013).

[21] M. E. Jamer, B. A. Assaf, G. E. Sterbinsky, D. Arena, L. H. Lewis, A. A. Saúl, G. Radtke, and D. Heiman, Antiferromagnetic phase of the gapless semiconductor V_3Al, Physical Review B **91**, 094409 (2015).

[22] G. M. Stephen, I. McDonald, B. Lejeune, L. H. Lewis, and D. Heiman, Synthesis of low-moment CrVTiAl: A potential room temperature spin filter, Applied Physics Letters **109**, 242401 (2016).

[23] Y. Qiu, Y. J. Hu, A. Taylor, M. J. Styles, R. K. W. Marceau, A. V. Ceguerra, M. A. Gibson, Z. K. Liu, H. L. Fraser, N. Birbilis, A lightweight single-phase AlTiVCr compositionally complex alloy, Acta Materialia **123**, 115 (2017).

[24] G. M. Stephen, G. Buda, M. E. Jamer, C. Lane, S. Kaprzyk, B. Barbiellini, D. Graf, L. H. Lewis, A. Bansil, D. Heimaz, Structural and electronic properties of the spin-filter material CrVTiAl with disorder, Journal of Applied Physics **125**, 123903 (2019).

[25] G. M. Stephen, C. Lane, G. Buda, D. Graf, S. Kaprzyk, B. Barbiellini, A. Bansil, and D. Heiman, Electrical and magnetic properties of thin films of the spin-filter material CrVTiAl, Physical Review B **99**, 224207 (2019).

[26] D. Betto, N. Thiyagarajah, Y.-C. Lau, C. Piamonteze, M.-A. Arrio, P. Stamenov, J. Coey, and K. Rode, Site-specific magnetism of half-metallic Mn_2Ru_xGa thin films determined by X-ray absorption spectroscopy, Physical Review B **91**, 094410 (2015).

[27] Y. Takamura, R. Nakane, and S. Sugahara, Analysis of $L2_1$-ordering in full-Heusler Co_2FeSi alloy thin films formed by rapid thermal annealing, Journal of Applied Physics **105**, 07B109 (2009).

[28] J. M. D. Coey, *Magnetism and Magnetic Materials* (Cambridge university press, 2010).

[29] B. Childs, W. Gardner, and J. Penfold, The magnetic susceptibility of vanadium between 20 and 293 K, Philosophical Magazine **4**, 1126 (1959).

[30] E. Fawcett, Spin-density-wave antiferromagnetism in chromium, Reviews of Modern Physics **60**, 209 (1988).

[31] B. G. Childs, W. E. Gardner, and J. Penfold, The magnetic susceptibility of vanadium-chromium solid solutions, Philosophical Magazine **5**, 1267 (1960).

[32] B. G. Childs, W. E. Gardner, and J. Penfold, The magnetic susceptibilities of vanadium-based solid solutions containing titanium, manganese, iron, cobalt and nickel, Philosophical Magazine **8**, 419 (1963).

[33] J. Emsley, *The Elements* (Oxford University Press, 1989).

[34] E. Şaşıoğlu, Nonzero macroscopic magnetization in half-metallic antiferromagnets at finite temperatures, Physical Review B **79**, 100406 (2009).

[35] H. Kurt, K. Rode, P. Stamenov, M. Venkatesan, Y.-C. Lau, E. Fonda, and J. M. D. Coey, Cubic Mn_2Ga thin films: Crossing the spin gap with Ruthenium, Physical Review Letters **112**, 027201 (2014).

[36] R. Stinshoff, A. K. Nayak, G. H. Fecher, B. Balke, S. Ouardi, Y. Skourski, T. Nakamura, and C. Felser, Completely compensated ferrimagnetism and sublattice spin crossing in the half-metallic Heusler compound $Mn_{1.5}FeV_{0.5}Al$, Physical Review B **95**, 060410 (2017).

[37] K. Siewierska, G. Atcheson, A. Jha, K. Esien, R. Smith, S. Lenne, N. Teichert, J. O'Brien, and P. Stamenov, Fermi level engineering in Mn_2Ru_xGa thin films by the variation of Mn and Ru content, arXiv preprint arXiv:2012.05736 (2020).

[38] P. Cao, H. Zhao, S. Liu, F. Tian, and Y. Wang, Ordering induced transformation from high-entropy to Heusler CrVTiAl alloy, Physics Letters A **383**, 125934 (2019).

[39] R. Zhang, Z. Gercsi, M. Venkatesan, K. Rode, and J. M. D. Coey, Pauli paramagnetism of cubic V_3Al, CrVTiAl, and related 18-electron Heusler compounds with a group-13 element, Physical Review B **103**, 174407 (2021).

[40] B. R. Ortiz, S. M. Teicher, L. Kautzsch, P. M. Sarte, N. Ratcliff, J. Harter, J. P. Ruff, R. Seshadri, and S. D. Wilson, Fermi surface mapping and the nature of charge-density-wave order in the kagome superconductor CsV_3Sb_5, Physical Review X **11**, 041030 (2021).

[41] B. Batterman and C. Barrett, Crystal structure of superconducting V_3Si, Physical Review Letters **13**, 390 (1964).

[42] B. Klein, W. Pickett, D. Papaconstantopoulos, and L. Boyer, Electronic structure, superconductivity, and magnetism in the C15 compounds ZrV_2, $ZrFe_2$, and $ZrCo_2$, Physical Review B **27**, 6721 (1983).

[43] R. Cohen, J. Wernick, K. West, R. Sherwood, and G. Chin, Mössbauer Studies of Au 197 in Alloys of Gold with Transition Metals, Physical Review **188**, 684 (1969).

[44] M. Lucas, J. A. Muñoz, O. Delaire, N. D. Markovskiy, M. B. Stone, D. L. Abernathy, I. Halevy, L. Mauger, J. B. Keith, M. L. Winterrose, Yuming Xiao, M. Lerche, and B. Fultz, Effects of composition, temperature, and magnetism on phonons in bcc Fe-V alloys, Physical Review B **82**, 144306 (2010).

[45] J. A. Muñoz, M. S. Lucas, O. Delaire, M. L. Winterrose, L. Mauger, Chen W. Li, A. O. Sheets, M. B. Stone, D. L. Abernathy, Yuming Xiao, Paul Chow, and B. Fultz, Positive vibrational entropy of chemical ordering in FeV, Physical Review Letters **107**, 115501 (2011).

[46] R. Wang, S. Wang, X. Wu, and J. Yang, Pressure induced structural instability of FeV intermetallic compound with B2 ordering, Journal of Alloys and Compounds **650**, 537 (2015).

[47] J. C. Krause, J. Schaf, M. da Costa Jr, and C. Paduani, Effect of composition and short-range order on the magnetic moments of Fe in $Fe_{1-x}V_x$ alloys, Physical Review B **61**, 6196 (2000).

[48] G. Shirane, R. Nathans, and C. Chen, Magnetic moments and unpaired spin densities in the Fe-Rh alloys, Physical Review **134**, A1547 (1964).

[49] M. Besnus and A. Meyer, Magnetic properties of the ordered and disordered $CrPt_3$ and CrPt phases, Physica Status Solidi (b) **58**, 533 (1973).

[50] F. Dupré, P. Menzinger, and P. Sacchetti, Spin density in Fe-Pd alloys, Il Nuovo Cimento B (1971-1996) **51**, 354 (1979).

[51] M. Bhatia, A. Singh, and T. Nandy, Volume size factor and lattice parameter in cubic intermetallics with the B2 structure, Intermetallics **6**, 141 (1998).

[52] T. Ziller, G. Le Caër, O. Isnard, P. Cénédèse, and B. Fultz, Metastable and transient states of chemical ordering in Fe-V nanocrystalline alloys, Physical Review B **65**, 024204 (2001).

[53] N. Miura, I. Oguro, and S. Chikazumi, Computer simulation of temperature and field dependences of sublattice magnetizations and spin-flip transition in gallium-substituted yttrium iron garnet, Journal of the Physical Society of Japan **45**, 1534 (1978).

[54] P. Rhodes and E. P. Wohlfarth, The effective Curie-Weiss constant of ferromagnetic metals and alloys, Proceedings of the Royal Society of London. Series A. Mathematical and Physical Sciences **273**, 247 (1963).

[55] A. Dos Santos, J. Krause, and C. Kuhnen, Electronic structure calculations and ground state properties of V_4N, FeV_3N and VFe_3N nitrides and ordered FeV_3 and VFe_3 compounds, Physica B: Condensed Matter **382**, 290 (2006).

[56] V. Moruzzi and P. Marcus, Magnetic structure of ordered FeAl and FeV, Physical Review B **47**, 7878 (1993).

[57] Y. Kakehashi and O. Hosohata, Curie-temperature" Slater-Pauling curve", Le Journal de Physique Colloques **49**, C8 (1988).

[58] G. P. Vassiley and M. Jiang, Thermodynamic optimization of the Co-Zn system, Journal of Phase Equilibria and Diffusion **25**, 259 (2004).

[59] J. Sanchez, J. Moran-Lopez, C. Leroux, and M. Cadeville, Magnetic properties and chemical ordering in Co-Pt, Journal of Physics: Condensed Matter **1**, 491 (1989).

[60] H. Tange, T. Tokunaga, and M. Goto, Magnetic moment and Curie point of disordered Ni–Mn alloys, Journal of the Physical Society of Japan **45**, 105 (1978).

[61] OpenMx, http://www.openmx-square.org.

[62] A. Szajek, The study of the elecronic structure of $CrPt_3$ alloy by the LMTO method, Acta Physica Polonica A **S2**, 967 (1992).

[63] G. Harp, S. Parkin, W. O'Brien, and B. Tonner, Induced Rh magnetic moments in Fe-Rh and Co-Rh alloys using x-ray magnetic circular dichroism, Physical Review B **51**, 12037 (1995).

[64] Y. A. Gribov and V. Fadin, Investigation of electrical resistivity and average magnetic moment per atom of Ni_3(Fe, Ti) and Ni_3(Mn, Ti) alloys, Soviet Physics Journal **24**, 389 (1981).

[65] J. MacLaren, T. Schulthess, W. Butler, R. Sutton, and M. McHenry, Electronic structure, exchange interactions, and Curie temperature of FeCo, Journal of Applied Physics **85**, 4833 (1999).

[66] D. C. Lee, A. Ghezelbash, C. A. Stowell, and B. A. Korgel, Synthesis and magnetic properties of colloidal $MnPt_3$ nanocrystals, The Journal of Physical Chemistry B **110**, 20906 (2006).

[67] S. Pickart and R. Nathans, Alloys of the first transition series with Pd and Pt, Journal of Applied Physics **33**, 1336 (1962).

[68] M. Besnus and A. Meyer, Order states and magnetic states of $CrPt_3$, Physica Status Solidi (b) **55**, 521 (1973).

[69] A. Sakuma, R. Umetsu, and K. Fukamichi, Magnetic structures and their stability in Mn_3Rh ordered and disordered alloys, Physical Review B **66**, 014432 (2002).

[70] J. Drijver, F. Van der Woude, and S. Radelaar, Order-disorder transition in Ni_3Fe studied by mössbauer spectroscopy, Physical Review Letters **34**, 1026 (1975).

[71] G. Longworth, Temperature Dependence of the 57Fe hfs in the Ordered Alloys $FePd_3$ and FePd near the Curie Temperature, Physical Review **172**, 572 (1968).

[72] Y.-X. Jiang, Yu-Xiao Jiang, Jia-Xin Yin, M. Michael Denner, Nana Shumiya, Brenden R. Ortiz, Gang Xu, Zurab Guguchia, Junyi He, Md Shafayat Hossain, Xiaoxiong Liu, Jacob Ruff, Linus Kautzsch, Songtian S. Zhang, Guoqing Chang, Ilya Belopolski, Qi Zhang, Tyler A. Cochran, Daniel Multer, Maksim Litskevich, Zi-Jia Cheng, Xian P. Yang, Ziqiang Wang, Ronny Thomale, Titus Neupert, Stephen D. Wilson and M. Zahid Hasan, Unconventional chiral charge order in kagome superconductor KV_3Sb_5, Nature Materials, **20**(10), 1353, (2021).

[73] M. Stevenson, E. Pace, C. Storm, S. Finnegan, G. Garbarino, C. Wilson, D. McGonegle, S. Macleod, and M. McMahon, Pressure-induced bcc-rhombohedral phase transition in vanadium metal, Physical Review B **103**, 134103 (2021).

[74] A. Reid, T. Sabine, and D. Wheeler, Neutron diffraction and other studies of magnetic ordering in phases based on Cr_2O_3, V_2O_3 and Ti_2O_3, Journal of Solid State Chemistry **4**, 400 (1972).

[75] Y. Kitaoka and H. Yasuoka, NMR investigations on the spin fluctuations in itinerant antiferromagnets. I. V_3Se_4 and V_5Se_8, Journal of the Physical Society of Japan **48**, 1460 (1980).

[76] S. Anzai and S. Ohta, Magnetic Properties of V_5Te_8, Journal of the Physical Society of Japan **49**, 2079 (1980).

[77] I. Galanakis and E. Şaşıoğlu, Ab-initio calculation of effective exchange interactions, spin waves, and Curie temperature in $L2_1$-and $L1_2$-type local moment ferromagnets, Journal of Materials Science **47**, 7678 (2012).

[78] H. Müller, W. Kockelmann, and D. Johrendt, The magnetic structure and electronic ground states of Mott insulators GeV_4S_8 and GaV_4S_8, Chemistry of Materials **18**, 2174 (2006).

[79] S. Son, M. J. Coak, N. Lee, J. Kim, T. Y. Kim, H. Hamidov, H. Cho, C. Liu, D. M. Jarvis, P. A. C. Brown, J. H. Kim, C. Park, D. I. Khomskii, S. S. Saxena, and J. Park, Bulk properties of the van der Waals hard ferromagnet VI_3, Physical Review B **99**, 041402 (2019).

[80] A. Behera, Alloys Based on Intermetallic Compounds. In Advanced Materials (Springer, 2022).

[81] D. Arčon, L. M. Schoop, R. J. Cava, and C. Felser, Evolution of magnetic fluctuations through the Fe-induced paramagnetic to ferromagnetic transition in Cr_2B, Physical Review B **93**, 104413 (2016).

[82] C. Zhao, K. Kang, J. C. Neuefeind, A. Schleife, and D. P. Shoemaker, In-plane magnetic structure and exchange interactions in the high-temperature antiferromagnet Cr_2Al, Physical Review Materials **5**, 084411 (2021).

[83] B. Kuhlow, Magnetic ordering in $CrCl_3$ at the phase transition, Physica Status Solidi (a) **72**, 161 (1982).

[84] D. Kozlenko, O. Lis, S. Kichanov, E. Lukin, N. Belozerova, and B. Savenko, Spin-induced negative thermal expansion and spin–phonon coupling in van der Waals material $CrBr_3$, npj Quantum Materials **6**, 1 (2021).

[85] I. Nakatani, H. Nose, and K. Masumoto, Magnetic properties of $CuCr_2Se_4$ single crystals, Journal of Physics and Chemistry of Solids **39**, 743 (1978).

[86] X. Zhang, T. Yu, Q. Xue, M. Lei, and R. Jiao, Critical behavior and magnetocaloric effect in monoclinic Cr_5Te_8, Journal of Alloys and Compounds **750**, 798 (2018).

[87] M. A. McGuire, H. Dixit, V. R. Cooper, and B. C. Sales, Coupling of crystal structure and magnetism in the layered, ferromagnetic insulator CrI_3, Chemistry of Materials **27**, 612 (2015).

[88] R. Jesser and O. Laborde, Magnétisme de $CrBe_{12}$ en champs intenses et résistivité électrique de $CrBe_{12}$ et de VBe_{12}, Journal de Physique **45**, 1819 (1984).

[89] R. Hempelmann and G. Hilscher, Ferromagnetism in Ti-Mn ternary hydrides, Journal of the Less Common Metals **74**, 103 (1980).

[90] M. R. K. Akanda, I. J. Park, and R. K. Lake, Interfacial Dzyaloshinskii-Moriya interaction of antiferromagnetic materials, Physical Review B **102**, 224414 (2020).

[91] D. Sprungmann, K. Westerholt, H. Zabel, M. Weides & H. Kohlstedt, Evidence for triplet superconductivity in Josephson junctions with barriers of the ferromagnetic Heusler alloy Cu_2MnAl. Physical Review B, **82**, (2010).

Chapter 6   Critical behaviour and weakly first-order transition in a topological ferromagnet CoS_2

6.1 Introduction

Since the discovery of insulators that are insulating in the interior but electrically conducting at the surface, the topology of electronic bands has attracted wide attention [1-3]. Research in non-magnetic topological materials has led to a succession of theoretical and experimental studies, involving topological insulators [3,4], Dirac semimetals [5-7] and topological Weyl semimetals [8]. Intriguingly, the combination of magnetism and topology can create a variety of novel topological quantum states [9-11] including a high anomalous Hall effect [12] and an anomalous Nernst effect [13] owing to Berry curvature and Weyl nodes, respectively. One of the few examples of a ferromagnetic topological material that was recently verified experimentally is CoS_2, which is nearly half-metallic [14]. Hence it is an interesting material for this thesis.

CoS_2 crystallizes in a cubic pyrite structure (space group $Pa\bar{3}$) shown in Fig. 6.1a. The cobalt atom is located at the centre of the octahedron formed by six sulphur atoms [15]. The splitting of the $3d$-orbitals in the octahedron coordination leads to a gap between e_g and t_{2g} bands [16]. The low-spin state cobalt has a formally divalent configuration, and the seven $3d$ electrons are distributed with four in spin-up states and the other three in spin-down states to give the low-spin configuration schematically shown in Fig. 6.1b. Therefore, the Fermi level just lies in the gap between t_{2g} and e_g in the spin-down state, forming a half-metal. This is further confirmed by the magnetic measurements (0.91 μ_B/Co) [14] and band structure measured by angle-resolved photoelectron spectroscopy [15]. Other calculations however

find a pocket of minority-spin electrons at the R point in the corner of the Brillouin zone of the pure compound [14] that leads to a peak in the density of states at the Fermi level that may explain the large electronic specific heat [17]. The minority-spin electron pocket has recently been confirmed [15] by angular resolved photoelectron spectroscopy that probes the bulk electronic structure. The same study also found a bulk Weyl point just below the Fermi level, connected by a Fermi arc to a Weyl point that is inferred to be just above the Fermi level, giving rise to surface states that are topologically protected. The Fermi arcs have majority-spin character. It suggests that the surface states associated with the Fermi arcs may contribute to the good catalytic properties of CoS_2 [14]. Recent literature on CoS_2 drew attention to its potential for spintronic applications with highly spin-polarized currents, albeit at low temperature [18], and its catalytic properties [19].

Although the critical behaviour of a powder sample has been reported, the only critical exponent discussed is δ, which is close to the value expected for an itinerant ferromagnet ($\delta = 5.0$) [20]. The present study examines the ferromagnetic phase transition at 120 K in detail and looks for the relation with its unusual electronic structure. The potential of CoS_2 as a magnetocaloric material is also reported.

6.2 Experiments

High quality CoS_2 single crystals were grown by the chemical vapour transport (CVT) method[13] starting from CoS_2 mesh powder (99.99%). The mixture of the CoS_2 powder (about 3 gram) with 3.5 mg/ml-tube volume $CoBr_2$ (99.99%) was sealed in a quartz ampoule, which was then put in an oven with a temperature gradient from 700 °C (source) to 640 °C (sink) for 14 days followed by quenching in water. The crystals obtained were octahedral, showing eight triangular {111} surfaces. The x-ray diffraction pattern was obtained with using CuK_α ($\lambda = 1.5405$ Å) radiation. The magnetization measurements were carried out on a single crystal with the magnetic field applied along a [111] easy direction using a 5T

---

[13] Single crystal CoS_2 was prepared by Dr. Yangkun He using the CVT method outlined in Chapter 2.3.

Quantum Design superconducting quantum interference device (SQUID) magnetometer. Thermomagnetic scans under 0.01 T were run to study the effective magnetic moments and to estimate the Curie temperature. Thermal scans in fields ranging from 0.01 T to 5 T were used to investigate the relation between the paramagnetic Curie temperature θ_p and the applied field. Isothermal magnetization curves $M(H)$ measured from 100 K to 130 K at temperature intervals $\Delta T = 2$ K were the basis for exploring the critical region.
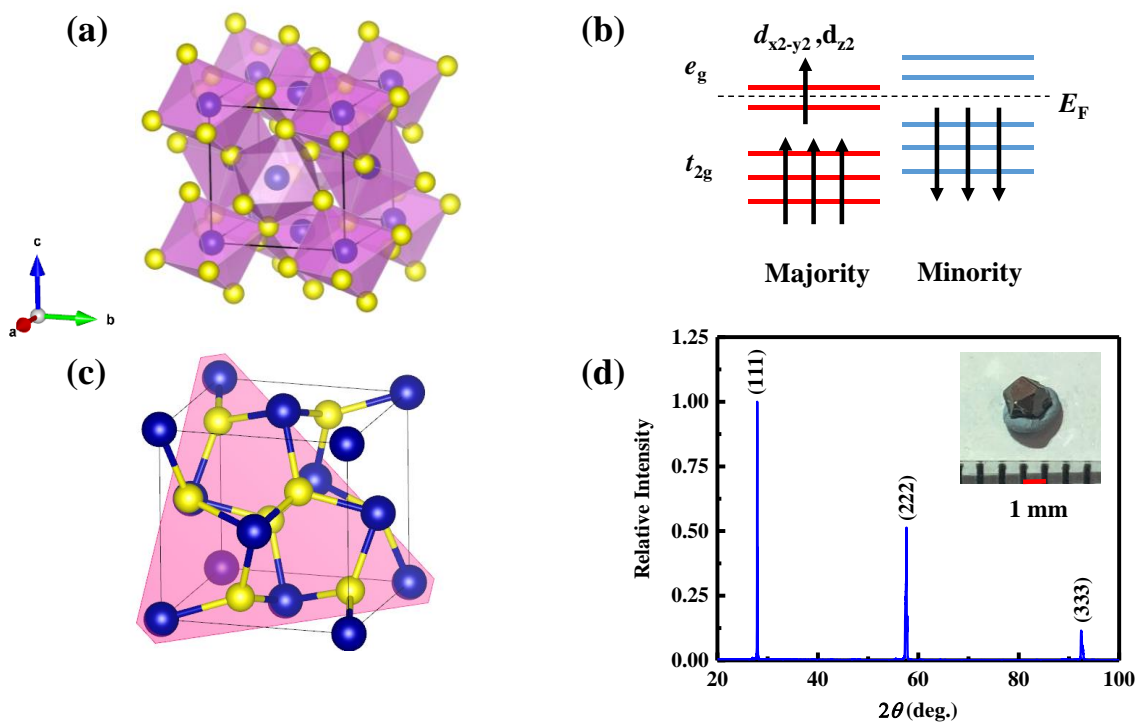
Fig. 6.1. Crystal structure of pyrite-type CoS_2. (a) The octahedron coordination is formed by six sulphur atoms around a cobalt atom. Blue and yellow atoms represent Co and S, respectively. (b) Schematic view of the splitting of the spin-up and spin-down $3d$ electron energy levels. (c) The easy axis of CoS_2 is along a $\langle 111 \rangle$ direction (perpendicular to the pink plane). (d) X-ray diffraction pattern from a (111) plane of the CoS_2 crystal, showing three peaks.

6.3 Results and discussion

CoS$_2$ crystallizes in the pyrite structure (Fig. 6.1a, c). Only (*l l l*) peaks were observed in the X-ray diffraction pattern on a (111) surface, shown in Fig. 6.1d. The lattice constant $a_0 = 5.537(8)$ Å, agrees well with previous literature [21-23]. The saturation moment at 4 K was determined as 0.94 μ_B, consistent with earlier reports [15,24,25].

The critical behaviour measured in the vicinity of the Curie temperature along a [111] direction is now discussed. A temperature-dependent $M(T)$ scan in 0.01 T is shown in Fig. 6.2a. The paramagnetic Curie temperature θ_p was obtained by fitting the inverse susceptibility in the paramagnetic state to a Curie-Weiss law $\chi = C/(T - \theta_p)$, where χ is the dimensionless susceptibility and C is Curie constant. The value of θ_p increases from 119.6 K to 127.1 K when the applied magnetic field is increased from 0.01 T to 5 T, as shown in Fig. 6.2b, which is similar to the behaviour of Rh$_2$CoSb [26] showing a tricritical point near its Curie temperature. The θ_p values obtained in low applied fields for CoS$_2$ are closer to its Curie temperature (119.8 K). The sharp change in field-dependence before 0.1 T is related to the weakly first-order transition, as shown below. An effective paramagnetic moment m_{eff} of 2.32 μ_B is calculated from the Curie constant $C = \frac{\mu_0 n m_{eff}^2}{3k_B}$, where k_B is the Boltzmann constant and n is number of magnetic atoms per cubic meter. According to the Rhodes-Wohlfarth plot of the ratio m_c/m_s versus Curie temperature, where $m_c = (\sqrt{1 + m_{eff}^2}$-1) and m_s is saturation moment, both in Bohr magnetons, the value $m_c/m_s = 1.67$ that we find for CoS$_2$ indicates that it is a partly itinerant ferromagnet [27].
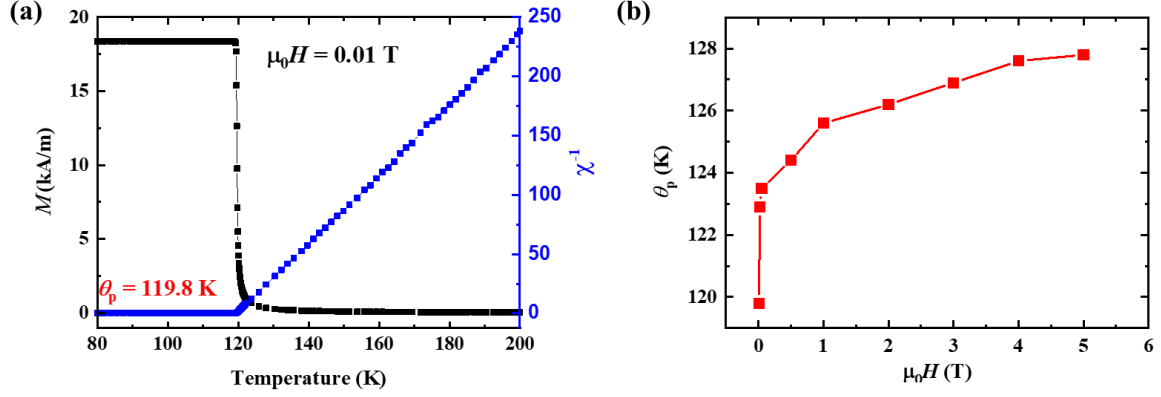
Fig. 6.2. (a) Left: Temperature dependence of the magnetization under a magnetic field of 0.01 T. Right: Inverse susceptibility (blue line) fit by the Curie-Weiss law (red line). (b) Magnetic-field dependence of θ_p along the easy axis of CoS_2.

The magnetic critical behaviour was studied by characterizing a series of interrelated critical exponents β, γ and δ around T_C [24]. The definitions of these exponents are

$$M_s(T) = M_0(-\varepsilon)^\beta, \ \varepsilon < 0, T < T_C, \tag{6.1}$$

$$\chi_0^{-1}(T) = \frac{h_0}{m_0}\varepsilon^\gamma, \ \varepsilon > 0, T > T_C, \tag{6.2}$$

$$M = DH^{1/\delta}, \ \varepsilon = 0, T = T_C, \tag{6.3}$$

where M_0, h_0/m_0, D are critical amplitudes [25] and ε is the reduced temperature defined as $\varepsilon = (T - T_C)/T_C$. The universal magnetic equation of state [28] is

$$M(H,\varepsilon) = \varepsilon^\beta f_\pm(\frac{H}{\varepsilon^{\gamma+\beta}}), \tag{6.4}$$

where $f_\pm$ are regular functions associated with the variables H and ε. Further simplifying this equation, it can be written as $m = f_\pm(h)$, where $m = \varepsilon^{-\beta}M(H,\varepsilon)$ and $h = \frac{H}{\varepsilon^{\gamma+\beta}}$. Here, f_+ is the function for $T > T_C$, while f_- is for $T < T_C$. It means that when the right values of β, γ and δ are found, scaled m and h will lie on two universal two curves, one

above T_C and the other below T_C. Any two of the critical exponents suffice to describe the static critical behaviour for a particular universality class, defined by the dimensions of space and the magnetic order parameter
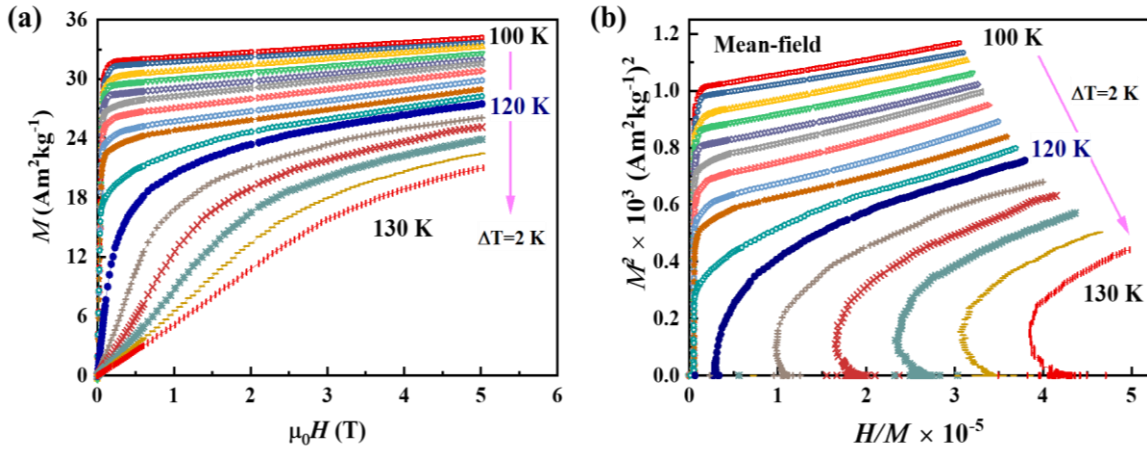

Fig. 6.3. (a) Initial isothermal magnetization curves measured along (111) around $T_C = 120$ K (navy blue curve) for single-crystalline CoS$_2$. (b) Arrott plots (M^2 vs $\mu_0 H/M$) near T_C. Note that the temperature interval ΔT is 2 K.

Fig. 6.3a exhibits the field-dependent isothermal magnetization curves measured along the easy axis across the critical region. The magnetization increases rapidly under low field and saturates at high field when $T < T_C$, whereas above T_C the shape of the curve is initially slightly concave and before becoming linear and then convex on approaching saturation. The standard method to determine the critical temperature using Arrott plots is based on mean field theory where $\beta = 1/2$, $\gamma = 1$ and $\delta = 1$ [29]. Fig. 6.3b shows the Arrott plots of M^2 versus $\mu_0 H/M$, where the isotherms are expected to be set of parallel straight lines, with one passing through the origin, the critical isotherm, determining the temperature T_C. Our plots are completely different from those expected from mean field theory of a second order phase transition.

Based on a criterion proposed by Banerjee [30], the slope of the Arrott plot can reveal the order of the transition order: a negative value indicates a first-order phase transition while

a positive one corresponds to a second-order phase transition. Obviously, the linear slope in the high-field region of our plots is positive, but it is noted that there is a convex downward curvature in the extremely low-field region, which was explained by Takahashi in terms of spin fluctuation theory [31]. However, the convex downward curvature and negative slope in CoS_2 is still evident when the temperature is a little higher than T_C, which is a sign of a weakly first-order transition accompanying the second-order Curie transition.
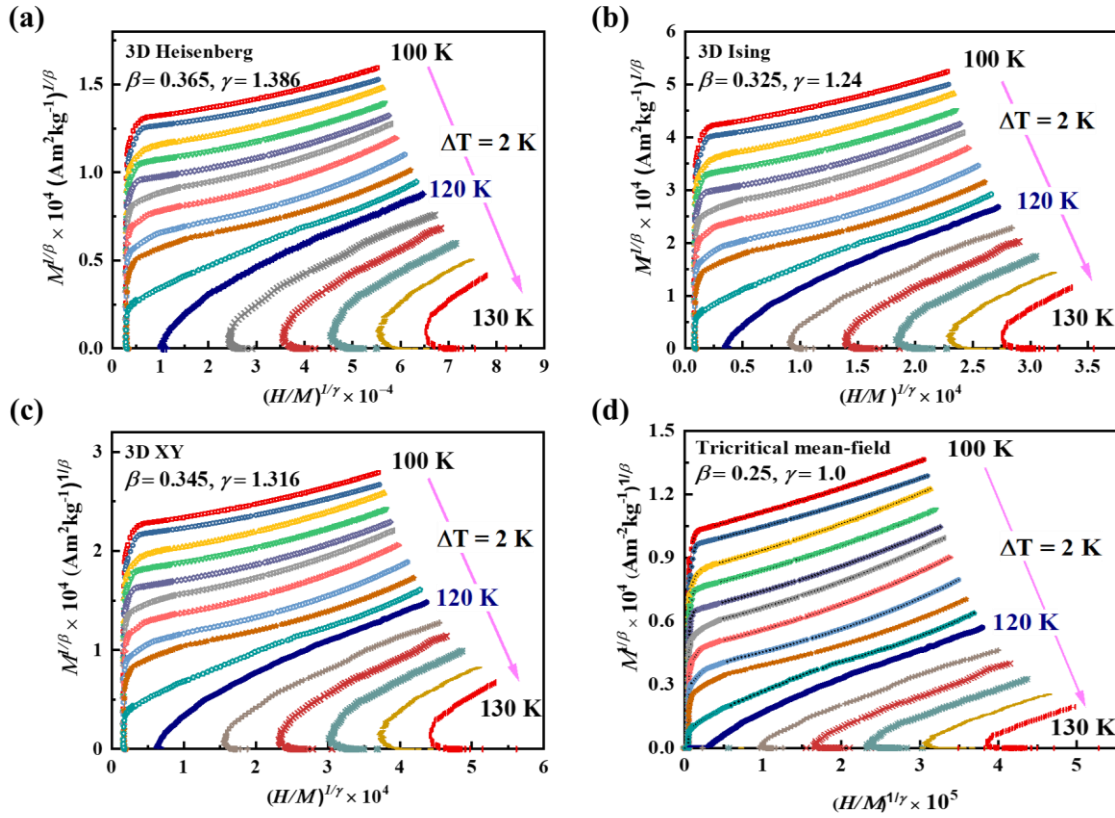
Fig. 6.4. The isotherms plotted as $M^{1/\beta}$ vs $(\mu_0 H/M)^{1/\gamma}$ with a (a) 3D Heisenberg model, (b) 3D Ising model, (c) 3D XY model and (d) tricritical mean-field model. Note that the temperature interval ΔT is 2 K.

The mean-field theory requires that the M^2 vs $\mu_0 H/M$ curves at various temperatures around T_C should be a series of parallel lines in the high-field region, but the curves shown in Fig. 6.3b are not linear. The conventional Arrott plot cannot successfully

characterize the critical behaviour of CoS_2. A better approach is the modified Arrott plot [32] deduced from the Arrott-Noakes equation $(H/M)^{1/\gamma} = a\varepsilon + bM^{1/\beta}$, where a and b are constants. A series of parallel straight lines of $M^{1/\beta}$ vs $(H/M)^{1/\gamma}$ at various temperature around T_C can be obtained if suitable values of β and γ are found, and the line should pass through the origin when $T = T_C$. Four models, 3D Heisenberg ($\beta = 0.365$, $\gamma = 1.386$), 3D Ising model (($\beta = 0.325$, $\gamma = 1.24$), 3D XY model ($\beta = 0.345$, $\gamma = 1.316$), and tricritical mean-field model ($\beta = 0.25$, $\gamma = 1.0$), are used to construct the modified Arrott plots [33] shown in Fig. 6.4. Among all these models, the tricritical mean-field model works the best, although it is not perfect. To further identify the best model, it is valid to use the normalized slope given by $NS = S(T)/S(T_c)$, where $S(T)$ is defined as $dM^{1/\beta}/d(H/M)^{1/\gamma}$. The ideal value of the normalized slope is 1.0 because the modified Arrott plot should consist of a series of parallel straight lines. Fig. 6.5 shows the plot of NS vs T for the four models, which further indicates that the tricritical mean-field model is the best of the four, although the description of the critical behaviour of CoS_2 still less than perfect.
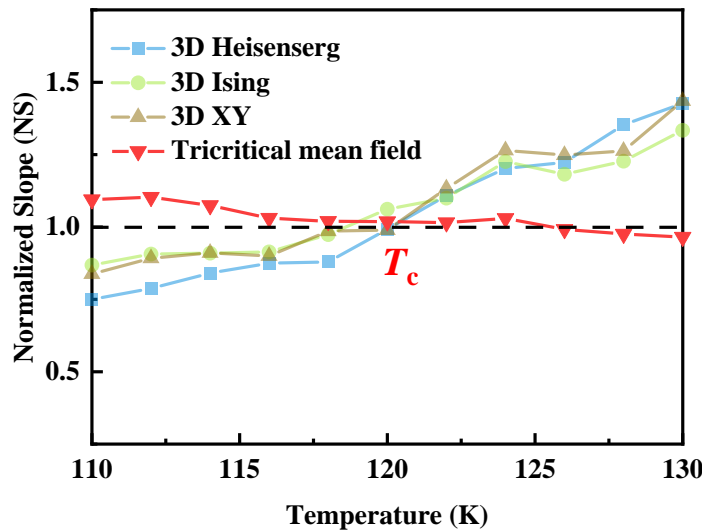

Fig. 6.5. Temperature dependence of the normalized slopes $NS = S(T)/S(Tc)$.

In order to obtain more precise critical exponents, an iteration method has been employed [34]. Linear extrapolation from the high-field straight lines of the isothermal curves yields the values of $M_s(T)$ and $\chi_0^{-1}(T)$, which are the intercepts on the axis, $M^{1/\beta}$ and $(H/M)^{1/\gamma}$. By fitting the data following the Eqs. 6.1 and 6.2, a set of modified values of β and γ will be obtained. They will be used to reestablish a new modified Arrott plot. The above procedure was repeated until the values of the critical exponents are stable. It should be noted that the obtained exponents by this method are independent of the initial choice of parameters, which ensures these critical exponents are reliable. Fig. 6.6a presents the temperature dependence of M_s and χ_0^{-1} accompanyed with fitting curves (solid line). The critical exponents $\beta = 0.196$, with $T_C = 119.9$ K, and $\gamma = 0.972$, with $T_C = 119.7$ K are obtained by fitting. The linear extrapolation from the high-field region to obtain the intercepts and select the proper values of critical exponents are very helpful to obtain a set of parallel straight lines in the high-field region. An alternative is to use the Kouvel-Fisher (KF) method [35] to determine the critical exponents. The KF equations are

$$\frac{M_s(T)}{dM_s(T)/dT} = \frac{T - T_C}{\beta} \tag{6.5}$$

$$\frac{\chi_0^{-1}(T)}{d\chi_0^{-1}(T)/dT} = \frac{T - T_C}{\gamma} \tag{6.6}$$

By taking this KF method, the slopes of $1/\beta$ and $1/\gamma$ can be acquired from the temperature dependence of $\frac{M_s(T)}{dM_s(T)/dT}$ and $\frac{\chi_0^{-1}(T)}{d\chi_0^{-1}(T)/dT}$, respectively. The method gives $\beta = 0.196$ and $\gamma = 0.925$ with $T_C = 119.8$ K as shown in Fig. 6.6b.

(a)

(b)

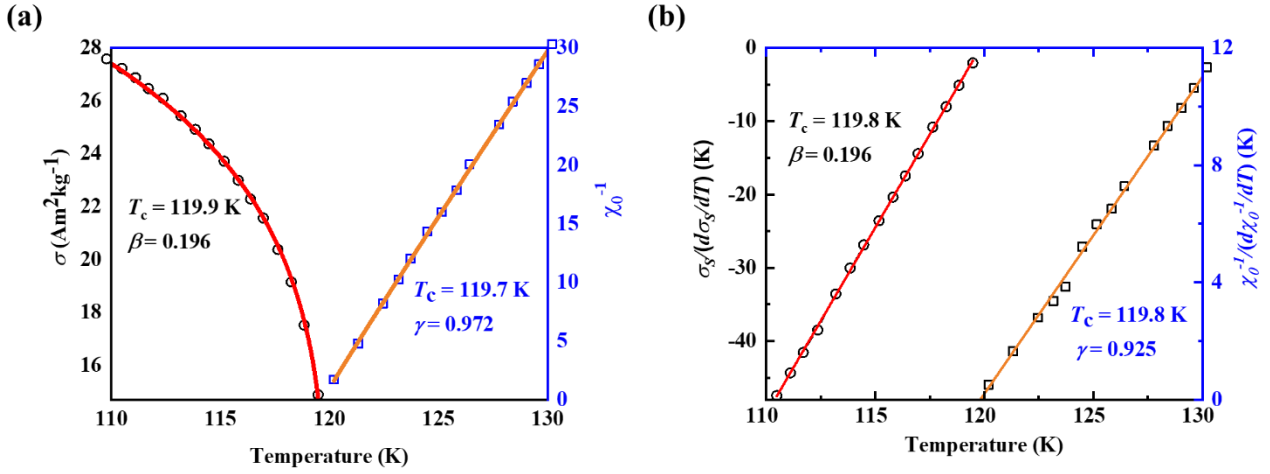
Fig. 6.6. (a) Temperature dependence of the spontaneous magnetization M_s (left) and the inverse initial susceptibility χ_0^{-1} (right). M_s (T) and χ_0^{-1}(T), based on the intercepts on the $M_s^{1/\beta}$ and $(H/M)^{1/\gamma}$ axes, respectively, which are given by the linear extrapolation of the high-field straight line of the isotherm curves using the modified Arrott plots. T_C and critical exponents are calculated by fitting Eqs. 6.5 and 6.6 (solid line). (b) The Kouvel-Fisher plot for the temperature dependence of the spontaneous magnetization M_s (left) and the inverse initial susceptibility χ_0^{-1} (right). Critical exponents β and γ are the slopes of the curves, and T_C is the exploration.
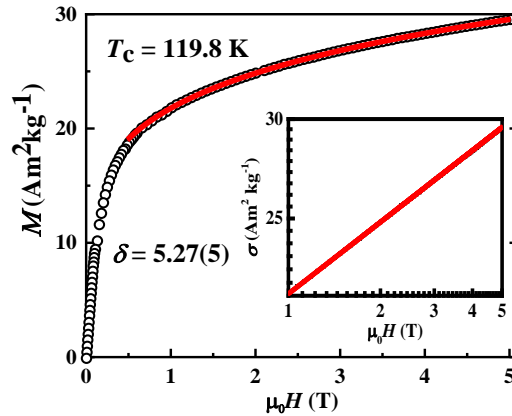

Fig. 6.7. The magnetization curve at T_C (119.8 K). The corresponding log-log scale plot is shown in the inset, whose slope in the high-field region is $\delta = 5.27$

The critical exponents deduced by the KF method agree with those generated by the modified Arrott plot within experimental error. The third critical exponent δ associated with the magnetization isotherm at T_C is determined by Eq. 6.3, where D is the critical amplitudes [35]. The isothermal magnetization $M(H)$ measured at the critical temperature $T_C = 119.8 \pm 0.2$ K is shown in Fig. 6.7 and the inset shows a log-log plot. Through fitting the high field slope in the isothermal curve of log-log scale, the critical exponent $\delta = 5.27$ is obtained. The expected value of δ can be deduced from the Widom scaling law $\delta = 1 + \frac{\beta}{\gamma}$ [29], where β and γ are determined by the modified Arrott plot ($\delta = 5.96$). Or it can be obtained by KF method ($\delta = 5.27$), which is consistent with Ref. [20]. These values of δ do not agree with each other, which suggests that the transition is not a second order phase transition. The difference suggests a weakly first-order transition.

In order to verify the reliability of the values deduced for the critical exponents β and γ and T_C, we adopt the scaling analysis, $m = f_\pm(h)$, mentioned above. Fig. 6.8a shows the scaled m ($= M|\varepsilon|^{-\beta}$) as a function of scaled h ($= \mu_0 H|\varepsilon|^{-(\gamma+\beta)}$), along with the same plot on a log-log scale in the inset. All of the experimental data in the high-field region fall on one of two independent branches, $T > T_C$ and $T < T_C$. Furthermore, the data in the low-field region above T_C collapse onto one as well. However, in the lower-field region below T_C, the experimental data do *not* collapse onto one curve, which is exactly the behaviour found in materials exhibiting tricriticality. This phenomenon usually arises at the boundary between a first-order phase transition and a second-order one and these two transitions will meet at a single point, which is called the tricritical point [36-38]. The critical behaviour of CoS_2 is similar to MnSi [39], which exhibits a first-order phase transition from conical to ferromagnetic states under an external magnetic field [40]. The tricritical point of magnetic field (H_{TCP}) separates first-order from second-order behaviour. That is to say, above H_{TCP}, the scaled curves should fall onto a universal curve, whereas below H_{TCP}, the scaling equation can no longer be used because of the first-order character. Thus, the turning point at the external field H_c on the m vs h curve on log-log scale reflects the boundary between the first-order and second-order behavior as shown in inset of Fig. 6.8a. The curve of H_c vs

T is shown in Fig. 6.8b, which decreases nearly linearly with temperature changing from 112 K to T_C. The points of H_c (= 0.034 T) and T_C (=119.8 K) meet at H_{TCP}. H_c is temperature-independent below 110 K. Although the extent of the first order transition in our single crystal of CoS_2 is weaker than that of MnSi, the scaling equation plot on a log-log scale for CoS_2 (inset of Fig. 6.8a) is totally different from that of a normal ferromagnet [41-45]. It suggests that the transition observed at T_C is weakly first-order.
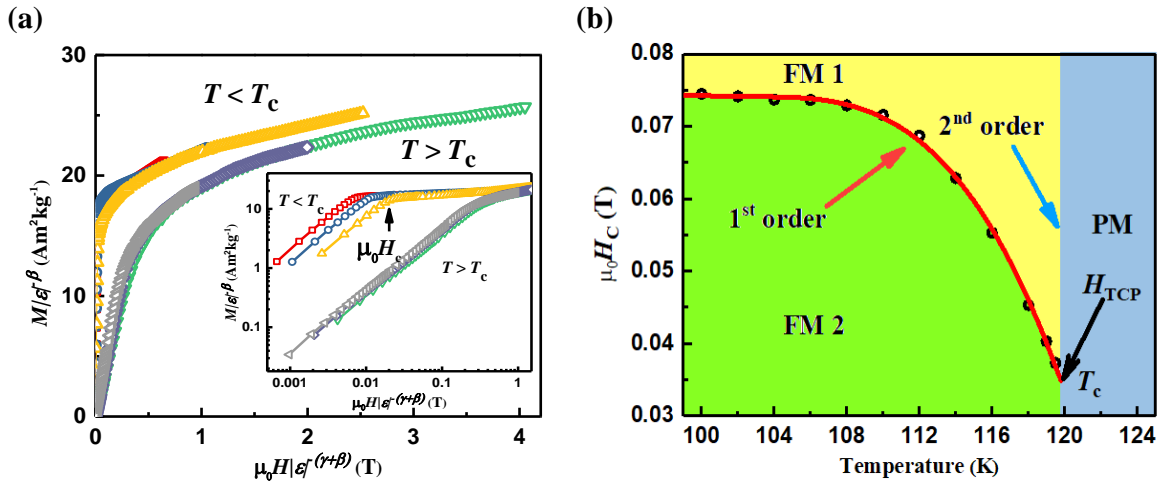

Fig. 6.8. (a) Scaling plots of renormalized magnetization m ($= M|\varepsilon|^{-\beta}$) vs renormalized h ($=\mu_0 H|\varepsilon|^{-(\gamma+\beta)}$) around the critical temperature for single crystal CoS_2. Inset: the same plot in log-log scale. The turning point H_c meets T_C at H_{TCP}. (b) The phase diagram of CoS_2 determined by fitting the external field $\mu_0 H_c$.

Comparing the critical exponents in different theoretical models, listed in Table 6.1, to those obtained for CoS_2, it seems that the pyrite cannot be categorized into any conventional universality class. Taroni *et al.* have conducted a comprehensive investigation of critical exponents for 2D magnets and find that the exponent β is within a window, $0.1 \leq \beta \leq 0.25$ [46]. Despite the fact that the single crystal structure of CoS_2 is clearly three dimensional, the exponent is in the range for 2D magnets. However, our value of β is similar as that expected from the tricritcal mean-field model, and it is similar to some other magnetic single crystals, such as $CrGeTe_3$, $CrSiTe_3$ and MnSi (Table 6.1), as well as some

manganite oxides [36, 47, 48]. Interestingly, these compounds show the same feature – a crossover from a first-order phase transition to a second-order ferromagnetic one at a tricritical point. Generally, a first-order transition is accompanied by a discontinuous volume change. Therefore, it is expected that there is a latent heat and a discontinuous magnetic entropy change at T_C

Table 6.1. Comparison of critical exponents obtained for CoS_2 with different theoretical models and related materials close to a tricritical point. (SC, single crystal)

Composition	Reference	T_C (K)	Method	β	γ	δ
$CoS_2{}^{SC}$	This work	119.8	Modified Arrott plot	0.196	0.972	5.959
			Kouvel-Fisher	0.196	0.925	5.719
			Critical isotherm	/	/	5.275
Mean field			Theory	0.5	1	3
3D-Heisenberg				0.365	1.386	4.8
3D-Ising				0.325	1.24	4.82
3D-XY				0.345	1.316	4.81
Tricritical mean-field				0.25	1	5

CoS$_2$	[20]	119.5		/	/	5.2
CrGeTe$_3^{SC}$	[49]	67.9	Modified Arrott plot	0.242	0.985	5.07
CrSiTe$_3^{SC}$	[50]	31		0.170	1.532	10.012
MnSi^{SC}	[39]	30.5		0.242	0.91	4.734
La$_{0.1}$Nd$_{0.6}$Sr$_{0.3}$MnO$_3$	[51]	249.5		0.257	1.12	5.17
La$_{0.9}$Te$_{0.1}$MnO$_3$	[37]	239.5		0.201	1.27	7.14

The magnetic entropy can be calculated by

$$\Delta S_M(T,H) = \int_0^H (\frac{\partial S}{\partial H})_T \, dH = \int_0^H (\frac{\partial M}{\partial T})_H \, dH \qquad (6.7)$$

where $(\frac{\partial S}{\partial H})_T$ and $(\frac{\partial M}{\partial T})_H$ is determined by the Maxwell's equation. $\Delta s_M(T,H)$ can be approximately expressed as $\Delta S_M(T_i,H) = \frac{\int_0^H M(T_i,H)dH - \int_0^H M(T_{i+1},H)dH}{T_i - T_{i+1}}$. Fig. 6.9a shows the calculated temperature dependence of $-\Delta S_M(T,H)$ in a field along the (111) direction of our single crystal. All the curves of the magnetic entropy change exhibit a peak around T_C and the peaks are broad and increasingly asymmetric with increasing field. The maximum value of the magnetic entropy change, $-\Delta S_M(T,H)$, around the ferromagnetic transition is 7.1 J kg^{-1} K^{-1} in an applied field change of 5 T. Comparing the result for CoS$_2$ with the previous reports on some magnetocaloric materials in Fig. 6.9b, it seems that ferromagnets with a high magnetic entropy change exhibit a first-order transition, while the materials with a second-order transition shows much smaller values, as low as 3 J kg^{-1} K^{-1}. The details of these ferromagnets were list in Table 6.2. The magnetic entropy change in CoS$_2$ is

exceptionally large for a system where the ions only have S = 1/2, a further indication of the first order character of the transition.

CoS$_2$ therefore exhibits a weakly first-order transition under low applied field while it is suppressed in high field. The entropy change is already comparable with the conventional magnetocaloric material Gd with S = 7/2 ($-\Delta S_M(T,H) = 9$ J kg^{-1} K^{-1} [52]). The transition in CoS$_2$ exhibits little hysteresis and it may be a promising material for magnetocaloric applications well below room temperature.
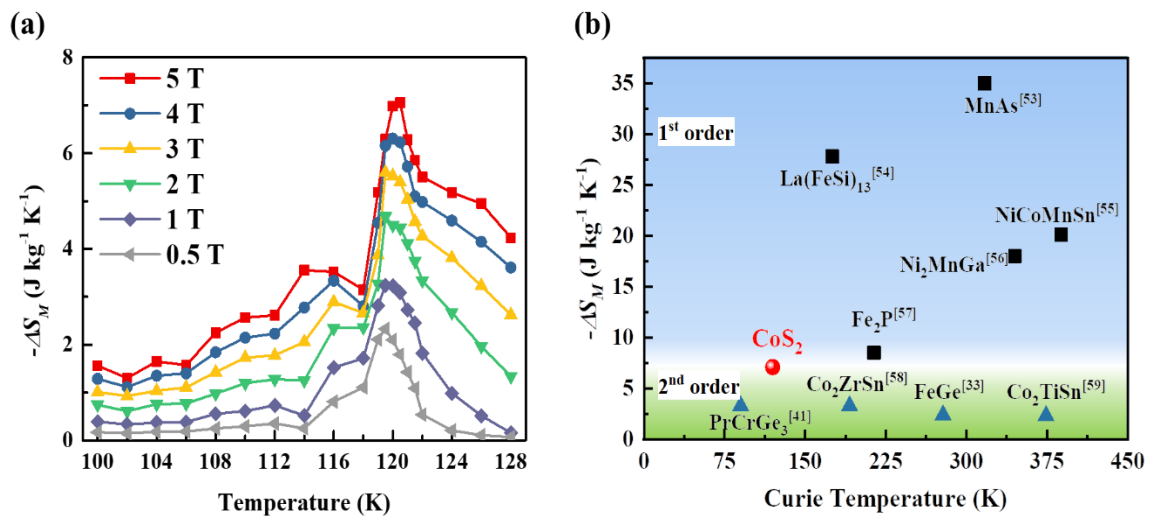
Fig. 6.9. (a) Temperature dependence of isothermal magnetic entropy change $-\Delta S_M(T,H)$ calculated from magnetization at various magnetic fields. (b) Comparison of the magnetic entropy change and the Curie temperature for some ferromagnetic materials. The materials with first-order phase transition exhibit large magnetocaloric effect, while the value for the materials with a second-order transition is much lower. CoS$_2$ is located at the boundary between the 1st order and 2nd order transition regions, but the entropy change is large in view of the low spin state S = ½ of the cobalt.

Table 6.2. Comparison of the magnetic entropy change and the Curie temperature for some ferromagnetic materials.

Materials	T_C (K)	$-\Delta S_M(T, H)$, $\Delta H = 5$ T (J kg^{-1} K^{-1})	Reference
CoS$_2$	119.8	7.1	This work
MnAs	317	35	[53]
La(FeSi)$_{13}$	175	27.8	[54]
NiCoMnSn	388	20.1	[55]
Ni$_2$MnGa	345	18	[56]
Fe$_2$P	214	8.5	[57]
PrCrGe$_3$	90.5	3.2	[41]
Co$_2$ZrSn	192	3.2	[58]
FeGe	279	2.3	[33]
Co$_2$TiSn	375	2.23	[59]

Finally, we return to the question raised in the introduction — is the order of the magnetic phase transition in CoS$_2$ related to the unusual topological electronic structure of the material? It is expected that *any* ferromagnetic phase transition in a cubic material, such as αFe, must involve a reduction of symmetry [60]. Iron with $\langle 100 \rangle$ easy axis anisotropy will become weakly tetragonal due to the influence of magnetostriction which couples magnetic symmetry breaking with a change in crystal structure — a ferromagnet can never be strictly cubic if there is any magnetostriction, however small. But this does not prevent a continuous phase transition at T_C if the point-group of the ferromagnetic phase is a subgroup of the point group of the paramagnetic phase. In CoS$_2$, (space group Pa$\bar{3}$) the point group is $2/m\bar{3}$ which can change continuously to $\bar{3}$ if the space group becomes R$\bar{3}$, consistent with the [111] easy axis [17].

There are two other conducting ferromagnets that exhibit topological features for which the critical behaviour has been studied. One is the van der Waals layer compound Fe_3GeTe_2 [61, 62]. This is an itinerant ferromagnet where the iron occupies two sites, the 4e sites which form a double layer sandwiching a layer of 2c sites that is itself isolated and sandwiched between layers of tellurium. The compound exhibits unusually large anomalous Hall and Nernst effects [63, 64], and hosts skyrmions [65]. The Curie temperature of 215 K, and strong uniaxial anisotropy arising from the 4e sites [66, 67] — the anisotropy field is 8 T, and the anisotropy energy is 1.29 MJm^{-3} [68], which reduces the effective spin dimension to 1. The spatial dimension is 3, because 2D magnetic systems must have isolated single sheets of magnetic ions. In ref. [69], the authors find critical behavior from modified Arrott plots and Kouvel-Fisher analysis that yields $\beta = 0.327$, $\gamma = 1.079$ and $\delta = 4.261$ that satisfy the Widom equality $\gamma = \beta(\delta - 1)^{-1}$. The exponents are fairly close to those expected from the 3D Ising model (Table 6.1), as might be anticipated from compound's structure. The other material is the Weyl semimetal $Co_3Sn_2S_2$ with Fermi arcs at the Fermi surface [70]. Here too, the data can be reduced using modified Arrott plots and Kouvel-Fisher analysis to yield exponents $\beta = 0.348$, $\gamma = 1.26$ and $\delta = 4.52$ that satisfy the Widom equality within experimental error. The behaviour of CoS_2 is quite different. The Arrott plots show a negative slope, indicating a first-order transition and the measured exponents do not satisfy the scaling law.

We think that the weakly first-order ferromagnetic transition in CoS_2 is connected with the appearance of the minority-spin electron pocket at the R point in the Brillouin zone below the Curie temperature. The transition is from a non-topological paramagnetic state to a topological ferromagnetic state with band inversion like that in a topological insulator. This cannot be a continuous transition; it is inevitably first-order because the ferromagnetic band structure is topologically protected. The other two topological ferromagnets are not reported to exhibit the band inversion seen in CoS_2. In fact, 5% Se reduces the Curie temperature of CoS_2 to 90 K and makes the transition strongly first-order with a thermal hysteresis of 2.5 K [71]. This is likely a result of increased band inversion due to broadening

of the e_g band.

6.4 Conclusion

We have presented a variety of evidence from static magnetic measurements that the ferromagnetic phase transition at 119.8 K in CoS_2 is weakly first-order. There is a tricritical point at the transition temperature. The first-order transition found in low fields is suppressed by an applied magnetic field of order 100 mT, which is sufficient to break the topological protection. The corresponding energy per site is of order 50 mK. Furthermore, we suggest that the ferromagnetic phase transition in any material that develops topologically protected band inversion at the Curie point will be first-order, and we suggest in Future Work a way to check this idea in the Co-Fe pyrites.

The calculated magnetocaloric effect near T_C is large in view of the low spin of S = ½ of the cobalt. There is very little hysteresis. Topological ferromagnets, especially ones with higher Curie temperatures, may be useful magnetocaloric materials.

6.5 Acknowledgement

References

[1] X. Qi and S. Zhang, Topological insulators and superconductors, Reviews of Modern Physics **83**, 1057 (2011).

[2] L. A. Wray, S.-Y. Xu,Y. Xia, D. Hsieh, A. V. Fedorov, Y. S. Hor, R. J. Cava, A. Bansil, H. Lin and M. Z. Hasan, A topological insulator surface under strong Coulomb, magnetic and disorder perturbations, Nature Physics **7**, 32 (2011).

[3] M. Z. Hasan and C. L. Kane, Topological insulators, Review Modern of Physics **82**, 3045 (2010).

[4] Y. Chen, J. G. Analytis, J.-H. Chu, Z. K. Liu, S.-K. Mo, X. L. Qi, H. J. Zhang, D. H. Lu, X. Dai, Z. Fang, S. C. Zhang, I. R. Fisher, Z. Hussain, Z.-X. Shen1, Experimental realization of a three-dimensional topological insulator, Bi_2Te_3, Science **325**, 178 (2009).

[5] S. M. Young, S. Zaheer, J. C. Teo, C. L. Kane, E. J. Mele, and A. M. Rappe, Dirac semimetal in three dimensions, Physical Review Letters **108**, 140405 (2012).

[6] Z. Wang, Y. Sun, X.-Q. Chen, C. Franchini, G. Xu, H. Weng, X. Dai, and Z. Fang, Dirac semimetal and topological phase transitions in A_3Bi (A= Na, K, Rb), Physical Review B **85**, 195320 (2012).

[7] Z. Wang, H. Weng, Q. Wu, X. Dai, and Z. Fang, Three-dimensional Dirac semimetal and quantum transport in Cd_3As_2, Physical Review B **88**, 125427 (2013).

[8] B. Yan and C. Felser, Topological materials: Weyl semimetals, Annual Review of Condensed Matter Physics **8**, 337 (2017).

[9] Y. Tokura, K. Yasuda, and A. Tsukazaki, Magnetic topological insulators, Nature Reviews Physics **1**, 126 (2019).

[10] F. Tang, H. C. Po, A. Vishwanath, and X. Wan, Comprehensive search for topological materials using symmetry indicators, Nature **566**, 486 (2019).

[11] K. He, Y. Wang, and Q.-K. Xue, Topological materials: quantum anomalous Hall system, Annual Review of Condensed Matter Physics **9**, 329 (2018).

[12] Q. Wang, Yuanfeng Xu, Rui Lou, Zhonghao Liu, Man Li, Yaobo Huang, Dawei Shen, Hongming Weng, Shancai Wang and Hechang Lei, Large intrinsic anomalous Hall effect in half-metallic ferromagnet $Co_3Sn_2S_2$ with magnetic Weyl fermions, Nature Communications **9**, 1 (2018).

[13] K. Geishendorf, P. Vir, C. Shekhar, C. Felser, J. I. Facio, J. van den Brink, K. Nielsch, A. Thomas, and S. T. Goennenwein, Signatures of the magnetic entropy in the thermopower signals in nanoribbons of the magnetic weyl semimetal $Co_3Sn_2S_2$, Nano Letters **20**, 300 (2019).

[14] N. B. Schröter, J. A. Krieger, D. Pei, Tianlun Yu, Samuel Stolz, T. Schmitt, P. Dudin, T. K. Kim, C. Cacho, A. Schnyder, A. Bergara, V. N. Strocov, F. de Juan, M. G. Vergniory, L. M. Schoop, Weyl fermions, Fermi arcs, and minority-spin carriers in ferromagnetic CoS_2, Science Advances **6**, eabd5000 (2020).

[15] V. Johnson and A. Wold, Crystal growth and magnetic properties of compositions in the CoS_2: $CoSe_2$ system, Journal of Solid State Chemistry **2**, 209 (1970).

[16] J. M. D. Coey, *Magnetism and Magnetic Materials* (Cambridge university press, 2010).

[17] H. Hiraka and Y. Endoh, Ferromagnetic Transition of Heisenberg Ferromagnetic Metal of CoS_2---Static Critical Properties, Journal of the Physical Society of Japan **63**, 4573 (1994).

[18] L. Wang, T. Chen, and C. Leighton, Spin-dependent band structure effects and measurement of the spin polarization in the candidate half-metal CoS_2, Physical Review B **69**, 094412 (2004).

[19] M. Cabán-Acevedo, M. L. Stone, J. Schmidt, J. G. Thomas, Q. Ding, H.-C. Chang, M.-L. Tsai, J.-H. He, and S. Jin, Efficient hydrogen evolution catalysis using ternary pyrite-type cobalt phosphosulphide, Nature Materials **14**, 1245 (2015).

[20] H. Nishihara, T. Harada, T. Kanomata, and T. Wada, Magnetization process near the Curie temperature of an itinerant ferromagnet CoS_2, Journal of Physics: Conference Series (IOP Publishing), **400**, 3, p. 032068 (2012).

[21] K. Adachi, K. Sato, M. Okimori, G. Yamauchi, H. Yasuoka, and Y. Nakamura, Magnetic anisotropy of CoS_2–torque and NMR measurements, Journal of the Physical Society of Japan **38**, 81 (1975).

[22] N. Mushnikov, T. Goto, A. Andreev, and S. Zadvorkin, Magnetoelasticity of CoS_2, Philosophical Magazine B **80**, 81 (2000).

[23] M. Straumanis, G. Amstutz, and S. Chan, Lattice parameters and expansion coefficients of FeS_2 (natural and synthetic), and of CoS_2, American Mineralogist: Journal of Earth and Planetary Materials **49**, 206 (1964).

[24] H. Stanley, *Introduction to phase transition and critical phenomena* (Oxford: Oxford University Press), Reviews of Modern Physics **71**, S358 (1971).

[25] M. E. Fisher, The theory of equilibrium critical phenomena, Reports on progress in physics **30**, 615 (1967).

[26] Y. He, R. Sibille, D. Chen, J. Kroder, T. Helm, W. Schnelle, C. Felser, and G. H. Fecher, Anisotropic magnetization, critical temperature, and paramagnetic Curie temperature in the highly anisotropic magnetic Heusler compound Rh_2CoSb, Physical Review B **103**, 214436 (2021).

[27] T. Kubodera, H. Okabe, Y. Kamihara, and M. Matoba, Ni substitution effect on magnetic and transport properties in metallic ferromagnet $Co_3Sn_2S_2$, Physica B: Condensed Matter **378**, 1142 (2006).

[28] P. Limelette, A. Georges, D. Je´rome, P. Wzietek, P. Metcalf, J. M. Honig, Universality and critical behavior at the Mott transition, Science **302**, 89 (2003).

[29] A. Arrott, Criterion for ferromagnetism from observations of magnetic isotherms, Physical Review **108**, 1394 (1957).

[30] B. Banerjee, On a generalised approach to first and second order magnetic transitions, Physics Letters **12**, 16 (1964).

[31] Y. Takahashi, On the origin of the Curie-Weiss law of the magnetic susceptibility in itinerant electron ferromagnetism, Journal of the Physical Society of Japan **55**, 3553 (1986).

[32] A. Arrott and J. E. Noakes, Approximate equation of state for nickel near its critical temperature, Physical Review Letters **19**, 786 (1967).

[33] L. Zhang, H. Han, M. Ge, H. Du, C. Jin, W. Wei, J. Fan, C. Zhang, L. Pi and Y. Zhang, Critical phenomenon of the near room temperature skyrmion material FeGe, Scientific Reports **6**, 1 (2016).

[34] A. Pramanik and A. Banerjee, Critical behavior at paramagnetic to ferromagnetic phase transition in $Pr_{0.5}Sr_{0.5}MnO_3$: a bulk magnetization study, Physical Review B **79**, 214426 (2009).

[35] J. S. Kouvel and M. E. Fisher, Detailed magnetic behavior of nickel near its Curie point, Physical Review **136**, A1626 (1964).

[36] D. Kim, B. Revaz, B. Zink, F. Hellman, J. Rhyne, and J. Mitchell, Tricritical Point and the Doping Dependence of the Order of the Ferromagnetic Phase Transition of $La_{1-x}Ca_xMnO_3$, Physical Review Letters **89**, 227202 (2002).

[37] J. Yang, Y. Lee, and Y. Li, Critical behavior of the electron-doped manganite $La_{0.9}Te_{0.1}MnO_3$, Physical Review B **76**, 054442 (2007).

[38] M. Phan, V. Franco, N. Bingham, H. Srikanth, N. Hur, and S. Yu, Tricritical point and critical exponents of $La_{0.7}Ca_{0.3-x}Sr_xMnO_3$ (x= 0, 0.05, 0.1, 0.2, 0.25) single crystals, Journal of Alloys and Compounds **508**, 238 (2010).

[39] L. Zhang, D. Menzel, C. Jin, H. Du, M. Ge, C. Zhang, L. Pi, M. Tian, and Y. Zhang, Critical behavior of the single-crystal helimagnet MnSi, Physical Review B **91**, 024403 (2015).

[40] A. Bauer, M. Garst, and C. Pfleiderer, Specific heat of the skyrmion lattice phase and field-induced tricritical point in MnSi, Physical Review Letters **110**, 177207 (2013).

[41] X. Yang, J. Pan, S. Liu, M. Yang, L. Cao, D. Chu, and K. Sun, Critical behavior and anisotropic magnetocaloric effect of the quasi-one-dimensional hexagonal ferromagnet $PrCrGe_3$, Physical Review B **103**, 104405 (2021).

[42] Y. Liu, V. N. Ivanovski, and C. Petrovic, Critical behavior of the van der Waals bonded ferromagnet $Fe_{3-x}GeTe_2$, Physical Review B **96**, 144429 (2017).

[43] S. Mondal, N. Khan, S. M. Mishra, B. Satpati, and P. Mandal, Critical behavior in the van der Waals itinerant ferromagnet Fe_4GeTe_2, Physical Review B **104**, 094405 (2021).

[44] K. Shinde, E. Lee, M. Manawan, A. Lee, S.-Y. Park, Y. Jo, K. Ku, J. Kim, and J. Park, Structural, magnetic, and magnetocaloric properties of R_2NiMnO_6 (R= Eu, Gd, Tb), Scientific Reports **11**, 1 (2021).

[45] X. Yang, J. Pan, K. Sun, Y. Shi, L. Cao, S. Liu, W. Gai, D. Chu, and M. Yang, Critical behavior and magnetocaloric effect of the ferromagnetic Weyl semimetal candidate $Co_{2-x}ZrSn$ single crystals, Journal of Alloys and Compounds **886**, 161118 (2021).

[46] A. Taroni, S. T. Bramwell, and P. C. Holdsworth, Universal window for two-dimensional critical exponents, Journal of Physics: Condensed Matter **20**, 275233 (2008).

[47] P. Sarkar, T. Roy, N. Khan, and P. Mandal, Unconventional critical behavior in a Sm-based ferromagnetic manganite: Effect of tricritical point, Physica B: Condensed Matter **583**, 412050 (2020).

[48] T. D. Thanh, N. T. Dung, N. T. V. Chinh, D. S. Lam, D. A. Tuan, and A. Gamzatov, Magnetic, magnetotransport and critical properties of polycrystalline $Pr_{0.7}Sr_{0.3}MnO_3$ located at the tricritical point, Journal of Alloys and Compounds **884**, 161046 (2021).

[49] G. Lin, H. L. Zhuang, X. Luo, B. J. Liu, F. C. Chen, J. Yan, Y. Sun, J. Zhou, W. J. Lu, P. Tong, Z. G. Sheng, Z. Qu, W. H. Song, X. B. Zhu, and Y. P. Sun, Tricritical behavior of the two-dimensional intrinsically ferromagnetic semiconductor $CrGeTe_3$, Physical Review B **95**, 245212 (2017).

[50] B. Liu, Y. Zou, L. Zhang, S. Zhou, Z. Wang, W. Wang, Z. Qu, and Y. Zhang, Critical behavior of the quasi-two-dimensional semiconducting ferromagnet $CrSiTe_3$, Scientific Reports **6**, 1 (2016).

[51] J. Fan, L. Ling, B. Hong, L. Zhang, L. Pi, and Y. Zhang, Critical properties of the perovskite manganite $La_{0.1}Nd_{0.6}Sr_{0.3}MnO_3$, Physical Review B **81**, 144426 (2010).

[52] Y.-f. Chen, F. Wang, B.-g. Shen, F.-x. Hu, J.-r. Sun, G.-j. Wang, and Z.-h. Cheng, Magnetic properties and magnetic entropy change of $LaFe_{11.5}Si_{1.5}Hy$ interstitial compounds, Journal of Physics: Condensed Matter **15**, L161 (2003).

[53] H. Wada and Y. Tanabe, Giant magnetocaloric effect of $MnAs_{1-x}Sb_x$, Applied Physics Letters **79**, 3302 (2001).

[54] B. Shen, J. Sun, F. Hu, H. Zhang, and Z. Cheng, Recent progress in exploring magnetocaloric materials, Advanced Materials **21**, 4545 (2009).

[55] H. Zhang, X. Zhang, M. Qian, L. Zhang, L. Zhang, S. Chai, and L. Yin, Martensite transformation behavior and magnetocaloric effect in annealed Ni-Co-Mn-Sn microwires, Materials Science and Engineering: B **274**, 115477 (2021).

[56] F.-x. Hu, B.-g. Shen, J.-r. Sun, and G.-h. Wu, Large magnetic entropy change in a Heusler alloy $Ni_{52.6}Mn_{23.1}Ga_{24.3}$ single crystal, Physical Review B **64**, 132412 (2001).

[57] L. Caron, M. Hudl, V. Höglin, N. Dung, C. P. Gomez, M. Sahlberg, E. Brück, Y. Andersson, and P. Nordblad, Magnetocrystalline anisotropy and the magnetocaloric effect in Fe_2P, Physical Review B **88**, 094440 (2013).

[58] X. Yang, J. Pan, K. Sun, Y. Shi, L. Cao, S. Liu, W. Gai, D. Chu, and M. Yang, Critical behavior and magnetocaloric effect of the ferromagnetic Weyl semimetal candidate $Co_{2-x}ZrSn$ single crystals, Journal of Alloys and Compounds **886**, 161118 (2021).

[59] U. Remya, S. Athul, K. Arun, S. Swathi, A. Dzubinska, M. Reiffers, and N. Ramamoorthi, Investigations on magnetic, magnetocaloric and transport properties of $Co_2Ti_{1-x}Sn_{1+x}$ (x = 0.25, 0.5) Heusler alloys, in AIP Conference Proceedings (AIP Publishing LLC, 2021), p. 020086.

[60] S. Yang and X. Ren, Noncubic crystallographic symmetry of a cubic ferromagnet: Simultaneous structural change at the ferromagnetic transition, Physical Review B **77**, 014407 (2008).

[61] Y. Zhang, H. Lu, X. Zhu, S. Tan, W. Feng, Q. Liu, W. Zhang, Q. Chen, Y. Liu, X. Luo, D. Xie, L. Luo, Z. Zhang, X. Lai1, Emergence of Kondo lattice behavior in a van der Waals itinerant ferromagnet, Fe_3GeTe_2, Science Advances **4**, eaao6791 (2018).

[62] H. J. Deiseroth, K. Aleksandrov, C. Reiner, L. Kienle, and R. K. Kremer, Fe_3GeTe_2 and Ni_3GeTe_2–Two New Layered Transition-Metal Compounds: Crystal Structures, HRTEM Investigations, and Magnetic and Electrical Properties, European Journal of Organic Chemistry **2006** (2006).

[63] J. Xu, W. A. Phelan, and C.-L. Chien, Large anomalous Nernst effect in a van der Waals ferromagnet Fe_3GeTe_2, Nano Letters **19**, 8250 (2019).

[64] K. Kim, J. Seo, E. Lee, K.-T. Ko, B. S. Kim, B. G. Jang, J. M. Ok, J. Lee, Y. J. Jo, W. Kang, J. H. Shim, C. Kim, H. W. Yeom, B.-J. Yang and J. S. Kim, Large anomalous Hall current induced by topological nodal lines in a ferromagnetic van der Waals semimetal, Nature Materials **17**, 794 (2018).

[65] J. Macy, D. Ratkovski, P. P. Balakrishnan, M. Strungaru, Y.-C. Chiu, A. F. Savvidou, A. Moon, W. Zheng, A. Weiland, G. T. McCandless, J. Y. Chan, G. S. Kumar, M. Shatruk, A. J. Grutter, J. A. Borchers, W. D. Ratcliff, E. S. Choi, E. J. G. Santos, and L. Balicas, Magnetic field-induced non-trivial electronic topology in $Fe_{3-x}GeTe_2$, Applied Physics Reviews **8**, 041401 (2021).

[66] H. L. Zhuang, P. Kent, and R. G. Hennig, Strong anisotropy and magnetostriction in the two-dimensional Stoner ferromagnet Fe_3GeTe_2, Physical Review B **93**, 134407 (2016).

[67] D. Kim, C. Lee, B. G. Jang, K. Kim, and J. H. Shim, Drastic change of magnetic anisotropy in Fe_3GeTe_2 and Fe_4GeTe_2 monolayers under electric field studied by density functional theory, Scientific Reports **11**, 1 (2021).

[68] N. León-Brito, E. D. Bauer, F. Ronning, J. D. Thompson, and R. Movshovich, Magnetic microstructure and magnetic properties of uniaxial itinerant ferromagnet Fe_3GeTe_2, Journal of Applied Physics **120**, 083903 (2016).

[69] B. Liu, Y. Zou, S. Zhou, L. Zhang, Z. Wang, H. Li, Z. Qu, and Y. Zhang, Critical behavior of the van der Waals bonded high T_C ferromagnet Fe_3GeTe_2, Scientific Reports **7**, 1 (2017).

[70] N. Morali, R. Batabyal, P. K. Nag, E. Liu, Q. Xu, Y. Sun, B. Yan, C. Felser, N. Avraham, H. Beidenkopf1, Fermi-arc diversity on surface terminations of the magnetic Weyl semimetal $Co_3Sn_2S_2$, Science **365**, 1286 (2019).

[71] T. J. Sato, J. W. Lynn, Y. S. Hor, and S.-W. Cheong, First-order transition in the itinerant ferromagnet $CoS_{1.9}Se_{0.1}$, Physical Review B **68**, 214411 (2003).

Chapter 7   Conclusions and Forward Plan

7.1 Conclusions

The purpose of our project was to search for new compensated ferrimagnetic half metal. We started with the investigation of rare-earth-free non-collinear ferrimagnets $Mn_{4-x}Z_xN$ (Z = Cu — Ge and Ag — Sn) and found that the non-collinear ferrimagnetism originates from the structure of the Mn^{3c} (111) Kagome planes with a small Mn-Mn interatomic separation that leads to frustration of the antiferromagnetic nearest-neighbour interactions. The tilt angle of the moments from the (111) planes, $\theta = 20°$, is smaller than previously thought. There is a choice of substitutions to achieve magnetic compensation at room temperature. The efficiency of different elements in this respect rises gradually with increasing valence electron number from group 11 (Cu, Ag) to group 14 (Ge, Sn). The Mn^{1a} moment is not sensitive to the dopants, while the Mn^{3c} moment peaks at Ni and Pd then drops with further valance electron addition. The higher efficiency of elements from 5th period is due to the larger lattice constant, which weakens the hybridization of Mn^{3c} and N and leads to an increase of m_{3c}. In addition, the tilt angle decreases with increasing m_{3c} and composition x. Based on the above results, the Ga compound with compensation at room temperature for x ≈ 0.26 is recommended for high-frequency spintronic applications.

Then, development of new fully compensated ferrimagnetic half metals, which have zero moment but exhibit magnetic order with 100% spin polarization, is targeted for spintronic applications. They are promising for low energy loss communications and high-frequency spintronics. Here, we explore ideal half metals following two directions: one is Mn-based Heusler alloys and the other one is Mn-free alloys.

In Mn-based half metals, the first material we introduced was fully compensated ferrimagnet $Mn_{1.5}V_{0.5}FeAl$, whose parent compound is ferrimagnetic half-metal Mn_2FeAl.

Its compensation and Curie temperatures are very sensitive to the unit cell volume, which is raised by manganese content or heat treatments. The results suggest that when the lattice parameter is less than 5.845 Å, compensation behaviour can be observed. With expanding the lattice parameter, the magnetic compensation disappears and the T_C increases, > 400 K. Then, we moved to another cubic Heusler ferrimagnetic half metal $Mn_2Fe_{1-x}V_xAl$, which is considered as a combination of Mn_2VAl ($Z_t = 25$) and Mn_2FeAl ($Z_t = 22$) with magnetic moments of opposite signs. The d^N- type band gaps of the 3d constituents in the alloys guarantee their half-metallicity, (Mn_2VAl: Mn^{8c} with d^3-type and V^{4b} with d^2-type gaps; Mn_2FeAl: Mn^{4c} with d^3-type and Mn^{4b} with d^5-type gap). The fully compensated ferrimagnetic half metal $Mn_2Fe_{0.75}V_{0.25}Al$ is realized. Through the analysis of its constituents' spin configurations, the mechanism of magnetic compensation was revealed. Knowledge of compensation in half-metals inspired us to develop new ideal fully-compensated ferrimagnetic half-metals with high T_C. The DFT calculations of distinguishing Heusler ordering, electronic structures and sublattice moments for $Mn_2Fe_{1-x}V_xAl$ agree well with our experiments, except for Mn_2FeAl, which is impossible to form with Heusler order in ingots because its equilibrium phase is A13 (β-Mn).

In Mn-free alloys, four Mn-free binaries (V_3Al/Ga) and quaternary Heuslers (CrVTiAl/Ga) with 18 valence electrons and ideally-ordered crystal structures, which have been theoretically predicted to be zero-moment half metals or spin gapless semiconductors, were not made successfully. The hull energy, describing the absolute phase stability, suggests a fully-ordered D0$_3$ binary or any Y-type quaternary variant is never the most stable solution for *any* of these compounds. Therefore, future claims based on first-principles calculations for the discovery of new ternary and higher intermetallic phases with useful physical properties should be critically screened for stability, at least with respect to disorder and known competing phase mixtures on the hull. Nevertheless, light itinerant elements in alloys provide a chance to obtain Mn-free ferrimagnets, through control of the local coordination and bond length. For example, the V magnetism of bcc $Fe_{1-x}V_x$ alloys in different ordered states reveals that the magnetism at V site is determined by the bond length. Generally, the shortest bonds of V sites (< 2.9 Å) are nonmagnetic; those with the longest

bonds (> 3.8 Å) are ferromagnetic; the V sites with bonds of 2.9 – 3.8 Å behave antiferromagnetically. In B2 ordered $Fe_{0.5}V_{0.5}$ ferrimagnetism is realized due to the antiparallel alignment of Fe and V moments. Itinerant alloys including weakly-polarized transition elements like Pt, Rh and Pd, display similar magnetic properties based on crystallographic and atomic order. Therefore, the magnetic moment of weakly-polarized elements provides an innovative way to develop new ferrimagnetic applications.

At last, we presented a variety of evidence from static magnetic measurements that the ferromagnetic phase transition at 119.8 K in CoS_2 is weakly first-order, which is distinguished by a tricritical point. The weakly first-order transition found in low fields is suppressed by an applied magnetic field of order 100 mT. The calculated magnetocaloric effect near T_C is large in view of the low spin of S = ½ of the cobalt, which may be useful for magnetocaloric applications.

7.2 Forward plan

7.2.1 Forward plan on ferrimagnet Mn_4N

From our experimental and theoretical study of the rare-earth-free non-collinear ferrimagnetic metals $Mn_{4-x}Z_xN$, the efficiency of different dopants in magnetic compensation rises gradually with increasing valance electrons from group 11 (Cu, Ag) to group 14 (Ge, Sn). Bulk Mn_4N with Ga dopants presents compensation at room temperature. Therefore, further efforts are required to grow $Mn_{4-x}Ga_xN$ thin films and explore their magnetic and transport properties. Thin film suitable for spintronic devices should have perpendicular anisotropy.

7.2.2 Forward plan on fully-compensated Mn-based ferrimagnets

The data collected so far indicate that the $Mn_{1.5}V_{0.5}FeAl$ (MVFA) compound is a promising fully-compensated Heusler half metal. The bulk material shows good properties as the theory predicted. Experimental techniques, such as neutron TOF (time of flight) diffraction patterns and Mössbauer spectroscopy (at room temperature), failed to reveal any sublttice

moments [1]. The way to obtain the information of the atomic sites is to make a single crystal. Now I am collaborating with Ross Smith in our group to grow MVFA thin films to investigate the sublattice behaviours at 4b and 4c/4d sites. We expect MVFA thin films will show similar properties to MRG, such as Hall effect, Kerr effect etc.

The other fully compensated ferrimagnetic half metal $Mn_2Fe_{1-x}V_xAl$ is obtained in $x = 0.25$ not in the expected alloy with $x = 0.33$ because of the imperfect atomic ordering. Annealing is not suitable for Fe-rich alloys due to the A13 structure. The higher difference of electronegativity between Co to Mn than that between Fe to Mn indicates that Co doping might be efficient to stabilize the XA structure and improves compensation as well as Curie temperatures. I'm going to prepare $Mn_2Fe_{1-x}V_xAl$ with Co doping to improve the compensation temperature to room temperature. Once the ideal alloy is obtained, then we will transfer it to thin films for spintronics.

7.2.3 Search for full-Heusler half metals without Mn

There were so many theoretically predicted Heusler compounds that seemed promising half metals with zero moment, but very few have been found to really exist. The limitation of Mn-based alloys is Mn diffusion into the MgO barrier that restricts the spintronic applications. Therefore, I will search harder for a Heusler compound without Mn to obtain a half metal with a low moment, compensation, high Curie temperature and high spin polarization, which would be an ideal Heusler half metal. To obtain a half metallic compound with compensation behaviour is also our expectation. The potential candidates include ternary alloy V_2FeAl, V_2FeGe, CoFe-based quaternary alloy, and VCrFeAl or VCrFeGe ones.

7.2.4 Verify the topological character of CoS_2 in the first-order transition

Since CoS_2 has been recently identified as a topological ferromagnet [2], the topological characteristics related to its physical properties attract our attention. Further, we would like to test the idea that the first-order transition has a topological character. Here, we

would look at the critical behaviour of truly half-metallic CoS_2 produced by a small amount of iron substitution [3,4]. Fe substitution behaves like the holes doping and moves the E_f down, which is close to the Weyl points and leads to loss of topological protection. Therefore, Fe doped compound should not be first-order. That is to say the influence of the Weyl points found in CoS_2 [2] is on the surface states, which should not have any measurable influence on the bulk specific-heat.

References

[1] R. Stinshoff, A. K. Nayak, G. H. Fecher, B. Balke, S. Ouardi, Y. Skourski, T. Nakamura, and C. Felser, Completely compensated ferrimagnetism and sublattice spin crossing in the half-metallic Heusler compound $Mn_{1.5}FeV_{0.5}Al$, Physical Review B **95**, 060410 (2017).

[2] N. B. Schröter, J. A. Krieger, D. Pei, Tianlun Yu, Samuel Stolz, T. Schmitt, P. Dudin, T. K. Kim, C. Cacho, A. Schnyder, A. Bergara, V. N. Strocov, F. de Juan, M. G. Vergniory, L. M. Schoop, Weyl fermions, Fermi arcs, and minority-spin carriers in ferromagnetic CoS_2, Science Advances **6**, eabd5000 (2020).

[3] C. Leighton, M. Manno, A. Cady, J. W. Freeland, L. Wang, K. Umemoto, R. M. Wentzcovitch, T. Y. Chen, C. L. Chien, P. L. Kuhns, M. J. R. Hoch, A. P. Reyes, W. G. Moulton, E. D. Dahlberg, J. Checkelsky and J. Eckert, Composition controlled spin polarization in $Co_{1-x}Fe_xS_2$ alloys, Journal of Physics: Condensed Matter **19**, 315219 (2007).

[4] I. Mazin, Robust half metalicity in $Fe_xCo_{1-x}S_2$, Applied Physics Letters **77**, 3000 (2000).